UNIVERSITÀ degli STUDI di CATANIA

UNIVERSITÀ DEGLI STUDI DI PALERMO

DOTTORATO DI RICERCA IN
SCIENZA DEI MATERIALI E NANOTECNOLOGIE
XXXIII CICLO

ANGELA TERRACINA

Chemical and Mechanical Stability of Copper Carboxylate Metal-Organic Frameworks

Supervisor:
Prof. Gianpiero BUSCARINO
(Unipa)

Coordinatore:
Prof. Giuseppe COMPAGNINI
(Unict)

TESI PER IL CONSEGUIMENTO DEL TITOLO DI DOTTORE DI RICERCA
November, 2020

A nonna Pina

e nonno Pino

After sleeping through a hundred million centuries we have
finally opened our eyes on a sumptuous planet, sparkling
with color, bountiful with life. Within decades we must
close our eyes again. Isn't it a noble, an enlightened way of
spending our brief time in the sun, to work at understanding
the universe and how we have come to wake up in it?

Richard Dawkins

Contents

Introduction

Metal-Organic Frameworks (MOFs) are a new class of porous crystalline materials, with great potentialities in a wide range of industrial applications. Composed of particular combinations of metallic knots and organic linkers, more than 70,000 different structures are currently recognized as MOFs. Their specific surface area typically exceeds 1,000 m^2/g, reaching sometimes even 10,000 m^2/g. Such a remarkable porosity is due to the possibility to combine up to 50 Å long *extended* organic molecules via different possible configurations, arising from the coordination geometry of the metallic junctions. If the metallic junction is composed of a polynuclear cluster arising from a *chelation* of two or more metal ions, it is called *secondary building unit.*

Such an extremely high surface area opens the doors for applications in gas storage (H_2, CH_4, ...) and then in the field of renewable energies. Furthermore, the metal sites may have a particular affinity with some gaseous substances, allowing to selectively adsorb pollutants like CO_2, NH_3, cyclohexane and many others, leading to potential applications in the removal of toxic industrial chemicals.

However, only very few applications have been already introduced in commercial use, mainly because of two big challenges: the extremely sensitivity to water (even to air moisture) and the typical poor packaging of MOFs, generally synthesized in the form of powders with low bulk density. Both the issues have been constantly investigated by researches, but several significant aspects are still unclear, like the hydrolysis/dissociation mechanisms induced by the interaction with water molecules or even finding cheap methods which allow to produce water-resistant or well-packaged MOFs without loss in porosity, crystallinity or performance.

In this thesis both these topics are covered, offering new useful points of view. Three different MOFs have been studied, composed of the same *secondary building unit* but different organic linkers which lead to markedly diverse properties. One of these MOFs, called HKUST-1 or Cu-BTC, has been one of the most investigated MOFs since its first appearing in a scientific journal in 1999. In fact, it is widely used as model for MOF research because of the ease of getting a high quality industrial-scale HKUST-1 material and for its peculiar properties as selective adsorbent. The other two MOFs, known as STAM-1 and STAM-17-OEt, are much more recent but very promising, especially in the research field. In fact, despite the similarities with HKUST-1, they resulted to have a high water stability and a flexible crystalline structure, which means that the crystal undergoes spontaneous lattice transitions when subjected to determined external stimuli. However, both their bulk densities and specific surface areas are very low like other

MOFs, and the reasons and the limits of their water stability are still unclear. A deeper understanding of this aspect would give a significant boost to the search of stable MOF structures.

The purpose of this thesis has been to deepen the stability limits of carboxylate MOFs like HKUST-1, in particular the *chemical* and the *mechanical stability*, trying to establish satisfying protocols that can enable to have a more compact and stable MOF. The comparison of the HKUST-1 properties with those of other similar MOFs like STAM-1 and STAM-17-OEt has been precious.

The thesis is divided in two parts. In the first one the most important theoretical backgrounds are discussed, with the aim to provide the fundamentals of the experimental techniques involved (chapter 1) and the current state of the art of the MOF research field, particularly focused on the topic above mentioned (chapter 2). The properties of the three different MOFs examined are discussed in detail, as well as their water stability and the effects of the mechanical compaction (when previously covered by literature).

Part two of the thesis focuses on my contribution in this research field. After chapter 3, where the synthesis processes and the treatments performed on the MOF samples are described, as well as the experimental setup employed and the measurement conditions used, the most significant results are discussed. More in detail, chapter 4 shows a systematic comparative study on the hydration effects on the three MOFs, necessary to understand the changes taking place in the materials when they are handled in air. Chapter 5 focuses on the effects of the mechanical pressure on HKUST-1, establishing the best compromise between packaging and correlated induced damages. Chapter 6 investigates on the water stability of three different forms of HKUST-1: monoliths, tablet obtained by mechanical compression and powder. Finally, the last two chapters are focused on the MOF STAM-17-OEt. In particular, chapter 7 reports on the investigation about the tableting of the powder material, whereas chapter 8 faces with the properties of toxic air removal of this MOF, studying the loading capacity and the structural stability of the material exposed to ammonia, when it is in powder form (single component) or grown into the pores of active carbon (composite).

Part I

Chapter 1

Theoretical background

In this chapter, a focused overview about the physics involved in the materials studied in this thesis and the experimental techniques employed is given. A very significant portion of the experimental results of this thesis has been obtained by the study of the magnetic properties of the MOFs. Such magnetic properties arise from the copper(II) ions present in the framework, arranged in dimeric cupric tetracarboxylate units. For this reason, a large part of the chapter, including sections 1.1 and 1.2, is dedicated to the magnetism in matter and then also to electron paramagnetic resonance (EPR) spectroscopy. Section 1.3 concerns the nuclear magnetic resonance (NMR) spectroscopy, theoretically very close to EPR technique, but which allows to monitor also the organic components of the MOFs. Similarly, Raman spectroscopy, treated in section 1.4, has made possible to check the whole material by studying the vibrational bands. Bulk techniques as X-ray powder diffraction (section 1.5) and nitrogen adsorption (section 1.6) have been also necessary for the evaluation of the crystallinity or porosity during the main steps of the experimental treatments induced in the samples, respectively. Lastly, section 1.7 describes the fundamentals of amplitude modulation AFM, a scanning technique which allows to investigate the surface morphology of the materials studied, while section 1.8 shows the main details on the thermogravimetric analysis (TGA) technique.

1.1 Magnetic properties of solids

Solids may show different magnetic responses when subjected to external magnetic fields. They may have either intrinsic permanent magnetic dipole moments or magnetic dipole moments induced by the applied magnetic field.[1] Conventionally, depending on the response of the material to the magnetic induction field $\mathbf{B}$, materials are grouped under the following three main categories:[1–3]

- diamagnetism;

- paramagnetism;

- ferromagnetism.

In order to study of the effects induced by $\mathbf{B}$ on the materials, it is opportune to define a field $\mathbf{H}$ as follows:

$$\mathbf{H} = \mathbf{B}/\mu_0 - \mathbf{M} \tag{1.1}$$

where, under the assumption of parallel fields, μ_0 is a scalar named *vacuum magnetic permeability* and $\mathbf{M}$ is the *magnetization*, namely the magnetic dipole moment per unit volume.[1,4] The field $\mathbf{H}$ depends solely on the conduction currents external to materials and consequently it is not influenced by the magnetic responses of materials to the field $\mathbf{B}$.[4] Magnetization $\mathbf{M}$ is in turn linked to the field $\mathbf{H}$ by the equation[1]:

$$\mathbf{M} = \chi\mathbf{H}. \tag{1.2}$$

For sake of clarity, hereafter the field $\mathbf{B}$ will be simply called *magnetic field*.

For a large variety of materials the dimensionless proportionality factor χ named *susceptibility* is a simple scalar quantity. In the following, we will always implicitly consider *isotropic* systems, thus having scalar susceptibilities.[2] The positive or negative sign, the temperature dependence and other characteristics of the susceptibility determine the magnetic behavior of the material.[1–3]

Diamagnetism is characterized by a magnetization which is opposite in direction to $\mathbf{B}$: for this reason, diamagnetic materials has a negative susceptibility. Diamagnetism arises straight from the *Lenz's law* and for this reason it constitutes an underlying property of matter; in fact, all atoms and ions produce a diamagnetic contribution because caused by the interaction of the magnetic field with the motion of electrons in their orbits.[1,3] Except in the case of superconductors that exclude all fluxes from their interiors and that can be considered perfect diamagnets in which $\mathbf{H}$=0 and χ =-1, $|\chi|$ is typically less than 10^{-5} and essentially independent of temperature.[1–3]

Paramagnetism pertains to those substances in which there are permanent magnetic dipole moments, associated with the intrinsic electron spin and the orbital motion of the electrons, that tend to line up in the direction of $\mathbf{B}$. The susceptibility is then positive, with typical magnitude of $\chi \simeq 10^{-4}$.[1–3] Since diamagnetic effects are present also in paramagnetic materials, χ can be written as the algebraic sum of a *diamagnetic susceptibility* χ^D and of a *paramagnetic susceptibility* χ^P: if χ^D dominates, the solid will be weakly repelled from $\mathbf{B}$ and the material is said to be diamagnetic; otherwise if χ^P is the leading contribution, the solid will be weakly attracted by the external magnetic field $\mathbf{B}$ and said paramagnetic.[1,3] Since for paramagnetic materials χ^D is generally negligible, in the following we will refer to χ^P simply with χ.

The tendency of permanent magnetic dipole moments to line up parallel to $\mathbf{B}$ is in opposition to the thermal motion effect which tends to mess up their directions.[1] For this reason, it can be proved that the susceptibility χ is temperature dependant, and it follows the so-called *Curie law*:

$$\chi = \frac{C}{T} \tag{1.3}$$

where $C = \frac{\mu_0 n \mu^2}{k}$ is a positive constant which strictly depends from the specific material, by the magnetic dipole moment μ and by the number of unpaired magnetic dipole moments per unit volume n; k is the Boltzmann constant.[1] This means that χ (and then M) increases on lowering the temperature.

The third category consists of *ferromagnetic materials*: they are characterized by a spontaneous magnetization $\mathbf{M}$ present even if no external field $\mathbf{B}$ is present.[1–3] These substances are strongly attracted by relatively weak fields and show susceptibilities as large as 10^5. They can be considered paramagnetic materials in which the atoms or molecules are able to exhibit a cooperative behavior within the so-called *domains*.[1,3] Generally, if subject to high temperatures which constitute a high disordering factor, the spontaneous magnetization vanishes and the solid become paramagnetic.[2] The *transition* temperature is called *Curie temperature* θ and it has a specific value for each material. Then, for $T > \theta$, the susceptibility of this kind of materials follows the following *Curie-Weiss law*[2]:

$$\chi = \frac{C}{T - \theta}. \tag{1.4}$$

Exchange interaction

The Curie-Weiss law of eq. 1.4 is valid in the event that the paramagnetic centers are well isolated from each other from a magnetic viewpoint.[3,5] If an interaction between the magnetic centers is present, such law has to be properly modified.[3,5] One of these cases is that of the magnetically coupled dimers composed of S=1/2 spins, in which the so-called *exchange interaction* has to be taken into account.[3,5,6]

Figure 1.1 shows four different cases involving four electron systems.[7] The differences are determined by the electronic disposition in the highest occupied energy levels of the given system.[7] If the highest occupied electronic level is orbitally non degenerate and two electrons are present, the ground state must be a *spin singlet* for the Pauli's exclusion principle (figure 1.1(a)).[7] However, if one of the two electrons is excited to an higher unoccupied orbital, the system may maintain the singlet state (figure 1.1(b)) or, under appropriate conditions, it may undergo a change of multiplicity by an intersystem crossing to a metastable *triplet state* (1.1(c)).[7] Otherwise, if the highest occupied electronic level has at least a two-fold orbital degeneracy, a triplet ground state is admitted (1.1(d)).[7]

All of the previous situations involving two electrons can be represented using the so-called *uncoupled representation* and then expressing the four different possible spin
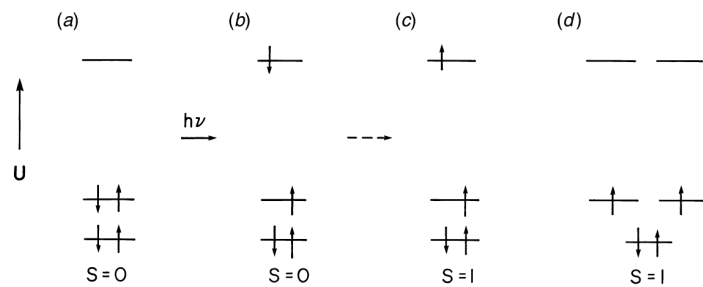

FIGURE 1.1: Energy levels and spin configurations for an example system with a total of four electrons. The lowest levels symbolize filled orbitals. (a) Singlet ground state; (b) singlet state after electronic excitation; (c) metastable triplet state after a radiationless process; (d) triplet ground state. Adapted from ref. [7].

states as simple product of the individual spin states $\alpha(1)$ and $\beta(1)$ for the first electron and $\alpha(2)$ and $\beta(2)$ for the second one, thus obtaining four combinations.[7] However, when the two electron interact considerably, the *coupled representation* may be more advantageous to combine the individual spin states.[7,8] The functions obtained are either symmetric or antisymmetric with respect to the exchange of the labels *1,2* representing the electrons.[7] More in detail, the antisymmetric function

$$\frac{1}{\sqrt{2}}\big[\alpha(1)\beta(2) - \beta(1)\alpha(2)\big]$$

has a S=0 spin state and then no multiplicity and it constitutes the *singlet state*.[7] The antisymmetric functions

$$\begin{cases} \alpha(1)\alpha(2) \\ \frac{1}{\sqrt{2}}\big[\alpha(1)\beta(2) + \beta(1)\alpha(2)\big] \\ \beta(1)\beta(2) \end{cases}$$

have S=1 spin state and then multiplicity equal to 2S+1=3, constituting the *triplet state*.[7] Singlet and triplet states are split apart in energy by the **electron-exchange interaction**, which can be described by the spin hamiltonian

$$\hat{\mathscr{H}}_{exch} = -\sum_{ij} J_{ij}\hat{S}_{1i}\hat{S}_{2j} = -\frac{1}{2}(\hat{\mathbf{S}}_1^T \cdot \mathbf{J} \cdot \hat{\mathbf{S}}_2 + \hat{\mathbf{S}}_2^T \cdot \mathbf{J}^T \cdot \hat{\mathbf{S}}_1)\ , \quad (i,j = x,y,z) \qquad (1.5)$$

where $\hat{\mathbf{S}}_1$ and $\hat{\mathbf{S}}_2$ are electron-spin operators for electrons 1 and 2 respectively and $\mathbf{J}$ is a 3×3 tensor which takes into account the electric/coulombic interaction between the two unpaired electrons (but not the magnetic one).

Considering only the isotropic part of the hamiltonian of eq. 1.5 and introducing the *isotropic electron-exchange coupling constant* (or only *coupling constant*) $J_0 = \frac{1}{3}tr(\mathbf{J})$, our hamiltonian is simply

$$(\hat{\mathscr{H}}_{exch})_{iso} = -J_0\,\hat{\mathbf{S}}_1^T \cdot \hat{\mathbf{S}}_2\,. \qquad (1.6)$$

To a first approximation, the value of J_0 is given by the following exchange integral

$$J_0 = 2\,\langle\phi_a(1)\phi_b(2)|\,\frac{e^2}{4\pi\epsilon_0 r}\,|\phi_a(2)\phi_b(1)\rangle \qquad (1.7)$$

where ϕ_a and ϕ_b are two different normalized spatial molecular-orbital wavefunctions evaluated for non-interacting electrons at r distance and ϵ_0 is the permittivity of the vacuum.[7]

Figure 1.2(a) shows the common scheme of a generic system composed of a S=0 singlet ground state and a S=1 triplet excited state, separated by an energy gap J_0. More in detail, J_0 is equal to $E(S = 0) - E(S = 1)$: thus, the sign of the coupling constant determines if the ground state is either the singlet or the triplet state.[7]
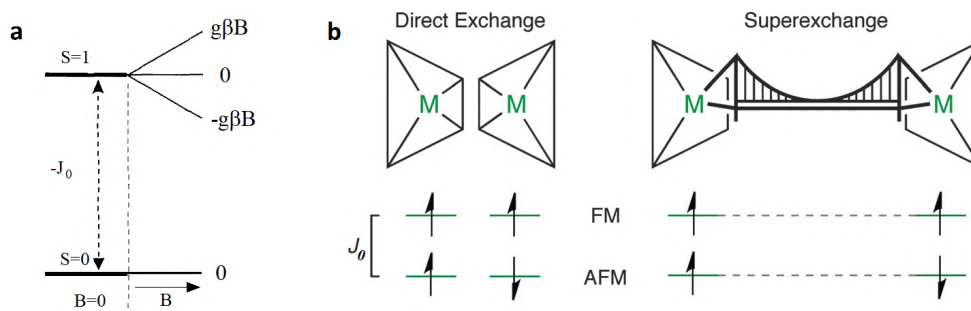
FIGURE 1.2: (a) Generic scheme of a system composed of a singlet ground state and a triplet excited state, separated by a distance in energy commonly indicated with J_0. (b) Differences between the direct magnetic exchange, in which two atoms interact in close prossimity, and the superexchange, where the interaction is mediated by diamagnetic bridging motifs. The exchange interaction can lead to a ferromagnetic (FM) or antiferromagnetic (AFM) coupling. Adapted from refs. [3] and [6].

In general, in the simple case of two identical species with S=1/2, three cases can occur:[3,5]

- if the interaction is small enough, the two spins are fully uncorrelated and they can be described as simple paramagnetic centers following the Curie law and then there is a null coupling constant $J_0 = 0$;
- if the two species are coupled originating a ground single state and a triplet state thermally populated, the coupling is said to be *antiferromagnetic* (as in figure 1.2) and $J_0 < 0$;
- in the opposite case, in which there is a ground triplet state and a singlet state thermally populated, the coupling is said to be *ferromagnetic* and $J_0 > 0$.

The *direct* exchange interaction, involving spatial superposition of the electronic wave functions, is rare; the most common case is that in which the two centers, typically paramagnetic metal ions, interact through ancillary diamagnetic atoms or groups of atoms (see figure 1.2(b)).[3,5,6] The latter situation is referred to as *superexchange*.[3,5,6] A relevant example is that of the copper(II) dinuclear compounds, that in 95% of the cases show antiferromagnetic interactions.[3,5] The magnetic interaction phenomenon within a molecule was discovered in 1951 precisely on a dimeric copper(II)-based compound, and it will be deepened in section 1.1.2.

1.1.1 Magnetic properties of copper(II) compounds

The three MOFs investigated in this thesis are copper-based materials. For this reason, it is important to briefly report on the main structural properties of copper when involved in compounds.

Cu^{2+} is a $3d$ transition metal ion with a d^9 electronic configuration, which allows a wide structural diversity of Cu^{2+} complexes, spacing from mononuclear, to binuclear or polynuclear species.[7,9,10] Such diversity depends on the versatility of its electronic configuration: in fact, the free ion is characterized by an unpaired electron and a five-fold degeneracy of the d orditals.[7,9,11]

The d orbitals fall into two classes: d_{xy}, d_{xz} and d_{yz}, pointing between the x, y and z axes, are labeled t_{2g} orbitals, whereas d_{z^2} and $d_{x^2-y^2}$ are named e_g orbitals and point along one and two of the axes, respectively.[11] The properties of the complexes based on copper (but also more in general of the transition metals) arise on the ways the orbital degeneration is removed.[9,11] The first orbital splitting in these two d subgroups is ensured by the presence of the *ligands*: in the *crystal field theory* the neighboring orbitals are modeled as negative points charges, whereas in the improved *ligand field theory* the molecular orbitals of the ligands overlap those of the central ion. The consequent removal of the degeneration can be described in terms of the symmetry of the complex originated, which in turn depends also on the coordination ion.[11]

Figure 1.3 shows the orbital spitting in the two groups e_g and t_{2g} caused by the establishment of an octahedral symmetry. If a free ion can be imagined as a spherically
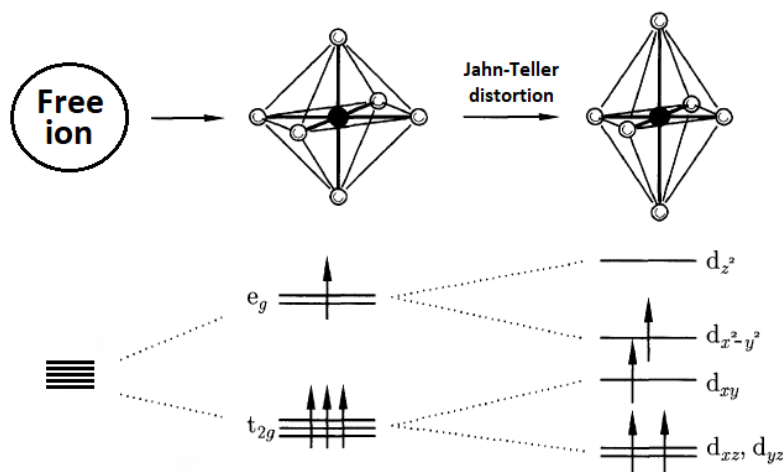
FIGURE 1.3: The effect on a metal transition ion of a crystal field in an octahedral environment and of a Jahn-Teller distortion leading to an *elongated* octahedral symmetry. Adapted from ref. [11].

symmetric environment, the octahedral symmetry imposes six discrete point charges (each lying at the vertex of an octahedron) on the surface of such sphere, making different the electrostatic interaction in the two groups of orbitals.[11] In the case of the tetrahedral symmetry, the order of the d orbital groups is the opposite of that shown in figure 1.3.

A further degeneration removal arises from the *Jahn-Teller effect*: H. Jahn and E. Teller demostrated that a non-linear molecule in a degenerate orbital state cannot be stable, but it distorts itself to obtain a splitting of the energy states, removing the degeneracy and lowering the energy of the system.[12–14] For this reason, the Jahn-Teller effect has important structural and electronic consequences in copper(II)-based complexes.[12–14] In the system of figure 1.3, for example, a distortion which leads to an *elongated* octahedron as final configuration is shown, with two longer axial and four shorter equatorial bond distances.[11,12,15,16] In the opposite case of a compressed octahedron, the Jahn-Teller effect produces an inverse order of the orbitals of each group.[12]

Mononuclear copper(II) complexes. A typical Cu^{2+} mononuclear compound is the hexaaquacopper(II) $[Cu(H_2O)_6]^{2+}$ complex ion, shown in figure 1.4.[12,15–20] It consists of a Cu^{2+} ion coordinated with 6 molecules of water in a Jahn–Teller elongated octahedral (O_h) geometry.[12,15–18] The central Cu^{2+} ion has an unpaired electron, which

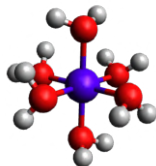FIGURE 1.4: $[Cu(H_2O)_6]^{2+}$ mononuclear Cu(II) complex. Produced from ref. [18].

confers to the compound paramagnetic characteristics. For this reason, in presence of a external magnetic field **B**, a diluted system of such mononuclear complexes typically follows the Curie trend.[7,9,11,18]

Dinuclear copper(II) compounds. We have already mentioned that if some polyatomic ligands provide appropriate connection pathways for exchange coupling between paramagnetic metal ions not directly bonded, a ferromagnetic or antiferromagnetic coupling may be established. This is the case of the compound with an "*anomalous*" magnetic susceptibility found by Guha in 1951 and then deepened by Bleaney and Bowers, that have elaborated a new law for the description of the temperature dependence of the magnetization.[3,10,21,22] Such compound was known at that time as *copper(II) acetate monohydrate* and it involves two Cu^{2+} ions coordinated in a square-pyramidal fashion by four oxygens, arising from the O-C-O carboxylate bridges (figure 1.5).[3,10,23] Its dimeric complex metallic core with structure $Cu_2(-COO)_4$ is typically known as *paddlewheel* unit, especially in the field of MOFs.[24] The two coppers are separated by a distance of ~ 2.64 Å.[3] A fifth out-of-plane bond is present on the two Cu^{2+} and it is
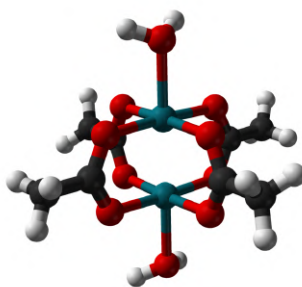
FIGURE 1.5: Copper acetate monohydrate. Produced from ref. [3].

generally occupied by a water molecule.[24] Omitting the water ligands, the paddlewheel can be represented as two squares connected by four carboxylates whereas, when found involved in a framework, the paddlewheel is like a square building unit with four points of extension. Copper acetate monohydrate is also characterized by methyl groups linked to the carbons of the carboxylate bridges (figure 1.5).[3,10]

In principle, each dimeric complex has different possible spin states: the magnetic properties of these compounds may depend by the nature of the bridging, by the axial ligands and by the coordination geometry around the copper atoms.[22] A schematic representation of the energy levels of a dinuclear system is given in figure 1.6.[25] In
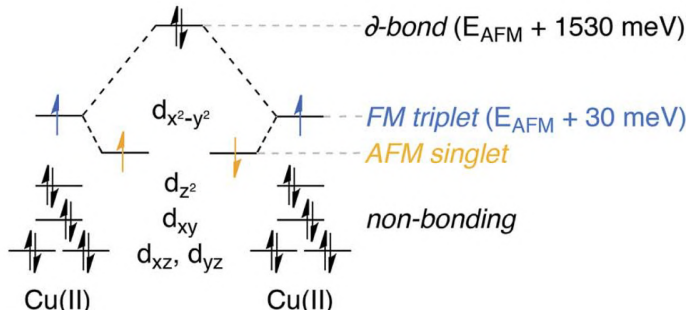
FIGURE 1.6: Possible spin states for a dimeric compound composed of two Cu^{2+} ions. Different configurations for the two unpaired electrons may lead to an antiferromagnetic (AFM) or a ferromagnetic (FM) coupling or to the establishment of a δ bond.[25]

general, three main types of interaction between the copper ions may be found in the paddlewheel: ferromagnetic coupling (by direct-exchange), antiferromagnetic coupling (by super-exchange), and formation of a δ bond, even though the latter is the least energetically favored.[23,25–27] Furthermore, experimental investigations on the structure of the paddlewheel unit pointed out that the metal-metal distance is too large for a direct exchange. In line with this expectation, the experiments on copper acetate monohydrate have shown that the dominant mechanism is the super-exchange interaction: the two unpaired electrons of the copper ions are coupled showing an antiferromagnetic character, with a magnitude of $J_0 \approx$ -300 cm^{-1}.[3,6,10,22,23] About 95% of copper(II) dinuclear compounds show antiferromagnetic interaction.[3]

It has been found that such rather large number could be due to the electronic structure of the carboxylate bridges: in fact, the $d_{x^2-y^2}$ orbitals of the two Cu^{2+} ions have a tail on the orbitals of the bridges, and through them the two unpaired electrons can interact.[23] More in detail, the exchange takes place through the $2p$ orbital of the oxygens, the $2p$ orbital of the carbon and the specific d orbital of the metal centers.[28,29] This means that if a Cu-O-C-O-Cu bridge bends decreasing the symmetry, then the overlap between the $d_{x^2-y^2}$ of the coppers and the $2p_x$ orbitals of the oxygens changes, leading in turn to a change in the J_0 value.[23] In general, very efficient magnetic interactions are observed when the binding bridges between the metal centers are short and well conjugated; in particular, carboxylates are among the preferable bridges, but also other types of connection may take place, like π-π interactions.[9,28,30] The presence of a super-exchange interaction leads to a new temperature dependence for the susceptibility, which is shown in the next subsection.

1.1.2 Bleaney-Bowers law

As already mentioned, in 1952 Bleaney and Bowers found a new dependence for the susceptibility from the temperature for this type of centers, which takes into account the effect of the population in the excited state of the coupled system on increasing the temperature.[3,5,10] The magnetic susceptibility expression derived by Bleaney and Bowers is:[3,7,10]

$$\chi = \frac{2Ng^2\beta^2}{kT[3 + exp(-J_0/kT)]} \, .\tag{1.8}$$

For $J_0 < 0$ (or else in the antiferromagnetically coupled systems), χ tends to zero at $T \approx 0$ because at low temperature the diamagnetic ground state is the only thermally populated, whereas it shows a maximum at higher T.[3] An example of this kind of trend is given in figure 1.7.
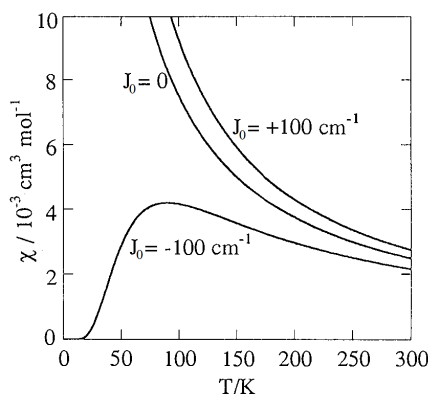
FIGURE 1.7: χ versus T curves in accordance with Bleaney-Bowers law for three hypothetic systems characterized by $J_0 = 0$ and $J_0 = \pm 100$ cm^{-1} (Zeeman factor imposed equal to 2 for sake of simplicity).[3]

1.2 Electron paramagnetic resonance (EPR) spectroscopy

Spectroscopic techniques, based on the study of the interaction between electromagnetic radiation and matter, are one of the most important sources from which our knowledge of the structure of molecules arises.[7,31–33] A common procedure is analyzing the *absorption spectra*, or else the measure of the attenuation of a beam of electromagnetic radiation upon crossing the material versus its frequency or wavelength.[7,31,32] Since any given photon with frequency ν carries an energy amount equal to $h\nu$ (where h is the *Planck constant*), each absorption band found in a spectrum at that given frequency ν represents a transition between two energy levels of the material investigated.[7,31,33] In EPR spectroscopy the frequency range 1÷1000 GHz is generally used.[7,31] In most spectroscopic studies, molecules interact with the electric field component of the electromagnetic radiation, if the necessary conditions are satisfied. Otherwise, in magnetic-resonance spectroscopy, a molecule containing a magnetic dipole interacts with the oscillating magnetic component of the light.[7,31,33]

The presence of a net electron angular momentum is a necessary condition for the applicability of EPR spectroscopy.[7,31] Each electron possesses an intrinsic magnetic dipole moment associated with its spin angular momentum but, since in most systems electrons are coupled in pairs with a net moment equal to zero due to the *Pauli exclusion principle*, only species containing one or more unpaired electrons possess a net spin moment.[7,31,34] In principle, an electronic magnetic moment may also arise from its orbital motion. However, this contribution is usually very small.[7,31]

Fixing the direction of the external applied magnetic field **B** along z, the component μ_z of the electron spin magnetic moment along this direction can be expressed as

$$\mu_z = -g_e\beta_e M_S \tag{1.9}$$

where $\beta_e = |e|\hbar/2m_e \approx 9.274 \times 10^{24}$ J T^{-1} is the Bohr magneton, $g_e \approx 2.002$ is the free-electron *spectroscopic splitting* or *Zeeman factor* and both are defined as positive quantities.[7,8,35] M_S indicates the z component of the electron-spin angular momentum that, for a single free or unpaired electron, can assume only the two possible values $+\frac{1}{2}$ and $-\frac{1}{2}$.[7] The individual-particle magnetic energy U is proportional to the magnetic moment and can be expressed as follows:[7,8,31,35]

$$U = -\mu_z B = g_e\beta_e B M_S \,. \tag{1.10}$$

Then, for a single unpaired electron:[7,8,34–36]

$$U = \pm\frac{1}{2}g_e\beta_e B \,. \tag{1.11}$$

It follows that the separation ΔU of two adjacent energy levels can be then expressed as:[7,8,31,34–36]

$$\Delta U = U_{upper} - U_{lower} = g_e\beta_e B \,. \tag{1.12}$$

ΔU increases linearly with the magnetic field.[7,8,31,35,36] A representation is given in figure 1.8, which concerns the simplest system which can be studied by magnetic resonance: a free electron with spin S=1/2 subjected to a external magnetic static field B.[7,31] The application of the field B causes a separation of the earlier degenerate energy states of the electron, that expands on increasing the magnitude of B.[7,31,34] Called ν the frequency of the incident electromagnetic beam, the resonance and then the transition between the two energy levels occurs when ΔU is equal to the energy of the photon, or else

$$\Delta U = g_e\beta_e B = h\nu \tag{1.13}$$

where in this case B indicates the magnetic static field value which satisfies the resonance condition.[7,31]

Figure 1.9(a) shows a standard absorption line with Lorentzian line shape as a function of the magnetic static field.[31] However, it is not the common aspect of an EPR spectrum. In fact, as it will be explained more in detail in section 3.2.1, in order to
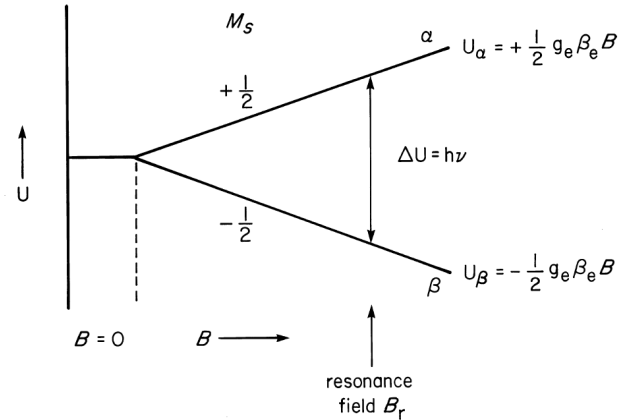
FIGURE 1.8: Energy-level scheme for a simple system consisting of a free electron showing EPR absorption under the effect of an applied magnetic field B.[7]
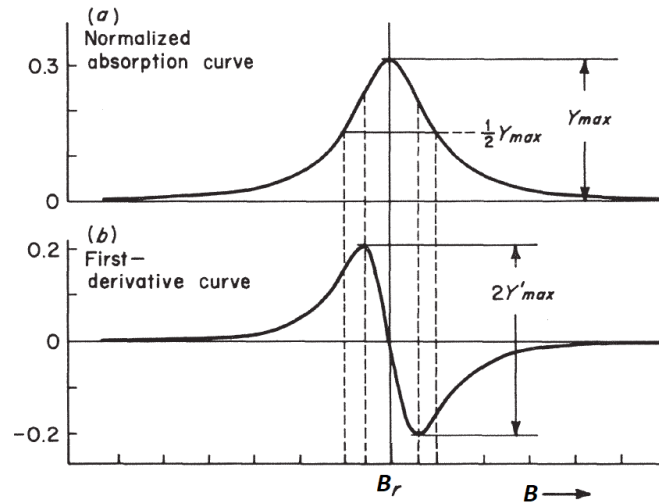
FIGURE 1.9: An example of (a) absorption spectrum following a Lorentzian line shape and (b) its correspondent first-derivative spectrum. Adapted from ref. [31].

reduce the signal-to-noise ratio, a secondary modulation field with a typical frequency of 100kHz is generally applied to the static magnetic field.[31] The output signal recorded by the detector will be then a signal with an amplitude modulated at 100 KHz (further details in section 3.2.1).[31] If the amplitude of this modulation field is small enough compared with the linewidth of the absorption curve, the amplitude of the detected 100-kHz output signal will be proportional to the slope of the absorption curve. In other words, for sufficiently small modulation amplitudes, the output signal will closely follow the first derivative of the absorption signal.[31] A common generic EPR line is then represented by figure 1.9(b).[31] It follows that the determination of the intensity of a line requires two consecutive integrations of the first-derivative spectrum.[31]

1.2.1 Spin relaxation and saturation of the absorption

As explained so far, EPR signal involves the absorption of electromagnetic radiation at a given frequency ν and under a static magnetic field of intensity B. Generally

the radiation source, usually a microwave oscillator, is characterized by an oscillating magnetic field with amplitude B_1 and fixed frequency ν.[7] After the absorption, the energy is lost in the form of heat by flowing from the spin system to the surrounding (commonly indicated with *lattice*) at exponential rate, by a process referred to as *spin-lattice relaxation*.[7] Such exponential rate, and therefore the coupling between the spins and the lattice, depends on a characteristic *spin-lattice relaxation time* τ_1.[7] For sake of clarity, called δU_0 the extra energy received by absorption at $t = t_0$, the excess energy δU is lost to the surrounding lattice with the following the exponential decay[7]

$$\delta U = \delta U_0 exp[-(t - t_0)/\tau_1] \tag{1.14}$$

The smaller is τ_1, the more efficient is the relaxation of the spin system.[7] If τ_1 is high the sample has a limited ability to dissipate the absorbed energy. This means that when the microwave power increases, the populations of the two energy levels involved in the resonance process tend to become equal, and then the system may not be able to absorb further resonant microwave radiation. The results is that no net energy is transferred between B_1 and the spin system and then the EPR signal disappears.[7,31] Such tendency is called *power saturation*: the power of the applied B_1 field should be experimentally adjusted on the basis of the specific spin-lattice relaxation mechanism of the sample studied.[7] In fact, in saturation conditions, the EPR curve may result distorted and with meaningless absolute intensity: clearly, this situation must be avoided.[7]

The dependence on the relaxation time and B_1 of the absorbed power can be found via a classical treatment by the Bloch equations.[7,8,35,36] By studying the dependence on time of the coordinates of the bulk magnetization vector $\mathbf{M}$ defined in eq. 1.2 in presence of external static and oscillating magnetic fields, it is possible to obtain the absorbed power by the expression

$$P_a(\omega) \propto \frac{B_1^2 \chi}{(1 + \gamma_e^2 B_1^2 \tau_1 \tau_2)^{1/2}} \, \omega \cdot Y(\omega, B_1) \tag{1.15}$$

where ω is the angular frequency of the oscillating field B_1, $\gamma_e = \frac{g\beta_e}{\hbar}$ represents the electron magnetogyric ratio, τ_1 is the magnetization relaxation time already discussed and associated to spin-lattice relaxation whereas τ_2 is the spin-spin relaxation time, associated to the mutual spin interaction. $Y(\omega, B_1)$ represents a Lorentzian lineshape dependent on the experimental conditions with the form

$$Y = Y_{MAX} \frac{\Gamma^2}{\Gamma^2 + (\omega - \omega_r)^2} \tag{1.16}$$

where $\Gamma = (1 + \gamma_e^2 B_1^2 \tau_1 \tau_2)^{1/2} \cdot \frac{1}{\tau_2}$ represents its linewidth and ω_r its maximum.[7] It is interesting to note the dependence on the susceptibility χ: the EPR signal intensity varying the temperature is proportional to the susceptibility of the system studied. From eq 1.15 we can obtain that, as long as $\gamma_e^2 B_1^2 \tau_1 \tau_2 \ll 1$, $P_a(\omega)$ is proportional to B_1^2 (linearity condition), whereas when $\gamma_e^2 B_1^2 \tau_1 \tau_2 \gg 1$ the absorption becomes constant

and the line will be strongly saturated.

1.2.2   Local fields and anisotropy factors

In the previous equations we have considered that the free electron interacts with an external static magnetic field $\mathbf{B}$. However, when considering spin systems involved in a real sample, in addiction to the applied field $\mathbf{B}$ there may exist supplementary local fields that we indicate as $\mathbf{B}_{local}$.[7,34] It follows that the effective magnetic field acting on the electron is:[7,34]

$$\mathbf{B}_{eff} = \mathbf{B} + \mathbf{B}_{local}\,. \tag{1.17}$$

$\mathbf{B}_{local}$ may be induced by $\mathbf{B}$ with a dependence on its magnitude or may be dependent on the sole orientation of $\mathbf{B}$ (but not on its intensity).[7] The former contribution is always present, whereas the latter requires that a magnetic nucleus is present in proximity of the electron. Considering the former case, we could simply replace $\mathbf{B}$ with $\mathbf{B}_{eff}$ in equation 1.13, but it is not practical. Otherwise, it is more convenient to retain $\mathbf{B}$ but introducing a variable g parameter so that:[7,34]

$$\mathbf{B}_{eff} = (g/g_e)\mathbf{B} = (1 - \sigma)\mathbf{B}\,. \tag{1.18}$$

The newly introduced parameter σ is analogous to the chemical shift used in NMR spectroscopy (see section 1.3).[7] g is the effective Zeeman factor used in EPR spectroscopy, and allows to extract information on the spin system surrounding.[7] In some cases $g \approx g_e$, but there are many systems showing significant discrepancies between g and g_e, providing reasonable identifications of the paramagnetic species involved.[7]

In the simplest case, the g factor is independent of the magnetic-field direction and, as a simple scalar, it can be easily estimated by the reversal formula of eq. 1.13, that is

$$g = \frac{h\nu}{\beta_e B} \tag{1.19}$$

where B is the magnetic static field value corresponding to the peak of the absorption EPR spectrum or, alternatively, also to the point at which the first-derivative spectrum changes sign (see figure 1.9). However, EPR spectra are so simple only for a limited amount of systems, that is those showing truly isotropic centers. Systems in which g is strictly a scalar constant are, for example, those with *cubic*, *octahedral* or *tetrahedral local symmetries*.[7]

More in general, $\mathbf{B}_{local}$ may depend on the orientation of the field $\mathbf{B}$ with respect to the symmetry axes of the paramagnetic center, leading to a dependence of g on the orientation. Such systems are defined *anisotropic*. For the anisotropic systems, the resonance condition of eq. 1.13 can thus be satisfied at more than one magnetic field value.[7] For this reason, it is common to define a 3×3 *g matrix* which allows to express the anisotropy in the energy as a function of the direction of the magnetic field $\mathbf{B}$.[7] Such matrix can be reduced to the three diagonal values, generally indicated as g_x, g_y and g_z.[7,34] For rhombic or *orthorhombic* local symmetry, we have three different diagonal

values; in cases in which a local *uniaxial* os simply *axial* local symmetry is present, two diagonal values are equal and then they are generally indicated as $g_x = g_y = g_\perp$ and $g_z = g_\parallel$.[7,34]

In order to obtain the values of the g factors, in the case of single crystal samples, one should rotate them and acquire the EPR spectrum along different directions, taking care to line up the field with the symmetry axes of the paramagnetic center.[7,34] In polycrystalline samples or else *crystalline powders*, as those involved in this thesis, we have a *"disordered"* collection of small mutually randomly oriented crystals. However, each single spin center preserves the same surroundings as it would have in a large crystal.[7] This means that the spectral parameters are expected to be the same (except for some peculiar situations).[7] Commonly, since small differences may exist form one powder grain to another, a *distribution* of g factors can be found, whose width is sometimes indicated with the label g_{strain}. Anyway, in powdered samples, the symmetry axis of the whole of small crystalline components may assume *all* possible orientations with respect to that of the magnetic field **B**.[7,34] Despite this, by acquiring a single EPR spectrum of a powdered sample is possible to easily extract the three diagonal values of the g matrix. In fact, for both the cases of axial or orthorhombic local symmetries, the distribution of such spin systems as a function of the angles θ and ϕ subtended by the directions of the symmetry axis and the magnetic field follows two well defined trends.[7] Figure 1.10 shows the idealized absorption and first-derivative EPR lineshapes in the case of axial (a-b) and orthorhombic (c-d) symmetry, respectively. As indicated, the values of the g factors can be found by eq. 1.19 using the B values corresponding to the peaks or to the sign change points (typically called *zero crossing points*) of the EPR curves.[7]
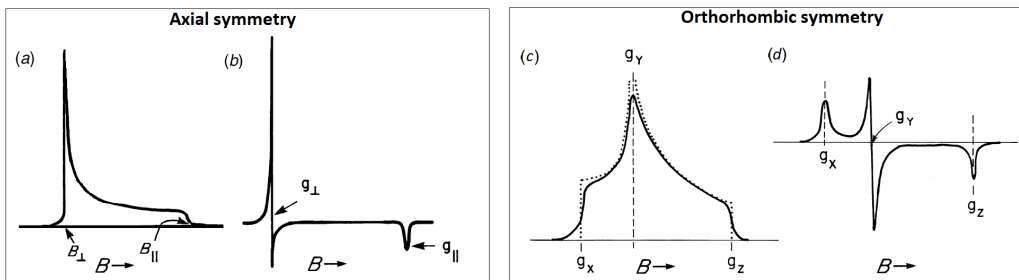
FIGURE 1.10: Idealized lineshapes for (a) absorption and (b) first-derivative EPR spectra (with $g_\parallel < g_\perp$) obtained for a polycrystalline sample containing spin centers in axial local symmetry; similarly, idealized lineshapes of (c) absorption and (d) first-derivative EPR spectra in the case of local orthorhombic symmetry (with $g_x > g_y < g_z$).[7]

1.2.3 Hyperfine interaction

Another important phenomenon to be considered is the electron-spin magnetic dipole interaction between electrons and nuclei in vicinity, that may lead to a further splitting of the energy level states.[7] In fact, some nuclei possess an intrinsic spin angular momentum I, corresponding to a multiplicity of nuclear-spin states equal to $2I + 1$. A magnetic moment μ_n can be associated with it.[7] For this reason, the interaction of a nucleus with

a static magnetic field $\mathbf{B}\|\mathbf{z}$ can be obtained in a similar way to that used for electrons. By spin-operator method, we can rewrite eq. 1.10 in operator form as follows:[7]

$$\hat{\mathcal{H}} = -\mathbf{B}^T \cdot \boldsymbol{\hat{\mu}} = -B\hat{\mu}_z \, . \tag{1.20}$$

Similarly to the electron magnetic-moment operator $\hat{\mu}_{ez}$ which is proportional to the electron-spin operator $\hat{S}_z$, the correspondent $\hat{\mu}_{nz}$ is proportional to the nuclear-spin operator $\hat{I}_z$.[7] Then:

$$\hat{\mathcal{H}}_e = -B\,\hat{\mu}_{ez} = +g\beta_e B \hat{S}_z \tag{1.21a}$$

$$\hat{\mathcal{H}}_n = -B\,\hat{\mu}_{nz} = -g_n\beta_n B \hat{I}_z \, , \tag{1.21b}$$

which define the electron and nuclear spin-Hamiltonian operators. Analogously to the electron case, if we suppose $I = \frac{1}{2}$, we can obtain an equivalent expression to eq. 1.11 for the energy values in this new case, which is $U_n = \pm\frac{1}{2}g_n\beta_n B = h\nu_n$, where $h\nu_n$ would be the photon energy that stimulate the nuclear transition. In summary, the interaction of a nucleus having an intrinsic spin angular momentum with a static magnetic field $\mathbf{B}$ leads to a splitting of the spin energy states.[7]

Under the assumption of the presence of a static external magnetic field $\mathbf{B}\|\mathbf{z}$ with a significant intensity so as to align electron and nuclear magnetic dipoles subject to dipole-dipole interaction, the resulting full spin Hamiltonian has the following expression, including also the term of *hyperfine interaction* between electron and nucleus:[7]

$$\hat{\mathcal{H}} = g\beta_e \mathbf{B}^T \cdot \hat{\mathbf{S}} - g_n\beta_n \mathbf{B}^T \cdot \hat{\mathbf{I}} + \hat{\mathbf{S}}^T \cdot A \cdot \hat{\mathbf{I}} \tag{1.22}$$

where $\mathbf{A}$ is the hyperfine 3×3 matrix.[7] A further deepening of the hyperfine matrix is out of the goals of this thesis, but for the sake of completeness it can be shown that it has the structure $\mathbf{A} = A_0 \mathbf{1}_3 + \mathbf{T}$, where A_0 is the so-called *isotropic hyperfine coupling "constant"* and $\mathbf{T}$ arises from the dipolar interaction and (except for the multiplicative constants) has the same structure of the dipolar matrix $\mathbf{D}$ that will be shown in the next section 1.2.4 (and also an analogous derivation).[7]

For a practical example of interest, we consider a Cu^{2+} ion, having an unpaired electron. Copper has two isotopes, ^{63}Cu and ^{65}Cu, both with a nuclear spin $I = \frac{3}{2}$: this means that a multiplet of $2I + 1 = 4$ spin states are found for each electron spin state. Because of the selection rule $\Delta M_I = 0$, the transitions may occur only between levels with the same M_I. For this reason, by studying systems with Cu^{2+} ions by EPR spectroscopy we will observe a multiplet of four lines. An ideal schematic illustration of what has been said is shown in figure 1.11.

1.2.4 Systems with two unpaired electrons

Since now, we have referred to systems with one unpaired electron and then S=1/2 spin. In this chapter, peculiar spin systems characterized by two electrons will be treated.
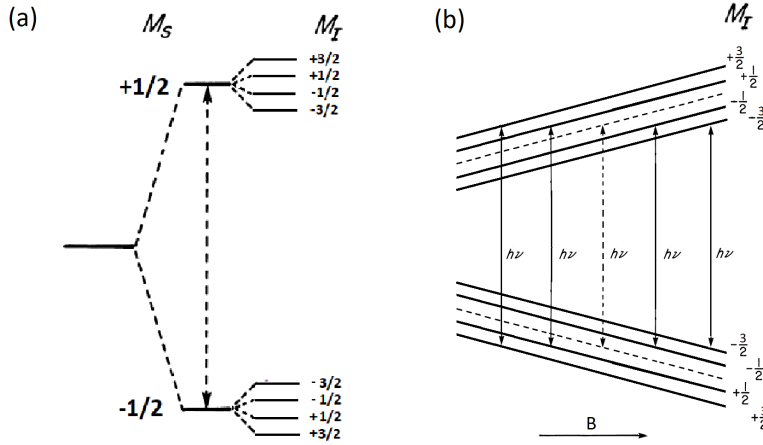
FIGURE 1.11: (a) Energy levels of a system with one unpaired electron and one nucleus with $I = \frac{3}{2}$. At a given field B, we observe a hyperfine effect on the splitting of the energy states. The dashed arrow represent the resonance that would have been at a proper frequency in absence of hyperfine interaction. (b) The dependence of energies on the magnetic field B is shown. The solid lines show the transitions induced by a constant microwave quantum $h\nu$. Again the dashed one represent the eventual resonance in absence of hyperfine interaction. The transitions shown are those allowed by the selection rule $\Delta M_I = 0$. Produced from refs. [7] and [37].

In section 1.1 we have already described the exchange interaction which is responsible for the energy separation between triplet and singlet state. The second important interaction to take into account is the ***anisotropic magnetic dipole-dipole interaction***, responsible for the removal of the three-fold degeneracy of the triplet state at zero magnetic field, an effect called *zero-field splitting*.[7] Such electron-spin-electron-spin dipolar interaction is given by the hamiltonian

$$\hat{\mathscr{H}}_{ss}(\mathbf{r}) = \frac{\mu_0}{4\pi} \left[\frac{\hat{\boldsymbol{\mu}}_1^T \cdot \hat{\boldsymbol{\mu}}_2}{r^3} - \frac{3(\hat{\boldsymbol{\mu}}_1^T \cdot \mathbf{r})(\hat{\boldsymbol{\mu}}_2^T \cdot \mathbf{r})}{r^5} \right] \tag{1.23}$$

or, replacing the magnetic-moment operators with the correspondent spin operators (see eq. 1.9),

$$\hat{\mathscr{H}}_{ss}(\mathbf{r}) = \frac{\mu_0}{4\pi} g_1 g_2 \beta_e^2 \left[\frac{\hat{\boldsymbol{S}}_1^T \cdot \hat{\boldsymbol{S}}_2}{r^3} - \frac{3(\hat{\boldsymbol{S}}_1^T \cdot \mathbf{r})(\hat{\boldsymbol{S}}_2^T \cdot \mathbf{r})}{r^5} \right] \tag{1.24}$$

where g_1 and g_2 are the g factors, assumed isotropic, for electrons 1 and 2.[7] For simplicity, we will also assume $g_1 = g_2 = g$.[7] Expanding the spin scalar product, introducing the total spin operator $\hat{\mathbf{S}} = \hat{\mathbf{S}}_1 + \hat{\mathbf{S}}_2$ and using useful commutation relations and the identity $r^2 = x^2 + y^2 + z^2$, the previous hamiltonian can be rewritten as follows:[7]

$$\hat{\mathscr{H}}_{ss}(\mathbf{r}) = \frac{\mu_0}{8\pi}(g\beta_e)^2 \frac{1}{r^5} \left[(r^2 - 3x^2)\hat{S}_x^2 + (r^2 - 3y^2)\hat{S}_y^2 + (r^2 - 3z^2)\hat{S}_z^2 + \right.$$
$$\left. - 3xy(\hat{S}_x\hat{S}_y + \hat{S}_y\hat{S}_x) - 3xz(\hat{S}_x\hat{S}_z + \hat{S}_z\hat{S}_x) - 3yz(\hat{S}_y\hat{S}z + \hat{S}_z\hat{S}_y) \right] \tag{1.25}$$

For mathematical reasons[7], it is possible to work separately with the triplet and singlet parts. Furthermore, the dipolar energy for the singlet state is zero. Eq. 1.25 can be thus

conveniently rewritten in matrix form:[7]

$$\hat{\mathscr{H}}_{ss} = \frac{\mu_0}{8\pi}(g\beta_e)^2 \begin{bmatrix} \hat{S}_x & \hat{S}_y & \hat{S}_z \end{bmatrix} \begin{bmatrix} \left\langle \frac{r^2-3x^2}{r^5} \right\rangle & \left\langle \frac{-3xy}{r^5} \right\rangle & \left\langle \frac{-3xz}{r^5} \right\rangle \\ & \left\langle \frac{r^2-3y^2}{r^5} \right\rangle & \left\langle \frac{-3yz}{r^5} \right\rangle \\ & & \left\langle \frac{r^2-3z^2}{r^5} \right\rangle \end{bmatrix} \begin{bmatrix} \hat{S}_x \\ \hat{S}_y \\ \hat{S}_z \end{bmatrix} \qquad (1.26a)$$

$$= \hat{\mathbf{S}}^T \cdot \mathbf{D} \cdot \hat{\mathbf{S}} \qquad for \ S = 0, 1 \,. \tag{1.26b}$$

We have now introduced the $\mathbf{D}$ matrix, which is symmetric and diagonalizable in $^D\mathbf{D}$.[7] $\mathbf{D}$ elements are averages over the electronic spatial wavefunction.[7] The diagonal $^D\mathbf{D}$ elements can be labelled D_x, D_y and D_z. The usual convention is that D_z is taken to be the principal value with the largest absolute magnitude while D_y (if $D_y \neq D_x$) has the smallest absolute magnitude.[7] Furthermore, from eq. 1.26a it can be calculated that the trace of $\mathbf{D}$ is zero ($tr(\mathbf{D}) = D_x + D_y + D_z = 0$).[7] Using the matrix $^D\mathbf{D}$ (or else, the principal-axis system of $\mathbf{D}$), eq. 1.26b becomes:[7]

$$\hat{\mathscr{H}}_{ss} = D_x\hat{S}_x^2 + D_y\hat{S}_y^2 + D_z\hat{S}_z^2 \,. \tag{1.27}$$

At this point we are ready to write the **effective spin hamiltonian for two interacting electrons**, simply adding the electron Zeeman term to eq. 1.6 and eq. 1.26b:[7]

$$\hat{\mathscr{H}} = g\beta_e\mathbf{B}^T \cdot \hat{\mathbf{S}} + \mathbf{S}^T \cdot \mathbf{D} \cdot \hat{\mathbf{S}} - \frac{1}{2}J_0\big[\hat{\mathbf{S}}^2 - \tfrac{3}{2}\mathbf{1}_3\big] \,. \tag{1.28}$$

Note that the third term of the hamiltonian of eq. 1.28 consists of the energy separation between the singlet and the triplet state and then it is a common constant for each of the three triplet states. For this reason, in the treatment of a S=1 spin system, it can be neglected.[7] Hereafter, the hamiltonian we consider is simply:[7]

$$\hat{\mathscr{H}} = g\beta_e\mathbf{B}^T \cdot \hat{\mathbf{S}} + \mathbf{S}^T \cdot \mathbf{D} \cdot \hat{\mathbf{S}} \tag{1.29a}$$

$$= g\beta_e\mathbf{B}^T \cdot \hat{\mathbf{S}} + D_x\hat{S}_x^2 + D_y\hat{S}_y^2 + D_z\hat{S}_z^2 \tag{1.29b}$$

$$= g\beta_e\Big(B_x\hat{S}_x + B_y\hat{S}_y + B_z\hat{S}_z\Big) + D_x\hat{S}_x^2 + D_y\hat{S}_y^2 + D_z\hat{S}_z^2 \tag{1.29c}$$

where in the last steps the assumption that the $\hat{\mathscr{H}}$ matrix can be diagonalized has been used (indeed, for present purposes, it is not necessary to know how the principal-axis system is oriented, but only that it exists).[7]

Even though it is often convenient to use the eigenfunctions $|M_s\rangle = |+1\rangle$, $|0\rangle$ and $|-1\rangle$ of $\hat{S}_z$ as a basis set, they are not eigenfunctions of $\hat{\mathscr{H}}_{ss}$. Consequently, they are eigenfunctions of $\hat{\mathscr{H}}$ only in the limit $B \to \infty$.[7] In order to find the eigenvalues of the hamiltonian $\hat{\mathscr{H}}$, we can express eq.1.29c in matricial form and then subtract the parameter U from all the diagonal elements and set the determinant equal to zero.[7] By imposing $\mathbf{B}\|\mathbf{z}$ (and then $B_x = B_y = 0$), the resolution becomes easier and at B=0 the

three energies obtained are:[7]

$$
\begin{cases}
U_x = -D_x \\
U_y = -D_y \\
U_z = -D_z
\end{cases}
\tag{1.30}
$$

Since $tr(\mathbf{D}) = 0$, there are only two independent parameters.[7] For this reason, it is common the introduction of the parameters D and E defined as:[7]

$$
\begin{cases}
D \equiv \frac{3}{2}D_z \\
E \equiv \frac{1}{2}(D_x - D_y)
\end{cases}
\tag{1.31}
$$

In terms of D and E, the spin-hamiltonian operator becomes:[7]

$$
\hat{\mathscr{H}}_n = g\beta_e \mathbf{B}^T \cdot \hat{\mathbf{S}} + D\left(\hat{S}_z^2 - \tfrac{1}{3}\hat{S}^2\right) + E\left(\hat{S}_x^2 - \hat{S}_y^2\right)
\tag{1.32}
$$

By the convention we are using, if $D > 0$ then $E \leq 0$. Commonly, they are expressed in cm^{-1}, by defining $\bar{D} \equiv D/hc$ and $\bar{E} \equiv E/hc$. However, their values depend on which axis is chosen as $\mathbf{z}$ and magnitude and sign of E strictly depend on the specific assignment of the axes $\mathbf{x}$ and $\mathbf{y}$.[7] However, the EPR line positions depend only on D and E relative signs.[7] Note that if $E = 0$, then $D_x = D_y$, meaning *uniaxial symmetry*, whereas, if $E \neq 0$, the system has *rhombic symmetry*, meaning that all three triplet states are non-degenerate at zero field.[7] These considerations are illustrated in figure 1.12. Note also that in the limit of D (and then E) very small, the two transitions indicated in figure lie at the same resonant B value.[7]
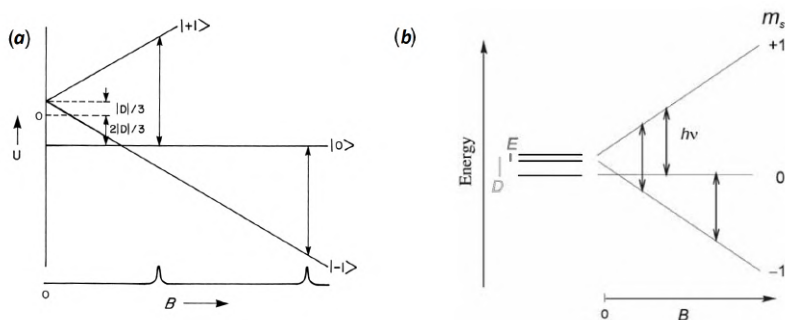

FIGURE 1.12: (a) State energies and corresponding eigenfunctions as a function of applied magnetic field B for a system with S=1 and $\mathbf{B}\|\mathbf{z}$ in the case of E=0 and D>0. The two $\Delta M_S = \pm 1$ transitions are indicated for a constant-frequency hypothetical spectrum. The eigenfunctions $|+1\rangle$ and $|-1\rangle$ show degeneration at B=0. (b) Corresponding scheme for the case $E \neq 0$, with the removal of the degeneration of the eigenfunctions $|+1\rangle$ and $|-1\rangle$ at B=0.[7,9]

Having determined the eigenvalues, it is also possible to find the eigenfunctions of the hamiltonian by solving the correspondent secular equation. They will result in linear combinations of the states $|M_S\rangle = |+1\rangle$, $|0\rangle$ and $|-1\rangle$.[7] As previously alluded, when B is sufficiently large in magnitude compared to $D' = D/g_e\beta_e$ and it is parallel to $\mathbf{z}$, the eigenstates $|M_s\rangle$ are eigenstates of the spin hamiltonian of eq. 1.29b, and then

the spin energies can be labeled by the values of M_S.[7] For this reasons, at high fields the selection rule $\Delta M_S = \pm 1$ is the only allowed, while $\Delta M_S = \pm 2$ transitions are forbidden.[7] However, as already mentioned, at low fields the eigenfunctions are linear combination of the states $|M_S\rangle$ and the quantum numbers M_S have to be considered no longer strictly applicable. If, as usual, one makes the choise to label the states with $|M_S\rangle$ also for low fields, then the selection rules of the previous case are no longer applicable.[7] Therefore, at low fields the $\Delta M_S = \pm 2$ (single-photon) transition is not forbidden and it can be seen in a normal EPR cavity, corresponding to a line in the region $g \approx 4$. This resonance has a quite small anisotropy associated, which makes relatively large the amplitude of the correspondent peak.[7]

EPR absorption spectra for randomly oriented triplet systems

Similarly to what seen for systems with one unpaired electron, it is possible to study both ordered mono-crystal and randomly oriented poli-crystalline materials.[7] In order to find a theoretical EPR absorption spectrum for a randomly oriented triplet system, the field separation ΔB of the two allowed $\Delta M_S = \pm 1$ transitions has been derived. The probability distribution for a given upper-field transition in situation of uniaxial symmetry is given by:[7]

$$P(B_{highfield}) \propto \frac{g\beta_e}{6|D\cos\theta|} \ . \tag{1.33}$$

The analysis can readily be extended to the case of rhombic symmetry, obtaining an analogous probability distribution. The absorption spectra and related first-derivative curves in both the cases of uniaxial and rhombic symmetry are shown in figure 1.13 (a-b) and (c-d), respectively. Note that the spectra shown include only the $\Delta M_S = \pm 1$ transitions. For this kind of systems involving pairs of coupled S=1/2 spin centers, the relation between a B resonant value and a g factor is not straightforward like that of eq. 1.13 valid for S=1/2 spin systems.[9,38] Wasserman and co-authors found that each of the six features that can be found in an EPR spectrum obtained for a triplet system corresponds to the following resonant B values:[9,38]

$$B_{x1}^2 = \left(\tfrac{g_e}{g_x}\right)(B_0 - D' + E')(B_0 + 2E') \tag{1.34a}$$

$$B_{x2}^2 = \left(\tfrac{g_e}{g_x}\right)(B_0 + D' - E')(B_0 - 2E') \tag{1.34b}$$

$$B_{y1}^2 = \left(\tfrac{g_e}{g_y}\right)(B_0 - D' - E')(B_0 - 2E') \tag{1.34c}$$

$$B_{y2}^2 = \left(\tfrac{g_e}{g_y}\right)(B_0 + D' + E')(B_0 + 2E') \tag{1.34d}$$

$$B_{z1}^2 = \left(\tfrac{g_e}{g_z}\right)\big((B_0 - D')^2 - (E')^2\big) \tag{1.34e}$$

$$B_{z1}^2 = \left(\tfrac{g_e}{g_z}\right)\big((B_0 + D')^2 - (E')^2\big) \tag{1.34f}$$

$$\tag{1.34g}$$

where B_0 is the resonant magnetic field value valid to a free electron ($B_0 = \frac{h\nu}{g_e\beta_e}$).[9,38] Note that for a system with axial symmetry $E' = 0$ and then $B_{x1}^2 \equiv B_{y1}^2$ and $B_{x1}^2 \equiv B_{y1}^2$, thus reducing the signals from six to four, as shown in figure 1.13(a).[7,37,38] In practice,
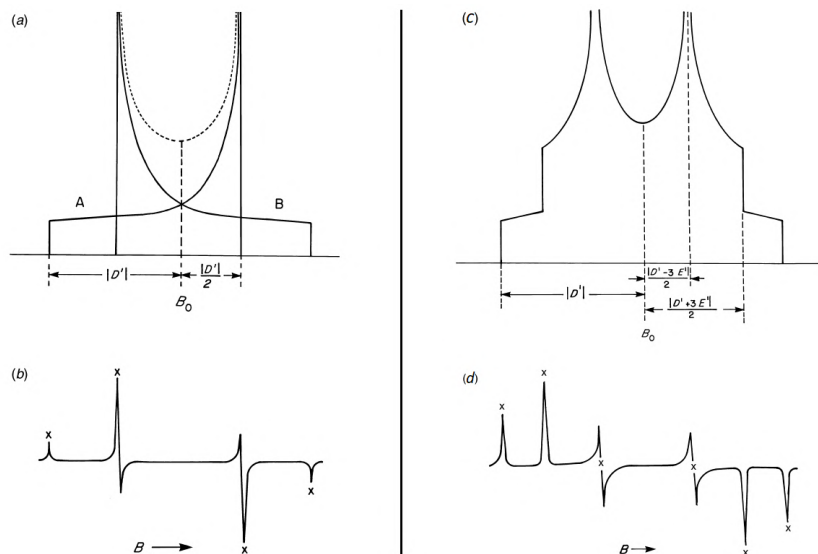
FIGURE 1.13: (a)Theoretical EPR absorption spectrum for a randomly oriented triplet system with E=0 and with fixed values for D, ν and $g = g_e$ and (b) correspondent first-derivative curve. Similarly, (c) Theoretical EPR absorption spectrum and (d) correspondent first-derivative curve for a randomly oriented triplet system with given values of E'≠0, D', ν and $g = g_e$.[7]

it may happen that not all peaks are easily detectable, because some broadening mechanisms may take place; in these cases the observed EPR lines are less than those predicted theoretically. .[7]

1.3   Solid-state NMR spectroscopy

Like EPR technique, NMR spectroscopy is a very sensitive spectroscopic technique able to investigate the local structure of a material at atomic scale level. Besides X-ray crystallography (see section 1.5), which can uncover the complete structure of some crystalline materials, NMR spectroscopy is the most direct tool for the identification of a given structure, even in solid-liquid mixtures.[39]

The basis concept of NMR spectroscopy is the same as the EPR spectroscopy, with the difference that the magnetic moment involved has a different nature. In fact, NMR spectroscopy is based on the intrinsic quantum-mechanical property of the nuclear spin angular momentum **I**. Since both protons and neutrons have spin quantum numbers $I = 1/2$, atomic nuclei may also possess a net overall non-zero nuclear spin angular momentum vector **I**. In section 1.2.3 we have already discussed that the vector **I** can be quantized along an arbitrary z axis in units of $\hbar$, such that

$$I_z = m_I \hbar \tag{1.35}$$

where m_I is a number spacing between $+I$ and $-I$ by integer steps, giving rise to a multiplicity of 2I+1 degenerate spin states in absence of externally applied magnetic fields.

A nucleus with non-zero I is said to be *spinning*.[39] The nuclear spin vector provides in turn a nuclear magnetic dipole moment that in this contest we express as $\boldsymbol{\mu} = \gamma \mathbf{I}$ or also, along z,

$$\mu_z = \gamma I_z \tag{1.36}$$

where γ indicates the nuclear *gyromagnetic ratio*, which depends on the nucleus involved.

The nucleus of hydrogen ^{1}H, the simplest atom, is composed of a single proton and then it possesses a nuclear spin vector $\mathbf{I}$. In the nuclei of heavier elements, protons and neutrons combine to define the overall spin: when both atomic and nuclear mass are even, then I=0; this is the case of atoms like $^{12}_6$C and $^{16}_8$O, which are therefore invisible to NMR spectrometers.[39] In contrast, if either the atomic number or the mass number is odd or if both are odd, that nucleus has magnetic properties.[39] Nuclei with $\mathbf{I} = \frac{1}{2}$ are also labeled as *spherical*, whereas those with $\mathbf{I} > \frac{1}{2}$ are indicated as *non-spherical* or *quadrupolar*. The class of $\mathbf{I} = \frac{1}{2}$ nuclei is the most easily examined in the NMR experiments. Except for oxygen, many of the most common elements found in organic molecules have at least one isotope with $\mathbf{I} = \frac{1}{2}$, like ^{1}H, ^{13}C, ^{15}N and ^{31}P. Carbon NMR experiments are really common and they are carried out on the ^{13}C, which has a natural abundance of 1.1%.[39]

A nucleus with spin number I=1/2 has a spin with thus two possible orientations: m_I=+1/2 and m_I=-1/2. The two corresponding spin states show an energy split in presence of external magnetic field. Likewise for EPR spectroscopy, we can express the Zeeman interaction energy U by an external magnetic field vector $\mathbf{B}$ directed along z as

$$U = -\mu_z B \tag{1.37}$$

and then the energy difference between the two energetically splitted spin states is

$$|\Delta E| = \gamma \hbar B. \tag{1.38}$$

This latter equation is valid also for nuclei with spin numbers I>1/2, because $\Delta m_I \neq \pm 1$ transitions are forbidden by selection rules. Correspondingly, the resonance condition which allows a nuclear spin transition takes place when the system interacts with electromagnetic radiation at the resonant Larmor frequency of

$$\omega_0 = -\gamma B \tag{1.39}$$

in units of rad· s^{-1} or

$$\nu_0 = \frac{-\gamma B}{2\pi} \tag{1.40}$$

in units of Hz. Generally, in NMR experiments the static magnetic field B has a value ranging from 4 to 24 T, whereas the Larmor frequency falls in the range $\sim 5 \div 1000$ MHz.

The effect of the absorption of a resonant pulse by the spin system is to alter its thermal equilibrium state, which can be restored by a spin-lattice relaxation.[40] The

laws governing this phenomenon are analogous to those described in EPR theory, the Bloch equations (see section 1.2): the relaxation involves an energy exchange between spin system and surrounding lattice and depending on the characteristic times involved, saturation effects may take place.[40]

1.3.1   The chemical shift

Another similarity with EPR spectroscopy is the important role played by the *local fields* surrounding the nuclei, which in NMR experiments are mainly generated by the electron clouds, with the net result of altering the effective B field that should be considered in the equations. The actual field B_{local} present at a given nucleus will strictly depend on the so-called *shielding* σ operated by the surrounding electrons, so that

$$B_{local} = B(1 - \sigma_i)\,. \tag{1.41}$$

The new resonance frequency can be obtained from eq. 1.40 by substituting B with B_{local}:

$$\nu_i = \frac{-\gamma B(1 - \sigma_i)}{2\pi}\,. \tag{1.42}$$

Imagining to compare a molecule having an electron-withdrawing group with the same molecule that lacks such group, the first one will have a minor electron density around a proton and then it will be less shielded; consequently, the resonance frequency will be higher (negative σ).[39–41] The Hamiltonian term associated with this frequency shift is a simple Zeeman operator.[40] The observable quantity in NMR experiments is exactly this frequency variation called *chemical shift*. Since its values are very small differences between large numbers (even as the 7$^{\text{th}}$ significant digit), for a better clarity the frequency value *zero* is arbitrary assigned to a reference signal, so that the relative frequency differences $\delta(\nu) = \nu_i - \nu_{ref}$ are measured in Hz/MHz or parts per million (ppm) downfield or upfield to the reference signal.[39–41] Clearly, the reference signal must come from the same isotope as the nuclei of interest: for ^{1}H, ^{13}C and ^{29}Si, the reference signal generally used is that arising from *tetramethylsilane (TMS)* $Si(CH_3)_4$, in which the 12 hydrogens and the 4 carbons are symmetry equivalent between them.

Called ν_{ref} the reference frequency, a frequency shift due to the shielding effect can be expressed as follows:[39]

$$\Delta\nu = \nu_i - \nu_{ref} = \frac{-\gamma B(1 - \sigma_i - 1 + \sigma_{ref})}{2\pi} = \frac{\gamma B(\sigma_{ref} - \sigma_i)}{2\pi}\,. \tag{1.43}$$

However, since with this expression the frequency differences still depend on the value of B, the chemical shift is generally defined as:

$$\delta = \frac{\Delta\nu}{\nu_{ref}} = \frac{\sigma_{ref} - \sigma_i}{1 - \sigma_{ref}} \sim \sigma_{ref} - \sigma_i \tag{1.44}$$

where in the last step it has been considered that the reference shielding σ_{ref} is chosen to be much less than 1.0.[39] Chemical shifts strongly depend on the particular element

investigated, and they are of order of few ppm in ^{1}H and several 100 ppm in ^{13}C and ^{31}P.[40] Correspondingly to the g matrix seen in section 1.2, also the shielding effects of the electron cloud have a matrix character, due to the possibility that a given applied field in one direction can induce a local field in another direction.[40]

1.3.2 Magic Angle Spinning NMR

Most of NMR experiments are performed in *liquid-state*, that is by dissolving the samples in solution. Liquid-state NMR spectroscopy provides narrow spectral lines, revealing even fine details about interactions among electrons and nuclei. The narrowness of these NMR lines is due to the isotropic averaging of tensor interactions performed by the Brownian motion and the rapid tumbling of the molecules in liquids.

However, there are materials like MOFs for which the micro-structure, crystallinity, diffusion, exchange of molecules, or grain size constitute significant properties and then it would make no sense to dissolve them, because those properties of interest may be destroyed and go lost.[41] For this reason, the *solid-state* NMR spectroscopy is the most used for MOF investigations. The main difference between the two methods is the extent and the type of molecular motion and the way it can affect the spin interactions.

The most common solid-state NMR application does not involve single-crystals but grinded powders containing numerous tiny crystallites, which can represent all possible orientations. Due to the similarity of the two techniques, the resulting *powder-pattern* would show chemical shift peaks with positions and features directly connected with the theoretical line-shapes seen for EPR absorption spectra (see figures 1.9 and 1.10), depending on the symmetry of the spinning nuclei investigated.[41] However, in contrast to liquid-state NMR spectra, the lines are generally very broad and resolving the individual crystals may become impossible. Therefore, for complex compounds involving (for example) tens of different crystallographic carbons, there will be a sizable number of overlapped powder patterns, leading to broad, complicated, featureless and uninterpretable spectra.[41]

In order to obtain, similarly for the liquid-state NMR experiments, simple spectra containing (at least namely) one narrow resonance per distinguishable nuclear site, the molecular motions in liquid are *imitated* by *magic angle spinning (MAS)* method.[40,41] It consists on putting the sample in a rotor causing the sample to spin; when the rotation axis makes an angle of $\sim 54.74°$ (that is the *magic angle*) with the **B** direction, the broad lines of the powder patterns may "*magically*" become narrow.[40,41] The reason can be qualitatively explained as follows. In general, the tensor interactions causing the chemical shift have both isotropic and anisotropic components. In the liquid-state NMR such tensor interactions are averaged by Brownian motions; the same happens by mechanically spinning the sample around an axis.[41] Considering that the anisotropic chemical shift depends on the orientation, it can be expressed in terms of a complete set spherical harmonics like the atomic orbitals. Since for symmetry reasons it can be proved that chemical shift tensors are invariant under inversion and that only terms up

to second order need to be taken into account, they can be expanded as a combination of the solely s and d orbitals, where s contribution represents the isotropic shift.[41]

Rapid spinning imposes an averaging of *every* tensor in the sample to an axial tensor, whose axis will be aligned with the spinning direction.[41] For this reason, beside the orbital s, only the d_z^2 orbital remains, whose functional form is given by

$$d_z^2(\theta) = \tfrac{1}{2}(3\cos^2\theta - 1) \tag{1.45}$$

and that becomes zero when $\theta = 54.74°$.[40,41] In summary, by putting in rotation a sample along a direction of $\theta = 54.74°$ in relation to the external magnetic field **B**, the powder patterns may narrow to sharp lines like in the liquid-state condition as long as the spinning speed is greater than their linewidth (in frequency units).[41] For this reason, the typical spinning speeds involved are of some kHz. Such method leads to the formation of the *spinning sidebands*, sharp lines flanking the *centerband* and spaced at the spinning frequency. However, this also means their number can be reduced by using large spinning rates, so that the sideband separation also becomes large.[41]

1.4 Raman spectroscopy

Raman spectroscopy is based on the Raman scattering effect, and it allows to investigate the vibrational properties of the molecules involved in the samples studied.[42,43]

When a monochromatic light beam with frequency ν_0 is incident on a solid, it may be scattered in two ways, by elastic or anelastic scattering mechanism (see figure 1.14). The elastic one is also called *Rayleigh* scattering and it produces scattered light having the same frequency of the incident beam (ν_0); the inelastic one is the Raman scattering, characterized by scattered beams having different frequencies compared to that of the incident one.[42,43] Such differences in frequency that we name $\pm\nu_m$ correspond to vibrational frequencies of the sample; the *Raman bands* $\nu_0 - \nu_m$ and $\nu_0 + \nu_m$ are called *Stokes* and *anti-Stokes lines*, respectively.[42,43] In other words, the vibrational frequencies are individuated in terms of the shift between the incident and the scattered beams.[42,43]

Scattering at ν_0 (Rayleigh)
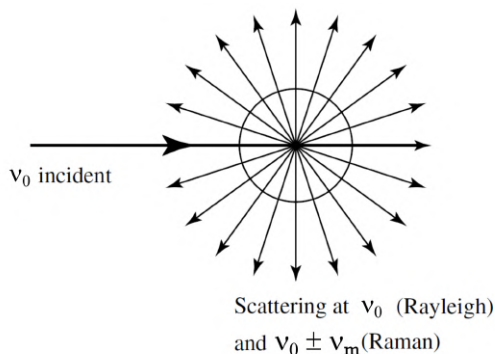and $\nu_0 \pm \nu_m$ (Raman)

FIGURE 1.14: Diagrammatic representation for Rayleigh and Raman scattering. Adapted from ref. [42].

Typically (except for techniques involving the Resonance Raman scattering), the frequency ν_0 is chosen in such a way that $h\nu_0$ does not correspond to any transition energy and then the photon of energy $h\nu_0$ cannot be absorbed in the spectroscopic sense: it may instead bring the system in a "*virtual state*" by a so-called *virtual absorption.*[42,43] However, since such state is not real, the incident light only perturbs the punched system which will quickly relax returning another photon.[42,43] In the case of Rayleigh scattering, this outgoing photon has the same frequency ν_0, because the system is returned to its starting energetic state.[42,43] In contrast, Raman scattering arises when, after the emission of the scattered photon, the system is in a different vibrational energetic state. Figure 1.15 gives a representation of the phenomenon.
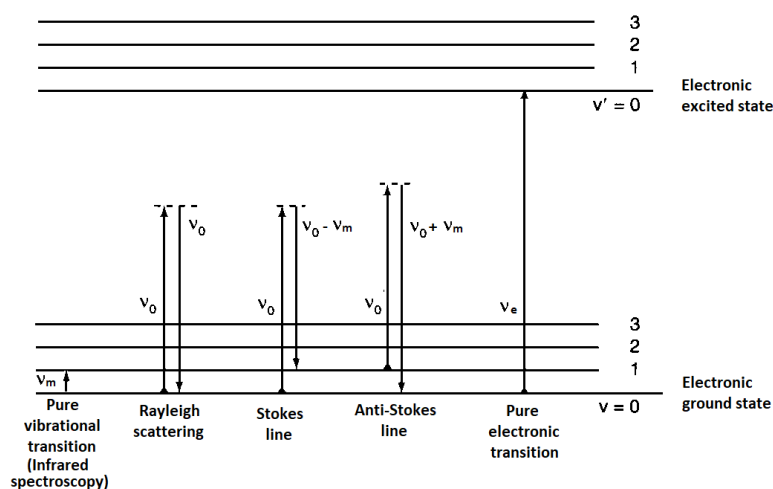

FIGURE 1.15: A photon of frequency ν_0 incident on a system may be *virtually absorbed* and be subsequently scattered back maintaining the same frequency (Rayleigh scattering) or with a frequency $\nu_0 \pm \nu_m$ (Raman scattering). Raman scattering involves a change in the vibrational state of the molecule punched. If ν_0 equals to ν_m, the photon may be absorbed leading to a pure vibrational transition (infrared spectroscopy), whereas if $\nu_0 = \nu_e$ an electronic transition may occur. The distancing between the energy levels is only representative and not to scale. Adapted from ref. [43].

Differently, the absorption of an incident photon at frequency ν_m, which leads to a pure vibrational transition, is the basis of infrared (IR) spectroscopy.[43]

Since the anti-Stokes line is found only if the system was in a vibrational excited state before the perturbation caused by the incident radiation, under normal conditions it is much less intense then the correspondent Stokes line.[42,43] In fact, as expected from the Maxwell-Boltzmann distribution, at a given temperature the $\upsilon = 0$ ground state will be much more populated then the $\upsilon = 1$ state.[42,43] Supplementary lines as $\nu_0 \pm 2\nu_m$ or $\nu_0 \pm 3\nu_m$ are only weakly allowed by the selection rules obtained for an anharmonic vibration.[42,43] For these reasons, it is customary to take into consideration simply the Stokes lines (except for specific applications like temperature measurements in which also the anti-Stokes line is fundamental).[43]

In principle, in polyatomic molecules, all the nuclei may perform their own harmonic oscillations, leading to very complicated vibrations.[43] However, every vibration can be expressed as a superimposition of a number of *normal vibrations* independent of each

other.[43] A Raman instrument detects these normal vibrations and their totality constitutes the Raman spectrum.[43] However, not all vibrations produce a Raman signal: at a first approximation a vibration is *Raman-active* only if the polarizability α is changed during the vibration. Polarizability α is defined as the proportionality constant between the external electric field strength E and the induced electric dipole moment $P = \alpha E$.[43] More precisely, defining q as the displacement from the equilibrium position during the vibration, a mode is Raman active if the derivative $\frac{d\alpha}{dq}$ near the equilibrium position is non-zero.[43] For these reasons, depending on the symmetry of a molecule/group of atoms, a particular vibrational mode may not be detected by Raman instruments.[43]

In the simplest case of a diatomic molecule, the vibrational frequency can be expressed as:

$$\tilde{\nu} = \frac{1}{2\pi c}\sqrt{\frac{K}{\mu}} \tag{1.46}$$

where K is the effective force constant associated to the chemical bond and μ is the reduced mass.[43] Therefore, $\tilde{\nu}$ is proportional to the square root of the force constant, meaning that it is correlated to the strength of the bond connecting the two atoms (even though a high K does not involve necessarily a strong bond).[43] Since $\tilde{\nu}$ is also inversely proportional to the square root of the reduced mass, the frequency also depends on the mass of the atoms involved.[43] Similar relations can be found for poliatomic molecules and then, for this reason, relying on the frequency value, in many cases it is possible to easily understand if the detected Raman band is related to a specific group of atoms or not.[43]

1.5   Powder X-ray Diffraction

X-ray Powder Diffraction (PXRD) is a bulk technique at the basis of *crystallography*, constituting a rapid and meaningful tool for the characterization of crystalline materials. It allows to reveal the crystal structure, to check the purity of a sample and then to identify an eventual mixture of more crystalline components.[44]

A crystal structure can be defined as a solid object in which a basic array of atoms is repeated periodically: if the simplest repeating motif is known, the characterization of the entire lattice is possible by simple translations along specific directions.[44,45] In this regard, an *unit cell*, the smallest repeating volume of the lattice with specific symmetry properties, can be characterized by three vectors or also by their lengths and the three interaxial angles typically called *lattice parameters*, as displayed in figure 1.16(a).[44,45] Since for a given lattice the choose of more than one unit cell is available, generally one considers the cell which shows the highest possible symmetry.[45]

The description of a specific lattice plane is conventionally done by using the Miller indices: a $(h\,k\,l)$ plane is the one that makes fractional intercepts of $1/h$, $1/k$ and $1/l$ with the axes a, b and c, respectively (see figure 1.16(b)). The indices are all integers, and if the plane is parallel to one or more axes (and then the place does not intercept them), the correspondent indices are set to 0.[44] A group of parallel planes characterized
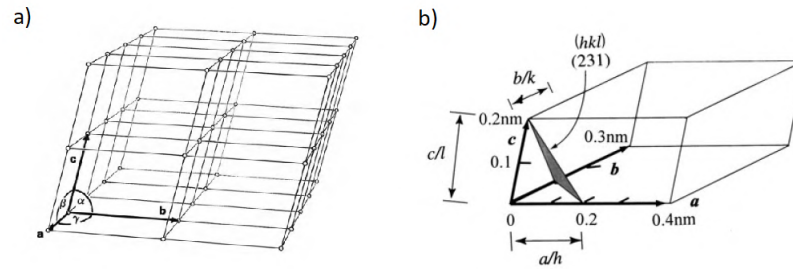
FIGURE 1.16: (a) Example of unit cell. a, b and c identify the three lenghts, whereas α, β and γ indicate the three angles. (b) Example of Miller indices for a plane. Adapted from refs. [45] and [44].

by the Miller indices $(h\,k\,l)$ can be also identified in terms of the common perpendicular **d** vector, indicated with $[h\,k\,l]$.[44]

X-rays are electromagnetic waves whose wavelengths ranges from about 10 to 10^{-3} nm, comparable to the atomic distance in a crystal.[44] The scattered light has the same wavelength of the incident X-ray beam, and it can be thought as spherical waves centered on the scattering atom. However, comparing the phase of two scattered waves, it generally shows a deviation Δ corresponding to their path difference. If Δ is an integer multiple of the wavelength λ, the two waves will have a *coincident phase* and they will combine reinforcing each other in a wave with double amplitude. In other words, waves with coincident phase can produce a detectable *diffraction beam*. At the same time, Δ depends on the direction of the wave in relation to the crystal orientation.

In order to know which paths may satisfy this phase condition, the most important method is given by the well-known *Bragg's law*

$$2d_{(hkl)} \sin\theta_{(hkl)} = n\lambda \qquad (1.47)$$

where $d_{(hkl)}$ is the interplanar spacing for the $[h\,k\,l]$ plane group, n is the integer number of wavelengths contained in Δ and also the order of diffraction, while $\theta_{(hkl)}$ is the incident angle to the plane $(h\,k\,l)$, which is also equal to the angle of the diffracted ray (see figure 1.17, where $\theta_{(hkl)}$ is simply indicated with θ).[44–47] 2θ is typically called
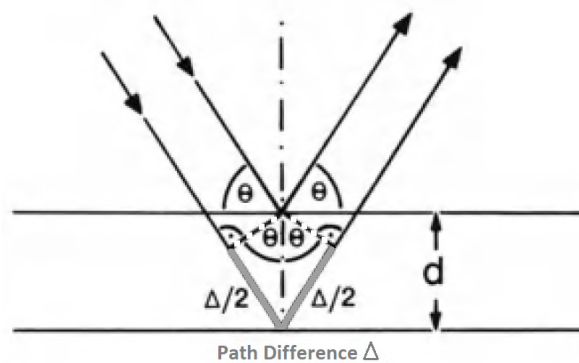

FIGURE 1.17: (a) Example of unit cell. a, b and c identify the three lengths, whereas α, β and γ indicate the three angles. (b) Example of Miller indices for a plane. Adapted from ref. [45].

In summary, in a lattice with interplanar spacing d', a diffracted beam will be detected only if it satisfies the Bragg's law. This means that the spherical waves centered on the atoms become *"cones"* of angular amplitude 2θ, which assume the form of *rings* when projected on a sphere or on the plane surface of a detector (see figure 1.18).[44,47,48] Each ring along such hypothetical sphere corresponds to a single Bragg angle 2θ, which
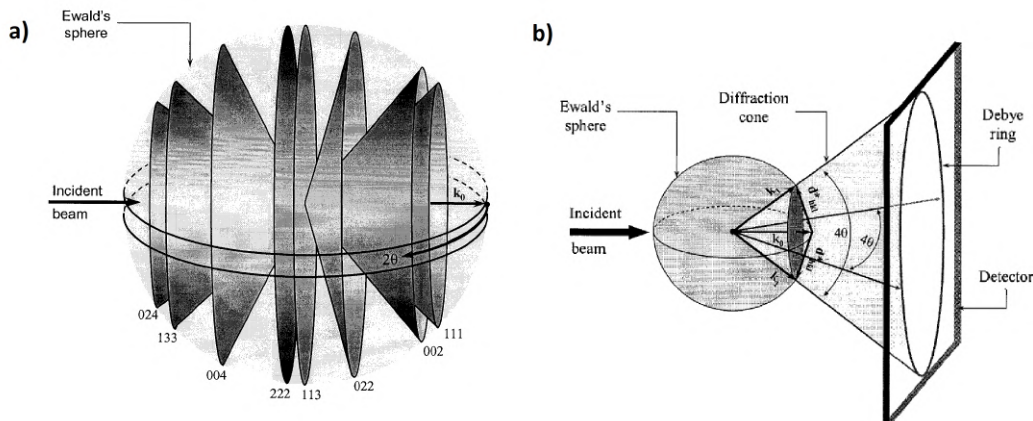

FIGURE 1.18: a) Diffraction cones of a as the result of the infinite number of the completely randomly oriented identical crystals in a polycrystalline sample upon irradiation with a monochromatic beam. Each cone corresponds to specific Miller indices. b) Each cone forms a circle on the surface of a sphere (*Ewald's sphere*), producing a so-called *Debye ring*. The radius of each Debye ring is proportional to $\tan 2\theta_{(hkl)}$.[47]

in turn corresponds to a $[h\,k\,l]$ family of planes.[45,47] There are different possible set-up for the acquisition of XRD patterns, but the logic involved is generally equivalent to that explained in the following.[44] In order to acquire the diffracted rays from a polycrystalline material composed of thousands of small crystals oriented along all possible diffraction directions of the lattice, the detector scans the sample through a certain range of 2θ angles, typically from $\sim 5°$ to $\sim 70°$.[44,47] All the diffracted X-rays are then detected, processed and counted. The final data are generally presented as *counts* as a function of the angle 2θ and it constitutes the *diffraction pattern* of the material, representing a characteristic *fingerprint* of that lattice (see figure 1.19).[44]

For a practical usefulness, the diffraction peaks need to be converted in d-spacings, allowing the identification of the lattice. This is possible by considering that a peak in intensity occurs at a given 2θ when the material contains lattice planes with suitable d-spacings, such that X-rays can be diffracted satisfying eq. 1.47. Greater separation occurs at higher values of ϑ.

It is has already previously identified, the identity of a material can be rapidly verified by simply comparing the position of the peaks in the PXRD pattern acquired with those in a reference one.

The intensity of the peaks in a PXRD pattern is also significant, but it depends on several factors, linked to both the atomic arrangement and the atomic species (the nuclei do not scatter, and then the scattering ability depends on the number and the
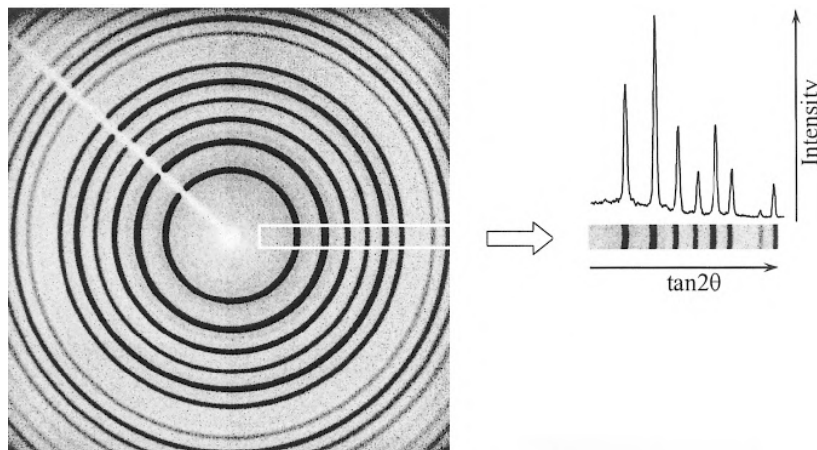
FIGURE 1.19: Example of X-ray diffraction rings for a given poly-crystalline material (LaB$_6$). The white box delineates the area in which the scattered intensity was integrated from the center of the image towards its edge in order to plot the resultant intensity as a function of $\tan 2\theta$.[47]

distribution of the electrons).[44,45,48] In the following, the most important factors are listed:

- *stucture factor*: its square modulus $|F|^2$ provides the intensity scattering for a given plane of a perfect crystal;

- *polarization factor*: it considers the polarization properties of the light upon the diffraction from the crystal as a function of θ;

- *multiplicity factor*: it represents the number of the crystal planes having the same spacing and structure factors because of symmetry conditions, despite the different orientations;

- *absorption factor*: it measures the reduction of X-ray intensity when it penetrates the powder sample along a given direction.

- *temperature factor*: it takes into account that the atoms in a crystal do not kept a fixed position because of thermal vibrations, whose amplitude increases with increasing temperature;

- *Lorentzian factor*: it is due to the fact that one can measure an appreciable intensity of a diffracted ray even at angles deviating slightly to that which satisfies eq. 1.47.[44,45]

For these reasons, a PXRD pattern can be easily used as a qualitative (yet sometimes even quantitative) assessment of the degree of crystallinity of the material: in fact, disorder leads to peak broadening. An eventual conversion to amorphous phases is detectable via PXRD measurements by a loss in peak intensities.[44]

1.6 Physisorption of gases and evaluation of surface area

Gas adsorption is a widely used tool for the study and the characterization of porous materials like MOFs.[49–52] In the field of solid materials, *adsorption* is defined as the *"enrichment of molecules, atom or ions in proximity of an interface"*.[49] The gas in the

fluid phase is then named *adsorptive*, whereas in the adsorbed phase is named *adsorbate* and the space it occupies is the *adsorption space*. The solid material involved is the *adsorbent*.[49] Two different types of adsorption are generally involved: physisorption and chemisorption. *Physisorption* takes place if the adsorptive brought into contact with the surface of the adsorbent by van der Waals forces, polarisation or similar molecular interactions. In contrast, *chemisorption* occurs when the adsorptive establishes actual chemical bonds with the solid material.[49] A different issue is whenever the adsorptive becomes part of the bulk material by penetrating the surface: in this case we talk of *absorption*.[49] The reverse process of adsorption falls under the name of *desorption*.[49]

The study of a porous material generally is done by the acquisition of both the adsorption and the desorption curves, defined as the amount of adsorbate as a function of the pressure of the adsorptive; if the two curves do not coincide, an *adsorption hysteresis* is present.[49] If the acquisition is done at constant temperature and equilibrium pressure of the gas, the adsorption curve is generally named *adsorption isotherm*.[49] The typical procedure used for MOFs involves the use of nitrogen as adsorptive and temperatures under the critical temperature of 77 K: for this reason, the pressure is generally plotted as *relative pressure p/p^0*, where p is the equilibrium pressure and p^0 the saturation vapour pressure at that temperature.[49]

When dealing with a porous material, it is common to distinguish the *external surface* from the *internal surface*, which is the surface of all of the pore walls. The accessibility of the pores depends on the dimension of the molecules used as probes.[49] The most accepted nomenclature used for these *nanopores* (i.e. pores with the upper limit of $\sim$100 nm) defines the following three sub-types:

- micropores: pores with widths not larger than 2 nm;

- mesopores: pores wide between 2 and 50 nm;

- macropores: pores with width exceeding 50 nm.[49]

When the surface coverage on the pore walls spreads and, depending on the adsorption conditions, the adsorbing space involves the entire accessible pore volume, the process is named *micropore filling*.[49] In this context, it is also possible to observe the phenomenon of the *pore condensation*, or else the gas condenses to a liquid-like phase in a pore, even if $p/p^0 < 1$.[49]

Figure 1.20 shows main six types of physisorption isotherms and two associated hysteresis loops.[49] Type I isotherms are typical of microporous solids with relatively small external surfaces: it has a saturation value, governed by the accessible micropore volume, and a steep uptake at low p/p^0 caused by adsorbent-adsorptive interactions in the micropores, which lead to the micropore filling. If the material have mainly micropores with width $< 1nm$, the type I(a) is found, otherwise if the material has a wider pore size distribution (within the range $1 \div 2.5nm$), then type I(b) is found.[49]

Type II isotherms is characterized of an unlimited uptake value at high p/p^0, which is proper of nonporous or macroporous adsorbent. The point B would represent the
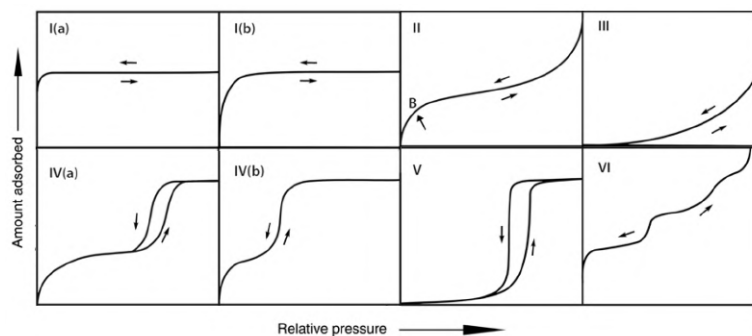
FIGURE 1.20: Six different physisorption isotherms and two related hysteresis loops.
Adapted from ref. [49].

completion of the coverage of a first layer with adsorbate and then the beginning of progressive coverage that occurs by the formation of multi-layers of adsorbate.[49]

In contrast, in type III isotherms there is a finite amount adsorbed at $p/p^0 = 1$ and no point B. The cases in which type III is observed are those characterized by an extremely weak interaction between adsorbent and adsorbate and then the adsorbed molecules form clusters around localized favorable sites.[49]

Type IV isotherms consists of an initial path similar to type II and a subsequent steep uptake followed by saturation. They are given by mesoporous adsorbents presenting pore condensation at high relative pressure values. They can show hysteresis (IV(a)) or be totally reversible (IV(b)).[49]

Type V isotherms has a shape similar to type III but with an upper limit. It is typical of microporous or mesoporous adsorbents which establish relatively weak interactions with the adsorbate (for example those between water and hydrophobic materials), which organizes itself forming clustering and then pore filling.[49]

Type VI isotherms are characterized by resolvable layer-by-layer adsorption and they are given by material with highly uniform nonporous surfaces.[49]

Evaluating the hysteresis loops (5 different types are identified in the current IUPAC classification) also allows to understand the features of the pore structure under consideration.[49] However a further deepening is out of the goals of this thesis.

1.6.1 Water isotherms

In order to learn about the sorption properties of a given MOF, another useful method involves the acquisition of a *water isotherm*, that is the use of moisture as adsorptive. As above mentioned, the data obtained gives information on the water content values at a given humidity value in condition of constant temperature and the type of curve generated allows to determine the eventual hydrophilic or hydrophobic character of the material examined, as well as the strength of the water-absorbent interaction.[51]

1.6.2 Breakthrough curves

In certain cases the study of the adsorptive performance of a material in industrial use may be useful, in order to test, for example, the capacity of that porous solid.[53] A common test is given by the *breakthrough curves*, in which a gas/vapor steam (typically air containing one or more adsorptives) flows through a bed of the studied material and the emergent stream is analyzed. In other words, a breakthrough curve is the time-resolved effluent adsorptive concentration of a fixed adsorbent.[53–55] They constitute an important characterization of the adsorptive separation technologies of a given material. This procedure is particularly common for activated carbons and zeolites.[53–55]

When a fixed bed of porous material is under a flux of adsorptive gas, the initial emergent stream is found adsorptive-free, and this continues as long as the bed can still adsorb; however after a certain time the solid bed approaches saturation because of the adsorbate and the adsorptive emerges at the outlet of the bed.[53–55] Its concentration increases until no further adsorption takes place, and both effluent and entry mixture have the same concentration. A breakthrough curve is then a plot of the duration of this test against the concentration of adsorptive in the effluent stream. The integration of the area above the curve provides the maximum loading of the adsorptive for that given bed.[53–55]

1.6.3 Assessment of the surface area by BET method

The Brunauer-Emmett-Teller (BET) method is the most widely used procedure to estimate the specific surface area of MOFs, even though its theoretical foundations are sometimes considered weak.[49,56,57] For this reason, in some cases, the *BET area* should be regarded as an apparent surface area, available for the adsorption of the specific adsorptive employed during the experiment.[49] The current standardisation of the calculation of the BET area involves the choice of nitrogen at boiling temperature (that is 77 K) as adsorbent. If correctly employed, even surface areas as low as $0.5 \div 1$ m^2 can be assessed, whereas for lower surface areas the use of krypton at 77 K is generally recommended.[49] The average area σ_m occupied by the N$_2$ adsorbate molecule in the complete monolayer, supposed "closed-packed", is assumed to be 0.162 nm^2.[49,56] For the application of the BET method it is necessary to transform the physisorption isotherm curve into the so-called "BET plot", calculating the BET monolayer capacity n_m.[49,56,58] The customary BET equation in linear form is

$$\frac{p/p^\circ}{n(1 - p/p^\circ)} = \frac{1}{\mathbf{n_m}C} + \frac{C-1}{\mathbf{n_m}C}(p/p^\circ) \tag{1.48}$$

in which n is the specific amount of nitrogen adsorbed at relative pressure p/p° and $\mathbf{n_m}$ is the specific monolayer capacity, while C is the "*BET constant*", a parameter exponentially related to the energy of the monolayer adsorption.[49,56–58] In order to find an unambiguous n_m, a linear region of the BET plot should be used. Generally, such linearity of the BET plot is found only in a restrict range of the isotherm, typically

within $p/p° = \sim 0.05 \div 0.30$.[49,56,57] This is equivalent to suppose that in this range monolayer formation occurs.[56] However, for microporous materials, the issue may be even more complicated because it may be impossible to recognize and separate the process of mono-layer adsorption from the micropore filling, and then the linear range may be much more difficult to locate.[49,56] Generally the pressure range considered does not exceed $p/p° = 0.1$.[49,56] For this reason, to improve the reproducibility of the results, the correct BET range is typically chosen by following this standard procedure:

1. the $i = 1/(\mathbf{n_m}C)$ intercept of the linear region must be positive, and then the quantity C should be positive;

2. the quantity $n(1-p/p^0)$ should continuously increase with p/p^0;

3. the p/p^0 value corresponding to n_m should be within the selected BET range.[49,56]

Once the linearity range has been found, the slope s and the intercept i can been found by a linear fit.[49,56–58] Since $s = (C-1)/(\mathbf{n}_mC)$, n_m can be find by

$$\mathbf{n_m} = \frac{1}{s+i} \qquad (1.49)$$

and then, the BET specific area $a_S(BET)$ is given by

$$a_S(BET) = \mathbf{n}_m \cdot \sigma_m \cdot N_{AV} \qquad (1.50)$$

where N_{AV} is the Avogadro's number.[49,56–58]

Some MOFs are flexible structures, or else they undergo structural transformations upon interaction with specific guest molecules, and for this reason their sorption behaviour is hard to interpret and then the calculated surface areas may even be meaningless (see section 2.1.4).[59,60] Some progresses in the development of new standard methods which take into account the non-rigid nature of such adsorbents have been made, but it is still ongoing.[49] For this reason, the current literature (as also this thesis) continues to be based on the standard BET methods we have presented in this section, bearing in mind of the meaning of the BET values found in these peculiar situations.

1.7 Amplitude modulation Atomic Force Microscopy

Scanning Probe Microscopies (SPM) are those microscopy techniques involving the generation of surface images using a physical *probe* which scans the surface, allowing to obtain both a physical-chemical and a morphological characterization of a surface in three-dimensional detail even down to the nanometer scale.[61,62] They all share the same operational elements, that is the use of a very sharp probe generally named *tip* and a *feedback mechanism* characterized by keeping constant a certain interaction parameter of the probe during the surface scanning.[61]

Among the SPM techniques, Atomic Force Microscopy (AFM) is one of most common and is splitted in more subtypes (amplitude modulation AM-AFM, frequency modulation FM-AFM, conducting AFM...).[61,62] The specific AFM technique used in this thesis is the amplitude modulation AFM, which corresponds to use the amplitude of forced oscillation of the probe as interaction parameter during morphology measurements.

Sometimes it is used to refer to AFM as a "*blind microscopy*" because it is based on *touching* the surface, unlike the conventional light or electron microscopes.[62] In the context of AFM, the expression of "*touching*" indicates an approaching to the surface to the point that surface-probe contact forces take place.[62] An AFM image is a "*2D matrix of numbers*", constructed by measures of *peak-to-valley* distances: these latter are obtained through a *feedback system*, which quantifies the vertical displacement of the probe during the scanning of the given surface.[62] The typical range is several micrometers vertically with a subnanometer height resolution, whereas the lateral ranges can go up to ∼100 µm with nanometric resolutions.[62]

More detailed descriptions about the electromagnetic forces involved and the core components of a AFM device are given in the next section.

Core components of AFM. Figure 1.21 shows a schematic illustration of the fundamental components for an AFM apparatus, that is the sharp tip/probe attached to the end of a flexible micro-cantilever, a focused laser beam, the quad photodiode and the chip.[62] When a tip vertically moves under the influence of a specific force bending
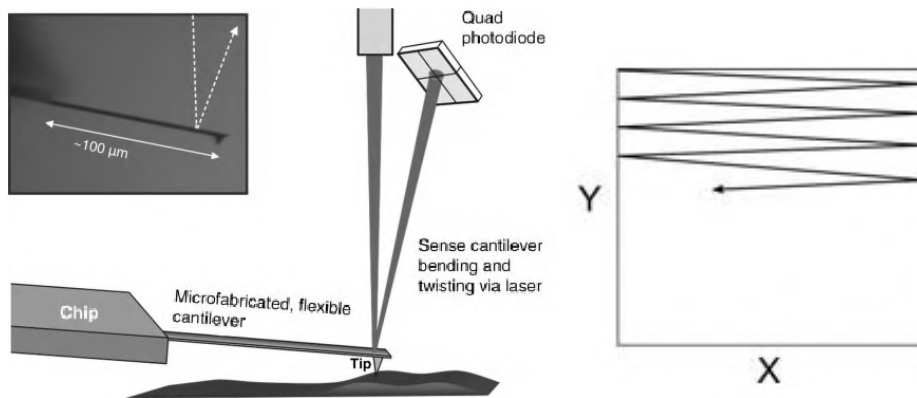

FIGURE 1.21: Essential components of an AFM device. The inset shows a light micrograph of a real cantilever/tip viewed from the side.[62,63]

the cantilever, the laser is reflected along a certain direction detected by the photodiode, allowing the quantification of the displacement.[62] In other words, the cantilever is the transducer which converts the forces sensed by the tip (see next subsection) into a measurable deflection. In the simplest case, one can imagine the tip in contact with a surface that is scanned by a *side-to-side* movement of the probe (Figure 1.21(b)) and by the measure of the vertical tip movement through the detection of the cantilever bending.[61,62] The lateral resolution of an AM-AFM device is mostly related to the tip's aspect ratio and shape.[61]

Since the idea behind the AFM method is to use the measure of the force between surface and scanning tip to reconstruct the morphology of the surface itself, it is strictly essential to know the main forces acting between tip and sample.[64]

1.7.1 Tip-Surface Interaction Forces

The total force involved in the tip-surface interaction gives rise to different effects and it is composed of diverse contributions at some distinctive distances, generally splitted in *long-range* and *short-range* forces.[61,64] They can be both attractive or repulsive, conservative or non-conservative and can also depend on the geometry of the system. The most important forces are discussed below. Several other forces are generally considered, but they are here omitted in the interests of conciseness.

The Lennard-Jones potential. The **van der Waals force** pertains atoms or molecules showing permanent electric dipole moments or that can be induced by another permanent dipole or even by fluctuations of the electromagnetic field, resulting from thermal or zero point quantum fluctuations.[61,64] It is a usually attractive long-range interaction. The dipole interaction potential scale as $1/r^6$, where r is the distance between atoms or molecules.[64]

In contrast the main short-range forces (i.e. for $d < 1$) arise from the effects of the overlap of the electron wave functions. In general they can be both repulsive or attractive; in fact, if such overlap reduces the total energy (meaning that the formation of a *chemical bond* is favored), the force will be attractive. However, further reducing the distance d, a repulsive interaction arising straight from *Pauli repulsion* takes place.

A frequently used model potential taking into account the two above mentioned forces is the *Lennard-Jones (LJ) potential*:[64]

$$U_{LJ}(r) = 4U_0\left[\left(\frac{R_a}{r}\right)^{12} - \left(\frac{R_a}{r}\right)^{6}\right], \tag{1.51}$$

where R_a is the distance at which $U_{LJ}(r) = 0$.[64] Figure 1.22 shows the LJ potential as a red line, whereas the two distinct contributions are shown in green (attractive $-1/r^6$ component) and blue (repulsive $+1/r^{12}$ component). Beneath, the corresponding force $F = -\partial U/\partial r$.[64]

Van der Waals force is additive and then for two groups of atoms the total interaction energy is the sum of all of the pair potentials. Because of its long-range nature, not only the atoms strictly close to the tip apex have a contribution to the van der Waals force but also those in a larger volume must be considered and summed up.[61,64] In order to calculate the net van der Waals force by adding all the individual dipole interactions established between tip and surface, a model for the *geometry* of the tip need to be defined. The two most common tip geometries involve the model of a *sphere-flat* and that of the *conical shaft capped with a half sphere-flat*.[61,64] Upon integration, the dependence

$$U(r) = 4U_0 \left[\left(\frac{R_a}{r}\right)^{12} - \left(\frac{R_a}{r}\right)^6 \right]$$
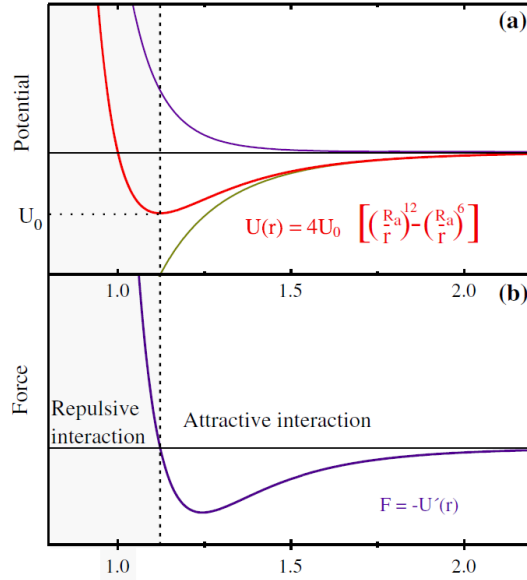
$$F = -U'(r)$$

FIGURE 1.22: The Lennard-Jones potential (red), commonly used as model potential for tip-sample interactions. The green and the blue lines show the attractive and the repulsive components, respectively. Beneath, the corresponding force. The boundary between attractive and repulsive regime is indicated by the dashed line, passing for the minimum of the LJ potential curve.[64]

of the Van der Waals potential on the distance D between the tip end and the scanned surface becomes $F \propto \frac{1}{D^2}$.[62]

Contact mechanics.   When the tip approaches the sample up to "come into contact" with its surface, besides the short-range repulsive force included in the LJ potential, another effect may take place: a change of the position of the atoms involved due to the elasticity of both tip and sample materials. In general, the effect is conceivable like a deformation of the surface of both the bodies involved when they are brought into *mechanical contact*; the entity of such deformation depends on the applied force and the properties of the materials.[61,64]

Capillary force: Under appropriate conditions of relative humidity (RH), generally satisfied at ambient condition, each hydrophilic surface is typically covered by condensed vapor, or else a layer of liquid water, whose thickness (generally ranging from 1 nm to several nanometers) depends on the RH value.[64] This implies that such spontaneous water condensation is one of the most challenging issues to deal with in AFM microscopy, because the tip will face capillary condensation and capillary adhesion forces, particularly in presence of asperities.[61,64] Whenever the tip approaches a surface with a gap distance comparable or lower than the so-called *Kelvin radius*[61,62], a water meniscus could be formed, as shown in figure 1.23. After the meniscus formation, if the tip-sample gap increases sufficiently, the meniscus could break, but such rupture will occur at a significantly larger distance than that at which it is was formed.[64] This attractive tip-sample force has then an hysteric nature. In certain cases, capillary forces could even
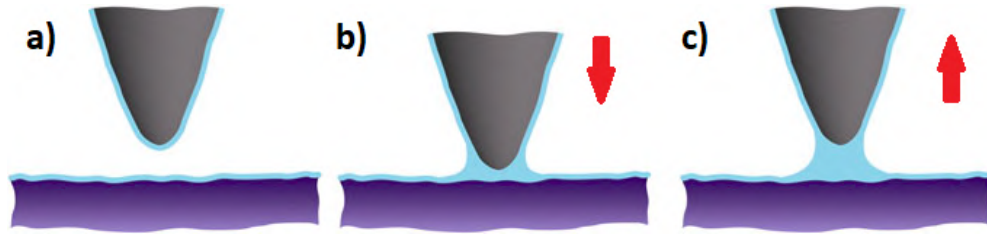
FIGURE 1.23: Capillary force. a) Both tip and sample are typically covered by a thin water layer at ambient conditions; b) when the tip approaches the surface, the gap between them fills with a water meniscus because of water condensation; c) when the tip moves back to the starting position, the water meniscus remains: this leads to the hysteric nature of the capillary force.[64]

disrupt the observed objects. Furthermore, since they can even reach an extent of 100 nN, they could dominate all other tip-surface forces.[61]

1.7.2 Amplitude modulation dynamic

AM-AFM is one of the most suitable AFM acquisition modes in ambient condition. The periodic oscillation of the cantilever is given by piezoelectric crystals, which convert an oscillating electric tension to a periodic mechanical response to be provided to the cantilever.[61,62] In AM-AFM the tip oscillates very close to the sample surface; the mechanically excitation is supplied at a fixed frequency (usually close to the first flexural resonant frequency), leading to an oscillation amplitude that is altered by the tip-surface interaction forces. The experimental observables are the amplitude of the oscillation and the phase shift lag between the external excitation (given by the piezoelectric crystals) and the tip motion.[61,62] More in detail, amplitude is exactly the feedback parameter used to map the topography of scanned surfaces. In fact the amplitude oscillation of the cantilever is different when the probe oscillates away or near the sample surface.

Once a specific amplitude value for the probe oscillation is fixed (*set-point amplitude* A_{sp}), the feedback system will ensure that such value will be maintained during all the scanning, moving properly the cantilever/tip system along the vertical direction whenever the tip-sample interactions change it.[61,62] In other words, if at a certain moment the tip shows an amplitude $A < A_{sp}$, the feedback system interprets it as an approaching of the sample to the tip and it will move vertically the probe in order to restore the initial tip-sample gap and then also the amplitude set-point value. Repeating the procedure during all the scanning, the surface profile can be reproduced by following the vertical movements of the cantilever operated by the feedback system.[61,62]

The value chosen for the *free amplitude* contributes to establishing the operation regime, that can be attractive (usually *noncontact*) or repulsive (*intermittent contact*).[61] The specific AM-AFM acquisition mode performed for the samples involved in this thesis is precisely the *intermittent contact mode*, also called *tapping mode*; this means that the tip is mainly subjected to the short-range forces (generally repulsive, as already seen in the previous subsection) because of the small tip/sample distances.[61,62] Therefore, the set-point amplitude should be carefully selected, because too high amplitude values

may induces strong mechanical contact irreversible effects on both the probe and the sample, affecting the measured morphology of the surfaces.

Even the phase changes are directly linked to changes in the surface properties, typically to energy dissipation processes.[61,62] This means that if in the same sample two different materials are present with similar superficial *height*, even if the amplitude changes cannot discriminate them, they can be both revealed by distinguishing the change in the phase values. The *phase imaging* may even be able to discriminate a crystalline phase from a molten one of the same material.[61] For this reason, generally two different AFM images are acquired: a *phase image* reporting information about the material composition homogeneity and a *morphological image* reconstructed by the height variations.[61,62]

1.8   Thermogravimetric analysis

Thermogravimetric analysis (TGA) is an experimental technique which allows to determine the thermal stability of a given material. The method consists in the continuous measurement of the sample mass as a function of an increasing temperature, generally under controlled atmosphere (inert gas, vacuum, or even ambient air,etc.).[65] In other words, this technique provides a quantitative measurements of the mass changes in a material, which can be associated with reversible processes (like molecular desorption) or irreversible thermal degradation, defining the upper limit of *thermal stability*.

The *thermogravimetric analyzer* consists of a precision balance equipped by a sample holder provided with a furnace that allows a programmable control of the temperature and of the increasing-rate, generally constant for all the time of the measurement. The result is typically reported as a mass change as a function of the temperature and called *TGA curve*.[65]

After the acquisition of a TGA curve, a material can be defined *"thermally stable"* in a given temperature range if no irreversible mass changes have been observed. In this way it is possible to find out the upper use temperature for the sample studied, beyond which the material degrades.

Since by varying the substance studied the thermal properties change, a complex material may show TGA curves with more than one inflection points. For example, as will be shown in chapter 2, MOFs generally show a continuous mass decrease up to about $390 \div 420$ K which is due to the loss of water/solvent molecules adsorbed within the pores of the matrix. The second inflection point generally represents the temperature at which the organic components separate from the inorganic ones and then it constitutes the upper limit of the thermal stability of that given MOF.[66]

Chapter 2

Metal-Organic Frameworks

Metal-Organic Frameworks (MOFs) are the first class of crystalline solids developed in the new area of research called *reticular chemistry*, which includes all those extended structures made by the assembly of different discrete chemical entities connected by strong bonds.[66] MOFs consist of single-ion or poly-nuclear metallic nodes joined together by organic linkers through strong bonds.[50,52,66,67] Nowadays, the number of MOFs catalogued is already of about 70,000 and keeps rising from year to year.[68] Despite the great variety, the resulting frameworks are typically highly porous and crystalline, with a porosity generally ranging from 1,000 to 10,000 m^2/g.[50]

In this chapter several topics concerning MOFs will be explored. In section 2.1 the fundamentals and general aspects will be explained, focusing in particular on the typical properties and potential applications of these materials. Two MOF sub-categories will be also introduced, which are the flexible MOFs and the composite MOFs, as well as a particular well-known metal cluster which constitutes the inorganic knot of all the MOFs studied in this thesis. In section 2.2 the issue of the MOF stability will be introduced from many points of view. In the following sections 2.3, 2.4 and 2.5 the three MOFs investigated in this thesis will be discussed and their state-of-art about physical and chemical properties, stability and knowledge of the processes in which they are involved will be explained.

2.1 Fundamentals of MOFs

2.1.1 Origin and developments of MOFs

In 1959 Saito and coworkers reported what are considered the first coordination networks: they were extended structures composed of metal ions (Cu^{2+}) directly connected by bis(alkylnitrilo) units.[69–71] Depending on the length of the linker unit, they obtained crystalline materials of varying dimensionality.[69–71] However, these materials were held together by rather weak non-covalent interactions (Metal-N-donor), and then the resulting coordination networks generally suffered from inherent architectural and chemical instability.[66] Despite this, they stimulated an important evolution in the synthesis of extended structures by the use of geometric design principles and molecular building unit approach. This interest has led to the synthesis of the first MOFs at the end of the century.[66]

The term *Metal-Organic Framework* was first coined in 1995 by Omar M. Yaghi for the publication of the compound $[Cu(BIPY)_{1.5}](NO_3)$.[66,72] The term simply indicated
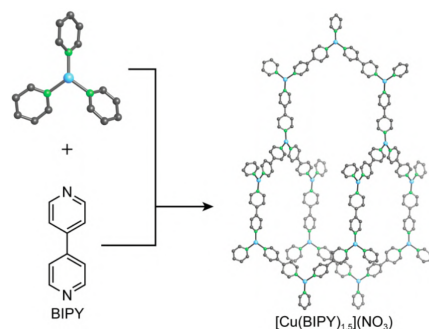

FIGURE 2.1: Connecting trigonal planar $Cu^{2}+$ single metal nodes with linear BIPY linkers, the 3D framework $[Cu(BIPY)_{1.5}](NO_3)$ is obtained. Color code: Cu, light blue; N, green; C, gray.[66,72]

the overall composition of metal ion and organic bridge, whereas "framework" was referred to the character of the structure.[66,72]

During the same year, another pioneering structure was synthesized: Zaworotko et al. reported the network $Zn(BIPY)_2SiF_6$, characterized by a potential empty space of about 50% of the unit cell volume.[66,73] However both these structures had the typical problems of coordination networks: collapse upon removal of solvents or exchange of ions in the pores, lack of design choices because of the single metal ion in the nodes, and absence of chemical stability because of the relatively weak bonds.[66]

To overcome the problems of coordination networks, an attempt has been made by introducing charged chelating linkers. This choice allowed to have an increased bond strength, resulting in a higher thermal and chemical stability. Furthermore, the charge on the linker could balance that of the metal centers and avoid the accumulation of ions or the interpenetration phenomenon.[66] The first charged linker used was the BTC (benzene-tricarboxylate) for the network $Co(BTC)(Py)_2$.[66,74] Because of the strong bond between the metal center and the charged BTC linker, the removal of the solvent did not lead to the collapse of the structure.[66,74]

Introduction of the SBUs. In very few years, in order to find a solution to the problems concerning stability and topological design, the concept of *secondary building units* (SBUs) were introduced, replacing the single metal-ion nodes used until then.[66] The SBUs are polynuclear clusters formed by a chelation of the metal ions: in this way the metal ions are held in place by the binding groups of the linkers, for example carboxylates.[50,52,66,68] The combination of SBUs with charged linkers lead to the formation of neutral and more stable frameworks.[66,74]

The first realization of this new concept was MOF-2 $Zn(BDC)(H_2O)$: its structure consists of dimeric $Zn_2(-COO)_4$ paddlewheel SBUs linked by benzenedicarboxylic (BDC) columns.[75] The stability allowed to obtain a stable MOF with a permanent microporosity, proved by the reversible gas adsorption measurements.[75] Furthermore when in 1999 MOF-5 was synthesized for the first time (figure 2.2(a)), it exhibited a

permanent porosity with a specific surface area higher than that of zeolites or other well-known porous solids like porous silicates and carbons.[50,66,76,77] The Langmuir surface of 2900 m^2/g was about 2-fold higher than that obtained for the known porous solids, so much that it seemed a misprint.[50,66,76,78] The permanent porosity found after the removal of the solvent from such materials marked a turning point in chemistry, so much that the term "MOF" started to be used for emphasize stability and porosity, generating a huge interest in the MOF development.[50,52,66,68]

By combining different organic linkers and inorganic SBUs with variable geometry and connectivity, it was possible to produce a wide range of 2D and 3D MOFs.[50,52,66,68] Currently, the IUPAC definition of MOF is *"A coordination network with organic ligands containing potential voids."*.[66]

In the following years another new class of interesting materials was added to the realm of reticular chemistry: when the formation of crystalline extended solids is realized by linking only organic building units, the resulting structure is called *covalent organic framework* (COF).[66,79] COFs are also porous and crystalline but they are out of the goal of this thesis and therefore will not be further explored in the following.[66,79]

Isoreticular MOFs. As already mentioned, by changing the combination of SBUs and organic linkers, it is possible to obtain a myriad of MOFs with different topology and porosity.[50,52,66] The porosity of a material is formally defined as the ratio of the volume of the pores to the whole volume occupied by the solid.[66] Pore shape and pore size have a direct impact on the sorption properties of the MOFs, and they are so important that MOFs are commonly described in terms of their uptake properties.[66] In general, the more is the length of the linker employed, the more is the pore size of the MOF, but the volume of the pores depends also from the topology of the obtained MOF.[50,52,66,80]

When two MOFs are composed of organic linkers of different sizes but the underlying topology of the frameworks is unchanged, they are *isoreticular* MOFs (IRMOFs).[66,80] The most known example of IRMOFs is that of the series based on MOF-5 (figure 2.2). MOF-5 is formed by ditopic BDC linkers and octahedral Zn$_4$O($-$COO)$_6$ SBUs,
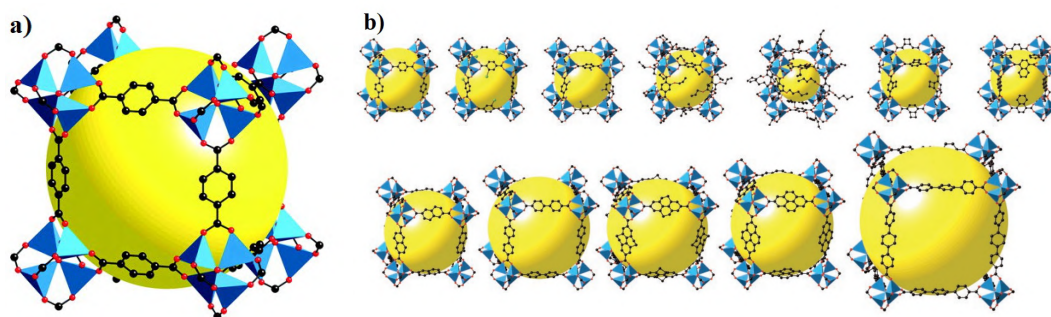

FIGURE 2.2: MOF-5 (a) and the IRMOF series based on it(b).[77,80]

formed in turn of four tetrahedral ZnO$_4$.[76,80] Saving the same SBU but different H$_2$BDC derivatives as organic linker of variable length, the topology remains unchanged for each

IRMOF of the series.[80] Another remarkable IRMOF series is that based on IRMOF-74: the isoreticular components have different pore sizes up to 98Å, value obtained for IRMOF-74-XI using a 50 Å long organic linker.[81]

2.1.2   A particular SBU: the dinuclear copper paddlewheel

As above mentioned, it is not sufficient only to use the same SBU to obtain isoreticular MOFs: the correct choice of the linker is fundamental. The three MOFs investigated in this thesis, HKUST-1, STAM-1 and STAM-OEt, show the same SBU but three organic linkers with different connectivity, that give to the three materials different topologies.[24,82,83]

This common SBU is a $Cu_2(-COO)_4$ dimeric cupric tetracarboxylate unit. It is the same unit constituting the copper acetate complexes discussed in section 1.1.1 and, as already defined in that contest, hereafter it will be named simply *paddlewheel*.[24,82,83] As previously discussed, the paddlewheels are composed of two Cu sites which can be both coordinatively unsaturated or saturated (see figure 2.3): in the former case the two Cu^{2+} ions are coordinated in a square-pyramidal geometry with a fifth out-of-plane bond typically occupied by polar molecules like water, whereas in the latter case their environment is square-planar.[22,24,25,84]
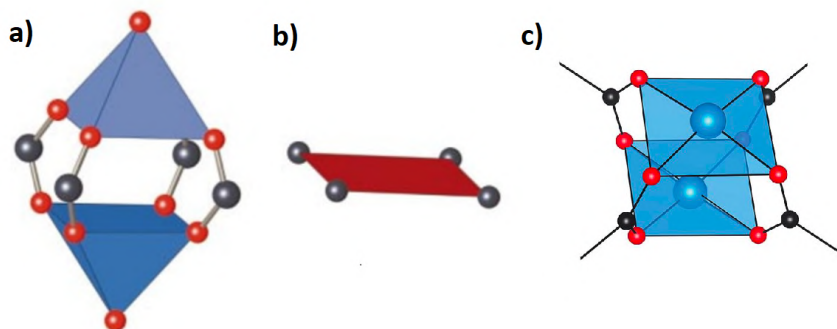

FIGURE 2.3: Two different configurations of the $Cu_2(COO)_4$ moieties: O, red; C, black; Cu-oxygen polyhedra, blue; hydrogens have been omitted. The polygon defined by the carbon atoms are red. More in detail, (a) represents the hydrated $[Cu_2C_4O_8](H_2O)_2$ cage: the bond with water changes the geometric arrangement of the Cu; (b) represents the square formed by the carbon atoms of the carboxylate bridges; (c) shows the square planar geometry of the Cu^{2+} ions in the dehydrated configuration. Adapted from refs. [25] and [85].

Bimetallic tetracarboxylate units like our copper paddlewheel are common features in MOFs, with the presence of different transition ions.[24,25,50,52] The paddlewheel shown in figure 2.3 may be formed even by zinc, iron, molybdenum, chromium, cobalt or ruthenium atoms.[50] Furthermore, the same copper paddlewheel present in HKUST-1, STAM-1 and STAM-17-OEt is also the SBU of the MOFs NU-111, PCN-14, NOTT-115 and many other.[25,26,86–88]

Due to the similarities with the copper(II) acetate monohydrate, all the considerations about the copper interactions done in section 1.1.1 are valid for the paddlewheel

unit. For example, also within the paddlewheel, the Cu-Cu distance is $\sim 2.61 \div 2.64$ Å, a so relatively short Cu⋯Cu distance that it might suggest a through-space interaction between their unpaired electrons establishing a δ bond, but the overlap between the two d orbitals is too small.[22]

For this reason, as found for copper acetate, this copper paddlewheel complex exhibits a rather high magnetic constant coupling J_0 (see section 1.1), due to a quite strong antiferromagnetic interaction established between the two copper ions. As already said, the main factor responsible of such rather high coupling is the electronic structure of the carboxylate bridges which provide a connection between the two unpaired electrons of the Cu^{2+} ions.[23]

More in general, its magnetic properties may strongly depend on the axial ligands and on the coordination geometry around the copper atoms.[22] In fact the geometry of the metal site has a strong impact on the order of the energy levels of the d orbitals, consequently determining the particular arrangement.[89] However, when the geometry of copper(II) is square planar, square pyramidal or even elongated octahedral, at the ground state we always found the $d_{x^2-y^2}$ orbital and a change in the axial ligand (for example from H_2O to NH_3) generally induces smaller variations in J_0, even though Da Silva and co-authors[27] affirmed to have observed a ferromagnetic behaviour when DFM was placed as axial ligand.[22,27,89]

As will be explained in the following sections, depending on the organic linkers to which it is connected within the framework, the paddlewheel may confer different magnetic features to the MOFs containing it, even though always in the context of antiferromagnetic coupling.

2.1.3 General properties and potential applications

Since MOFs are a large class of crystalline materials, by exploiting the crystalline structures, the high surface areas, the tailorable pore openings and sizes, we can find in literature a wide range of potential applications.[50–52,90–94] In general, the most important properties are considered to be the ultrahigh gas storage capacities, high selectivity in gas separations and the ability to harvest water or toxic gases from air.[50,52,66,90–96] Such properties make MOFs outstanding candidates for the development of MOF-based technologies in a wide range of research field, and in particular in the clean energy research. For example, they can give a strong contribution to the resolution of the problem of the environmental pollution and the reduction of carbon dioxide emissions because of their excellent results in capture of CO_2 and in hydrogen storage.[90,93,94]

Staying on the theme, among the possible solutions for the diminishing of air pollution is the petroleum replacement in favour of alternative fuels like methane; however, no efficient enough storage methods have been developed to implement this new strategy in the automotive industry. In contrast, MOFs showed promising performances even in methane storage, achieving very remarkable uptakes of methane.[95,97]

Anyway, the literature which investigate the selection or the storage/capture of gases by MOFs is very wide, and it involves many different substances, from water to nitrogen monoxide, or from ammonia to other harmful pollutants, even toxic metals.[51,52,90,92,98–100]

In those case in which the chemical composition of the MOFs is not toxicologically damaging, they can even find biological and medical application, for example as delivery vehicles for therapeutic agents.[92] In these cases, it becomes significant processing MOFs into specific shapes and then preparing thin films or membranes.[92,101,102]

The tunability of MOFs has allowed to adjust the electronic properties of some MOFs, discovering porous conductive frameworks: such combination of porosity and conductivity provides possible applications as supercapacitors or electrocatalysis.[66]

It is important to clarify that some of the potential applications here mentioned are not limited only to the fundamental research, but several chemical and automobile companies are actually focusing on their development.[66] This is reasonably possible because the industrial scale synthesis is already available for some MOFs.[66]

For example, in 2016 the first commercial application of MOFs technology was announced by the company *Decco* and registered under the name of *TruPick*, for the prevention of the fruits and vegetables ripening in storage.[103] The technology exploits the adsorbent propriety of a MOF (undisclosed for commercial reasons) for the storage and release of 1-methylcyclopropene, a synthetic plant growth regulator. Inhibiting the exchanges of the gases released by the ripening fruits among the neighboring fruits, they could slow down the ripening in the large storage facilities up to nine months.[103]

Still more recently, in 2019, a sorption-based atmospheric water harvesting device has been patented: thanks to the strong water adsorption of a specific MOF, it is able to collect water from the air even at low relative humidity (RH) percentages, powered by the sunlight.[104]

Unfortunately, the technological leap for the most of the potential applications has not yet happened because of the *stability problems* they exhibit. The topic is developed in section 2.2.

2.1.4   Flexible MOFs

Despite MOFs are extended structures, a small fraction of them is capable of allowing motion of their constituents of great amplitude without collapses neither deterioration of the frameworks in solid state, as a response towards particular external physical or chemical stimuli like guest inclusion, heat, etc.[59,60,66] In the so-called *flexible MOFs*, also indicated sometimes as *"third generation of functional MOFs"*, the framework undergoes a force which brings about a structural change: there may be broken/formed bonds or distortions in bond lengths or angles.[59,60,66,105] Such motion may also affect the entire framework: this is the case of the *breathing MOFs*, that undergo a global and substantial change in the internal voids after these external stimuli, which supply the necessary energy for the structural change.[59,66] Such a significant change is generally accompanied by a variation in the pore volume, resulting from the expansion or contraction of the

voids.[59,66] In fact, in some cases these materials are able to transform between *open pore* and *closed pore* or also *narrow pore* and *large pore* forms.[59]

A scheme of some motions showed by flexible MOFs in response to a guest-host interaction are shown in figure 2.4.
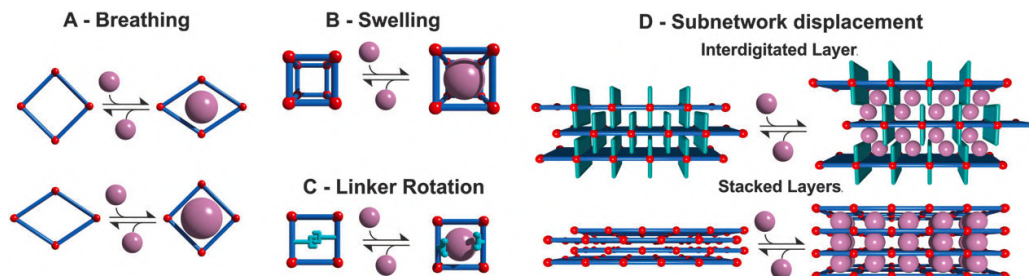

FIGURE 2.4: Examples of different flexibility modes shown by some flexible MOFs. Classes A and B are always characterized by a change in unit cell volume, while In class C and in some cases also D, the unit cell volume does not change. Adapted from ref. [59].

In general, flexible MOFs show a full retention of the long-range order even after a breathing motion: a completely unexpected property if we compare them with the traditional crystalline solids.[59,106] Such a long-range order allows to make a crystallographically accurate analysis of the two (*bi-stable MOFs*) or more (*multi-stable MOFs*) states in which we can find a flexible MOF.[59,66,106]

As we can see in the following section, flexible MOFs have peculiar potentiality for commercial applications, because they are a perfect combination of crystalline order of the network with a global and cooperative structural transformability.[59,60] Two of the three MOFs investigated in this thesis are flexible: STAM-1 and STAM-17-OEt.[82,83] Their properties will be explained in detail in sections 2.4 and 2.5, respectively.

2.1.5 Composite MOFs

A *composite* can be defined as a multi-component (at least two) material with (non-gaseous) multiple phases but with at least one continuous phase, in which each component retain its own identity and can contribute with appropriate properties to the whole system.[102,107–110] Recently, several reports have been published about *composite MOFs*, that is MOFs combined with other suitable materials, improving the pristine properties of the single components and bringing about novel functionalities, broadening the applications to new fields .[102,107–110] For example, it has been typically observed an enhancement of physicochemical properties like the chemical stability (see section 2.2), the possibility of template effects, ease of handle, improvements in mechanical strength and porosity, and then an enhancement of the performances in gas adsorption or separation.[102,107–110] Suitable materials with which arrange MOF-based composites may be small bio-molecules, nano-particles, polymers, nano-fibers, specific substances like drugs or metals, and so on.[102,107–109] Figure 2.5 shows some significant examples of composite MOFs reported in literature.[102,111–114]
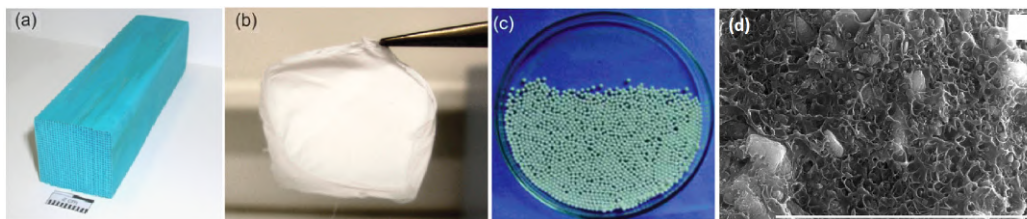
FIGURE 2.5: Example of MOF composites: (a) HKUST-1 *monolith* grown on a cordierite network;[111] (b) a combination of ZIF-8 and PVP forming a fiber mat;[112] (c) HKUST-1/PAM beads (PAM stands for polyacrylamide);[113] (d) SEM image showing the inorganic crystal of MOF-5 within an amorphous polymer matrix of acrylonitrile butadiene styrene (ABS); the scale bar represents 10 µm.[102,114]

Among MOF-based composites like MOF-silica or MOF-organic polymers, particularly promising is the integration of MOFs with carbon-based materials, including different allotropes such as active carbon, nanotube, fullerene, graphite, etc.[102,107–109] These particular composites may combine the extraordinary properties of MOFs with the typical high mechanical and elastic strength, electronic and optical properties of the carbon-based materials, that are frequently transferred to the combined systems.[108] An enhancement of the water/chemical stability has been proved for MOF-carbon composites.[108] For example, upon combination with graphene oxide (GO) which, although hydrophilic, also consists of graphene-like layers, the composite material turns out to be more hydrophobic than the pure virgin MOF.[108]

As a first approximation, they can be divided in two subcategories: composites in which MOFs are in the continuous phase and those in which MOFs are in the discontinuous phase.[107–109,115] The former category is more commonly used (for example for application as drug delivery), whereas the members of the latter are principally prepared with the aim of changing the size, the shape or to facilitating the handling and are interesting in applications like small molecule separation, purification and catalysis.[108,109] The subtype of our interest is precisely this last one. For this reason, we will regard carbon as the dominating component and then the matrix material, whereas the MOF constitute the functional species.[108] MOF/carbon composites can be synthesized with widely varying approaches, then the combination with the carbon matrix may take place in different ways: the MOF could grow on the carbonaceous scaffolds, could be directly synthesized within the carbon matrix or also mixed with it.[108] When the matrix is the MOF and is used for the encapsulation of different substances, two suggestive expressions are used to name two opposite encapsulation strategies: *"ship in a bottle"* method, where the secondary entity is grown inside a pre-existing MOF matrix, or otherwise *"bottle around ship"* method, if the MOF is synthesized around such functionalising entities.[109,115] A scheme is given in figure 2.6.

Although the situation approached in this thesis is reversed because our matrix will be a carbon-based material and the MOF the encapsulated entity (see section 3.1.8), the synthesis process that will be described may be considered an extension of the *"ship in a bottle"* method, because the growth of the MOF takes place during confinement within cavities of the matrix. When it is sufficient a *"one pot"* synthesis, the *"in situ growth"*
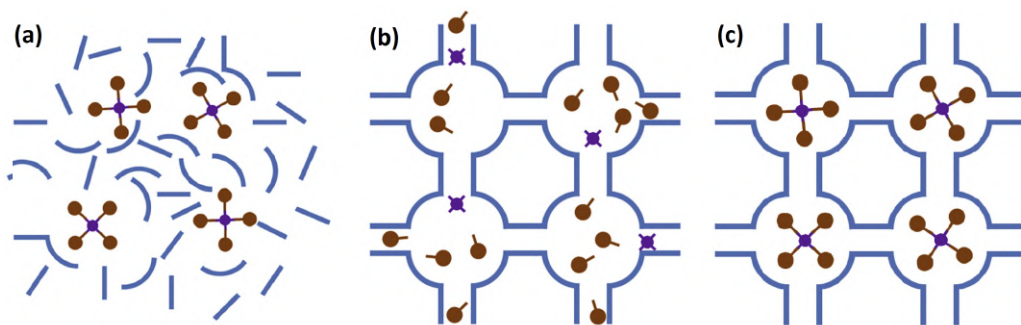
FIGURE 2.6: The formation of MOF-based composite materials with the two approaches: (a) "bottle around ship" and (b) "ship in a bottle"; (c) shows the the final product prepared by any of the two methods.[109]

takes place simply immersing the matrix into a solution containing the precursors of the MOF we wan to grow, building the MOF both in the internal/external surface. This method has also been widely used in the cases in which the matrix were silica or alumina microspheres.[107]

2.2 Stability of MOFs

In the wide variety of MOF compounds, involving structures with completely different properties from each other, a general requirement is the *stability*. We can define different types of stability: (1) with *chemical stability* we refer to the ability to resist chemical treatments without any significant change of the overall structure (when present, the changes are generally easily estimable with the sole X-ray diffraction), whereas the correspondent ability to withstand thermal treatments is called (2) *thermal stability* (typically assessed with TGA and/or X-ray diffraction, for example); (3) the *mechanical stability* is a property defining if the given material resists to external forces (and it is measurable evaluating the tensile strength for example); (4) finally, a MOF has *architectural stability* if it retains its structural integrity after the removal of guest molecules (for example after the evacuation of the solvent or other chemicals used during the synthesis), verifiable also by X-ray diffraction .[66]

The evacuation of the lattice at the end of the synthesis is a crucial step because having the pores emptied is necessary for most applications (for example gas storage or separation, etc.), but MOFs may be damaged by the process involved, sometimes losing the porosity.[66,105,116,117] This was the problem of the first MOFs, whose structure collapsed upon solvent removal.[66] In fact, outgassing a MOF by a treatment under vacuum may signify the development of significant capillary forces or surface tension, which in turn can produce a full or partial collapse of the lattice.[117] This issue is generally highlighted by a significant discrepancy between measured and estimated surface area.[116,117]

As shown in figure 2.7, MOFs suffering this problem are sometimes defined "1st generation MOFs".[105] Fortunately, MOFs belonging to the 2nd generation onwards are architectural stable, and they possess a stable porosity even upon a complete
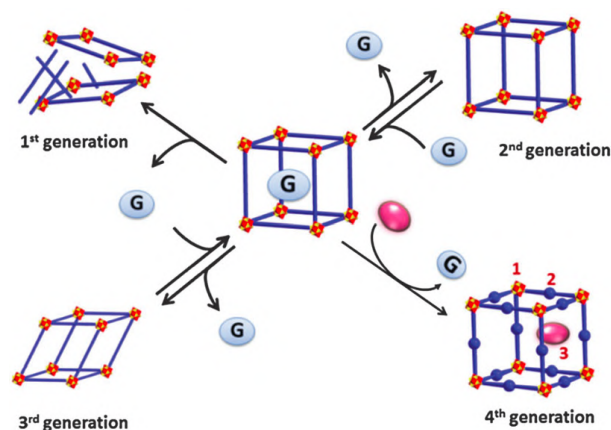
FIGURE 2.7: A subdivision of MOFs in *generations*: the *1st generation MOFs* collapse upon guest removal, *2nd generation MOFs* retain their porosity upon outgassing, whereas *3rd generation MOFs* show architectural stability but also dynamic properties upon evacuation. The *4th generation MOFs* category include those materials which can sustain post-synthetic modification.[105]

outgassing.[26,50,52,105,117] More in detail, if the "2nd generation MOFs" are robust and relatively rigid compounds, the "3rd generation MOFs" are flexible and dynamic to external stimuli (see section 2.1.4). Sometimes also a "4th generation" is defined, to indicate the MOFs architecturally stable to the point of withstand substantial post-synthetic modifications. Like all the MOFs of the so-called 2nd and 3rd generation, also the MOFs studied in this thesis are architectural stable. Furthermore, since their thermal stability is also well-known and largely guaranteed up to 550 K, traditional outgassing methods consisting in heating the MOF under low pressures are easily applicable, allowing to a complete outgassing of the as-made material.[24,83,105,116,118,119] This process is very frequently called *activation process.*[116]

Differently, the investigation on the mechanical and chemical stability of carboxylate MOFs like HKUST-1, STAM-1 and STAM-17-OEt is a hot topic of the current MOF research and also the heart of this thesis, and for this reason a more detailed deepening about these two properties in MOF compounds is given in the sections 2.2.1 and 2.2.2, respectively. A further digression on the state-of-art strictly regarding the three MOFs studied in the present thesis can be found in the sections 2.3, 2.4 and 2.5.

2.2.1 Mechanical stability: the problem around the densification of MOFs.

As above mentioned (section 2.1.3), even though the potential applications are countless, the commercial successes are still very few. One of the reasons is that, in general, the conventional large-scale synthesis processes produce MOFs in the form of powder with low density, a property not generally recommended for many industrial applications.[101,120] Furthermore loose powders have a low mechanical strength or limited volumetric gas storage density, they are hard to handle and their use can contaminate gas storage

tanks.[101,120–122] Applications involving gas storage or similar require high thermal conductivity, a good stability in humid and reactive environments, and moreover a high volumetric hydrogen storage density.[101,120,123] Similar problems have been encountered for the storage of hydrogen, methane or carbon dioxide (CO_2).[101,120,123]

For this reason, a wide part of the MOF literature of the last years dealt with the densification of MOFs to improve the overall performances as long as they can be suitable for the commercial applications required.[101,120] Figure 2.8 shows an overview of the main differences between the properties of the powdered and densified MOFs.
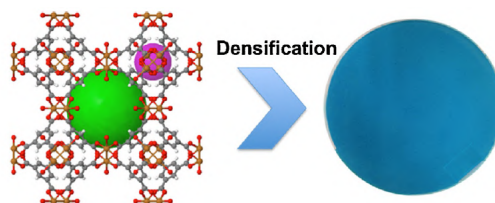
Properties	Powdered MOFs	Densified MOFs
Mechanical strength	low	high
Thermal conductivity	low	high
Packing density	low	high
Stability towards water	poor	better
Chemical stability	poor	better
Volumetric density	low	high
Gravimetric density	high	compromised
Surface area	high	compromised
Pore volume	high	compromised
Crystallinity	crystalline	reduced crystallinity

FIGURE 2.8: Comparison between the properties of MOFs in powdered and densified form.[101]

The densified MOF products can have the forms of pellets, beads, monoliths, or also film coatings and they can be obtained by several different processes.[101] Among the most employed strategies there is the mechanical compaction, utilized with or without the addition of a chemical binder.[101,120]

The usefulness in the employ of chemical binders is the improvement of the mechanical strength and of the thermal conductivity of the MOFs.[101,124] However, binders may reduce the adsorption capacity of the densified MOF, for example partially filling its pores.[101] For this reason, in the following we will focus only on mechanical compaction without the use of any binder.

Nevertheless, the mechanical compaction seems to have always a cost: the more the density of the densified MOF increases, the more its structural properties are compromised.[101] For most of the MOF pellets, the best compromise is obtained when the density of the pellet is close to 0.5 g/cm^3.[101] Figure 2.8 cleary shows that if upon densification the volumetric and the packing density, the stability and the mechanical strength increases, on the other hand the gravimetric density, the surface area, the pore volume and the cristallinity are compromised, sometimes even dramatically.[101]

In conclusion, the ideal target to reach for the technological leap and the industrial employment is to identify a simple densification strategy which may improve the volumetric packing, the mechanical strength and even the stability under humid conditions,

without any reduction of the surface area, pore volume and cristallinity.

In the following section 2.3.3 the literature on the densification of HKUST-1 is exposed. In contrast, until now, no works have been done on the densification of the MOFs STAM-17-OEt and STAM-1.

2.2.2 Chemical stability: *"Water is everywhere!"*

"Water is everywhere!" is the overture of the review about the water adsorption in MOFs written by Canivet and co-authors.[125] In fact, even though in section 2.1.3 we have mentioned that MOFs have great potentialities for methane or hydrogen storage and for the capture of carbon dioxide from flue gases,[52,66,90,93–95,125,126] outside of the laboratories, natural or industrial gas steams, or even the simple air, have generally a significant percentage of water vapor/humidity and therefore the MOF behaviour in the presence of water is a critical aspect to investigate (see figure 2.9).[51] In fact, for
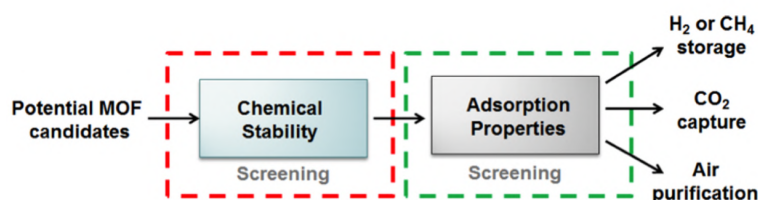
FIGURE 2.9: A simplification of the importance of MOF water stability for the application in the real world.[51]

example, water vapor is one of the main component in industrial flue gas, then it cannot be ignored when studying the CO_2 capture.

Unfortunately, even the first discovered MOFs, MOF-5 and HKUST-1, turned out to be strongly water-sensitive with critical consequent effects and also afterwards it has been remarked that, generally, MOF performances in humid environments are typically not enough to fit the industrial requirements.[51,125,126] Even an eventual dehydration step of bio-fuel streams is unthinkable, because it would require an energy exceeding that released by the combustion process itself.[51] It is also true that certain soluble MOFs called *Bio-MOFs* are interesting for *in vivo* medical applications, for example as drug carriers.[90,92,125] For all these reasons, the search for the chemical stability of MOFs is considered one of the main challenges of this research field and deep investigations on both the water stability and on the degradation mechanism of MOFs are of utmost importance.[51,125–127]

Before continuing, it is useful to point out that, when we define a MOF as *"water stable"*, we mean that, after handling it in laboratory air and/or exposing it to a reasonable amount of air moisture, the porous structure has been retained.[51] The easiest experimental methods that are used at this purpose are the comparison of PXRD patterns and BET surface tests carried out before and after the exposure.[51] However, they are not sufficient to ensure the stability and to understand the mechanism involved in the structural stability or instability of the given material, and then multi-technique

approaches are generally required.[51] When water stability of MOFs is proved uniquely by acquisition of PXRD patterns, it is actually considered only at a low confidence level.[51] In fact, PXRD technique cannot catch sample solubility (with consequent loss of solid phase content), formation of amorphous areas or superficial structural collapses leading to internal inaccessibility to adsorbates.[51] In addition, from an industrial point of view, it may be crucially important that the water-stable material can return to its original form at the end of each cycle of adsorption/gas separation or purification, and therefore in this cases a *reversible hydration process* may be required.[51]

Structural factors linked to water stability

After several efforts and compared studies, some structural factors governing the stability of MOFs in presence of water have been individuated.[51] A complete scheme of what is going to be discussed is shown in figure 2.10.
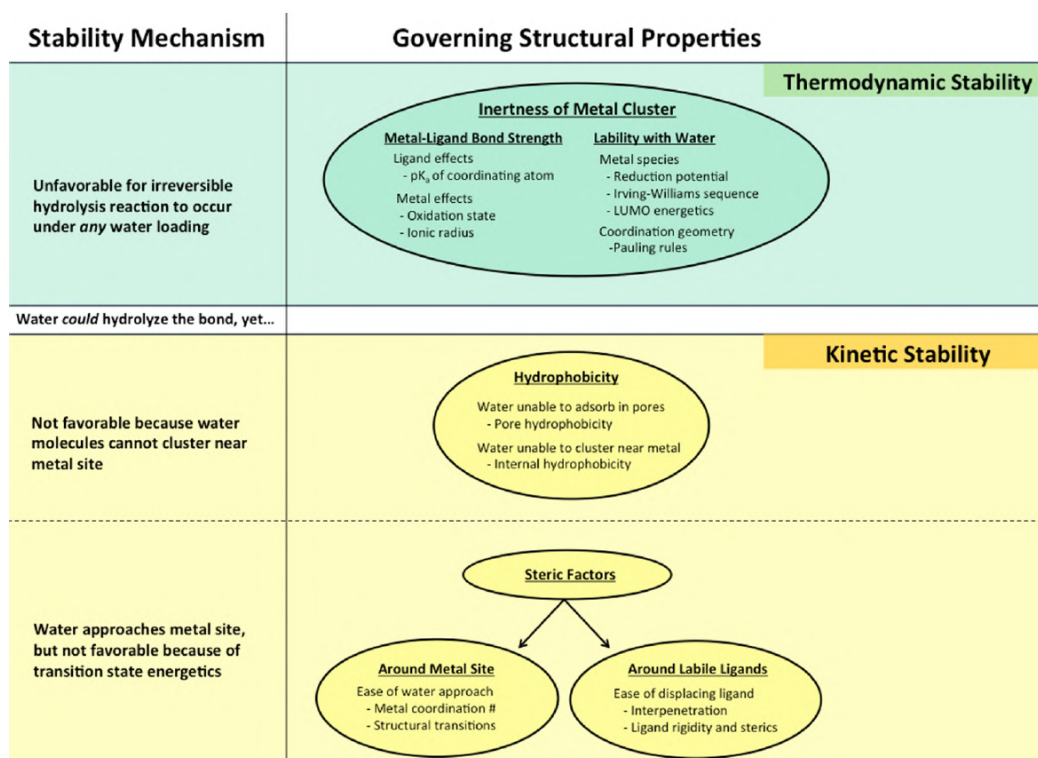
FIGURE 2.10: The main structural factors governing the water stability in MOFs.[51]

Generally, water resistance of MOFs may depend on both electronic and steric effects of the ligand on the metal node.[51,125] In fact, the main structural property that makes a MOF water stable is the inertness of the metal cluster: in this case the degradation mechanism is not favored.[51,125] Another point of view for the study of the (in)stability of a MOF is to evaluate the strength of the metal-ligand coordination bond, because it represents the weak point of the structure.[51]

Following this reasoning, the water resistance has been linked to the pK_α of the ligand: the more high is the constant, the stronger is the metal-ligand bond.[125,127] A MOF is then defined *thermodynamically stable* when it is found stable after long-term

exposure in aqueous solutions.[51] Such *thermodynamic stability* is governed by the free energy of the hydrolysis or ligand displacement reactions.[51] However, this is not the case of the MOF studied in this thesis: the Cu^{2+} ions involved in the paddlewheel units of HKUST-1, STAM-1 and STAM-17-OEt are not inert.[24,51,82,83,125,126] In particular, Cu^{2+} ions are electrophilic whereas the water oxygen is nucleophile, consequently water can favorably coordinate with the metal cluster.[24,51,82,83,125,126]

Despite this, even if a MOF has not an inert metal, there are cases in which we can talk of *kinetic stability*: this latter property is governed by the activation energy barrier, which depends on the specific pathway of the eventual dissociation reaction.[51] For example, kinetic factors which can play an important role in the increase in hydrolysis activation energy are hydrophobicity and ligand sterics.[51] The reasoning at the basis is that a dissociation mechanism takes place only if the oxygen of a water molecule can sufficiently approach the metal to allow the establishment of an interaction between the electron orbitals.[51,125] In addition, it is also necessary that the energy associated to such interaction is large enough to exceed the activation energy barrier of the reaction.[51,125] It is expected that MOFs which have this characteristic decompose if submerged in liquid water but that are stable after exposure to high humidity conditions.[51] Despite this, there are few notable exceptions which does not have inert metals, but are thermodynamically stable: probably in some cases there are kinetic factors so strong that make the barrier of the irreversible degradation fatally high.[51,128,129] Two main degradation mechanisms acting in MOFs exposed to water have been outlined:

1. the ligand displacement reaction, which involves the inclusion of a water molecule into the metal-ligand bond ($M^{n+}-L^{n-} + H_2O \longrightarrow M^{n+}-(OH_2)^{\cdots}L^{n-}$);

2. the hydrolysis reaction, involving the breakage of the metal-ligand bond and the dissociation of the water molecule ($M^{n+}-L^{n-} + H_2O \longrightarrow M^{n+}-(OH)^- + HL^{(n-1)-}$).[125,127]

The more diffused dissociation mechanism in the MOF field is the latter and, as shown in the following section, it is also the reaction that occurs in HKUST-1. For this reason, in the following we will talk only about hydrolysis. Pore hydrophobicity can also avoid the water adsorption into the pores of the MOF or can simply prevent the formation of clusters around the metal centers.[51] Water clustering seems to have a significant contribution in promoting degradation reactions in the pores of MOFs.[51,130,131] For example, some works reported studies about the degradation mechanism in IRMOFs, showing that the breakage of the metal-oxygen bonds happened only after the formation of water clusters next to the metal center.[130,131]

As it is probably clear at this point, a deep understanding about the breakdown mechanism of MOFs interacting with water is a crucial step for their development in commercial or industrial applications and technologies.[51,125,126] In the following sections, the state of the art about the stability of the MOFs investigated in this thesis will be deepened.

2.3 HKUST-1

HKUST-1 (Hong Kong University Science and Technology) or $Cu_3(BTC)_2$ was synthesized in 1999 by Chui and coworkers, and it is formed by copper paddlewheels and tritopic benzene-1,3,5-tricarboxylate (BTC) linkers.[24] It has a face-centered-cubic crystal lattice, with three distinct internal pores, displaying openings of about 9, 11 and 14 Å, respectively.[24,25,132]

Figure 2.11 shows HKUST-1 material under two different points of view: (a) the copper paddlewheel linked with four BTC linkers and (b,c) the network formed by the combination of such clusters along the two different directions [100] and [111], respectively.
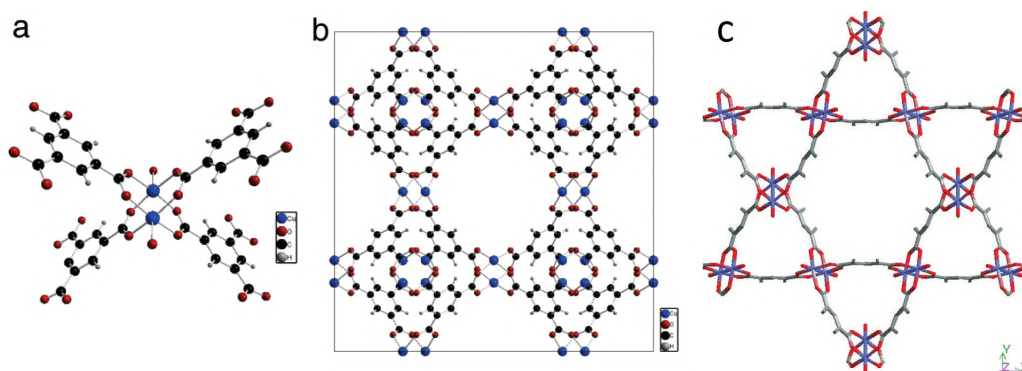
FIGURE 2.11: HKUST-1 moieties: (a) the paddlewheel unit coordinated with four BTC linkers; the two water molecules of crystallization are shown only by the oxygen atoms. (b) HKUST-1 network viewed down the [100] direction and (c) down the [111] direction. Adapted from refs. [133] and [24].

By standard synthesis protocols, HKUST-1 crystallises with a water molecule coordinated to each Cu^{2+} ion.[24,25,84] The dehydrated material is obtained by a simple heating process at about $370 \div 420$ K under low pressure.[24,25,84] The desorption of the water molecules from the copper ions leads to the changing of the color of the MOF from turquoise to dark-blue.[24,84,119]

The channels we can see along the [100] direction (figure 2.11 (b)) have a size of about ~ 1 nm, whereas seeing through the [111] direction (figure 2.11 (c)) it is possible to individuate large hexagonal-shaped windows with a honeycomb arrangement, with the metal clusters at the vertices and a diagonal of ~ 18.6 Å. Its bulk density is about ~ 0.4 g/cm^3, whereas its calculated crystalline density (for a dehydrated HKUST-1) is ~ 0.88 g/cm^3.[97,134]

Synthesis protocols. Since 1999, many different synthesis protocols have been defined to obtain free-defects HKUST-1.[24,135,136] Changing the precursors or synthesis parameters like temperature, the degree of crystallinity or the presence of unwanted side products may be altered.[135] Even other morphological properties like the internal porosity may slightly change by varying the synthesis conditions.[135] The most common

method employed for the synthesis of HKUST-1 and MOFs in general is the solvothermal reaction.[105,126,137] However, since the HKUST-1 powder material used during the PhD has been not synthesized by my own but it was purchased form Sigma Aldrich, a detailed description of the synthesis procedures can be considered out of the scope of this thesis.

Thermal stability. The thermal stability of HKUST-1 can be easily determined by TGA analysis, as shown in figure 2.12(a).[119] Observing the heating of an as-made sample
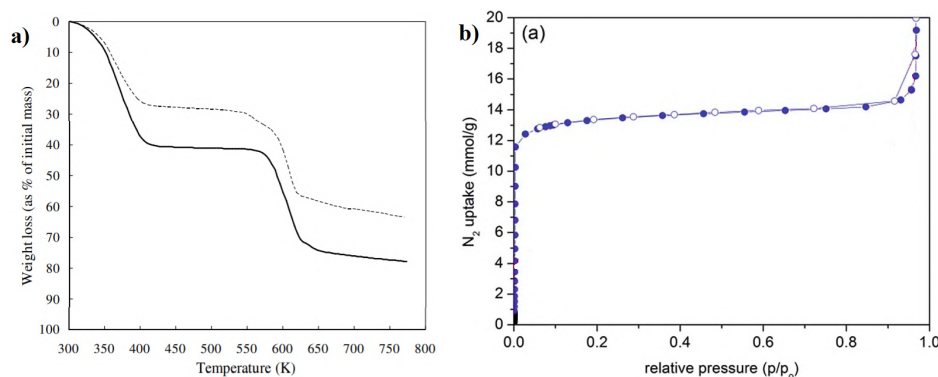
FIGURE 2.12: (a) TGA analysis of HKUST-1 obtained by a heating rate of 5 K/min in inert atmosphere; (b) nitrogen isotherm obtained for a HKUST-1 powder sample at 77 K. Adapted from refs. [119] and [138], respectively.

of HKUST-1, up to about 420 K the material looses the volatile solvents and/or water stood in the pores, involving about 40% of the total weight of the sample.[119] After a range of steady weight up to ~550 K (that can be considered the "true" weight of the MOF), a second significant loss of weight can be observed, indicating a degradation of the material.[119] Such loss of about 60% of weight is due to the decomposition of the BTC linker and then the sample retains the sole CuO as final product. For this reason, we can consider HKUST-1 material thermally stable up to ~550 K.[119]

Porosity. The inner porosity can be evaluated by acquiring nitrogen isotherms: an example is given in figure 2.12(b).[139] The curve displayed is referable to a type I isotherm, indicating a narrow pore size distribution of the micropores and a strong adsorbate-adsorbent interaction (see section 1.6). The hysteresis is almost totally missing. The value of its BET surface area changes from one article to another, but it generally ranges between $1500 \div 1900$ m^2/g.[97,121,136,139–141]

Diffraction pattern. As previously mentioned, all of the MOFs are typically highly crystalline materials and therefore each MOF generally has a characteristic diffraction pattern with sharp peaks. A common method to easily check the degree of crystallinity of a MOF is by acquiring a PXRD pattern of the sample under consideration. The typical diffraction pattern obtained for HKUST-1 is shown in figure 2.13. Comparable PXRD patterns obtained for HKUST-1 can be found in many other works.[83,84,135,139–141,143] By simulations, each peak has been attributed to a specific reflection, as indicated in figure
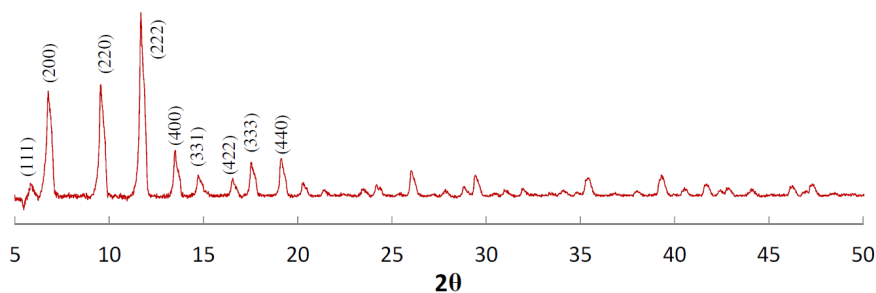
FIGURE 2.13: PXRD pattern obtained for HKUST-1. On the main peaks, the correspondent reflections are indicated. Adapted from refs. [135] and [142].

2.13. Two additional peaks have been detected in some experiments at about 11.5° and 15.0°, ascribed to the reflections (311) and (420), respectively.

Raman spectrum. Prestipino and co-authors[84] investigated the vibrational properties of HKUST-1 by Raman spectroscopy. They acquired Raman spectra before and after outgassing the MOF, obtaining spectra with different features. Similar results have also been obtained by Todaro and co-authors.[144] An example of these studies is shown in figure 2.14. The Raman spectrum of HKUST-1 can be virtually divided in two re-
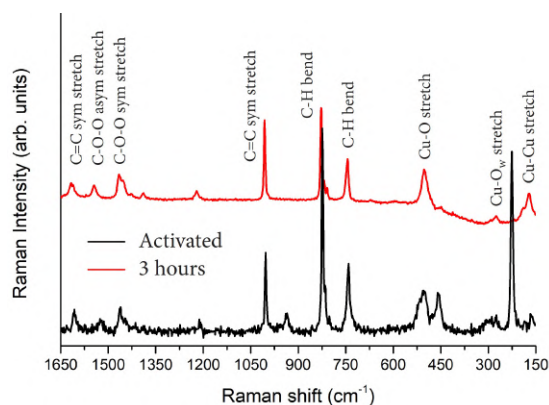
FIGURE 2.14: Raman spectra of the HKUST-1 sample in both activated (black line) and hydrated configuration (red line - acquired after about 3 hours of exposure to air moisture). Each spectra have been separately normalized for the amplitude of the resonance peaked at $\sim$1005 cm^{-1}. Adapted from [144].

gions: the first region involves the bands between 150 and 600 cm^{-1}, corresponding to vibrational modes directly involving the Cu^{2+} ions; from 700 to 1700 cm^{-1} the bands are associated with the organic part of the framework, or else the benzene ring and the carboxylate bridges.[84,144,145] More in detail, following the attribution done in literature, the raman spectrum of as-made (or hydrated) HKUST-1 may be described as follows:[67,84,144–146]

- at 177-190 cm^{-1} we recognize the band known as a doublet assigned to stretching modes of the Cu-Cu dimers;
- the peak at 278 cm^{-1} is attributed to an out-of-plane stretching of the Cu-O$_{\text{water}}$ (i.e. the oxygen of the water molecule bound to the Cu^{2+} ion);

- the peak at 500 cm^{-1} is assigned to the stretching modes of the bond Cu-O involving the copper ion and one of the carboxylate oxygen atom;
- the bands at 747 and at 830 cm^{-1} are ascribed to two out-of-plane bending modes of the benzene rings (C-H);
- at 1007 and 1616 cm^{-1} the bands pertain to the symmetric stretching mode of C=C of the benzene rings.;
- the peaks at 1388, 1461 and 1544 cm^{-1} are attributed to the symmetric and a-symmetric stretching modes of the COO groups.[67,84,144–146]

After the water removal, few but evident changes can be found in the spectrum (see figure 2.14). As it is reasonable to expect, since the Cu^{2+} ions are the species most directly involved in the activation process, the bands of the first region are the most interested in the changes and we can observe a doublet peaked at 515 and 460 cm^{-1} instead of a single peak at 500 cm^{-1}, and the vanishing of the doublet at 177-190 cm^{-1} which leaves the place to an intense blue-shifted single component peaked at 228 cm^{-1}.[84,144,145] The high-frequency modes (those pertaining to the organic component of the lattice) are not affected by the water removal/adsorption of the material.[84,144,145] Prestipino and co-authors[84] suggested that the strong blue-shift of the peak at 228 cm^{-1} is a consequence of the reduction of the Cu−Cu distance, estimated from 2.64 to 2.50 Å.

Solid-state ^{13}C NMR spectrum. Another technique which has been employed to study the properties of carboxylate MOFs is NMR spectroscopy, although the paramagnetism of the Cu(II)-based MOFs generally makes difficult the assignment and the interpretation of the spectral resonances.[147–152] Figure 2.15 shows the solid-state ^{13}C magic-angle spinning (MAS) NMR spectra acquired for HKUST-1 with changes in the hydration state of the sample involved and the numbering scheme of the carbons related to the MOF structure.[147] HKUST-1, in fact, exhibits three crystallographically distinct
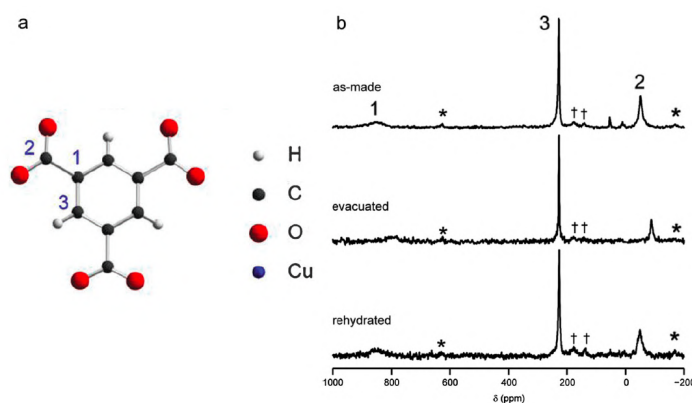

FIGURE 2.15: (a) The BTC linker structure with the numbering scheme used in the work of Dawson and co-authors[147,148] is shown. (b) A ^{13}C MAS NMR spectrum acquired for HKUST-1 is displayed; the symbol ∗ indicates spinning sidebands whereas the symbol † denotes a BTC-based impurity. Adapted from ref. [147].

C-species, which result in three resolvable resonances in the spectrum.[147,151] In the as-made HKUST-1, Dawson and co-authors[147] observed the three resonances at -50, 228 and 853 ppm and they assigned them to C1, C3 and C2, respectively. The unambiguous assignment required a ^{13}C isotopic enrichment of the BTC linkers constituting the MOF (the same method was used for STAM-1, section 2.4) Previously, Gul-E-Noor and co-authors[151] mistakenly assigned the resonance at 50 ppm at C2 and considered that at 228 ppm a contribution of both C1/C3. After evacuation of the material, significant shifts of -58 and -37 ppm were detected in the resonances C1 and C2, respectively, suggesting a change in the spin and electron distribution caused by dehydration.[147,151,152] The authors observed that such changes were reversible, because the resonances were found to be at the initial position upon exposure to atmospheric moisture.[147]

2.3.1 Magnetic Properties

The dinuclear copper paddlewheel is a well-known example of Cu^{2+} ions which establish an antiferromagnetic coupling (see section 1.1.2 and 2.1.2).[3] For this reason, it is not surprising that the copper paddlewheel-based MOF HKUST-1 has remarkable magnetic properties inherited from its SBUs. The first evidence of such magnetic properties for HKUST-1 has been found by Zhang and co-authors.[153] They studied the MOF with two different molecules coordinated with the Cu^{2+} ions: pyridine and H_2O. They acquired for both systems the magnetic susceptibility as a function of the temperature obtaining the two slightly different curves shown in figure 2.16.[153] The susceptibility
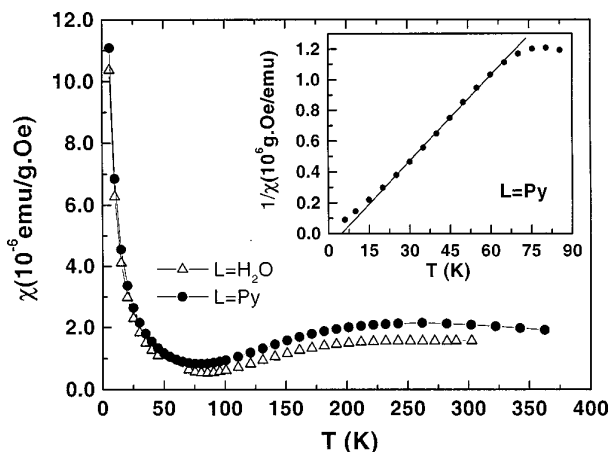
FIGURE 2.16: Magnetic susceptibility of $Cu_3(BTC)_2L_3$, with L=pyridine $(- \bullet -)$ or L=H_2O $(- \triangle -)$. In the inset the Curie-Weiss trend at low temperature is shown.[153]

decreases with decreasing of the temperature, until reaching a minimum at $\sim 70-80K$ K, revealing the presence of a strong antiferromagnetic coupling of the copper ions within the paddlewheels, similar to those observed for the individual dimer units.[3,153] A further lowering of the temperature shows that the susceptibility increases again. This trend is different from that shown by systems like copper acetate, which has a very low susceptibility in the range 5-70 K.[153] The authors suggested the existence of a weak ferromagnetic coupling among different paddlewheels at low temperature allowed by a

magnetic/electronic communication among the dimers mediated by the planar BTC ligands, which would explain such anomalous rise in intensity at low temperature.[153] Not long after, Pöppl and co-authors[133] found that large susceptibility at low temperature is due to the presence of extra-framework cupric ion species with $S = 1/2$ spin value which they called *"species A"* and which therefore follows a Curie-Weiss law.[133,154] These copper-based species has been identified as $[Cu(H_2O)_6]^{2+}$ complexes, and they would arise from monomeric Cu^{2+} ions that have not reacted during the synthesis process to form the paddlewheel clusters, but have been subsequently established bonds with six water molecules in either square pyramidal or elongated distorted coordination.[133,154]

The evidence of such secondary copper-based complexes has been highlighted by an EPR investigation on HKUST-1 carried out at different temperatures. The spectra they obtained (displayed in figure 2.17(a)) show strongly temperature-dependent features.[133,154]
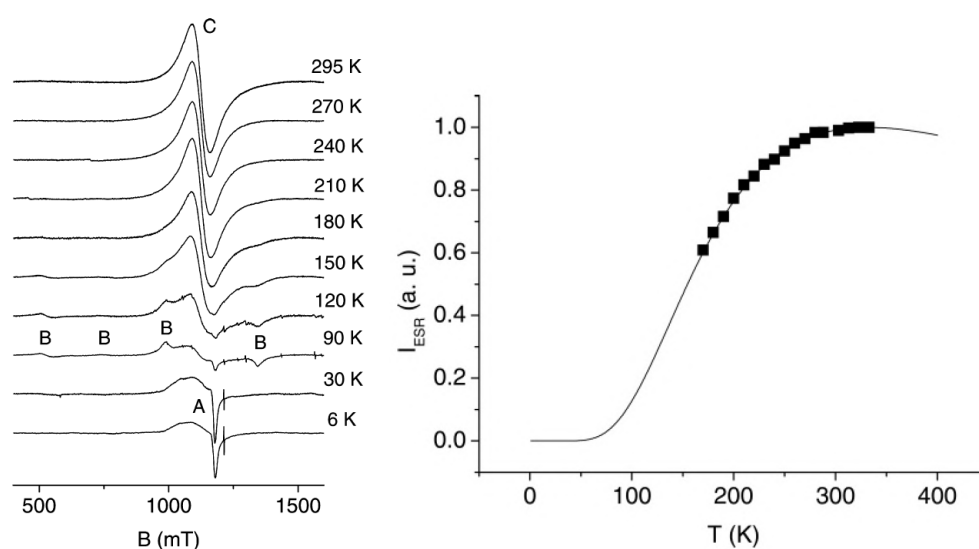
FIGURE 2.17: (a) EPR spectra obtained in Q-band at different temperatures for HKUST-1. (b) Intensity of the EPR signal as a function of the temperature. Adapted from [133].

In particular, the existence of the species A inside the HKUST-1 sample is suggested from the spectra acquired at low temperatures: at temperatures T<90 K the EPR signal is comparable with the typical feature pertaining to Cu^{2+} ions having a $S = 1/2$ electron spin and interacting with the $\hat{\mathbf{I}}^{\mathbf{Cu}} = 3/2$ nuclear spin of the copper nuclei.[133] However the Cu hyperfine peaks are barely resolved because of relaxation processes probably due the high local concentration of Cu^{2+} ions.[133] The spectroscopic parameters for the species A have been obtained considering the standard spin Hamiltonian

$$\hat{H} = \beta_e B \mathbf{g} \hat{S} + \hat{S} \mathbf{A}^{\mathbf{Cu}} \hat{\mathbf{I}}^{\mathbf{Cu}} \tag{2.1}$$

where $\mathbf{A}^{Cu}$ is the tensor describing the Cu hyperfine interaction. The optimized Hamiltonian parameters found by the authors are shown in table 2.1.[133]

TABLE 2.1: Hamiltonian Parameters Resulting from EPR spectral simulation obtained for a sample of HKUST-1 by Pöppl and co-authors (species A=Cu^{2+} monomers; B=Cu^{2+} dimers at T≈100 K; C=Cu^{2+} dimers at T>160 K).[133]

Species	g_1	g_2	g_3	A_1^{Cu}	A_2^{Cu}	A_3^{Cu}	D	E
				cm^{-1}	cm^{-1}	cm^{-1}	cm^{-1}	cm^{-1}
A	2.059	2.063	2.377	0.0010	0.0014	0.0148		
B	2.060	2.060	2.369				0.320	< 0.004
C	2.164	2.164	2.164					

At very low temperatures, the signal arising from the cupric monomers is dominant compared to that arising from the dimeric species, in spite of their limited amount. This is because, at such temperatures, the S=1 triplet energetic state is statistically not populated enough to make their contribution easily detectable, whereas the Curie susceptibility of the S=1/2 spin centers is very large. The authors have estimated that the Cu^{2+} ions organized in $[Cu(H_2O)_6]^{2+}$ monomers are no more than 3% of the total Cu^{2+} ions observed in the HKUST-1 sample.

Acquiring EPR spectra for HKUST-1 material at temperatures ranging from 90 to 180 K, the signal arising from the dimers appears. More in detail, the spectra show a superimposition of two different signals: the anticipated multicomponent signal of the dimeric Cu^{2+} complexes (or else, the paddlewheels of the MOF) named *"species B"* and also the broad isotropic resonance of an unexpected *"species C"* (figure 2.17).[133] The spin Hamiltonian which describe the paramagnetic centers of the species B is the already discussed eq. 1.32, here expressed again only for sake of clarity:

$$\hat{\mathscr{H}}_n = g\beta_e \mathbf{B}^T \cdot \hat{\mathbf{S}} + D\big(\hat{S}_z^2 - \tfrac{1}{3}\hat{S}^2\big) + E\big(\hat{S}_x^2 - \hat{S}_y^2\big)$$

and it pertains to centers with spin S=1. By spectral simulations it is possible to estimate the spin Hamiltonian parameters (table 2.1).[133] At temperatures higher than 180 K, the contribution of the species B disappears from the EPR spectra and the signal observed pertains only to the species C, with an intensity which increases with the temperature, reaching a maximum at $\sim$ 320 K (figure 2.17 (b)).[133] Such temperature dependence follows the trend expected for exchange-coupled dimers that follow the Bleaney-Bowers equation. More in detail, the authors found that data obtained for the species C are consistent with those of S=1 spin centers with antiferromagnetic coupling constant $J_0 \approx -370$ cm^{-1}, comparable with the typical singlet-triplet splitting of other antiferromagnetically coupled Cu^{2+} dimers as copper(II) acetate monohydrate.[3,133]

From a spectroscopic point of view, the species C has a Lorentzian line shape and a temperature independent $g = 2.164$ value. The agreement of such g value with the mean

g value of species B combined with the J_0 constant estimated, led to the conclusion that the signal C pertains to the S=1 exited state of the copper dimers. The transformation of the EPR signal arising from the S=1 spin centers from the anisotropic features of the species B to a such isotropic line-shape of the species C suggests the presence of an additional spin exchange among the paddlewheels across the BTC ligands, presumably through the π orbitals: an exchange coupling constant of ~ 0.5 cm^{-1} would be sufficient to give such effects observed in the EPR spectra.[133] The reason why this effect becomes significant only at high temperatures may be that the population of the excited S=1 state of the coupled Cu^{2+} ions becomes larger and therefore the average distance among the dimers being in the excited state decreases, leading to a progressively more efficient exchange process along the network. The overall result is an increase in intensity for the isotropic signal (species C) at the expense of the anisotropic one.

Todaro and co-authors[140] also studied in detail the EPR signal of HKUST-1, but using the X-band. The experimental results shown in this thesis have been acquired by a spectrometer working in the X-band too, therefore the work of Todaro and co-authors shows an essential benchmark. They acquired spectra restricting the temperature values at 77 and $\sim$300 K (room temperature). The spectra obtained for an activated sample of HKUST-1 at the two temperatures are shown in figure 2.18.[140] As already mentioned, at
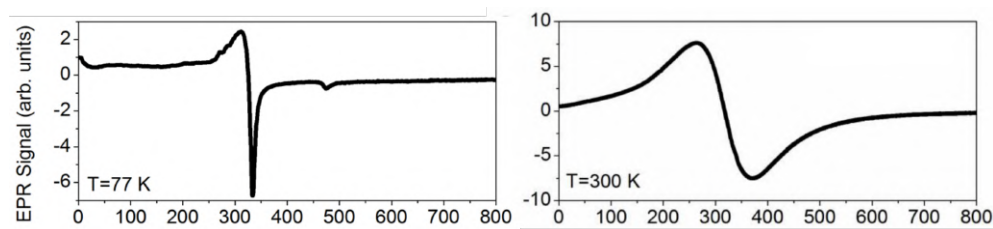
FIGURE 2.18: (a) EPR spectra of activated HKUST-1 obtained at T=77 K and T=300 K in X-band. Adapted from ref. [140].

77 K the spectrum of the activated HKUST-1 is characterized by both the contribution of the extra-framework $[Cu(H_2O)_6]_2^+$ monomeric complexes and that of the Cu^{2+} dimers of the paddlewheels.[133,140,154] The resonance arising from the monomers consists of a peak centered at 325 mT with a peak-to-peak line width of $\sim$ 24 mT; the four lines of the hyperfine structure are barely evident on the positive peak.[140] The resonance pertaining to the paddlewheels is much weaker at this temperature, but clearly identifiable in the small peaks at 12 and 470 mT.[140] At 300 K the signal arising from the paddlewheels consists of a large and symmetric peak centered at 318 mTwith a peak-to-peak line width of $\sim$108 mT.[140] No trace of the cupric monomers can be detected at room temperature. In order to obtain the hamiltonian parameters of the two paramagnetic centers, the authors used the same Hamiltonian models used by Pöppl and co-authors.[140] The results obtained are shown in table 2.2.[140] The values calculated are well comparable with those of Pöppl and co-authors (table 2.1).[133]

TABLE 2.2: Hamiltonian Parameters Resulting from EPR spectral simulation obtained by Todaro and co-authors for the spectrum of a sample of activated HKUST-1 acquired at 77 K (E"(Cu) = Cu^{2+} dimers).[140]

Species	g_1	g_2	g_3	A_1^{Cu}	A_2^{Cu}	A_3^{Cu}	D	E
				cm^{-1}	cm^{-1}	cm^{-1}	cm^{-1}	cm^{-1}
Cu^{2+} monomers	2.08	2.07	2.35	0.001	0.0014	0.014		
E"(Cu)	2.07	2.07	2.32				0.330	0

2.3.2 Water stability

It is well-known that massive hydration conditions or water cycles seriously compromise the structure and the performances of HKUST-1.[37,51,67,83,125,138,140–142,144,146,155–158] However, only few works face the water degradation issue at atomic scale level.

Among the various point of views and different hydrolysis models, the main cornerstone is that HKUST-1 is a very hydrophilic MOF: in fact, it is well-known that polar molecules like water have a large affinity for the Cu^{2+} of the paddlewheel of the MOF and those on the Cu^{2+} are defined open-metal sites.[51,84,125,141,143,150,156,157,159,160] In contrast to some other MOFs which may show the coordination sites blocked by the ligands, in HKUST-1 the metal sites are on the interior of the pores, making the Cu sites accessible.[135] For this reason, the dehydration of this kind of MOFs is also frequently named *"activation process"*, because it makes the open metal site active. If the color of the dehydrated MOF is dark violet/blue navy, it only takes few minutes of exposure to air moisture to drastically change it to light turquoise.[84,140,157,161,162]

However, the copper ions are not the only possible adsorption sites for water when HKUST-1 interacts with it. In this regard, several systematic searches of all the potential and preferential adsorption sites have been deeply carried out via molecular simulations.[142,159,163–165] In figure 2.19 the main potential adsorption sites of HKUST-1 are represented with the spheres marked by the numbers I, I', II and III. It has been observed that a water molecule preferentially adsorbs very close to Cu^{2+} and then in sites I and I', whereas apolar molecules like methane adsorb preferably at the site III.[159] More in detail, site I is also the first siting and it corresponds to that occupied by the water molecule directly coordinated with Cu, whereas in site I' there are water molecules bonded with water molecules adsorbed at site I through hydrogen bonds.[142,159] Gul-E-Noor and co-authors[150] confirmed and deepened this result experimentally by a ^{1}H MAS NMR study. They studied the water-MOF interaction for HKUST-1 during a continuous hydration under air moisture for 80 hours. Their interpretation of the data is based on the idea of a hydration process which can be divided in 2 main steps:

1. during the first phase of air exposure they observe the progressive adsorption of water on the unoccupied metal site (i.e. site I), detecting a co-existence of
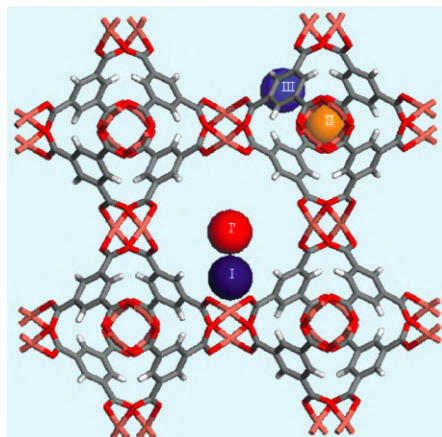
FIGURE 2.19: Representation of sorption sites I, I', II, and III in the structure of HKUST-1 viewed along the [100] direction. Copper atoms in pink, oxygens in red, carbons in grey, hydrogens in white.[142]

paddlewheels with one and two water molecules per Cu pair (species H_2O-I and H_2O-II, respectively). As the hydration time increases, the number of paddlewheels with two water molecules grows up to 20 hours. The authors estimated an instant value of $1.2H_2O$/Cu at exposure time of 9 h 30 min.[150]

2. after 20 hours they observe the appearing and the increasing of a new signal which arises from paddlewheels with more than two water molecules per Cu pair (species H_2O-III), due to the addition of a second water molecule per Cu site (i.e. the occupation of site I'). From the 56th to the 80th hour, only this signal is detected on the NMR spectra with no further changes in intensity.[150]

It is noteworthy that the resonance lines of species H_2O-I have a higher chemical shift than H_2O-II: the authors suggest it is a consequence of the different coupling of the two unpaired electrons if the one or both the metal centers are bonded to water.[150] In fact, along with the different distribution of spin density, even the coordination environment of the copper ions change, switching between square planar to square pyramidal, and therefore when there is $1H_2O$/Cu pair, the two Cu^{2+} have different environment and coordination mode.[150] Grajciar and co-authors[163] also confirmed that the free paddlewheel and that with one Cu^{2+} center occupied are not equivalent, because the second adsorption results slightly weaker than the first one.

Similar information can be extracted studying the HKUST-1 water isotherm, an example of which is shown in figure 2.20.[141] In the lower pressure range ($p/p_0 = 0.1 \div 0.3$), the curve consists of a two-step trend, indicating two distinguishable processes: presumably, the water coordination to the copper sites and, subsequently, either the filling of rest of the large hydrophilic pores or the filling of the smaller pores, which lack of metal sites and then have a hydrophobic character, enhanced by the BTC linkers.[141] Concerning higher relative pressures, at about $p/p_0 = 0.4$ there is a saturation region and after $p/p_0 = 0.9$ another slight increase, probably due to the condensation of water inside the pores.[141] The small hysteresis of the desorption branch can be attributed
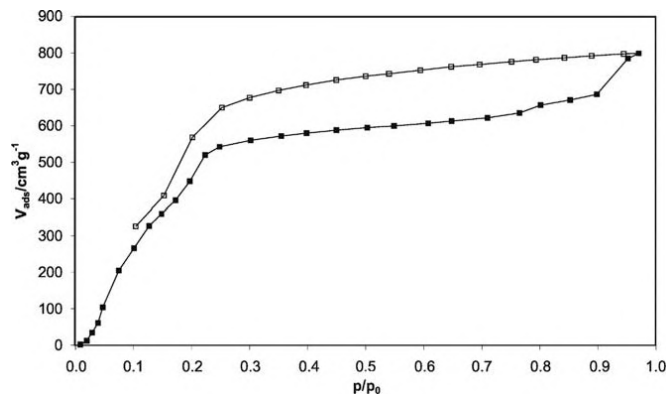
FIGURE 2.20: Water adsorption (—■—) and desorption (—□—) isotherm acquired for HKUST-1 at 298 K.[141]

to the strong hydrogen bonds established among the water molecules adsorbed.[141] A residual of not-desorbed water was observed in the lower pressure range: the cause is probably the chemisorbitive nature of the bonds established by the water molecules on the copper sites, meaning that high temperatures are necessary to fully desorb such molecules.[51,141]

Models concerning water degradation of HKUST-1

Many works have drowned possible decomposition processes taking place in HKUST-1 framework and the scope of this section is to offer an overview of the main common cornerstones. However, it is quite difficult to summarize them in a single model, because each work is based on experimental setups which has involved different environments with different relative humidity, different time of exposure, hydration conditions and temperatures. For example, although all of these works generally show PXRD patterns with drastic reduction in the intensity of the peaks or a dramatic decrease of the BET area values after a certain degree of hydration, it is hard to definitively establish after which hydration level this phenomena occur and, even more important, what happens at atomic scale level.[51,83,125,140,142,157] Despite this, with some precautions, it is possible to define a general description of the water degradation process.

For example, a common conclusion is that the decomposition mechanism starts with the breakage of one or more Cu-O bonds of the paddlewheels.[51,83,125,140,144,146,155,163–167] *Ab initio molecular dynamics* (AIMD) simulations have shown that the introduction of water molecules in the framework leads to a "*violent oscillation*" of the Cu-O bond length, whereas the first occupation of the metal site causes a distancing between the copper and all of the adjacent oxygens.[165] The paddlewheel unit with the elongated Cu-O bond lengths may be considered a precursor state for the hydrolytic breakdown of the MOF.[165] However, it has been estimated that high water concentrations occur for the trigger of the hydrolysis.[165] Many works have individuated in the water condensation (or clustering) inside the pores the necessary condition for the begin of the hydrolysis in HKUST-1.[51,125,127,142,146,157,161,168] This is an idea which has been widely

applied to MOFs, as already mentioned in section 2.2.2. The presence of condensed water as the hydrolysis begins was experimentally determined by Tan and co-authors[146] through pressure and temperature dependence studies. In contrast, they observed that the structure of the MOF remained intact when the experimental conditions did not favor the condensation. Similarly, Giovine and co-authors[168] showed that HKUST-1 samples exposed to water vapor significantly above the boiling temperature (about 420 K) were surprisingly stable, whereas they were readily hydrolyzed at lower temperatures like 350-370 K, at which water can condense. In general, we can sum up by saying that depending on the water content in HKUST-1 network, different decomposition products are observed.[140,146,151,158]

The details about the degradation process caused by water

One of the most significant identification of such decomposition products has been done by Todaro and co-authors, by the use of EPR spectroscopy.[140] In the following the structural processes which take place in HKUST-1 by interaction with air moisture for a long time will be explained in detail. The products of the decomposition have been extrapolated by analyzing the changes registered in the EPR spectra acquired at both 77 and 300 K, which are reported in figure 2.21 and 2.22, respectively.[140]
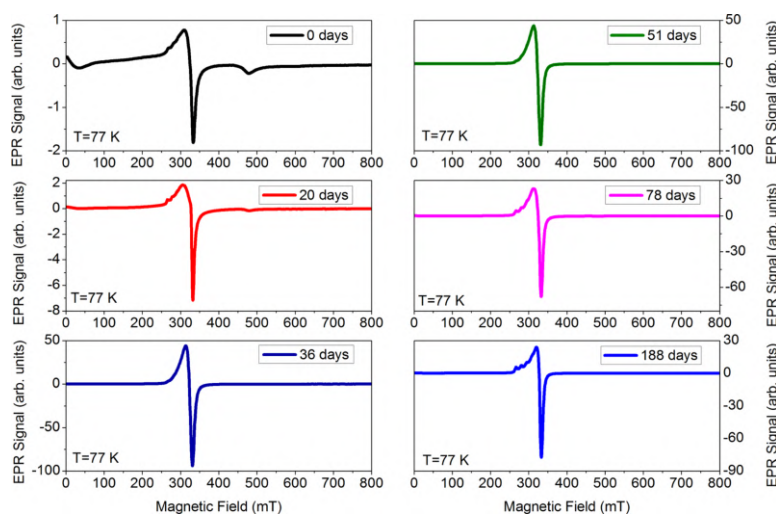
FIGURE 2.21: EPR spectra obtained at 77 K for a sample of HKUST-1 powder at different times of exposure to air moisture.[140]

Enabling the hydration of the HKUST-1 sample only through the small opening of the long and narrow EPR tube (about 0.3 cm diameter and about 16 cm in length), they have been able to slow down the hydration treatment so that they could analyze each step of the process in great detail.[140] Combining their results with other similar studies, the main stages of the decomposition pathway are resumed in the following paragraphs.[37,140,155,158,165]

First stage. The water adsorption on the Cu sites. As above mentioned, the preferential adsorption site in HKUST-1 is on the copper, then the first stage is the
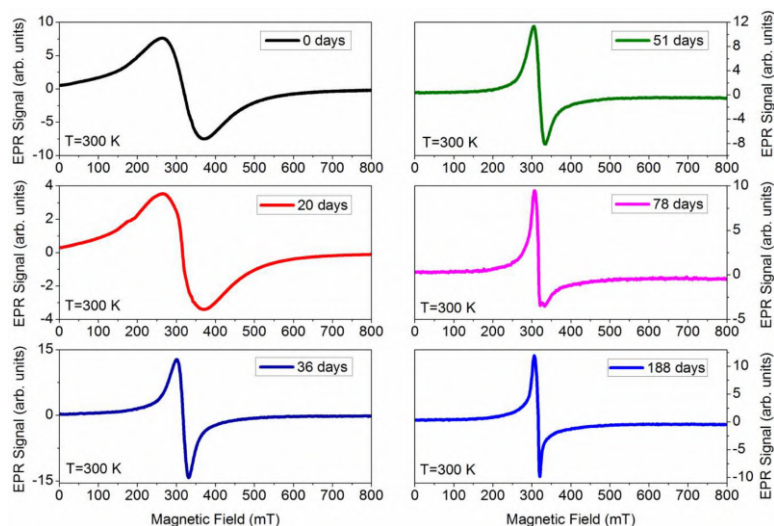
FIGURE 2.22: EPR spectra obtained at 300 K for a sample of HKUST-1 powder at different times of exposure to air moisture.[140]
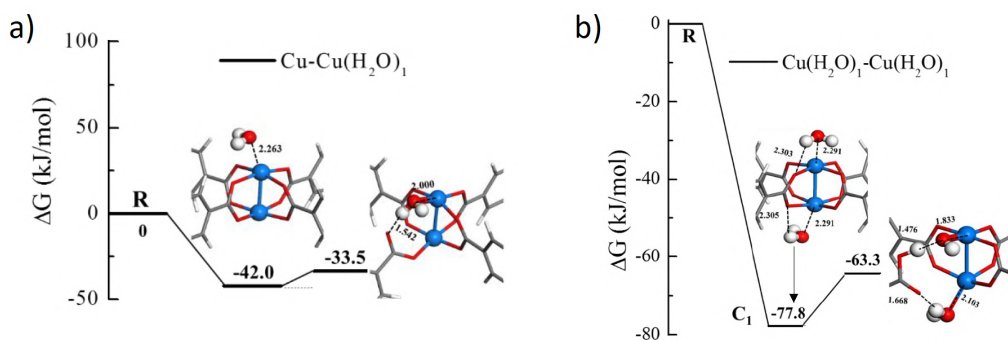

FIGURE 2.23: A selection of the calculated possible steps of the paddlewheel in presence of one (a) and two (b) water molecules per Cu pair during the hydrolytic process. Adapted from ref. [165].

simple adsorption of the water molecule on the Cu^{2+} ions. In fact, upon adsorption, the oxygen of the adsorbed H_2O share a free electron pair with the Cu^{2+} ion, establishing an out-of-plane bond.[51,165] This would lead to an elongation of the Cu-O bonds.[165] Xue and co-authors[165] observed by DFT calculations that the first adsorbed water molecule may already tilt down and break the Cu-O bond, leading to a ligand displacement (see figure 2.23). However, water dissociation is both thermodinamically and kinetically unlikely at this stage, and therefore hydrolysis is not favoured at this low water loading.[165] The elongation of the Cu-O bonds causes also an expansion of the dimensions of the unit cell of the framework, detectable by PXRD.[140]

Todaro and co-authors observed during the first 20 days of exposure to air moisture only reversible changes to the EPR spectra of their sample. As already mentioned, the paramagnetic centers present in an activated HKUST-1 sample are the solely E"(Cu) (that is the S=1 spin centers of the coupled paddlewheel of the activated HKUST-1) and $[Cu(H_2O)_6]^{2+}$ centers. The main effect observed during this period of 20 days is a strong reduction (about 65%) of the intensity of the signal obtained at room temperature: a
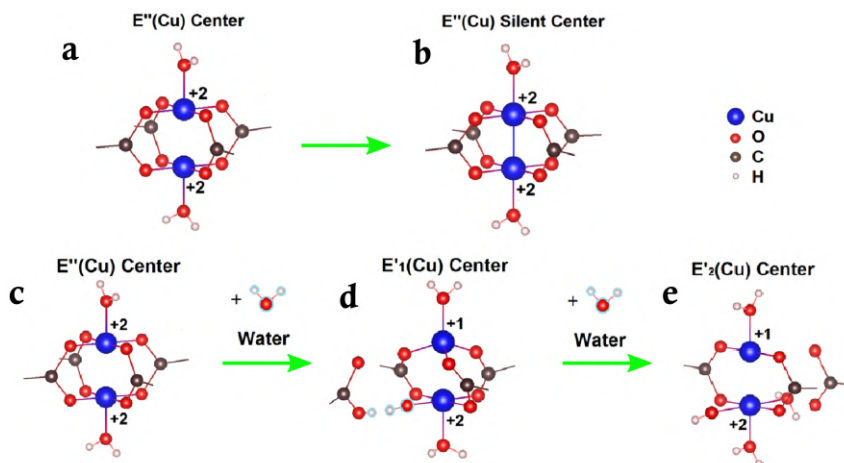
FIGURE 2.24: Schematic representation of the evolution of the copper paddlewheel in HKUST-1 upon exposure to air moisture. The different magnetic centers are labelled: (a,c) E"(Cu), (b) silent E"(Cu), (d) E'$_1$(Cu), (e) E'$_2$(Cu). Adapted from ref. [140].

possible interpretation given by the authors was a drastic reduction of the concentration of E"(Cu) centers.[140] Such effect would be due to the formation of a σ bond between the Cu^{2+} ions within the paddlewheel.[140] The formation of this bond would not damage irreversibly the network, but it would make the paddlewheels involved EPR silent.[140] Also the BET area values obtained do not show any reduction, supporting the hypothesis of a preserved framework. Furthermore, a complete recover of the EPR signal can be obtained by a simple activation process.[140] In figure 2.24, this stage is represented by the transition from (a) to (b). However, subsequent measurements carried out by EXAFS fits showed that there is a distancing of the two Cu^{2+} ions, making the establishment of a σ bond between them hardly probable. For this reason the question has remained open but, whatever may be the reason, the first stage consists of a reversible change occurred in a softly hydrated material.

Second stage. The beginning of the hydrolysis From the 20th to the 50th day, Todaro and co-authors[140] observed drastic changes in the EPR spectra of their samples. Those obtained at room temperature showed a narrowing of the resonance, whereas those acquired at 77 K exhibited an intense resonance centered at about 320 mT, similarly to the peak ascribed to the S=1/2 spin centers of the $[Cu(H_2O)_6]^{2+}$.[140] Similar changes in the EPR signal have been also found elsewhere.[37] According to their interpretation, such changes are due to the appearing of a new paramagnetic center within the material, which has been named E'$_1$(Cu).[140] This new EPR signal would arise from the progressive formation of Cu^{2+}/Cu^{1+} paddlewheels, which contribute to the EPR signal as S=1/2 spin centers. More in detail, the oxidation state of one of the copper of the paddlewheels (the non silent ones) changes from 2+ to 1+, and the resulting Cu^{1+} ion is EPR silent: the EPR signal of E'$_1$(Cu) centers arise only from the single Cu^{2+} of the pair in such new paddlewheel structures (figure 2.24(d)).[140]

The hydrolysis of the Cu-O bonds, leading to the partial detaching of a carboxylate

bridge and the reduction of the coordination number from 5 to 4, allows the change in the oxidation state and in the geometry, which becomes tetrahedral.[140] The adsorbed water substituting the ligand is dissociated and it has transferred one of the two hydrogens to the oxygen of the carboxylate bridge, with a very low barrier.[165] However, this configuration is only metastable because it suffers of a relevant local strain, and it quickly relaxes to another structure. The presence of strain is also suggested by the absence of the hyperfine structure on the peak centered at ~ 320 mT.[140]

This stage of the process is already irreversible: it has been demonstrated that the activation process is not sufficient to recover the initial EPR signal and the peaks of the diffraction pattern also show a significant reduction. This stage can be therefore taken as the beginning of the hydrolysis.[140]

Also other works have found a lowering of the coordination of the copper units which leads to the formation of Cu^{2+}/Cu^{1+} centers, modifying the catalytic performances and the chemical reactivity.[169]

Xue and co-authors[165] found that at least three or more water molecules per paddlewheel in its local environment occur to totally detach one ligand from the paddlewheel itself.[165] However, their model of "decomposed paddlewheel" obtained via DFT calculation was slightly different: in their structure the correspondent Cu-O bond involving the other Cu^{2+} has been broken by ligand displacement and even though the whole ligand has been consequently detached, each copper ions maintained the same number of bonds, because the water oxygens take the place of the carboxylate oxygens (figure 2.23(b)).

Third stage. The relaxation into a more stable configuration From the 50th to the 180th day, Todaro and co-authors[140] observed a further progressive narrowing of the resonance at 300 K and the presence of the characteristic hyperfine quadruplet on the main peak of the pattern obtained at 77 K (figures 2.21 and 2.22). The last stage of the decomposition process described by Todaro and co-authors involves the relaxation leading from the E'$_1$(Cu) to a new S=1/2 spin center named E'$_2$(Cu) (figure 2.24(e)), occurred by a further detaching of a second carboxylate bridge from the Cu^{2+}/Cu^{1+} paddlewheel of the E'$_1$(Cu) center.[140] The structure correspondent to the E'$_2$(Cu) center has two detached carboxylate bridges facing one another, so that the Cu^{1+} has a T-shaped configuration and the Cu^{2+} ion coordinates to a water molecule, maintaining the square-pyramidal geometry.[140] The characteristic hyperfine quadruplet, again easily resolvable in this last stage, indicates the relaxing of the strain individuated in the E'$_1$(Cu) center.[140] The authors did not exclude the possibility of the formation of a paddlewheel Cu^{1+}/Cu^{1+}, because it would be full EPR silent and then not detectable by the experimental technique they employed.[140]

A further possible final stage. Todaro and co-authors suggested that the E'$_2$(Cu) center is stable enough to be considered the final stage of the decomposition process.[140] In contrast, Poppl and co-authors have also studied the degradation process occurred

in HKUST-1 upon exposure to air moisture, and they individuated a strong similarity between the spectroscopic parameters of the final product of the decomposed HKUST-1 and those of the $[\text{Cu}(\text{H}_2\text{O})_6]^{2+}$ monomeric complexes.[37,158] For this reason, they suggest that in the final products of the decomposition process of HKUST-1 exposed to air there are coppers completely cut off from the framework and possibly arranged in mononuclear complexes.[158]

Final considerations

In the last years, several efforts has been spent on the research of methods to preserve HKUST-1 (or more in general water sensitive MOFs) from destructive interaction with water.[142,166,170,171] Some works have tried to introduce hydrophobic component which would fill the pores limiting the possibility of water condensation or to build a kind of *surface barrier* like an external hydrophobic layer.[142,166,170,171] Unfortunately, these methods typically require a not negligible price in terms of pore accessibility.[142,170]

Other studies have focused on the fact that hydrolysis induces superficial defects creating a sort of surface barrier, which prevents the interaction of the internal pores with eventual external gases or substances. In principle, healing such surface barrier might recover the properties of the pristine MOF.[172–174] For example, Müller and co-authors[172] found an easy method to dissolve such surface defects and then recover the pristine performances, but the dissolving process led to a loss of about 20% in mass of the material. Finally, McHugh and co-authors[83] suggested that hydrolytic stability can be induced in a MOF like HKUST-1 introducing *sacrificial bonds* between the Cu centers and the carboxylate ligands. Such idea led to the design of the MOF STAM-17-OEt, and therefore will be shown more in detail in section 2.5.

2.3.3   Densification of HKUST-1: tablets and monoliths

In literature many works have focused on the effects of the compaction on HKUST-1, whereas few information can be found about the synthesis of this MOF in a monolithic form. In the following, the results obtained by the most significant studies will be briefly exposed.

Mechanical compaction of HKUST-1

Several studies have been conducted about the densification of HKUST-1 powders, trying to find the optimal compromise between a gain in volumetric and packing density versus a loss of its structural properties like crystallinity, pore volume, etc.[101,120] Ideally, such loss should be avoided, whereas the density should reach or at least approach the crystalline density.[101,120] However, most of the works has shown, via PXRD or isotherm acquisitions, that the structure of HKUST-1 collapses at very modest applied pressure values, like few MPa.[101,120] In this context, the specific surface BET area of the tablets is a significant indicator, because a loss of surface area upon the compaction indicates a degradation of the porous framework of HKUST-1.

One of the first works was that of Kim and co-authors[136], which prepared pellets both with and without the employ of a binder, starting from powder obtained by a bench scale synthesis. Because of the sole addition of the binder in the powder, the authors observed a decrease in the BET surface area from 1737 to 963 m^2/g, that is a loss of about 45%.[136] The binder-free samples, that is the pellets produced by the use of mechanical pressure alone, showed also a strong decrease in the BET surface area, loosing the 96% of the surface area using a pressure value of 34 MPa.[136] The complete data obtained for the BET values are provided in table 2.3. Also the PXRD measurements showed a progressive strong decrease in the cristallinity of HKUST-1.[136] The overall performances about H_2O and CO_2 adsorption resulted compromised after the pelletization of the powders.[136]

Peterson and co-authors[139], preparing HKUST-1 pellets without any chemical binder and purchasing the pristine MOF from Sigma Aldrich, obtained better results, even though with severe reductions in both crystallinity and surface area (see table 2.3). The XRD patterns acquired after the application of pressure values of 7 and 70 MPa showed that the disposition of the peaks is maintained, but a partial collapse of the structure is suggested by the decreasing of the signal-to-noise ratio as the pressure increases.[139] Investigating the pore size distribution, the authors have noted a decrease in micropores

TABLE 2.3: A summary of the most important results in literature concerning the tableting of HKUST-1 powders. The table reports the tableting pressures and surface areas of the tablets.[121,136,139,175]

Authors	Pressure	BET surface area	Difference in BET area
	MPa	m^2/g	in percentage
Kim et al.[136]	Powder	1737	
	2.5	1147	-34%
	5	1007	-42%
	10	953	-45%
	15	529	-70%
	34	71	-96%
Peterson et al.[139]	Powder	1698	
	7	1045	-38%
	70	892	-47%
Bazer-Bachi et al.[121]	Powder	1897	
	27	1377	-28%
	80	1184	-38%
	400	452	-76%
Dhainaut et al.[175]	Powder	1288	
	14	1191	-7%
	24	1145	-11%
	62	1133	-12%
	121	1091	-15%

accompanied by an increase in mesopores, probably due to the breakage of some bonds during the pelletization process.[139]

Bazer-Bachi and co-authors[121] produced pellets of different types of MOFs.[121] Those regarding HKUST-1 have been produced starting from commercial powders purchased from Sigma Aldrich. Also in this case the decrease in BET surface area is significant (see table 2.3). They even report about *"prohibitive changes induced by pressure"*.[121]

Better results have been obtained by Dhainaut and co-authors[175], which prepared pellets using a rather complex methodology, by a Medel'Pharm STYL'ONE Evolution tableting instrument. With this system they were able to control the compression speed ramp and the dwell time.[175] They measured 1288 m^2/g of BET surface area for the activated powder (synthesized using the spray-drying technology[176]), a quite low value for HKUST-1 material and a bulk density of 0.48 g/cm^3.[175] The tablets obtained using a maximum pressure value 121 MPa showed a BET surface area 1091 m^2/g and a bulk density of 0.90 g/cm^3 (see table 2.3 for the results obtained at different pressure values).[175] Then, the highest loss of specific surface area is of about 15%. Anyway, as they admitted, such good results arise (at least partially) from the compression protocol they developed, but it is too complex to be used at industrial scale.[175] Furthermore, their initial value for the BET area is relatively small compared with the common values found in literature. For this reasons, the commercialization of well-performing HKUST-1 tablets still require further efforts.

Monolithic HKUST-1

Monoliths of MOFs, together with binder-less pellets, are considered the most recommended form of densified MOFs for a large range of applications.[101] In figure 2.5 we have seen an example of "monolithic HKUST-1" produced by leaving that the MOF grows up on a different pre-synthesized structure.[111]

Limiting the search only among the homogeneous (although still poly-crystalline) HKUST-1 monoliths, the first attempt of realization may dated back to 2014, by Ahmed and co-authors.[177] Starting from copper acetate and BTC as precursors, they synthesized it using a so-called *powder-packing* synthesis; an illustration of the process and of the final product is shown in figure 2.25 (a) and (b), respectively. After the synthe-
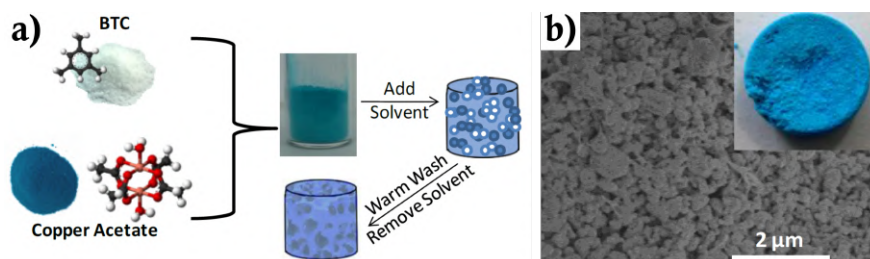
FIGURE 2.25: (a) Synthesis process for the obtaining of a HKUST-1 monolith by powder-packing synthesis. (b) Images of the surface of the monolith obtained. The shape is retained from the mould used. Adapted from ref. [177].

sis, their particle-aggregated monolith (with particle sizes of about 300 nm) appears

with an irregular surface that suggests a rather poor mechanical strength (see figure 2.25(b)).[177] Furthermore, no details about the density of the material have been published, even though the authors showed that their product was highly crystalline and with a BET surface of 1240 m^2/g.[177]

In 2018 another synthesis method has been published. Tian and co-authors[97] developed a sol-gel process which yields a glassy-look monolith, highly compacted and mechanically resistant. Figure 2.26 shows both a scheme of the sol-gel process employed (a) and of the synthesized monolith (b).
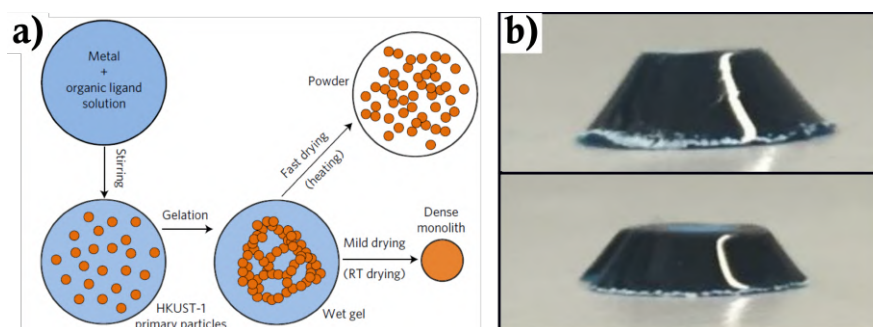
FIGURE 2.26: (a)Synthesis process for the obtaining of HKUST-1 monolith for Tian and co-authors by sol-gel process. (b) Images of two monoliths obtained. Adapted from ref. [97].

A solution of BTC and ethanol was mixed with a solution of $Cu(NO_3)_2 \cdot 2.5\,H_2O$ and ethanol at room temperature.[97] After centrifugation and repeated washing in ethanol, the sol-gel product was dried in an incubator at room temperature overnight, and with a subsequent treatment at about 400 K under vacuum overnight.[97] In a similar way they synthesized a powder sample for comparison just drying the washed solid at 400 K without waiting drying firstly at room temperature.[97] In fact, one of the key factors of this monolithic synthesis is that the first drying process of the sol-gel product needs to be obtained under mild conditions: in this way the mechanical stress caused by vapour-liquid meniscus interface of the ethanol into the pores of the material is avoided, and the obtaining of a continuous phase is possible.[97] The other two key factors highlighted by the authors are: 1) the small size of the primary particles, which is around 51 ± 10 nm; 2) the fast nucleation and crystal growth of the particles, which allows the formation of a crystalline lattice instead of an amorphous one.[97] The morphology of the monolith can be varied, shaping the monolith as required, for example for packing efficiently an eventual tank. In summary, the procedure is simple and efficient even though it has been proposed only in terms of a bench-scale synthesis.[97] The final monolith has several good properties, which are shortly explained as follows:

- **Specific surface area:** the authors obtained a BET surface are of 1193 m^2/g for the monolith, a rather low value if compared with the average 1750 ± 150 m^2/g generally obtained for HKUST-1 in powder form.[97,121,136,139–141] Despite this, the N$_2$ adsorption curve showed the distinctive Type I isotherm shape, and

the *volumetric* BET surface area obtained of 1288 m^2/cm^3 is higher than that of their powders (796 m^2/cm^3).[97]

- **Bulk density:** the material has a minimal amount of interstitial spaces, thus the measured bulk density reached 1.06 ± 0.05 g/cm^3, a bit larger than the crystal density of traditional HKUST-1, that is about 0.88 g/cm^3.[97] The discrepancy was explained assuming the co-presence of a denser amorphous phase.[97]

- **Methane uptake:** the authors assert that this HKUST-1 monolith is *"the first example of an adsorbent -including MOFs but also other traditional porous materials such as activated carbons and zeolites- that can achieve the US DOE (Department of Energy) target"* concerning the methane uptake, which is established at a value not lower than 263 cm^3/cm^3 (STP) at room temperature and 65 bar, and equivalent to the storage capacity of an empty tank at 250 bar.[97,178]

Because of these very interesting properties, in this thesis we have realized sol-gel HKUST-1 monoliths. The details of the synthesis and the subsequent results are shown in section 3.1.4 and 6, respectively.

2.4   STAM-1

In 2011, M. Infas H. Mohideen and coworkers synthesized the MOF STAM-1 (ST Andrews MOF-1): this structure contains the same SBU of HKUST-1 but a different organic linker, that is the monomethyl BTC (mmBTC) (figure 2.27).[82,118] Basically, if the common solvent used for the preparation of HKUST-1 is 50:50 ethanol:water, for the preparation of STAM-1 it is sufficient to change the solvent to a 50:50 methanol:water mix. In fact, the presence of the methanol leads the BTC linker to a selective monomethil esterification.[82,118]

STAM-1 has a formula of $Cu(C_{10}H_6O_6)(H_2O) \cdot 1.66\,H_2O$ and its structure consist of a peculiar arrangement of paddlewheels which leads to an alternation of hydrophilic and hydrophobic channels (figure 2.27-b).[82] Furthermore the interaction with water molecules causes significant changes in the unit cell parameters of the framework, making the material a flexible MOF (see section 2.1.4).[82,118] Its flexibility combined with the particular pores gives it unusual adsorption properties.[82,118] The pore size of the hydrophilic channel is no more than ~ 5.65 Å with triangular windows of ~ 4 Å.[82,118] Its activation temperature is ~ 423 K.[82,118] The flexibility of the MOF caused by the guest sorption is easily detectable from the high-resolution XRD data, which reveal small but significant changes in the unit cell parameters during the hydration or dehydration of the material (see figure 2.28).[82,118] However, the structure of the dehydrated STAM-1 has not yet been clearly determined from crystallography. It is only clear a slightly lowering of the symmetry, from trigonal to triclinic, and a recover of the original symmetry upon rehydration.[82,147]
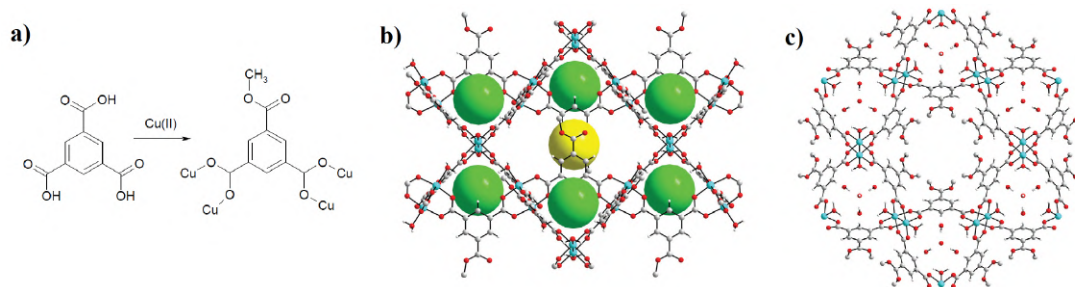
FIGURE 2.27: (a) Monomethyl esterification of the BTC linker leading to the formation of STAM-1. (b) The up and down orientation of six "cups" formed by the arrangement of the paddlewheels leading to porous layers with two kind of pores: hydrophilic (green spheres) and hydrophobic (yellow spheres). (c) Overall structure of STAM-1: the empty channel are those lined by the ester groups, whereas those filled with water are the hydrophilic channels. Adapted from ref. [82].
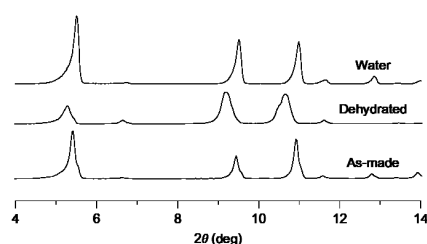

FIGURE 2.28: Powder XRD patterns (CuKαradiation) of as-made (bottom), dehydrated (middle) and rehydrated (top) STAM-1.[82]

Solid-state ^{13}C MAS NMR spectra. Via solid-state ^{13}C cross-polarization MAS NMR spectra, Dawson and co-authors[147] revealed more information about the two stable configurations of STAM-1, by studying the changes during the dehydration of the material.[82,118,147] The ^{13}C MAS NMR spectra acquired for STAM-1 are shown in figure 2.29 (a). The crystal structure of as made STAM-1 shows seven crystallographically-distinct C species, numbered following the scheme displayed in figure 2.29 (b), similar to that previously seen for HKUST-1.[147] Each C species results in a resonance in the ^{13}C NMR spectrum.[147] The resonances observed at -50, 227 and 853 ppm have comparable isotropic shifts as those detected in HKUST-1, and therefore they have been assigned to C2, C3 and C1, respectively.[147] The resonance peaked at 49 ppm is assigned to C7 because it is characteristic to methyl ester, whereas those observed at 181, 178 and 174 ppm are ascribed - in order - to the carbons C4, C5 and C6.[147] Upon dehydration several changes in the spectrum are detectable, which suggest a lowering of symmetry: in the C2 region at least two resonances appear, and a similar splitting is observed for the C3 peak at 224 ppm, suggesting the presence of magnetically inequivalent C2 and C3 sites in the dehydrated material.[147] Furthermore, the C4-C6 peaks undergo a broadening involving the whole region ranging from 160 to 195 ppm.[147] The broadening suggests the presence of a certain degree of disorder proper to the dehydrated lattice configuration, but which disappears when the MOF is rehydrated under atmospheric moisture.[147] More recently, another work based on NMR spectroscopy carried out by
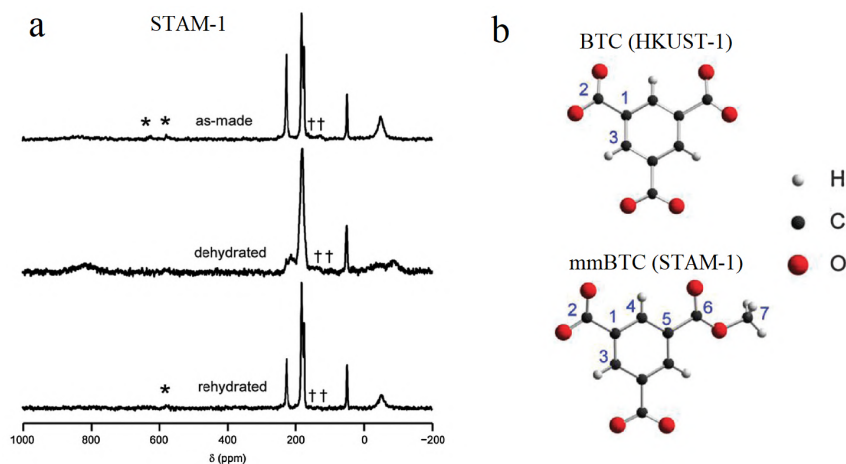
FIGURE 2.29: (a)^{13}C MAS NMR spectra of as-made, dehydrated and rehydrated STAM-1. The * denote spinning sidebands and † denote BTC-based impurities present in the sample. Adapted from ref. [147].

Dawson and co-authors provided clarifications on the dehydrated lattice of STAM-1, establishing that very likely the flexibility observed upon dehydration is due to a change of the inter-paddlewheels interactions, which are broken when water molecules binds to ^{13}C.[148] Such considerations have been done on the basis of the similarity of the STAM-1 NMR spectra with those of the MOF STAM-17-OEt (see section 2.5), whose structure had been previously determined with confidence for both as made and dehydrated configuration.[83,148] These weak bonds, which are broken upon hydration, are called *"crumple-zones"*, and because of that, STAM-1 has been defined as a *hemilabile* MOF, as STAM-17-OEt. Further explanations on the hemilability mechanism can be found in section 2.5 and 2.5.1.

Surface area evaluation. Figure 2.30 shows the nitrogen isotherm curve obtained for STAM-1 at 77 K.[118] The curve is a simple Type I isotherm, indicating a narrow size distribution of the pores, with a specific surface area calculated via BET method of about 200 m^2/g. This value is about half of that calculated by molecular simulations
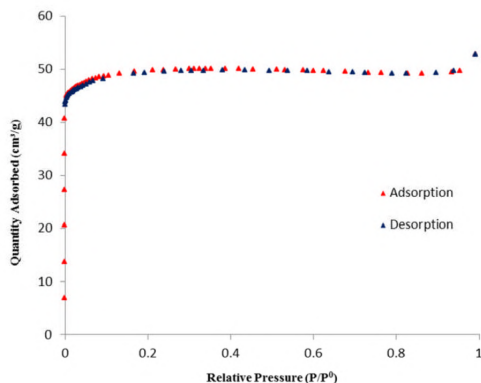
FIGURE 2.30: Adsorption (red) and desorption (blue) nitrogen isotherm acquired at 77 K for STAM-1.[118]

($420 \ \mathrm{m^2/g}$) and, furthermore, it does not show any trace of the double-barrelled nature of the channels of this material.[118] For this reasons the authors suggested that only one type of channel system is available for the nitrogen adsorption.

2.4.1 Magnetic properties

As it may seem reasonable to expect, since the SBU of STAM-1 is the copper paddlewheel, even this MOF shows magnetic properties, with comparable features to those observed for HKUST-1 material. Mkami and co-authors[179] reported a set of EPR spectra acquired for STAM-1 at different temperatures and its susceptibility curve, shown in figure 2.31 (a) and (b), respectively. As expected, the susceptibility curve shows a
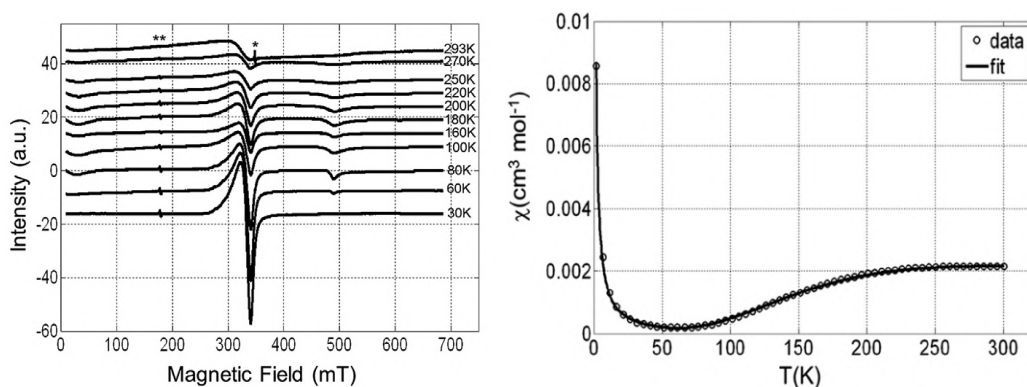
FIGURE 2.31: (a) EPR spectra of STAM-1 recorded at different temperatures at X-band. The peaks marked by * and ** correspond to signals arising from the experimental set-up. (b) Magnetic susceptibility curve as a function of the temperature, obtained experimentally (○) and by simulation (-).[179]

trend typical for strong antiferromagnetic interactions between the two Cu^{2+} of the dimeric paddlewheel. By fitting the data, the authors obtain a coupling constant of about $J_0 \approx -334 \pm 4 \ \mathrm{cm^{-1}}$.[179] Also in this case, the presence of uncoupled monomeric Cu^{2+} in the sample is observed by a Curie-Weiss trend at low temperature, and it requires the inclusion of a Curie term per S=1/2 spins in the Bleaney-Bowers equation. The contribution of these latter paramagnetic centers has been estimated at around 10%.[179]

The similarity with HKUST-1 is also shown by the dependence of the EPR spectra by temperature: the three species defined by Pöppl and co-authors are observed also for STAM-1 at comparable temperature ranges. At 200÷300 K a single broad resonance with g=2.160±0.002 is observed, whose intensity decreases with temperature.[179] At lower temperatures, the signal arising from the S=1 spin centers is observed in two resolved resonances, with positions comparable to those of HKUST-1 ($\approx$20 and $\approx$490 mT).[179] By simulation, the authors obtain |D|=0.337±0.001 $\mathrm{cm^{-1}}$, E$\approx$0 and the g values $g_1=g_2=2.060\pm0.002$ and $g_3=2.340\pm0.005$.[179] At T<50 K the triplet state get depopulated in favour of the ground state S=0, leading the paddlewheel to become diamagnetic. For this reasons, at T<50 K only the peak assigned to the monomeric

copper complexes is observed, centered at 320 mT, but, in contrast to what seen for HKUST-1, no trace of hyperfine interaction is detected.

2.4.2 Water stability

STAM-1 is considered by literature a water stable MOF, even though its hydrolytic stability has been proved only by the analysis of PXRD patterns and water adsorption/desorption cycle measurements. Figure 2.32 shows the PXRD patterns of as-made and rehydrated STAM-1. No changes are observed between the patterns, leading to the
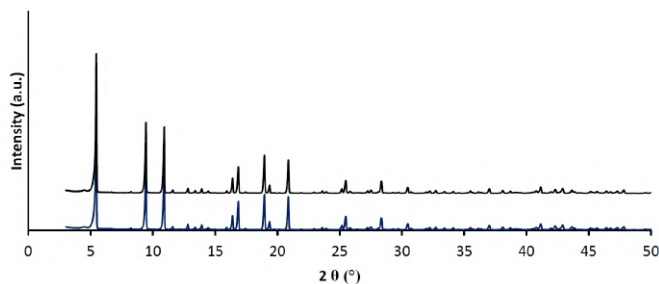

FIGURE 2.32: PXRD patterns of as-made STAM-1 (blue line) and STAM-1 after submersion in water (black line).[83]

conclusion that STAM-1 has hydrolytic stability. The water cycle measurements showed that the water uptake remains constant for the whole duration of the experiment (120 hours).[83] The cause of its stability has been attributed to the presence of the "crumple-zones", particular inter-paddlewheel interactions defined for STAM-17-OEt by McHugh and co-authors.[83] The stability mechanism of STAM-1 involving the crumple zones has been assumed only on the basis of the comparability of the changes shown in the NMR spectra of STAM-1 and STAM-17-OEt upon dehydration, and for this reason it will be explained in detail in section 2.5.

2.5 STAM-17-OEt

The third MOF studied in this thesis is STAM-17-OEt. It is part of the STAM series and it has been synthesized by McHugh and coworkers in 2018.[83,118] STAM-17-OEt is composed of dinuclear copper paddlewheels connected by 5-ethoxy isophthalate linking units, forming a flexible 2-dimensional framework with a kagome-type topology.[83] The structure of STAM-17-OEt is shown in figure 2.33.

The as-made material has two types of one-dimensional channels extended perpendicularly, sheet after sheet, through the whole depth of the lattice: the first type has a triangular cross-section and it contains both the coordination and the disordered water molecules; the second type of channel has a hexagonal cross-section and it contains the ethyl groups of the linkers, disordered over two possible symmetry-related sites (figure 2.33).[83] The paddlewheels are all equivalent and the two coordinated water molecules form simple hydrogen bonds with the carboxylate O atoms of the sheets above and below.[83] This configuration is portrayed in figure 2.34. Upon dehydration, the coordi-
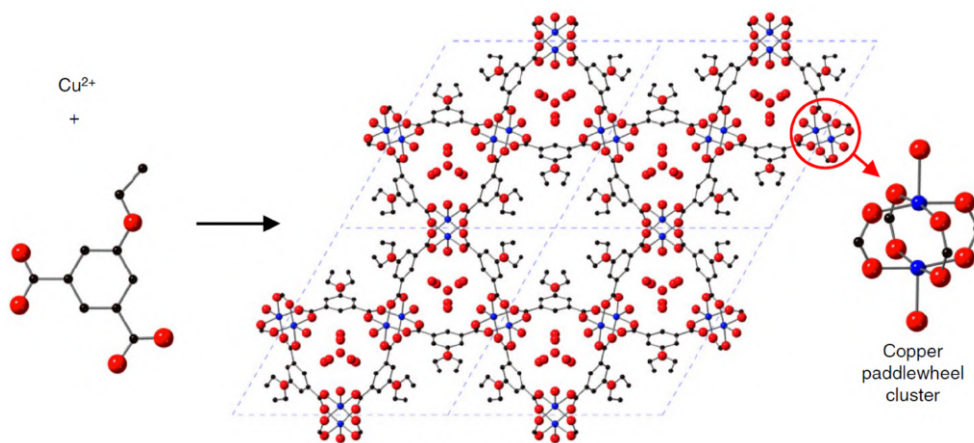
FIGURE 2.33: Structure of STAM-17-OEt, formed by paddlewheel dimers and 5-ethoxy isophthalate linking units. The ethyl groups are illustrated in both the two possible orientation, each 50% probable. The copper atoms are pictured as blue spheres, the oxigens in red and the carbons in black, whereas H atoms have been omitted for clarity. Adapted from ref. [83].
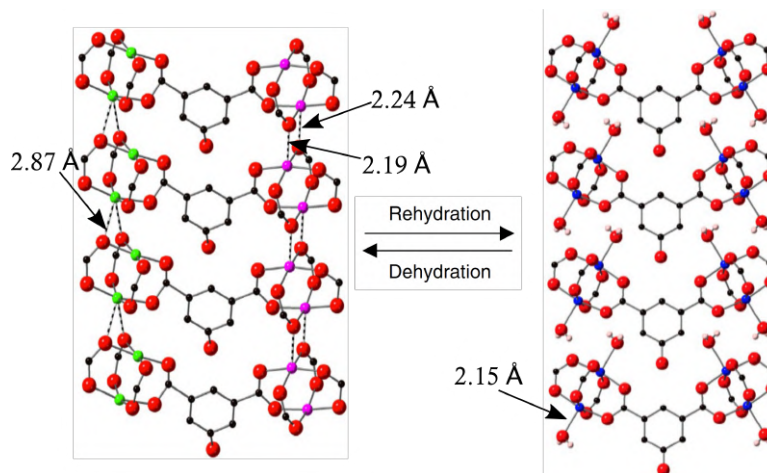

FIGURE 2.34: Comparison of the dehydrated and hydrated structure of STAM-17-OEt. For clarity, H atoms of the organic linker and C atoms of the alkyl chains have been omitted. Adapted from ref. [83].

nated water molecules have been removed and the configuration sensibly changes.[83]

In the dehydrated (or activated) STAM-17-OEt, the framework consists of two distinct groups of paddlewheels with four crystallographically unique Cu centers.[83] The paddlewheels of the first group are characterized by weak bonds involving the copper ions of one paddlewheel and the two oxygen atoms of the paddlewheel lying in the adjacent sheet, with Cu···O distances between 2.8 and 3 Å (figure 2.34).[83] Differently, the paddlewheels of the second group are characterized by weak bonds established by pairing the Cu−O of one paddlewheel with the O−Cu of that one lying in the sheet directly above or below, with shorter interdimer Cu···O distances of about 2.2 Å (figure 2.34).[83]

Rehydrating again the MOF, for example by an exposure to air moisture, the original as-made structure is obtained again, with the breaking of all those weak Cu···O

bonds that had been established in the activated framework upon dehydration.[83] The reversibility of this single crystal-to-single crystal transition accompanied by the breaking of some bonds, makes the MOF *hemilabile*. The name has been coined by analogy to ligands used in homogeneous catalysis.[83] The unit cell dimensions change from a=18.576(12)Å and c=6.8056(6)Å of the as-made STAM-17-OEt to a=33.028(3)Å and c=5.2047(6)Å for the dehydrated structure. The pores of STAM-17-OEt are rather small, and this has repercussions on its BET surface area, which is about 58 m^2/g.

The flexibility of the material is also easily seen by acquisition of solid-state ^{13}C NMR spectra. Figure 2.35 shows the spectrum of both as-made and dehydrated STAM-17-OEt. The resonances have been fully assigned to the 7 chemically distinct carbons of the material. The broad resonance for C1 is observed only in the vertical expansion of figure 2.35(e), whereas the resonances C3+C5 are overlapped at room temperature.[83] The most evident difference between the NMR spectrum of the hydrated material and
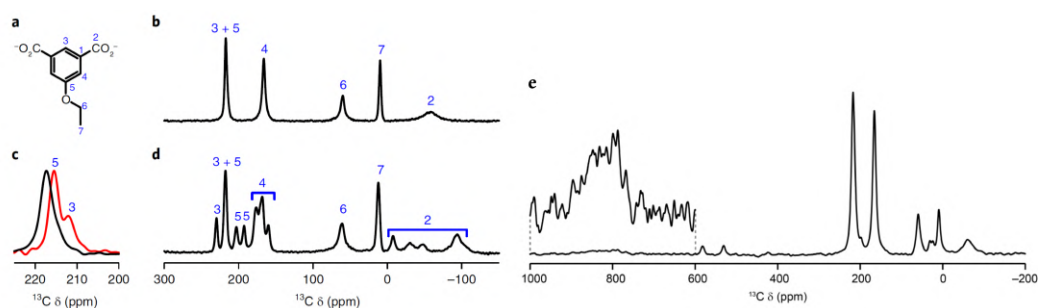
FIGURE 2.35: Solid-state ^{13}C NMR data for STAM-17-OEt in as-made and dehydrated form. a)Numbering scheme for the C atoms. b)^{13}C (14.1 T, 37.5 kHz MAS, 298 K) NMR spectrum of as-made STAM-17-OEt. c)Expansion of the C3+C5 resonance of as-made STAM-17-OEt. d) ^{13}C (14.1 T, 40 kHz MAS, 298 K) NMR spectrum of dehydrated STAM-17-OEt. e)^{13}C (14.1 T, 40 kHz MAS, 298 K) NMR spectrum of STAM-17-OEt with the inset showing a vertical expansion of the region 1000 ÷ 600 ppm. The resonance of C1 is assigned at about ∼ 830 ppm. Adapted from ref. [83].

that of the dehydrated one is the number of peaks pertaining to each C atom: in fact, in the hydrated material the spectrum is composed of single resonances but in the dehydrated spectrum some of the single signals split into 2 (for example for C3), 3 (C5 or C4) or even 4 (C2) resolvable peaks.[83] These changes are more pronounced for C2 because it is the carboxylate carbon and then the closest one to the paddlewheel units, whereas the resonances pertaining to the carbons of ethyl groups, C6 and C7, are not influenced by the dehydration process.[83]

2.5.1 Interaction with water and ammonia

STAM-17-OEt, as STAM-1, showed a strong chemical stability in humid environments. The material has been tested by a PXRD comparison before and after a submersion in water for one year at room temperature (figure 2.36). The comparison shows very little changes, then they concluded that the cristallinity and then the overall structure of the sample has been retained.[83] Under comparable conditions, HKUST-1 showed a crystalline structure critically degraded after only two days.[83] Such water stability has
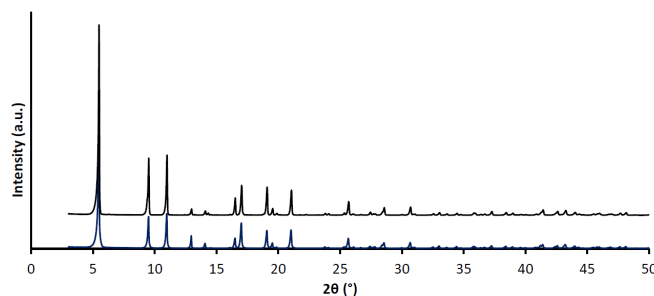
FIGURE 2.36: PXRD patterns of as-made STAM-17-OEt (blue line) and STAM-17-OEt after submersion in water for 1 year (black line).[83]

been also confirmed by water cycling experiments conducted on a time range of 120 hours and by infrared spectra acquired before and after five days of exposure to atmosphere of 90% humidity.[83] Furthermore, studying the trend of the mass of both STAM-17-OEt and HKUST-1 during the five days of exposure, they observed two different developments. STAM-17-OEt shows only an initial mass gain with no further changes: water interacts only with the free Cu sites of the material.[83] HKUST-1 shows a similar immediate increase in mass, but it lasts for about 20 hours, after which there is a progressive loss in mass.[83] The explanation of the author is that the water molecules in HKUST-1, breaking the Cu-O bonds, interact also with "extra" Cu sites not available in the initial dehydrated MOF, leading to the collapse of the structure.

The water stability of a MOF so chemically similar to HKUST-1 is very surprisingly, and therefore finding the reasons is significant. By density functional theory calculations, estimated the energy of the lattice in the two configurations, they found that the formation of the weak inter-paddlewheels Cu-O interactions adds stability to the structure.[83] Therefore, the breakage of such bonds by water molecule requires energy: this energy cannot be spent to break the structure down as happens in HKUST-1.[83] Such model is shown in figure 2.37. In other words, the inter-paddlewheels interactions act as "crumple
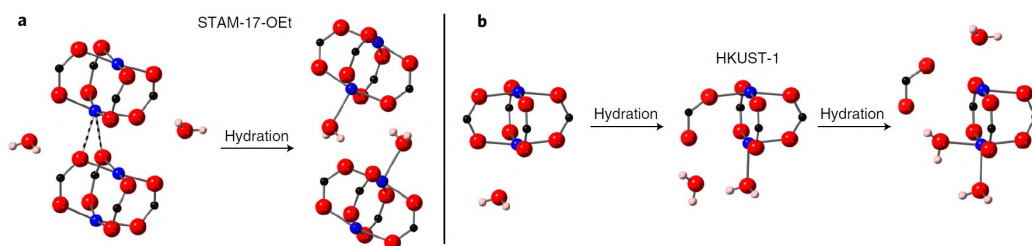
FIGURE 2.37: Effect of hydration on the paddlewheel units of the MOFs STAM-17-OEt and HKUST-1. Adapted from ref. [83].

zones" of the auto-vehicles: they direct energy of the "collision" with a water molecule away from the key metal-oxygen bond of the paddlewheel. Since this mechanism is no present in HKUST-1, the energy released by the water molecule upon adsorption on the Cu^{2+} metal center can be used to break the Cu-O bond, opening up new metal sites for subsequent water adsorption (fig 2.37(b)).[83] However, the authors admitted the possibility that the stability of STAM-17-OEt may be correlated to the limited porosity of

the material.[51,83]

Ammonia adsorption.   STAM-17-OEt shows good potentialities in the removal of
ammonia vapours from the air.[83] Ammonia micro-breakthrough tests were done allow-
ing ∼20 mg of MOF to interact with both dry or humid gases containing an ammonia
gas concentration of 500 ppm.[83] The data, displayed in figure 2.38, showed that the
ammonia capacity of STAM-17-OEt increases slightly over the five days of exposure to
humidity, without reaching a plateau, while HKUST-1 showed (at the same conditions)
a prior larger increase but a subsequent drop to levels comparable to the original capac-
ity of the material. The results have been interpreted as a confirm of the cooperative
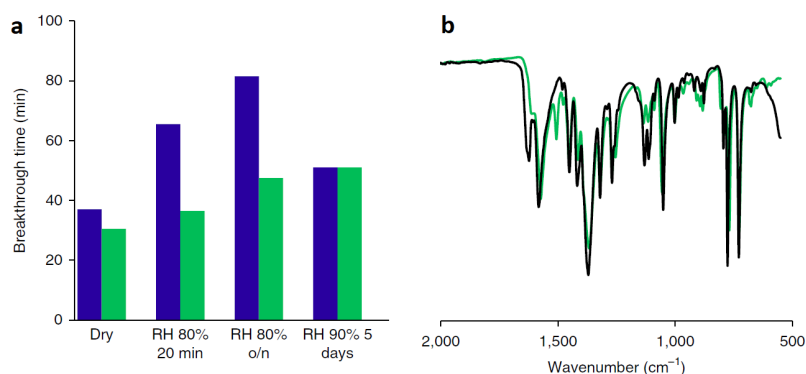
FIGURE 2.38: (a) Breakthrough time to reach 10% of influent concentration for am-
monia on HKUST-1(blue) and STAM-17-OEt (green) at different conditions: dry, 20
minutes under 80% RH, overnight under 80% RH and 5 days under 90% RH.[83] (b)
Infrared spectra obtained for STAM-17-OEt before (green) and after (black) the ex-
posure to ammonia.[83]

ammonia/water adsorption already observed previously in other MOFs like HKUST-1
and as a improved hydrolytic stability of STAM-17-OEt during the days of exposure to
humidity.[83,180]

Part II

Chapter 3

Experimental section

This chapter shows a brief description of the preparation and the synthesis methods of the different samples, as well as the main information on the instrumental setup used for each experimental technique.

3.1 Synthesis and preparation of MOF samples

This section describes the synthesis preparation of the samples involved in this thesis and the treatments performed on them.

All chemicals used for the MOF syntheses were purchased from commercial sources and used without further purification.

3.1.1 HKUST-1 powder

HKUST-1 in activated powder form was purchased from Sigma Aldrich. For convenience, the content of one bottle of 10 g of powder purchased was divided in many vials containing about 150 mg of MOF each by using a glove box under nitrogen atmosphere. The glass vials filled by HKUST-1 powder have been sealed by abundant parafilm and stored until the moment of their use. Nevertheless, in order to avoid potential hydration effects due to infiltration of water molecules into the vials during the staying of the MOF, prior to use the content of each vial has been generally subject to a short activation process of ~1 hour at 420 K in air, except when expressly indicated.

Figure 3.1 shows optical images of HKUST-1 powder. The sample exhibits a micrometric granular morphology.
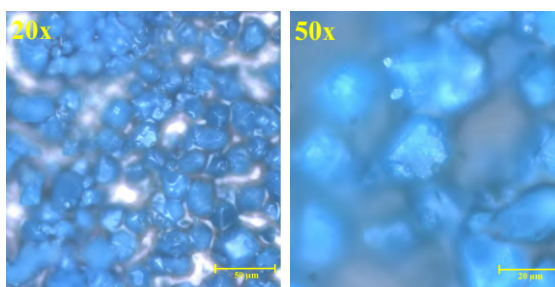
FIGURE 3.1: Optical images of HKUST-1 powder.

3.1.2 STAM-1 synthesis

STAM-1 was synthesized as described by Mohideen and co-authors.[82,118] 2.0 mmol of Cu(NO$_3$)$_2$· $_3$(H$_2$O) (0.483 g) and 2.0 mmol of 1,3,5-Benzenetricarboxylic acid H$_3$BTC (0.421 g) were dissolved in 20 ml of MeOH/H$_2$O (50:50) solution. The solution was mixed for 15 minutes at ambient temperature prior to be heated in an oven (preheated at 383 K) within a Teflon-lined stainless steel sealed autoclave and then heated at 383 K for 7 days. Afterwards, the autoclave was naturally cooled down to room temperature. The product synthesis (blue crystals, with yield about 95%), was isolated by Buchner filtration, washed with water and acetone and then dried in air. Once completely dried, it constitutes the so-called *as-made* STAM-1 sample.

3.1.3 STAM-17-OEt synthesis

STAM-17-OEt was synthesized as described by McHugh and co-authors.[83] The synthesis of this MOF requires more steps, due to the necessity of producing the linker precursors. The precursors and the final linker are shown in figure
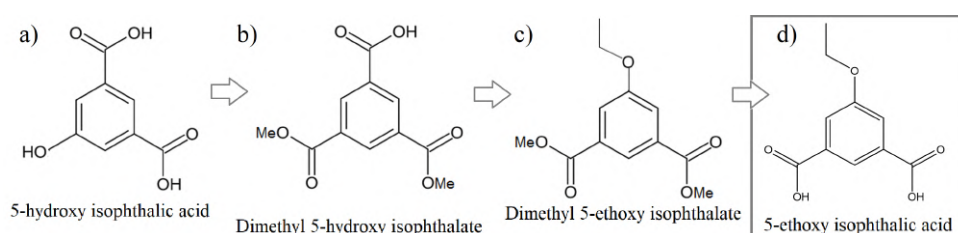
FIGURE 3.2: Linker precursors and the linker 5-ethoxy isophthalic acid used for the synthesis of STAM-17-OEt: a) 5-hydroxy isophthalate, b) dimethyl 5-hydroxy isophthalate, c) dimethyl 5-ethoxy isophthalate, d) 5-ethoxy isophthalic acid.

Dimethyl 5-hydroxy isophthalate.   This precursor was synthesized by literature method.[181] A suspension of 5-hydroxy isophthalic acid (53.40 g, 293.20 mmol) in methanol (625 ml) was prepared, to which concentrated sulfuric acid (19.5 ml) was added. The mixture was heated up to 358 K to reflux for 8 hours. The solution was then cooled and washed with copiously distilled water (about 675 ml). A white precipitate was thus produced and suspended in distilled water (100 mL) before further filtering, in order to remove the solvent under reduced pressure, providing the product as a white solid (48.72 g, 231.80 mmol, 79% yield) that will be left to dry in air.

Dimethyl 5-ethoxy isophthalate.   Also this precursor was synthesized by literature method.[182] Dimethyl 5-hydroxy isophthalate (11.44 g, 54.43 mmol) and potassium carbonate (13.69 g, 99.06 mmol) were dissolved in acetone (260 ml). The mixture was then heated to reflux for about 100 minutes. Without cooling, iodoethane (5.00 mL, 62.50 mmol) was added and the reaction was left to further reflux overnight (for ∼18 hours). Upon cooling to room temperature, the mixture was placed in a rotavapor until the complete removal of the solvent. The resulting solid was taken-up in DCM (300

mL) and distilled water (300 mL). The mixture was extracted with further DCM (3 x 200 mL) and the produced organic layers were washed separately with brine (saturated aqueous of anhydrous magnesium sulfate, $\sim$ 100 mL) and dried over anhydrous magnesium sulfate. The solvent was removed under reduced pressure to provide the product as a white solid (12.44 g, 52.22 mmol, $\sim$96% yield).

5-ethoxy isophthalic acid. The final linker was finally synthesized starting from the dimethyl 5-ethoxy isophthalate by literature method.[183] Potassium hydroxide (11.99 g, 213.70 mmol) and dimethyl 5-ethoxy isophthalate (10.05 g, 42.18 mmol) were dissolved in methanol (250 mL). Afterwards, the solution was heated up to 350 K to reflux overnight (for $\sim$18 hours). Upon cooling to room temperature, 2M hydrochloric acid (250 mL) was added to the solution and the resulting precipitate was collected by vacuum filtration. At this point, the white solid was repeatedly washed with copious distilled water until the washings reached pH $\sim$5-6; the product was then dried in air for several days (8.55 g, 40.68 mmol, 96% yield). Obtained by scarping the compact white solid mass, the linker had a light, fluffy aspect.

STAM-17-OEt. Synthesis of STAM-17-OEt. STAM-17-OEt was synthesized by heating copper acetate Cu(OAc)$_2$. H2O (5 g, 1.00 mmol), 5-ethoxyisophthalic acid (4.75 g, 1.00 mmol) and distilled water (360 ml) in a stainless-steel sealed autoclave at 383 K for 3 days. To maximize the yield, before using, the 5-ethoxyisophthalic acid was roughly grinded. After cooling to room temperature, the product obtained was filtered and the solid was washed with abundant ethanol (in order to remove unreacted linkers) before drying in air. The yield was 7.5 g, 0.76 mmol, 81%. Once completely dried, it constitutes the so-called *as-made* STAM-17-OEt sample.

Figure 3.3 shows two optical images acquired for the STAM-17-OEt powder. They
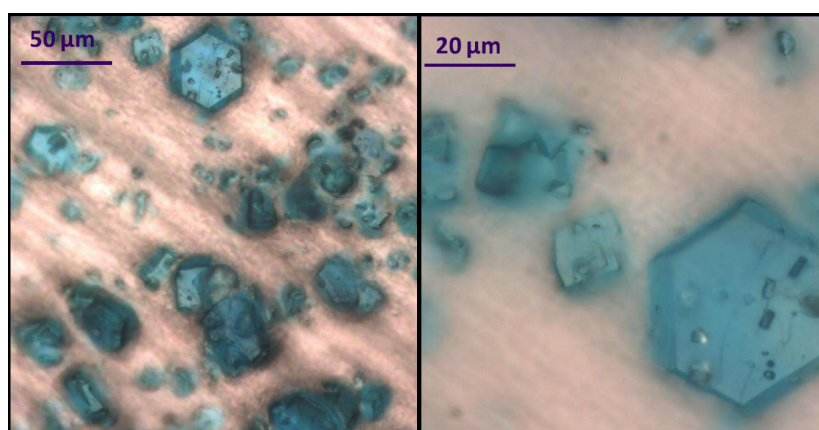

FIGURE 3.3: 20x (left) and 50x (right) optical images of the powder STAM-17-OEt.

show that the morphology of the material consists of single grains of variable sizes, ranging from few to some tens of micrometers.

3.1.4   HKUST-1 monoliths synthesis

The synthesis procedure follows the description reported in literature by Tian and co-authors.[97]

Two different solutions of ethanol (10 ml) have been prepared with 130 mg of BTC and 155 mg of $Cu(NO_3)_2 3H_2O$, respectively. Once mixed together, the resulting combination have been stirred for 10 minutes at room temperature. Then, in order to collect the light blue solid part, the mixture was centrifuged for 10 minutes. After washes in ethanol for 10 minutes (15 ml, 3 times), most of the solvent has been removed and the product was left to dry at room temperature overnight.

The monolith just after the overnight drying, or else the *as made* monolith, is shown in figure 3.4. Its surface is smooth, without trace of micrometric granular structure, in
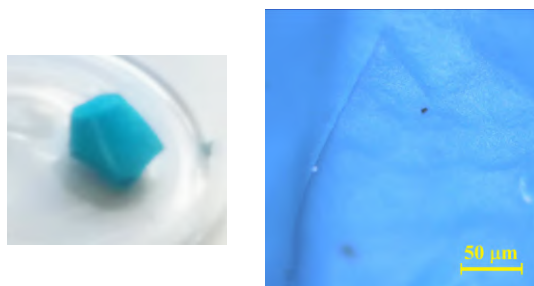
FIGURE 3.4: (left) Photographic image of an *as made* HKUST-1 monolith after the overnight drying, before the activation; (right) optical image of its surface acquired by a microscope.

contrast to the standard HKUST-1 powder (see figure 3.1).

3.1.5   MOF activation

After the above mentioned overnight drying at room temperature common in all of the synthesis procedures, the synthesized materials (STAM-1 powders, STAM-17-OEt powders, HKUST-1 monoliths) have been activated at ~ 420 K overnight at low pressures. Simplifying for sake of clarity, the equipment employed consists of an oven which allows to introduce a Schlenk flask tube. This tube can accommodate even 15 vials simultaneously. Upon its filling with the vials (containing, in turn, the MOFs), the Schlenk flask tube can be sealed and connected to a vacuum pump, reaching pressure minima ranging between $7.0 \times 10^{-3} \div 6.8 \times 10^{-4}$ Torr. In the meanwhile, the oven allows to heat the MOF contained in the vials up to the desired temperature (420 K)

The following morning, after turning off the oven and waiting for a natural cooling to room temperature, the connection with the vacuum pump has been interrupted and argon gas has been introduced in the Schlenk flask tube, thus filling also the vials containing the samples. Once removed the vials from the Schlenk flasks tube, they have been sealed by a blowtorch.

With an analogous procedure, MOFs can be activated even when contained in glass capillary, for PXRD pattern acquisitions (see 3.2.4). Prior to the insertion in the capillary it is generally necessary to slightly grinder the material, to make the grains smaller. Dealing with capillaries, the sealing after the activation is made by a simple lighter.

For other samples like HKUST-1 tablets and whenever expressly declared in the following, a softer and simpler activation process has been performed, using standard pressure and shorter time. These details are further discussed in the apposite paragraphs.

3.1.6 Preparation of HKUST-1 tablets

In order to meet the needs of an eventual future large-scale industrial production, HKUST-1 tablets have been made by using a compaction protocol as simple as possible.

The content of each vial of ~150 mg of HKUST-1 powder was transferred in an EPR glass tube and then thermally treated in oven for 1 hour at 420 K. Then, the powder was placed inside a pill maker under a hydraulic press. Each sample was pressed for 10 min by applying a specific mechanical pressure. Two different pill makers and manometers were used (for pressure application and reading, respectively) depending on the range of pressure to be applied. In fact, for pressures from 0 to 30 MPa and for 40 MPa, the circular sections of the pill makers were 0.5 and 1.3 cm^2, respectively. The uncertainties in the corresponding pressures are about 3 and 10%, respectively. A set of samples was obtained, by using the following values of pressure: 1, 3, 10, 20, 30, or 40 MPa. In the following, all these samples will be referred to as "tablets", even though those obtained with values of pressure lower than 30 MPa were not found to form mechanically stable tablets (see figure 3.5).
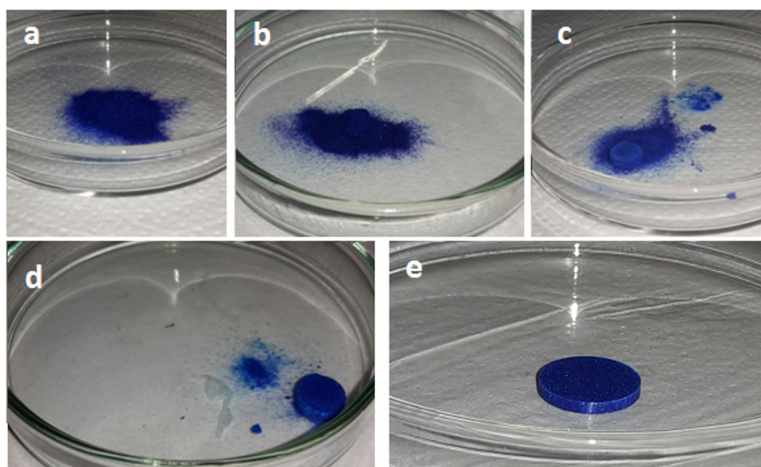
FIGURE 3.5: A-type tablets: a) 1 MPa, b) 3 MPa, c) 10 MPa, d) 20 MPa, e) 40 MPa.

After preparation, each tablet was crushed and put into an EPR tube that was then sealed with parafilm. The samples were monitored by EPR spectroscopy for about 5 weeks after preparation. The following compact notation will be used in the present paper to indicate the various samples: "name-pressure-days after preparation", where "name" is a capital letter, which may be A or B. The letter A indicates that the sample

was not heat-treated after the preparation of the tablet; inversely the letter B indicates that the sample was activated after ∼2 h from the tableting (again in air for 1 hour at 420 K).

In the compact notation, "pressure" indicates the nominal pressure used to prepare the tablet and "days after preparation" indicates the time lapsed from the preparation of the tablet to the date of the measurements. In addition, two hydrated tablets were also produced, obtained by using two different hydration methods. For the former tablet, before tableting at 40 MPa, the powder was kept in air into a Petri for 20 min (powder H1), whereas for the second tablet, the parent powder was exposed to air moisture in a 1 cm diameter glass vial for about 2 h (powder H2). This latter method ensures a softer hydration process compared to that made with Petri, as also confirmed by the fact that its color remains almost unchanged after 2 h of exposure. Hereafter, we will refer to

FIGURE 3.6: Hydrated powder samples before the tableting for H1-40 MPa and H2-40 MPa tablets respectively.

these two last tablets with the name "H1-40 MPa" and "H2-40 MPa", respectively (see figure 3.6).

A sample of virgin activated HKUST-1 material in powder form was also studied, for comparison, and hereafter it will be simply referred to as "powder". Finally, to indicate when a sample was reactivated, the mark "-reactivated" is added just at the end of its compact name. Tableting, aging, and handling of all powder and tablet samples have been conducted in air at about 70% RH.

Figure 3.7 shows optical images of HKUST-1 B-40MPa tablet. It clearly show that the B-40MPa tablet actually preserves the main granular morphology of the pristine material (figure 3.1), as it consists of well-packaged grains of HKUST-1. This aspect has been deepened by AFM studies shown in chapter 5.

3.1.7   Preparation of STAM-17-OEt tablets

Dehydrated powder samples of STAM-17-OEt obtained as already explained were subject to mechanical compaction in order to obtain a set of tablets, in an analogous way to the above mentioned HKUST-1 tablets. The pristine powder sample is termed simply "activated powder". The set of STAM-17-OEt tablets (named set A) have been produced starting from about 150 mg of activated powder, by placing them inside a pill maker under a hydraulic press and then by pressing for 10 minutes via application of
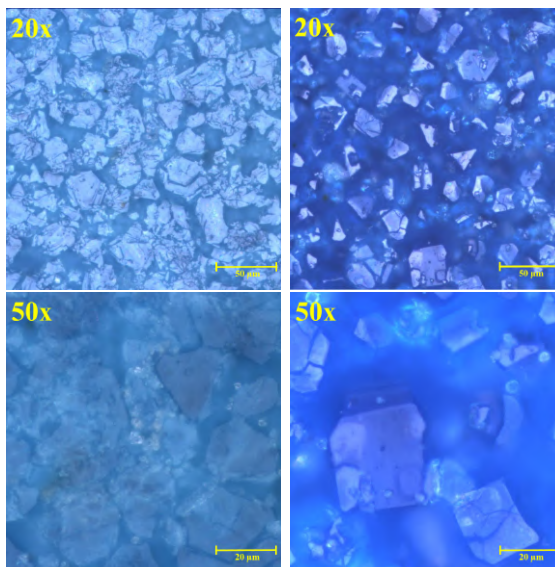
FIGURE 3.7: Optical images of HKUST-1 tablet B-40MPa.

a mechanical pressure, precisely: 3, 20, 50, 100, 150 or 200 MPa. Also for this tablet set, in the following, all of them will be referred to as "tablets". After preparation, each tablet was crushed and reactivated at ambient atmosphere at T= 420 K overnight. In order to study the effect of humidity on the compacted MOF, a rehydration process has been done, by keeping each sample in an open vial exposed to air moisture (RH~70%) for about 2 hours. A second set of tablets has been produced (named set B), with the only difference that the starting powder samples have been previously kept exposed to air moisture for about 20 minutes on a petri dish.

Figure 3.8 shows photographic images of some of the tablets produced.
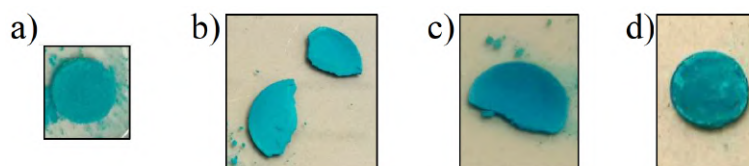
FIGURE 3.8: Photographic images of some of the samples: a) tablet pressed at 200 MPa of set A, b-c-d) tablets pressed at 50, 100, 200 MPa of set B, respectively.

Figure 3.9 shows two optical images acquired for the 100 MPa (set B) sample. The compaction of the grains is well evident, but the granular form of the material is virtually unaltered (see for comparison figure 3.3). These aspects have been deeper investigated by AFM acquisitions, whose results are shown in chapter 7.

3.1.8 STAM-17-OEt activated carbon composite samples

The growth of carboxylate MOFs within activated carbons was previously reported by Casco and co-authors[184] and then further developed by Fleker and co-authors[185], which based their research on HKUST-1 in order to improve the mechanical stability of the
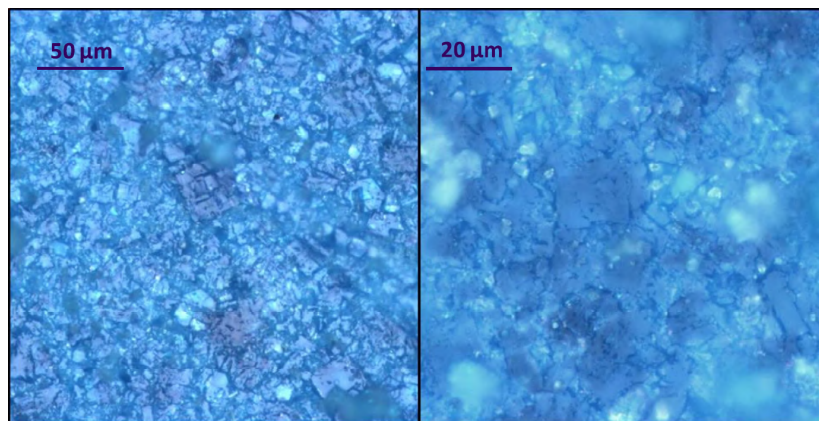
FIGURE 3.9: 20x (left) and 50x (right) optical images of the surface of the STAM-17-OEt tablet produced with a pressure of 100 MPa (set B).

MOF (the former) and to impart electrical conductivity into an otherwise nonconducting material.

STAM-17-OEt activated carbon composite materials were synthesized by an in-situ process, shown schematically in figure 3.10. The BPL activated carbon was purchased from Chemviron Carbon Ltd. The final product is a black granular material, optically similar to the pristine unimpregnated carbon samples. Three weight percentages of STAM-17-OEt@BPL were produced, with 77%, 51% and 39% w/w MOF loading and henceforth named STAM-17-OEt@BPL_1, STAM-17-OEt@BPL_2 and STAM-17-OEt@BPL_3 respectively. The percentage loadings are based on the assumption of a 100% yield of STAM-17-OEt: under this condition, the percentage 77% indicates, for example, that each gram of carbon has 0.77 g of MOF added.

FIGURE 3.10: Main steps of the synthesis of the STAM-17-OEt@BPL composite materials.

The three different samples have been realized by varying the relative quantities of MOF precursors. For example, STAM-17-OEt@BPL_1 was prepared by suspending BPL activated carbon (244 mg, 20.32 mmol) and 5-ethoxy isophthalic acid (125 mg,

0.60 mmol) in distilled water (10 mL), before stirring at 318 K for 2 hours. At this point, also copper acetate monohydrate (119 mg, 0.60 mmol) was added and stirring at 318 K for a further 2 hours. Afterwards, the temperature was increased to 368 K and the mixture was stirred for a further 3 days. In order to remove eventual MOF grains synthesized outside the carbon matrix, the suspension was centrifuged at 6000 rpm for 10 minutes, and the solid was washed with distilled water (15 mL). The same centrifuging and washing cycle was repeated a further 3 times. At the end, the solid was left drying in air.

Similarly, the other two samples have been produced, using the same quantity of BPL carbon but appropriately changing the quantities of STAM-17-OEt precursors: 5-ethoxy isophthalic acid (83 mg and 68 mg respectively) and 1 equivalent of copper acetate monohydrate (79 mg and 65 mg respectively), resulting in composites with 51% and 39% STAM-17-OEt by weight.

Such a large granular form of STAM-17-OEt@BPL composites, made by incorporation of MOF into a granular matrix, provides a fundamental property for functional filtration materials, in contrast to typically unusable powdered MOF.

3.1.9 Further hydration methods applied on MOFs

A large part of the thesis has also been dedicated to the study of the effect of controlled hydration on MOFs. In particular, the data collected can be grouped in two main studies: the first involves the comparison of the three MOFs HKUST-1, STAM-1 and STAM-17-OEt in powder form, whereas the second concerns the sole HKUST-1 but in three differents forms, that is powder, tablet and monolith.

Hydration effects in comparison between HKUST-1, STAM-1 and STAM-17-OEt. Upon the synthesis of STAM-1 and STAM-17-OEt, the two MOFs were activated as described in section 3.1.5. The obtained dehydrated samples of STAM-1 and STAM-17-OEt and the pristine HKUST-1 samples are hereafter termed as "*Activated*". Activated samples of about 150 mg per each MOF were exposed to about 100% RH at room temperature for 60 days. During this period, the samples were monitored using several experimental techniques. After the 60 days of exposure, the materials were reactivated at T = 420 K overnight.

Hydration effects in comparison between three different HKUST-1 forms: powder, tablet and monolith. In the same way we have hydrated the three MOFs in powder form, we have undergone hydration by exposure to about 100% RH a B-40 MPa tablet of HKUST-1 (see section 3.1.6) and a monolith, for a maximum of 24 hours. The samples have been studied by EPR spectroscopy.

Figure 3.11 shows a set of photographic images which highlight the effects of hydration during the 24 hours of exposure of the three samples.
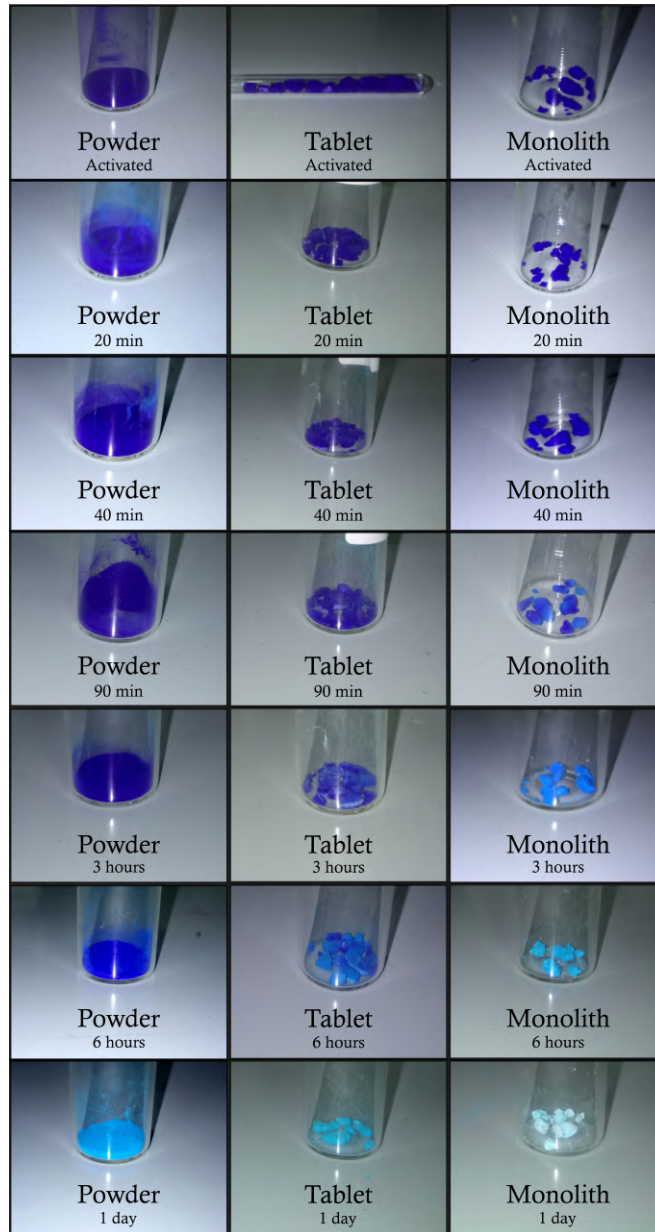
FIGURE 3.11: Composition of photographic images showing the effects of different times of exposure to moisture in condition of ∼100% RH for three different samples of HKUST-1: powder, B-40 MPa tablet, monolith.

Treatments with ammonia

In order to study the interaction between the MOF STAM-17-OEt and ammonia, we prepared water solutions containing ammonia in different percentages. Starting from a stock solution with ∼30% (w/w) of ammonia and then density of ∼0.88 g/cm^3, we diluted it adding determined amount of distilled water until we reached the desired dilution. Considered that the weight/weight concentration is given by

$$\frac{Weight}{Weight}\% = \frac{Weight_{solute}}{Weight_{solution}} \times 100 = \frac{Weight_{solute}}{Weight_{solute} + Weight_{solvent}}, \qquad (3.1)$$

and estimating that 10 ml of our initial 30% solution have a weight of 8.8 g and then $8.8 \cdot 0.30 = 2.6$ g of solute, we have estimated the amount of solvent (distilled water) to add for the obtaining of each desired dilution.

The concentration of the diluted solution obtained have been: 0.1%, 0.2%, 0.5%, 2.5%. We have also treated one sample with the stock solution (30%) and another one with simple distilled water (named "0%" for simplicity).

Directly inside an EPR glass tube, about 40 mg of STAM-17-OEt powder was firstly hydrated suspended it in pure distilled water, mixed for few minutes, and then dried by a glass desiccator for about 1 hour. This initial step was made in order to verify the stability of the MOF to the liquid water.

Subsequently, except for the 0% sample, we treated again each sample with about 30 µl of ammonia solution. The amount of solution added was chosen in order to completely cover with the liquid the powder content inside the narrow EPR tube. After a further drying treatment via desiccator, the samples were ready to be characterized.

3.2 Instrumental setup

The following subsections provide a short description of the experimental equipment used for the acquisition of the measurements reported in this thesis. For each of the method described in chapter 1, we portray a more or less fine description on the fundamental functioning of each instrument and the main details about the measuring condition employed for the acquisition of the data. A particular attention is reserved to the EPR setup, described below.

3.2.1 EPR spectrometer

EPR measurements have been acquired by a Bruker EMX micro spectrometer. The block scheme of the instrument is shown in fig. 3.12(a).

The oscillating magnetic field with amplitude previously called B_1 is emitted by a Gunn diode constituted by a GaAs junction. It falls in microwave range, at about ~ 9.6 GHz (commonly called X band). The radiation power sent to the sample, which reaches a maximum of 200 mW, can be regulated by the operator via a variable attenuator. The attenuation induced is typically measured in decibel (dB).

The attenuated radiation is driven by a *circulator* device through a wave-guide towards the sample, typically placed at the center of a rectangular-shaped *resonant cavity*. This latter, positioned between the electromagnets, is characterized by high conductibility side walls (usually covered by silver and gold) and is able to store the microwave energy. At the center of this small *box*, its normal modes ensure a minimum of the electric field and a maximum of the magnetic field: this allows the observation of a magnetic dipole transition avoiding those of electric dipolar nature. The entering of the radiation within the cavity is allowed by a mobile *iris* (see fig. 3.12(b)), a component of dieletric material with the role to optimize the coupling between the impedance of both the wave-guide and the cavity.
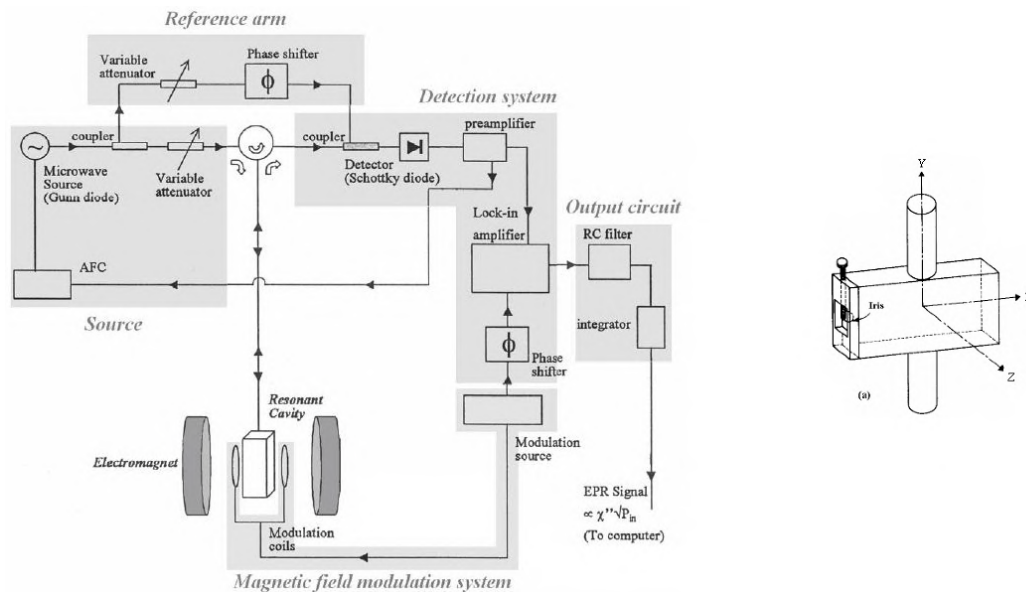
FIGURE 3.12: a)Block diagram of the Bruker EMX micro spectrometer: b) schematic illustration of the resonant cavity. Adapted from ref. [186].

The two electromagnets placed at the sides of the resonant cavity are equipped with coils, responsible of the static magnetic field previously indicated with **B**. It can reach a maximum magnitude of 1 T, with a homogeneity of $\sim 10^{-3}$ on a $\Delta X \cdot \Delta Y \cdot \Delta Z = 5 \cdot 22 \cdot 10$ mm^3. The absolute magnitude B values, which are reported in the x-axis of the EPR spectra, is given by an Hall probe, ensuring an accuracy of $8 \cdot 10^{-2}$ mT; however, the *relative* B values (or else, the B *differences*) are measured with a precision of $\sim 8 \cdot 10^{-4}$ mT.

As already mentioned in section 1.2, the introduction of a *modulation field B_m* is necessary to enhance the signal-to-noise ratio. This additive magnetic field parallel to **B** and produced by two coils merged in the walls of the cavity, has modifiable frequency ($5 \div 100$ kHz) and intensity (order of magnitude of $\sim 10^{-4}$ T). As a consequence of the introduction of the modulation field, the static magnetic field **B** will oscillate between B-B$_m$ and B+B$_m$ and will produce a modulated absorption intensity, oscillating at the same frequency of B_1 and in phase with it. The amplitude of B_1 should be varied in order to have an approximately linear absorption profile in correspondence of the range B-B$_m$ $\div$ B+B$_m$.

The detector which analyzes the output signal of the resonance cavity is a *Schottky diode*, constituted by a tungsten-silicon (metal-semiconductor) junction. Through the use of the *reference arm*, connecting the radiation source with the diode, this latter generates a current signal, I, proportional to the square root $\sqrt{P}$ of the incident power. The output signal produced by detector is modulated as B_1 and with an amplitude proportional to the difference in intensity I(B-B$_m$)-I(B+B$_m$).

This signal is then measured by the *lock-in amplifier* and its amplitude at the frequency of the modulation field represents the detected EPR signal. Noise components are further reduced by the *output circuit*, which consists of a RC low-pass filter and an

integrator: the former has a T_{RC} response time (properly chosen by the operator) and attenuates the signal components with frequency greater than $1/T_{RC}$, whereas the latter integrates the detected signal for a T_{conv} time. At a first approximation, the during of a single measurement is given the product of the number of point constituting the spectrum (1024 in our case) and T_{conv}.

In proximity of the resonance magnetic field B_r, the resonance frequency of the cavity shifts because of a change in the impedance of the system involving cavity and sample. In order to still match the resonance frequency of the cavity at all B values (that changes linearly in time) during the spectrum acquisition, an *automatic frequency control (AFC)* system introduces an amplitude modulation at 76.8 kHz on the microwave radiation and a correction of the phase. This modulated signal is superimposed with the microwave signal arising from the cavity: if the resonant frequency matches that of the diode, the total signal results not modulated at 76.8 kHz. Alternatively, if the two frequencies are different, an error is produced and by a change of the voltage applied to the Gunn diode the matching can be reestablished.

Experimental conditions

The spectra shown in this thesis have been acquired changing the intensity of the static field **B** from 0 to 800 mT and by using a modulation field with intensity equal to 1 mT and 100 kHz frequency. The times T_{RC} and T_{conv} have been maintained fixed at 328 and 164 ms, respectively. The gain of the receiver have been changed depending on the intensity of the measured signal at the chosen power value.

Because of the possible saturation effects described in section 1.2.1, the appropriate microwave power value needs to be chosen with particular care. A valid attenuation value for the given system can be found by verifying if the obtained EPR signal increases linearly with the square root of the microwave power applied (*linearity range*). This procedure of acquisition of the EPR signal as a function of the microwave power is defined as the acquisition of the *saturation curve*. All the microwave power values used during the experiments reported in this thesis lie in the linearity range of the correspondent sample. Generally, it has been used the highest power value of such range.

However, in order to be able to make meaningful quantitative comparisons, all the spectra shown in the following chapters were standardized for the different experimental parameters and for their mass. All of the samples were generally investigated by acquiring spectra at two different temperatures, 77 and 300 K.

The sample-holders used for the measurements involve *quartz (CFQ) EPR tubes* and a *dewar flask*. The latter is a double-walls glass container which allows to perform the measurements at low temperatures, by minimizing heat transfers between inside and outside. In the case of measurements performed at 77 K, the dewar flask is filled with liquid N_2 and the sample inside reaches the thermal equilibrium with the liquid nitrogen by direct conduction trough the EPR glass tube walls. In contrast, for the measurements performed at room temperature, the dewar flask contains simply air (besides the sample and the EPR glass tube).

The reproducibility of the EPR measurements is guaranteed with a typical error of $\pm 5 \div 10\%$ of the registered intensity, mainly arising from uncertainty over the position of the sample inside the resonant cavity.

Spectral simulations of EPR spectra were carried out using the EasySpin ESR simulation package.[187]

Spin concentration

In order to estimate the concentration of paramagnetic centers responsible of a given resonance, the area under the specific absorption EPR line must first be calculated via a double integral calculation. An estimation of the concentration was done by comparing the obtained double integral with that of a reference sample, whose spin concentration was determined by the spin echo technique, with an absolute accuracy of 20%.[188] The calculation involves the following equivalence:

$$Spin\,Concentration = K \times normalized\,area \qquad (3.2)$$

in unity of spin/cm^3, where the dimensionless K factor depends on the temperature (5.95×10^{10} and 1.49×10^{10} for measurements performed at 300 and 77 K, respectively).[188] The area under the absorption curve must be normalized by square root of the incident power, the receiver gain, the amplitude of the modulation field, the integration time and the sample weight.[188]

3.2.2 NMR spectrometer

For NMR spectroscopy, solid-state ^{13}C magic angle spinning (MAS) NMR spectra were recorded using a Bruker Avance III spectrometer. A simplified scheme of the instrument is shown in figure 3.13. The magnet generates the magnetic field **B** required to induce
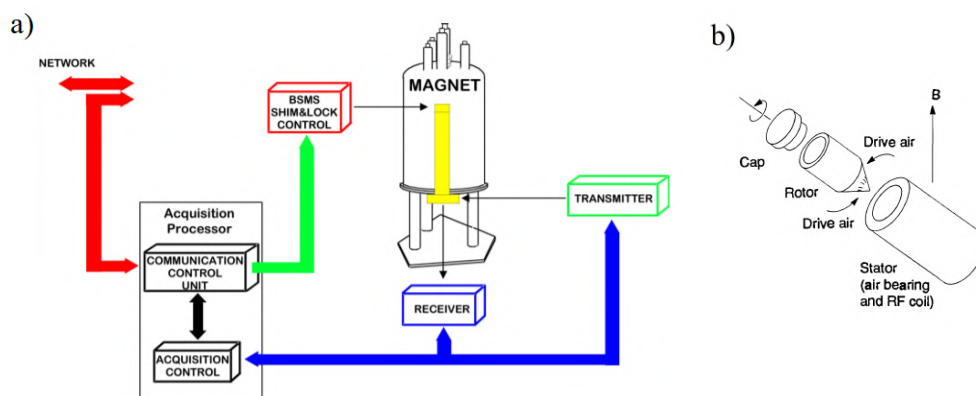
FIGURE 3.13: (a) Simplified architecture overview of a generic Bruker Avance spectrometer and (b) components of a magic angle spinner.[41,189]

NMR transitions. The *magnet core* is composed of a large coil of current which carries wire shaping a solenoid. At the center of this coil there is a very intense static magnetic

field where the sample to be analyzed is placed. A so-called *shim system* (a particular type of current coils) is used to maximize the homogeneity of the magnetic field. In order to maintain a superconducting system, the magnet core is cooled to low temperatures using liquid nitrogen or even helium. Bruker Avance III spectrometer, is equipped with three different B field strengths, 9.4, 14.1 and 20.0 T.

Clearly, the strength of the magnet is selected according to the frequency of the NMR signals arising from hydrogen atoms, because they are strongly connected physical quantities (see section 1.3). As a result, the stronger the magnet field, the higher the hydrogen frequency: a 500 MHz magnet, which corresponds to a strength equal to 11.7 T, deals with chemical samples that, placed in the magnet for analysis, has ^{1}H NMR signals at a frequency very close to 500 MHz.

A *lock system* ensures that the magnetic field surrounding the sample is not modulated by external disturbances and does not vary during all the measurement.

A high performance preamplifier (HPRR) situated at the basis of the magnet is responsible for the magnifying of both the input and output signals of the sample, typically very weak, minimizing the losses along the cables.

The sample is inserted into a *magic angle spinner*, ensuring a rotation along an axis of $\sim 54.74°$ in relation to the magnetic field.

To carry out the solid-state ^{13}C MAS NMR measurements which led to the results shown in this thesis, the samples were packed into standard zirconia rotors with an outer diameter of 1.9 mm. The spinning speed was fixed at a MAS rate of 37.5 kHz, in order to make negligible the splitting of the lineshape into a series of spinning sidebands, which may arise from the incomplete averaging. A magnetic field B with value of 14.1 T was used, with a Larmor frequency of 150.9 MHz. Spectra were recorded with a rotor-synchronized spin-echo pulse sequence with an echo delay of one rotor period (26.7 μs). Signal averaging was carried out for between 24,576 and 106,496 transients with a recycle interval of 0.1 s. Chemical shifts are reported in ppm relative to $Si(CH_3)_4$, using L-alanine as a secondary solid reference ($\delta(CH_3) = 20.5$ ppm).

3.2.3 Raman spectrometer

Raman measurements were performed by two different instruments. Despite this, both share the main technical elements.

Most of the Raman spectra were acquired by a μ-Raman Bruker SENTERRA. It combines the Raman spectrometer with a confocal microscope, which allows to resolve in a microscopic scale the sample zone involved in the measurement. Figure 3.14 shows the block diagram of the Raman spectrometer.

The microscope uses an incandescent lamp and two objectives: a "20×" working at a distance of 1.3 mm and a "50×" working at 0.38 mm. The acquisition of digital images is possible because of a trinocular microscope coupled with a video camera.

For the Raman measurements a laser emitting at 532 nm (visible range) is employed, with a power that can range from 0.2 to 20 mW. The power can be regulated by a
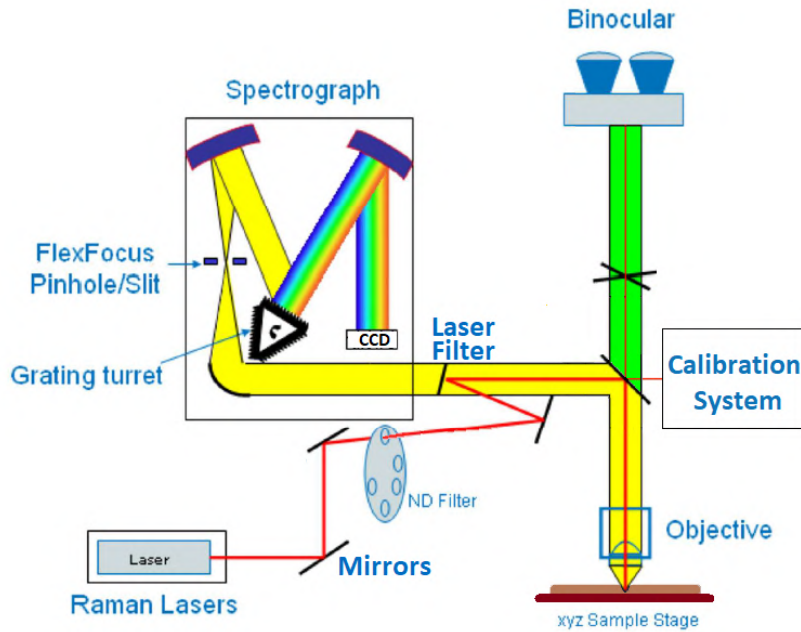
FIGURE 3.14: Block diagram of the µ-Raman spectrometer Bruker SENTERRA. Adapted from ref. [190].

sequence of neutral density filters (ND filter), which attenuate the radiation incident on the sample.

The radiation that scatters from the sample is acquired in the opposite direction and collected by the same objective but it arrives to the spectrograph only after some steps. Firstly, it passes across a system of mirrors and a notch filter, which reduces the Rayleigh component of the radiation but leaves unvaried the intensity of light with a Stokes-shift that exceeds $\sim$50 cm^{-1}. Then, a pinhole/slit allows the spatial selection of the collected radiation using, for measurements in *non-confocal mode*, slits with two possible openings (25×1000 µm^2 and 50×1000 µm^2) and, for the confocal mode, pinholes with two different diameters (25 and 50 µm), enhancing the vertical and lateral space resolutions. At this point, the radiation is dispersed by an instrument grating, which can be selected by the operator on the basis of the desired resolution and the spectral range, between one at 400 lines/mm and the other at 1200 lines/mm. For the high resolution of 3÷5 cm^{-1} the spectra can space the range $53 \div 3700$ cm^{-1}, whereas for the low resolution of 9÷15 cm^{-1} the investigated range is $50 \div 4478$ cm^{-1}.

The Raman spectrum is finally recorded when the radiation is detected by the CCD system, constituted by a matrix of 1024×256 pixels and thermoelectrically cooled down to 218 K. The operator can select the values of the integration time (exposure time to radiation) and co-addition (number of repetitions).

During the measurement, the sample lies on a mobile support equipped by a motorized device operable by software. Once it has been optically focused via software, the position reached coincides with that optimized for the Raman acquisition.

In order to acquire Raman measurements on the samples involved in this thesis, a

nominal laser power of 0.2 mW has been used, with the aim of avoiding sample modification, with an integration time of 30 s for each spectrum and 10 co-additions. The objective used was the "50×", with a aperture of 50×1000 µm^2. In order to eliminate luminescence effects, a broken-line baseline has been subtracted to each spectrum. During the measurements, the samples were kept in air on a laboratory slide.

Additional in-situ µ-Raman measurements were performed by a Horiba LabRam HR-Evolution spectrometer (CHAB laboratories at ATeN center, University of Palermo), equipped with a 532 nm excitation laser with a nominal laser power attenuated up to 0.1 mW (measured before the microscope lens). As above mentioned, the functioning is fully equivalent to that shown in figure 3.14. The resolution is 6 cm^{-1}. The instrumentation allows to put the sample within a high-pressure Linkam THMS600PS cell at 420 K, with a heating ramp of 100K/min, in atmospheric pressure. This cell has been used to acquire Raman spectra of a sample in a condition close to the post-activation.

The Raman spectra showed in the following chapters have been acquired by using the µ-Raman Bruker SENTERRA instrument, except where specifically indicated.

3.2.4 PXRD instrumentation

There are two main instrumental techniques used for the acquisition of the PXRD pattern of a given sample: that based on the usage of disks (figure 3.15(a)) and that based on the glass capillaries (figure 3.15(b)). The former requires the filling of a silicon crystal
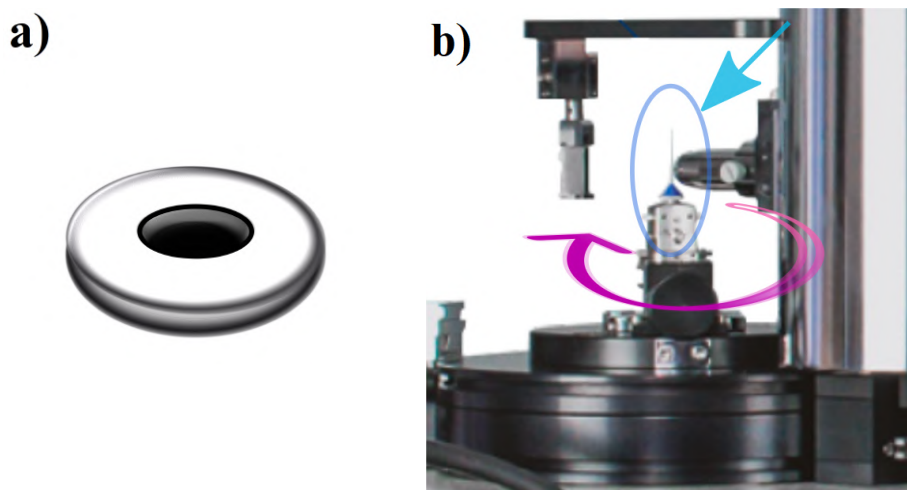
FIGURE 3.15: a) Stylized picture of a typical PXRD (empty) sample holder disk. b) Photografic image of a glass capillary mounted on the spinning component of a STOE STADI P primary beam monochromator diffractometer (adapted from ref. [191]).

sample holder, ensuring a very smooth and leveled surface of the powdered sample. The latter involves the loading of the powder within a very sharp glass capillary with typical diameters of 0.5 mm, which can be easily sealed by a blowtorch or a simple lighter. This

makes possible the measurement of activated MOF samples (see section 3.1.5).

The patterns shown in this thesis were acquired by using both these techniques, depending on the needs.

For the experiment about the comparison on the hydration effects on HKUST-1, STAM-1 and STAM-17-OEt kept in high humidity conditions, PXRD patterns were collected at room temperature on a STOE STADI P primary beam monochromator diffractometer using a copper anode, Cu K1, which produced monochromated X-rays at 1.5406 Å. The samples were contained in glass capillaries having 0.5 mm diameter. For the *activated* MOF samples, the MOF powders were inserted within the capillary glasses, subject to an overnight activation process and then sealed by the usage of a lighter(see section 3.1.5).

At the same way, the PXRD patters of the *as made* monolithic HKUST-1 were collected.

The cristallinity of HKUST-1 tablets (and relative powder sample used for comparison) was studied using a PANalytical X'Pert PRO high-resolution diffractomer with Cu Kα1 radiation (λ= 1.5406 Å) in the range from 5 to 60° 2 ϑ using step of 0.016° per 100 s at fully opened X'Celerator detector. The powdered samples were loaded into disks of 3 mm depth. Unit cell parameters fit was performed using Topas Academic v.6 software package (A. Coelho, Coelho Software, Brisbane, Australia, 2016).

For the STAM-17-OEt tablets, the PXRD diffraction patterns were collected using a PANalytical Empyrean with Cu X-ray tube and primary beam monochromator 90 (CuKα1). Measurements were performed at room temperature (about 300 K). The powdered samples were loaded into disks of 3 mm depth.

Similarly, diffraction patterns of the composite STAM-17-OEt samples were collected. Measurements were performed at room temperature without any activation prior to recording.

3.2.5   Adsorption instrumentation

Nitrogen isotherms

The BET surface area of the samples studied in this thesis have been estimated via acquisition of nitrogen adsorption isotherms. For most of them a Micromeritics ASAP 2020 surface area and porosity analyzer has been used. Figure 3.16 shows this instrument and its main components.

Two independent programmable degassing systems allow the simultaneous preparation of two samples, with accurately controlled heating profiles. The degassing temperature can be changed via 1 K increments from room temperature to 723 K.

It is also provided of a 3-Liter dewar for the storing of liquid nitrogen at 77 K, allowing up to 72 hours of unattended measurements. The pressure range covered can go from 0 to 950 mmHg, with a resolution of 0.1 mmHg.

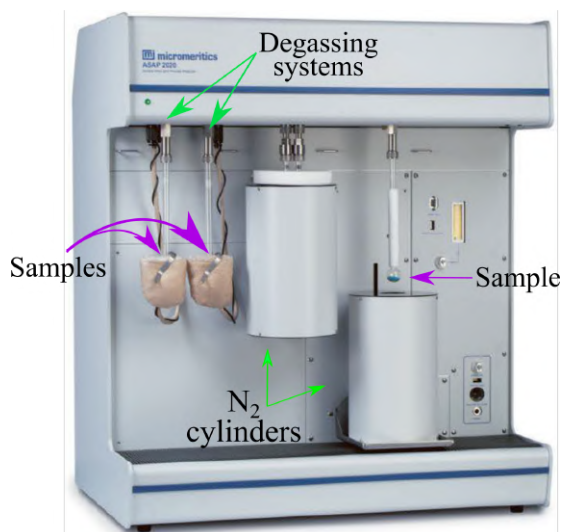It can investigate a pore size range from 3.5 to 5000 Å.

FIGURE 3.16: Photographic image of a ASAP 2020 instrument employed for the BET area determination. The main parts are labeled and indicated by the arrows.[192]

Nitrogen BET analysis for the samples whose results are shown in chapters 4, 6 and 8 has been performed by this instrument. BET surface areas have been calculated using the Rouquerol method. About 120 mg of powder for each sample has been activated at 420 K overnight prior to measurement.

For the samples whose results are shown in 5, the BET specific surface determination was based on a N_2 isothermal measurements performed with a IMI-HTP manometric sorption analyzer (Hiden Isochema, Inc.). Also in this case, before the measurements, the samples were outgassed at 420 K overnight. In the case of MOF tablets, they were measured as-prepared, without any grinding.

Water isotherms

Water sorption isotherms were measured using an IGA-100 gravimetric analyser (Hiden Isochema Ltd) at 25 °C in the relative pressure vapour range from 0.002 to 0.90. Before the measurements, samples were degassed at 150 °C for 12 hours.

Breakthrough curves

Ammonia micro-breakthrough testing is performed using a micro-breakthrough apparatus. The set-up allows the testing of porous materials against known concentrations of challenge gases. Samples of ∼20 mg are placed on a metal frit inside a sample chamber and ammonia gas at a concentration of 450 ppm is passed through the sample at a flow rate of 55 mL/min. The effluent concentration is monitored using a photoionization detector (Phocheck Tiger). All experiments are performed at 298 K.

3.2.6   AFM microscope

A schematic experimental setup for the AM-AFM detection is shown in figure 3.17.
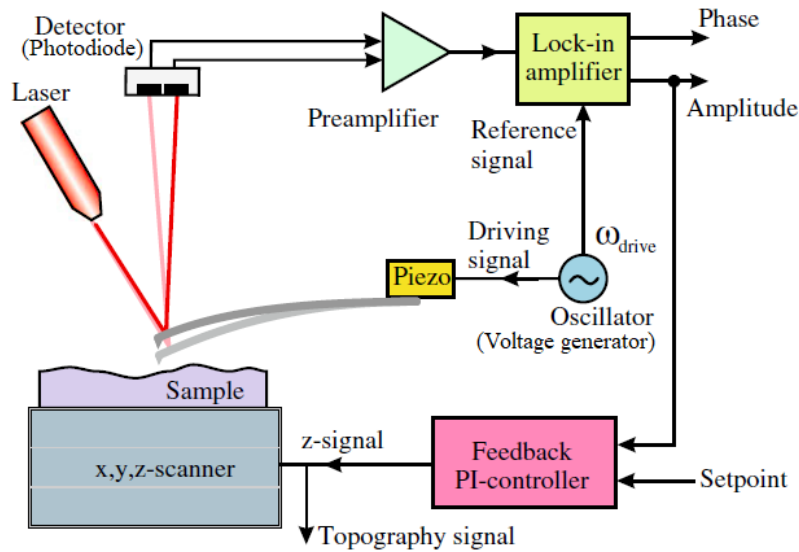
FIGURE 3.17: Block diagram of a typical atomic force microscope for amplitude modulation measurements. Adapted from ref. [64].

A sinusoidal driving signal at a given frequency ω_{drive} is generated by an oscillator. Such signal excites the piezoelectric, driving so the base of the cantilever, which results in turn in a cantilever oscillation with amplitude A. When the tip approaches the sample because of a z-movement of the cantilever, the oscillation amplitude changes as a result of the tip-sample interaction.

Suppose that at a certain tip-sample gap d1, the setpoint amplitude is A1. Moving along the xy plane, depending on the morphology of the sample surface, this gap will change. Suppose also for example that the gap decreases, from d1 to d2: the consequence is a deviation of the oscillation amplitude from A1 to another called A2. The amplitude is checked by measuring the cantilever deflection as a function of time, by evaluating the beam deflection in a photodiode. The signal from the photodiode is then converted by the electronics to a voltage signal proportional to the cantilever deflection. This voltage signal oscillates at the frequency ω_{drive} and has an amplitude proportional to that of the cantilever. At this point, the lock-in amplifier measures the amplitude of the signal at frequency ω_{drive} and produce as output a quasi-DC signal containing the information of the amplitude deviation, that arrives as input signal to the feedback system.

This latter is a z-feedback controller which, after the elaboration of the input signal, is able to determine the appropriate z-movement/signal necessary to keep constant the oscillation amplitude. Maintaining a constant oscillation amplitude corresponds, at a first approximation, to maintain a constant tip-sample distance; therefore we can say that the feedback controller compensates the amplitude changes adapting the z-signal to a value equivalent to the step height. The oscillation amplitude A1 is recovered until the subsequent change in tip-sample distance.

The lock-in amplifier is also tasked with providing a phase signal, measuring the differences between that of the driving signal and that of the cantilever oscillation. In contrast to the amplitude, the phase signal is a *free signal*, which is not used for the

feedback, but it contains useful information on the tip-sample interaction, as mentioned in section 1.7.

For the AM-AFM imaging a Bruker FastScan Bio Microscope was used. It allows to acquire high-quality images in tapping mode, achieved with variable scan rates. It is provided of a 5 MP digital camera which can cover a viewing area from 130 to 1040 µm. Different AFM modes can be used. The vertical noise is maintained below 40 pm for fast scanning on scales from sub-nanometer to hundreds of nanometers in height, without loss of resolution. It can reach tip-velocity of 2 mm/s with 1% of tracking error on the x-y plane and 12 mm/s along the z direction.

The AFM images shown in this thesis have been acquired by working in soft tapping mode and using a FAST-SCAN-A probe, consisting in a 27 µm long triangular Silicon Nitride cantilever with silicon apical tip and with the following characteristics: 1400 kHz resonant frequency, 17 N/m force constant and about 5 nm apical radius.

The size of the AFM images in chapter 5 is 10 µm $\times$ 10 µm or 15 µm $\times$ 15 µm, depending on the local surface properties. Those of chapter 7 have a size of 3 µm $\times$ 3 mm or 3 µm $\times$ 1.5 µm.

3.2.7 Thermogravimetry measurements

Thermogravimetry measurements were performed by a Q5000 IR apparatus (TA Instruments).

The heart of the instrument is the high performance thermobalance, that is maintained at a constant temperature of 40.00 °C by a well-insulated chamber. The weights are measured with an accuracy of $\pm 0.1\%$ and a precision of $\pm 0.01\%$. The sensitivity is lower than 0.1 µg and the resolution is less than 0.01 µg.[193]

The samples are heated by an IR furnace composed of four symmetrically-placed IR lamps and a silicon carbide IR-absorbent enclosure, which ensures uniform heating of both the pan and the sample. The temperature range can go from room temperature to 1470 K, with an accuracy close to 1 K. The linear heating rate can range from 0.1 to 500 K/min. The precise temperature control is provided by thermocouples.[193]

A purge gas system allows the gas to flow directly across the sample. The pressure can be lowered up to 10^{-2} Torr.[193]

The measurements were performed under the nitrogen flow of 25 cm_3/min for the sample and 10 cm_3/min for the balance. The weight of each sample was about 3 mg. The experiments were carried out by heating the sample from room temperature to 923 K with a rate of 10 K/min. The temperature calibration was carried out using the Curie temperatures of standards (nickel, cobalt, and their alloys).

Chapter 4

Hydration effects on HKUST-1, STAM-1, STAM-17-OEt

The structural instability in humid environment of the majority of metal organic frameworks (MOFs) is a challenging obstacle for their industrial scale development. For this reason the starting point of this thesis for all the subsequent experiments about MOF densification is a systematic study of the hydration effects of the given materials. In particular, in this chapter a detailed investigation on the different effects of water exposure on the local and long-range structures of the three MOFs HKUST-1, STAM-1 and STAM-17-OEt is reported.

EPR spectroscopy allowed us to characterize in detail for the first time the different phases occurring during the hydration of each MOF. In particular, the moment of the adsorption of the first water molecule on each copper ion has been identified and portrayed. The effects of such soft hydration led to a similar reversible evolution in all of the three MOFs.

In contrast, when a higher degree of hydration was reached (more than few hours at 300 K and 100% RH), we observed the three MOFs embarked on different paths: the evolution of HKUST-1 was not reversible because of its well-known tendency to hydrolysis but, in contrast, we proved the reversibility of the water effects in STAM-1 and STAM-17-OEt even at atomic scale level.

The data also include XRD, NMR measurements and BET surface area calculations of all the samples and, for the first time, we also report on a Raman characterization of both STAM-1 and STAM-17-OEt, repeated for each phase of the hydration.

4.1 Results

In the following, we report on the results obtained by monitoring the three MOF samples with different techniques during 60 days of exposure to hydration in condition of 100% RH at room temperature.

4.1.1 Crystallographic characterization

Figures 4.1, 4.2 and 4.3 show the most significant PXRD patterns acquired for HKUST-1, STAM-17-OEt and STAM-1, respectively. The diffraction pattern of activated HKUST-
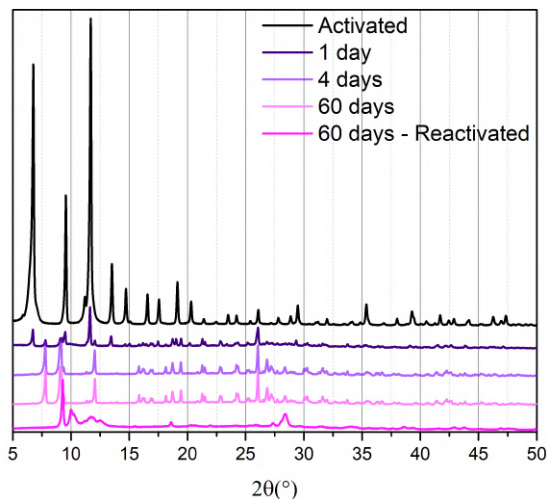
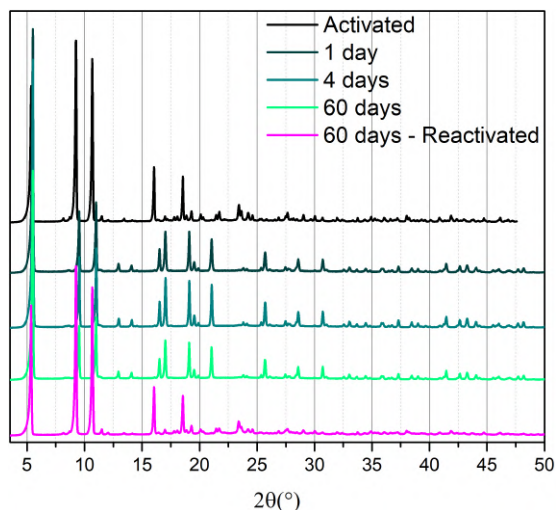FIGURE 4.1: PXRD patterns acquired for HKUST-1 during the 60 days of hydration.

FIGURE 4.2: PXRD patterns acquired for STAM-17-OEt during the 60 days of hydration.

1 (Figure 4.1, black line) shows the well-known characteristic peaks of this material (see figure 2.13).[140–142,156–158] The pattern acquired after only 1 day of exposure to humidity shows a drastic decrease of the intensity of the peaks and the appearance of several small new peaks. For longer exposure times the pattern changes completely, indicating the formation of a new phase. The reactivation treatment after 60 days does not recover the pristine structure and the PXRD pattern remains completely different from the original activated material (acquired before the exposure). The PXRD pattern of the activated STAM-17-OEt and its change upon hydration (Figure 4.2) have already been studied.[83] As explained in section 2.5, STAM-17-OEt is hemilabile, meaning it reversibly changes the lattice configuration during the hydration or dehydration processes.[83] Figure 4.2 shows that the pattern changes significantly after one day of hydration, but then does not change more upon further hydration, maintaining its properties. Figure 4.4 shows the PXRD patterns of a sample of STAM-17-OEt activated and hydrated for 1.5 and 6 hours: the PXRD pattern of the sample hydrated for 1.5 hours clearly shows the peaks
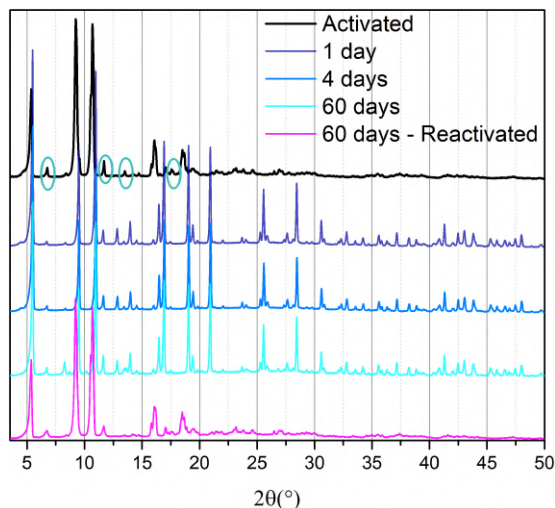
FIGURE 4.3: PXRD patterns acquired for STAM-1 during the 60 days of hydration. The peaks in the blue circles are those attributed to the presence of HKUST-1 in literature[82].

of both the activated and the hydrated material whereas, by 6 hours of exposure, the material is fully in the hydrated form. The necessary amount of water (or also, the time
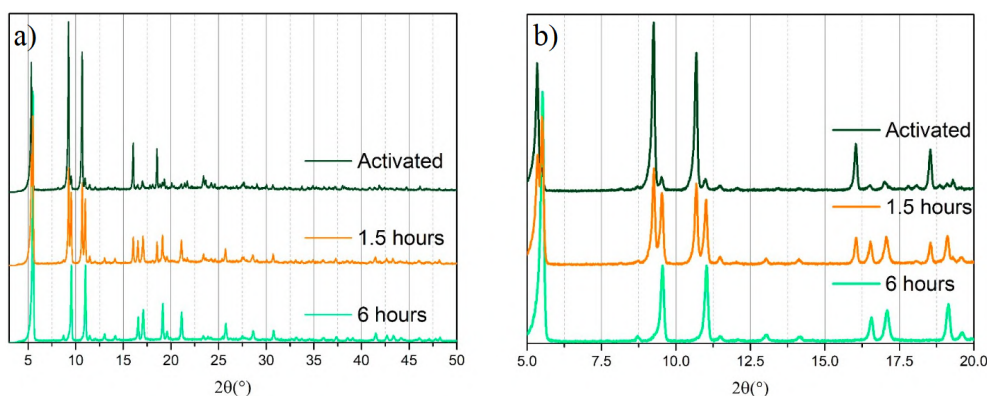
FIGURE 4.4: (a) Powder XRD patterns of STAM-17-OEt activated and after 1.5 and 6 hours of exposure. (b) Enlargements of the same patterns in the range 5÷20°.

of exposure) that drives the crystal to the transition is collected in the range of about 1.5 and 6 hours of exposure. The pattern obtained for the material after its reactivation (60 days-reactivated) is virtually indistinguishable from that of the initial activated material. This full recovery of the activated material after hydration is of fundamental importance because it proves that the changes due to the extensive hydration to which the sample has been exposed are completely reversible.

Figure 4.3 shows the PXRD pattern of the activated STAM-1 (black line). The small peaks highlighted with blue circles do not pertain to STAM-1 lattice.[82] In literature, their presence has been ascribed to a significant percentage of HKUST-1 impurities, which inevitably form owing to the equilibrium between BTC and monomethyl BTC present during the synthesis of STAM-1.[82] As for STAM-17-OEt, The PXRD pattern of STAM-1 changes after 1 day of hydration and then does not change again for the

rest of the 60 days exposure. Again, the structural changes are reversible and, after reactivation, the PXRD pattern matches that of the pristine activated STAM-1. The crystal transition after the first dehydration of the material has been already observed previously.[82] The peaks at about 6.5° and 11.5° attributed to HKUST-1 are still visible in the pattern of the reactivated STAM-1 sample. Very probably, they may concern small grains of HKUST-1 embedded in a hydrophobic environment in STAM-1 material.

4.1.2   EPR study

Comparison between the activated samples.   EPR spectra of activated HKUST-1, STAM-17-OEt and STAM-1 sample obtained at 77 and 300 K are reported in figure 4.5(a) and (b), respectively. We have already described in detail the resonances present
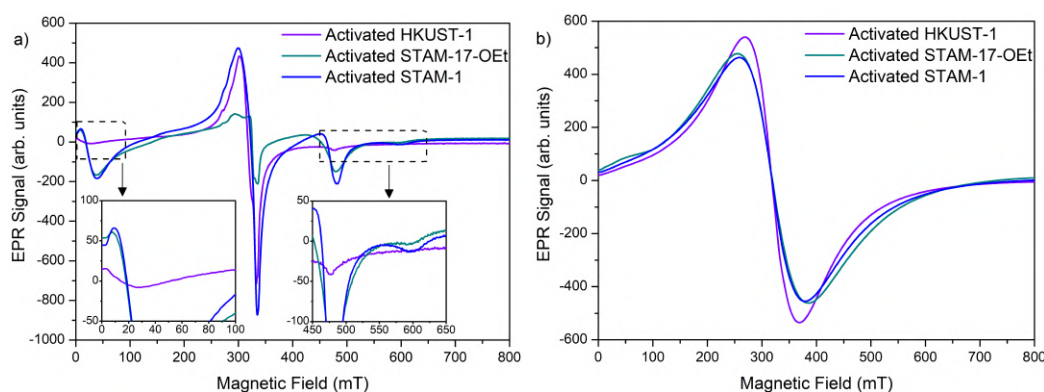
FIGURE 4.5: Comparison of the EPR spectra acquired at (a) 77 and (b) 300 K for HKUST-1 (violet), STAM-17-OEt (green) and STAM-1 (blue).

in the HKUST-1 spectra (see section 2.3.1). Briefly summarizing, the spectrum at 77 K is mainly characterized by three peaks, whose those at about 14 and 470 mT arise from the triplet state of isolated paddlewheel dimers, whereas the more intense resonance centered at about 350 mT is assigned to the extraframework monomeric complexes $[Cu(H_2O)_6]^{2+}$, defects formed during synthesis.[133,140] At 300 K only a large symmetric resonance is observed in the spectrum, assigned to the triplet centers.[133]

In section 2.4.1 also the EPR spectra of STAM-1 have been discussed. Both STAM-1 and STAM-17-OEt exhibit similar spectroscopic features at the two temperatures. In particular, at 77 K the peaks ascribed to the triplet component are more intense for STAM-1 and STAM-17-OEt than for HKUST-1, and an additional fourth small peak ascribed to the triplet centers is detectable at about 600 mT. At 300 K the resonances observed for both the STAM materials are centered at the same field but slightly wider than that of HKUST-1, with a peak-to-peak width of about 127 mT. These small differences can be attributed to the slightly more dilute network of dimers within STAM-1 and STAM-17-OEt, which reduces the inter-dimer exchange coupling interactions.[133]

Evolution with time at 100% RH.   The EPR spectra acquired at 77 and 300 K for HKUST-1 exposed to 100% RH for different time are reported in figure 4.6. For the sake of clarity, only the most representative spectra are reported and some of them

have been vertically scaled as indicated in the legends. In line with the work of Todaro
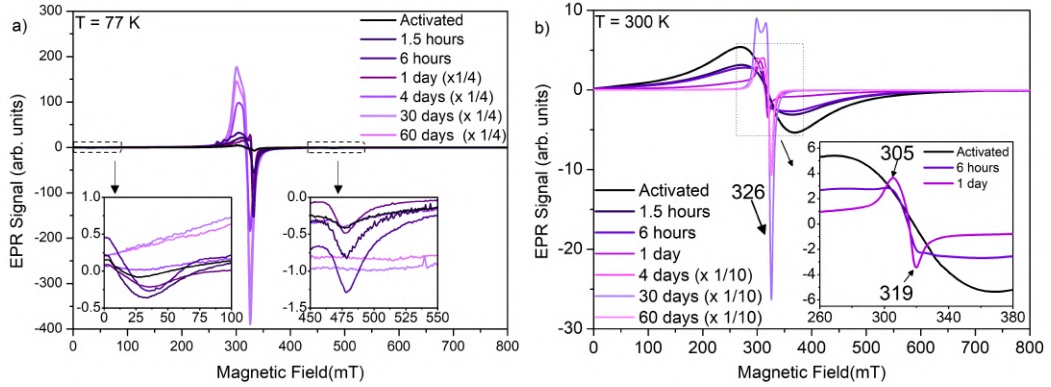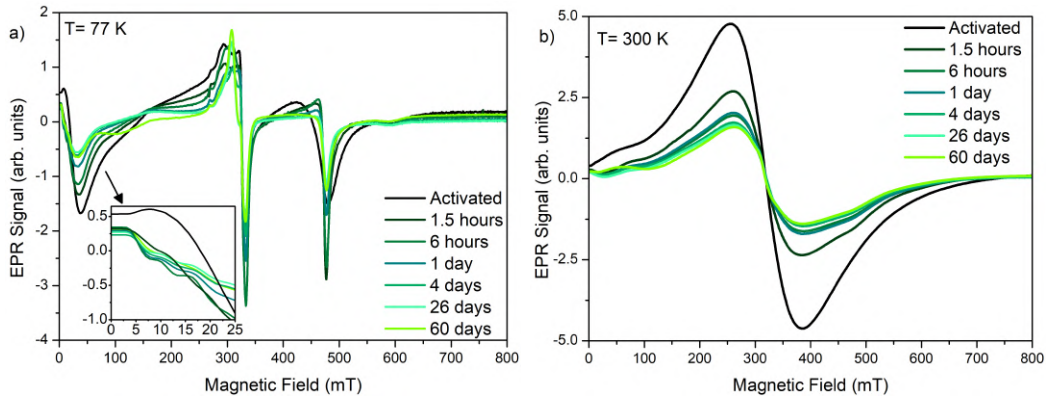

FIGURE 4.6: EPR spectra obtained for HKUST-1 acquired at (a) 77 and (b) 300 K after exposure to humidity for the indicated times.

and co-authors[140], at 300 K after few hours of hydration only a reduction down to 60% of the intensity of the EPR signal is observed, whereas the spectra acquired at 77 K show a small increase in intensity of the central peak. After 6 hours of exposure, a new signal is observed at about 320 mT at both temperatures. This effect, observed also by Todaro and co-authors[140], was ascribed to paramagnetic centers originating from the hydrolysis of a fraction of the Cu paddlewheels within the network (see section 2.3.2). From the 4th day on, we have continued to observe further significant changes of the line shape and increase in intensity of the EPR signals at both the temperatures.

The EPR spectra obtained at 77 and 300 K for the STAM-17-OEt sample exposed to 100% RH for different time are reported in figure 4.7(a) and (b), respectively. The
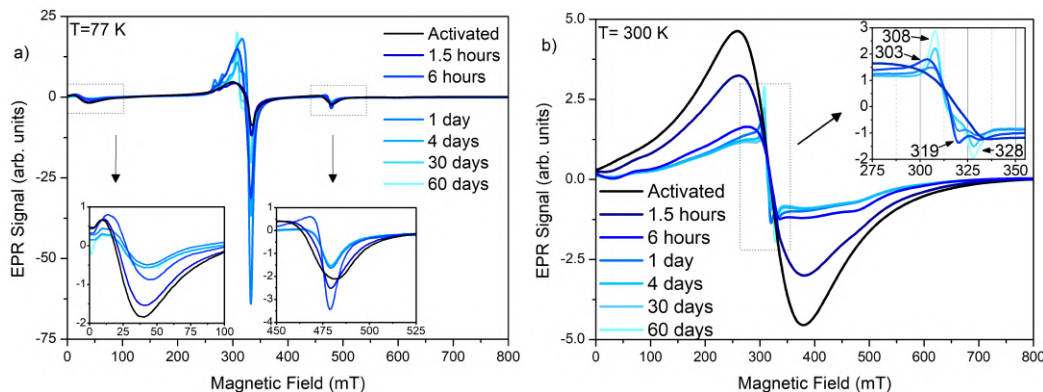

FIGURE 4.7: EPR spectra obtained for STAM-17-OEt acquired at (a) 77 and (b) 300 K after exposure to humidity for the indicated times.

spectra acquired at 300 K point out that, similar to HKUST-1, the intensity of the signal decreases of about 60% during the first 6 hours of exposure. However, the appearance of two small shoulders at about 50 and 480 mT is also observed. For exposure times longer than 6 hours, no other significant change takes place. In fact, both the intensity and the line shape of the resonance remain almost the same until the end of the 60 days of observation. Concerning the spectra acquired at 77 K, during the first few hours of

exposure, the main change observed is the narrowing of the peak at 480 mT. It is also noteworthy the progressive shift of the peak at 20 mT to lower fields, accompanied by the appearance of a fine structure (see the expansion in figure 4.7(a)). For exposure times longer than 6 hours, the signal of the triplet centers reduces slightly in intensity and there are small chenges to the line shape of the central peak.

The EPR spectra obtained at 77 and 300 K for the STAM-1 sample exposed to 100% RH for different time are reported in Figure 4.8(a) and (b), respectively. Concerning

FIGURE 4.8: EPR spectra obtained for STAM-1 acquired at (a) 77 and (b) 300 K after exposure to humidity for the indicated times.

the measurements obtained at 300 K, a decrease in the intensity of the signal and the appearance of two small shoulders at about 50 and 480 mT are again observed during the first hours of exposure to 100% RH, similar to those of STAM-17-OEt. After 6 hours, a new narrow peak is superimposed to the main line and increases its amplitude progressively. This component is similar to that observed for HKUST-1. As seen in the insert in figure 4.8(b), this new peak becomes more structured with prolonged hydration, with two clearly resolved negative peaks at 319 and 328 mT. Looking at the spectra acquired at T=77 K, we can note that within the first hours of hydration the peak at 480 mT narrows and the peak at 20 mT shifts to higher fields. In the range from 6 hours to 1 day of exposure, the spectra show a reduction of the intensity of the triplet signal and the increase in the intensity of the central peak. The spectra acquired from day 1 to 60 show no significant changes in the triplet contributions to the EPR spectrum (20, 480 and 600 mT). In contrast, the signal detected at 350 mT has a slight evolution.

Reactivation of the hydrated samples.   After 60 days of exposure to 100% RH, the three samples have been reactivated. Figures 4.9(a) and (b) show the spectra of the activated, hydrated and reactivated HKUST-1 acquired at 77 and 300 K, respectively. As expected, at both temperatures the spectra of HKUST-1 do not recover their pristine features, but rather the spectra acquired after the reactivation are dominated by a sharp resonance at 320 mT. In figure 4.10, the spectra of the activated, hydrated and reactivated STAM-17-OEt acquired at 300 K are compared. With the same scheme, figure 4.11 shows those of STAM-1. After reactivation, the spectra acquired at 300 K
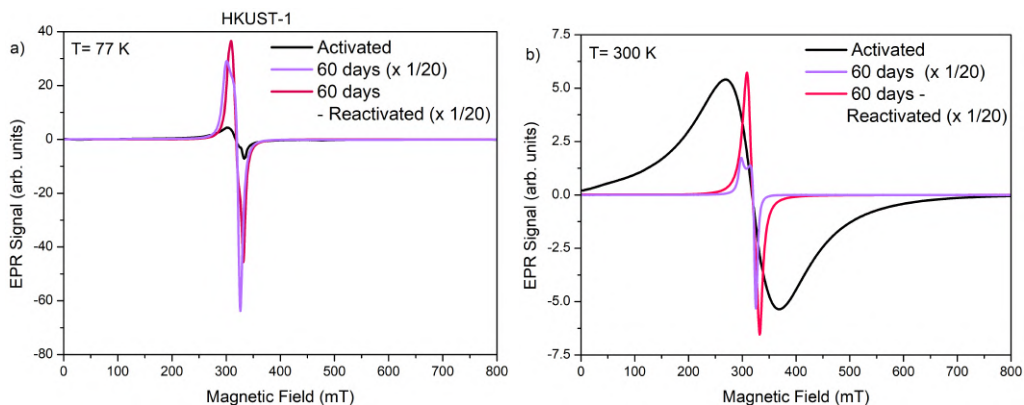
FIGURE 4.9: EPR spectra obtained for HKUST-1 acquired at 77 (a) and 300 K (b) before the starting of the exposure (black), after 60 days of exposure (clear violet) and after the subsequent reactivation (magenta).
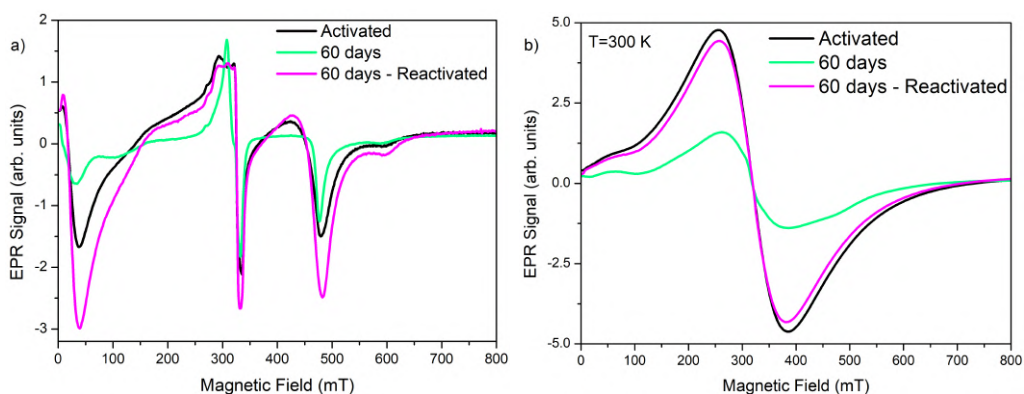

FIGURE 4.10: Comparison of the EPR spectra obtained STAM-17-OEt acquired at (a) 77 and (b) 300 K before the starting of the exposure (black) after 60 days of exposure (green) and after the subsequent reactivation (magenta).

for both the STAM materials recover the EPR signal of the activated material, with a comparable intensity and line shape, within the repeatability uncertainty of the EPR measurements. Even the spectrum acquired at 77 K of STAM-1 recovers its original properties. The spectrum of the reactivated STAM-17-OEt shows the peaks arising from the triplet centers with a slightly higher amplitude compared to that observed in the spectrum of the pristine material, but nevertheless the overall line shape is virtually indistinguishable.

4.1.3 Raman analysis

Figure 4.12 shows the Raman spectra of the three activated MOF, prior to exposure to 100% RH. However, since this part of the Raman measurements were carried out in air and each acquisition required several minutes, the reference samples used in the following graphs may be considered to correspond to materials that have been subjected to hydration for about 20 minutes.

The spectrum of HKUST-1 shows its characteristic peaks, which are well-established in literature and have been discussed in section 2.3.[84,144,145] The spectra of STAM-1 and
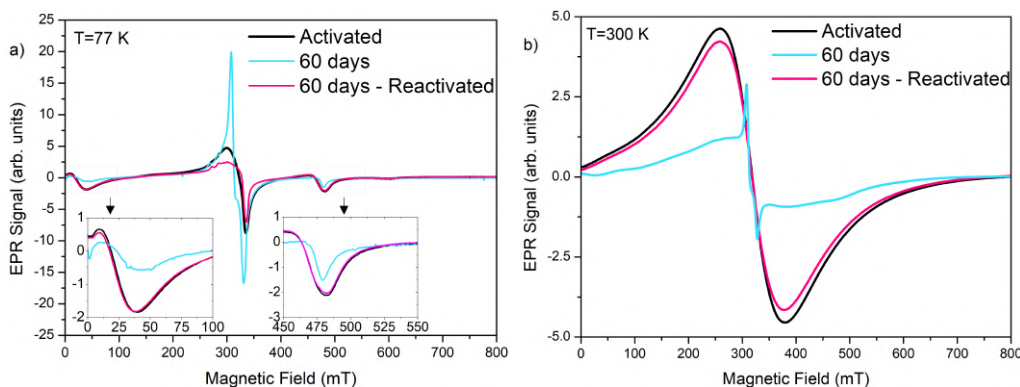
FIGURE 4.11: EPR spectra obtained for STAM-1 acquired at (a) 77 and (b) 300 K before the starting of the exposure (black), after 60 days of exposure (light blue) and after the subsequent reactivation (magenta).
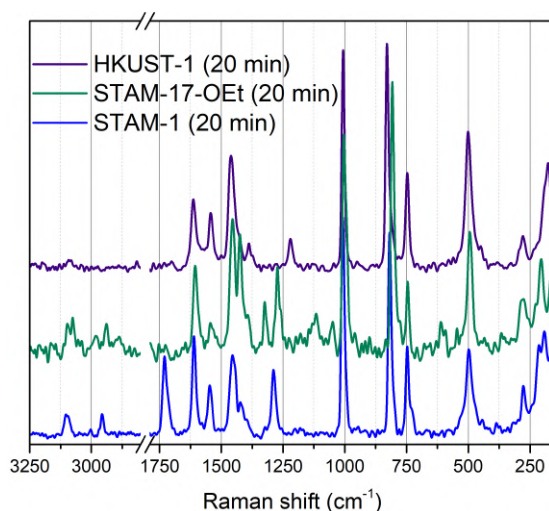

FIGURE 4.12: Raman spectra of HKUST-1 (violet), STAM-17-OEt (green) and STAM-1 (blue), recorded under air and corresponding to around 20 min of hydration.

STAM-17-OEt show slight different peaks, mainly due to the different organic linkers present in these MOFs.

In STAM-1, the peak at about 177 cm^{-1} is not detected but a new band at 214 cm^{-1} is well evident: it is reasonable to assume that the doublet at 177-190 cm^{-1} of HKUST-1 moves to a new doublet at 192-214 cm^{-1} and then it can be ascribed to stretching modes of the Cu-Cu dimers. A similar effect was found for the peak at 1388 cm^{-1} (ascribed to the symmetric stretching modes of the COO groups for HKUST-1) which shifts to 1422 cm^{-1}. Finally, the new peak at 1729 cm^{-1} is reasonably due to the methyl ester of the organic linker.

Similarly, in the spectrum of STAM-17-OEt the doublet of the Cu^{2+} ions is further shifted to 200-221 cm^{-1}. At 355 and 1134 cm^{-1} there are two small peaks attributable to the aliphatic chain of the linker, whereas the peak at 1326 cm^{-1} may be ascribed to a bending mode of the H-C-H group.[145] Even the signal at 1519 cm^{-1} can be related to a bond of the organic linker. The peak at 1425 cm^{-1} replaces that at about 1544 cm^{-1} present in both HKUST-1 and STAM-1, attributed to a-symmetric stretching modes of

the COO groups. It should also be noted that the peak at 830 cm^{-1} in the spectrum of HKUST-1 (ascribed to one of the two out-of-plane bending modes of the benzene rings) shifts to 818 cm^{-1} for STAM-1 and to 807 cm^{-1} for STAM-17-OEt, whereas the peak at 747 cm^{-1} (correspondent to the other bending mode) remains stable in its intensity and position.

The assignment of the single peak that is present in the range of 1200-1300 cm^{-1} for all three samples (1220 cm^{-1} in HKUST-1, 1272 cm^{-1} in STAM-17-OEt and 1289 cm^{-1} in STAM-1) is still unclear. In addition, new signals have been observed for STAM-1 and STAM-17-OEt in the region between 2800 and 3100 cm^{-1}. More precisely, for STAM-1 two bands at 2956 and 3100 cm^{-1} have been detected whereas for STAM-17-OEt we can resolve bands at 2934 cm^{-1}, 2984 cm^{-1} and the doublet 3078-3097 cm^{-1}. According to the literature, all these bands are attributable to aromatic C-H vibrations.[194]

Evolution with time and reactivation. Figure 4.13 shows the evolution of the Raman spectrum of HKUST-1 during the 60 days of exposure to humidity. Also in this case, the spectrum of the sample hydrated for about 20 minutes is considered as reference. The spectra acquired after 20 minutes, 6 hours and 1 days of exposure to humidity have similar spectroscopic features whereas, from the fourth day onwards, several differences can be detected. All the signals lower than 500 cm^{-1}, i.e. ascribed to the bonds involving the Cu^{2+} ions, disappear, the band at 747 cm^{-1} decreases significantly in intensity, and all the signals related to the COO$^-$ groups change both intensity and position. The reactivation does not recover the spectrum of pristine HKUST-1.
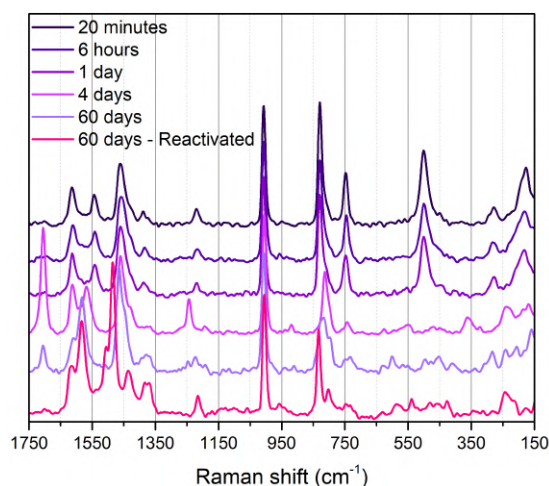

FIGURE 4.13: Raman spectra obtained for HKUST-1 during the 60 days of the exposure to humidity.

Figures 4.14 and 4.15 show the evolution of the Raman spectra during the 60 days of exposure to humidity for STAM-17-OEt and STAM-1, respectively. The spectra of both MOFs remain virtually unchanged both during the exposure and after the reactivation. The only difference detected for STAM-17-OEt is a slight change of the intensity of the peaks at 1134 and 1519 cm^{-1}, whereas for STAM-1 a small reduction of the relative intensity of the peak at 214 cm^{-1} (belonging to the doublet 192-214 cm^{-1}) is
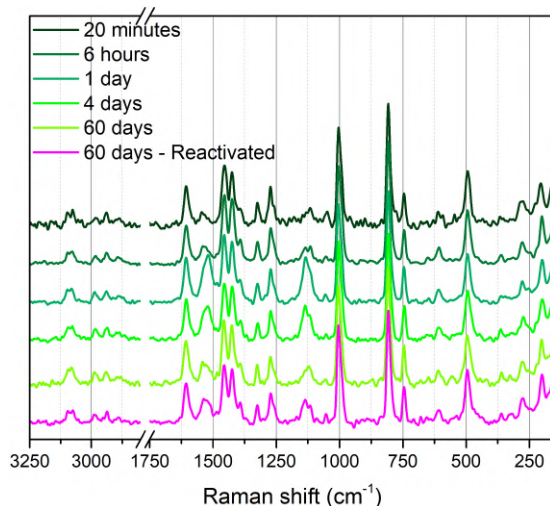
FIGURE 4.14: Raman spectra obtained for STAM-17-OEt during the 60 days of the exposure to humidity.
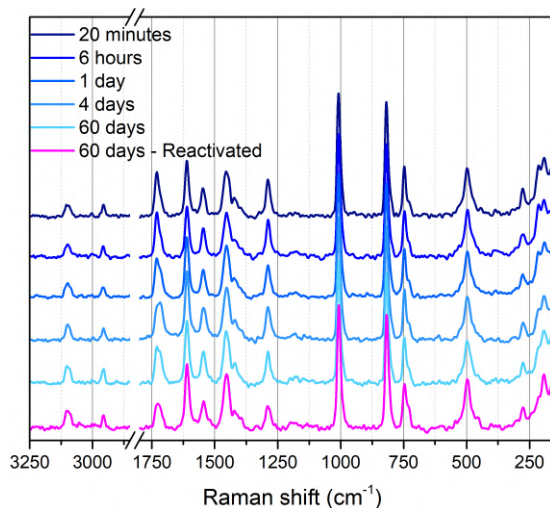

FIGURE 4.15: Raman spectra obtained for STAM-1 during the 60 days of the exposure to humidity.

observed. However, we have verified that this effect is related to the inhomogeneity of the sample, and not to the hydration of the material. This feature is shown more clearly in figure 4.16, where we report a set of spectra acquired for STAM-17-OEt in different spatial positions in a single sample hydrated for a specific amount of time. As shown, a significant variability of the intensity of these peaks is well recognizable, without a connection with the time of the exposure.

Raman spectra acquired at 420 K.   Raman spectra of the *"Activated"* and *"60 days-Reactivated"* samples of the three MOFs were also acquired using the Linkam cell, maintaining the samples at 420 K to preserve them from possible hydration effects during the measurement period. For this reason, the Horiba LabRam HR-Evolution spectrometer has been used (see section 3.2.3). The Raman spectrum of Activated HKUST-1 (figure 4.17) is comparable to those reported in literature[84,144] (and shown in figure 2.14): it
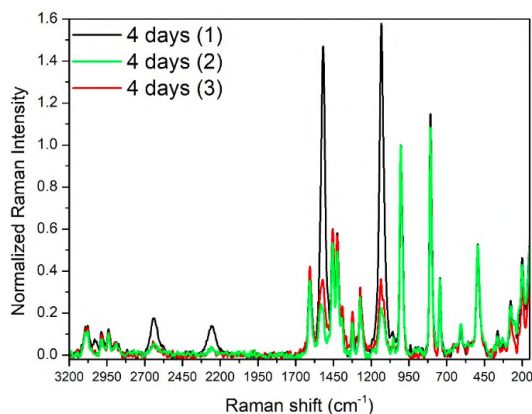
FIGURE 4.16: Raman spectra of STAM-17-OEt after 4 days of exposure acquired in different grains of the material.
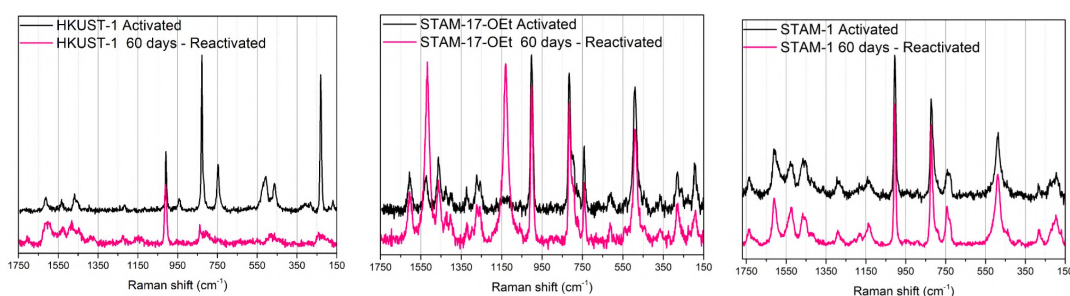

FIGURE 4.17: Raman spectra of HKUST-1 (left), STAM-17-OEt (center) and STAM-1 (right) before and after the treatments.

differs from the spectrum acquired after small exposure to air as an intense peak at 230 cm^{-1} replaces the doublet at 177-190 cm^{-1}, and two new peaks are observed at about 460 and 940 cm^{-1}, respectively.[84,144] In contrast, the spectra acquired in these conditions for both STAM-1 and STAM-17-OEt do not show significant differences from the spectra of figures 4.14 and 4.15.

4.1.4   NMR measurements

Figure 4.18 shows the ^{13}C NMR spectra of HKUST-1 after activation and exposure to humidity. The activated material shows three signals at 784, 228 and –88 ppm, assigned to C1, C3 and C2, respectively (see section 2.3).[147] Upon exposure to humidity for 1 day, the local structure of the material changes significantly and new resonances are observed at 205, 192, 185, 168 and 157 ppm (similar to those observed by Gul-E-Noor and co-authors[150], although that study also observed some intensity at 135 and 125 ppm). The region of the spectrum below 0 ppm, corresponding to carboxylate groups bound to a copper dimer, contains three resonances at –47, –82 and –101 ppm. The range of shifts suggests possible hydrated dimers (–47 ppm), coordinatively unsaturated sites (CUSs, –82 ppm) and an unknown arrangement giving rise to the resonance at –101 ppm. Resonances related to the decomposition product are also observed at 675 and 589 ppm, which suggests two new types of quaternary C associated with a carboxylate
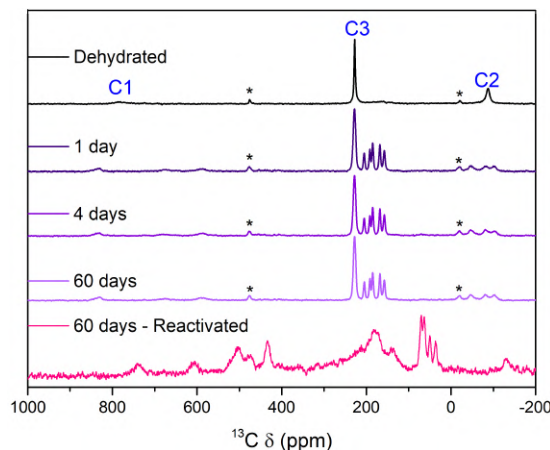
FIGURE 4.18: ^{13}C (14.1 T, 298 K, 37.5 kHz MAS) NMR spectra of a series of HKUST-1 samples treated as indicated. * = spinning sideband

interacting with copper dimers. The experimental conditions used by Gul-E-Noor and co-authors[150] did not allow observation of C_1 or C_2 resonances of the decomposition products so comparison with literature is not possible.

The HKUST-1 sample exposed to 97% RH for 60 days was also studied at variable temperature, with the heating profile $RT \rightarrow 263K \rightarrow 298K \rightarrow 333K \rightarrow 298K$ and the acquired spectra are shown in figure 4.19. It can be seen that, upon heating and
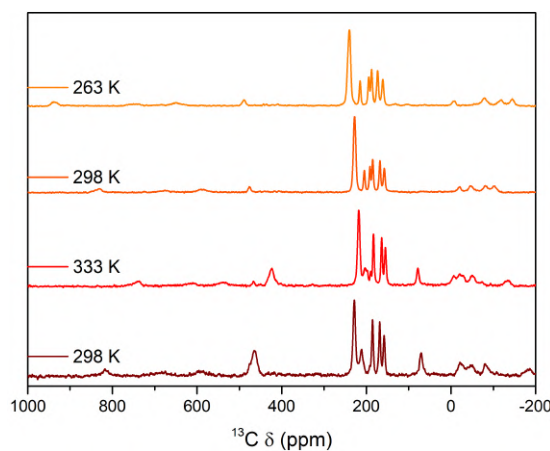

FIGURE 4.19: Variable-temperature ^{13}C (14.1 T, 37.5 kHz MAS) NMR spectra of HKUST-1 exposed to 97% RH for 60 days. The sample was cooled from room temperature to 263 K, heated to 298 K and then 333 K, and then cooled back to 298 K (bottom spectrum).

then cooling back to 298 K, the material undergoes an irreversible change with a new resonance appearing at 211 ppm (replacing the one at 205 ppm), the resonance at 192 ppm essentially disappears, and new resonances appear at 71 and -184 ppm. The three resonances at 187, 170 and 160 ppm appear unchanged in position, shape and relative intensity, perhaps suggesting that there are initially two decomposition phases or motifs present, one of which is more stable to heating than the other. Dehydration of the decomposed material leads to a very complicated spectrum (figure 4.19, bottom spectrum) with distinct resonances identifiable at 738, 608, 504, 475, 433, 217, 178, 137,

71, 63, 50, 36, 25, -134, -185 and -442 ppm (although this latter signal may be a spinning sideband of the resonance at –185 ppm).

Figure 4.20 shows the ^{13}C NMR spectra (recorded at 298 K) of STAM-17-OEt after activation, exposure to humidity and reactivated. The spectrum of activated STAM-17-
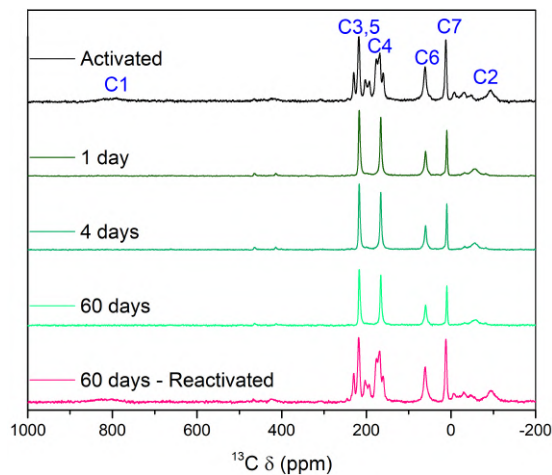

FIGURE 4.20: ^{13}C (14.1 T, 298 K, 37.5 kHz MAS) NMR spectra of a series of STAM-17-OEt samples treated as indicated.

OEt is identical to that reported in the literature (and in figure 2.35).[83,148] After one day of hydration, STAM-17-OEt reaches the hydrated configuration (figure 2.35) and the spectrum does not change over the course of the following days. The spectrum of the reactivated material is identical to that of the activated material, confirming the complete recovery of the local structure of the MOF.

As for STAM-17-OET,[83] also the ^{13}C NMR spectra of activated STAM-1 have previously been reported and assigned (see figure 2.29).[82,147,148] Figure 4.21 shows the ^{13}C NMR spectra of STAM-1 after activation, exposure to humidity and reactivation. As
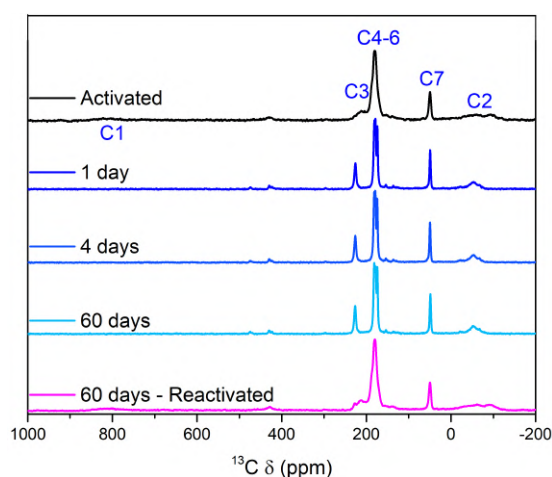

FIGURE 4.21: ^{13}C (14.1 T, 298 K, 37.5 kHz MAS) NMR spectra of a series of STAM-1 samples treated as indicated.

STAM-17-OEt, a change of the spectrum can be observed after the first day of hydration, with no further changes observed on prolonged hydration. Upon reactivation, the

spectrum is virtually indistinguishable to that of the initial activated material.

4.1.5 Nitrogen isotherms and BET calculation

Figure 4.22 shows the nitrogen isotherms of the three material after hydration for different numbers of days. The surface areas were estimated by fitting the adsorption curves
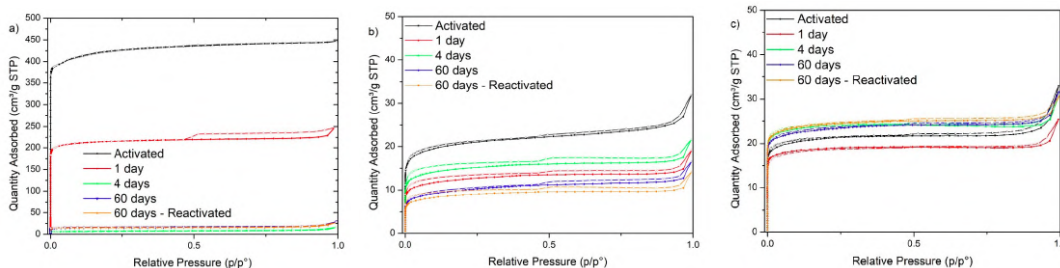

FIGURE 4.22: Nitrogen isotherms of HKUST-1 (a), STAM-1 (b), STAM-17-OEt (c) at different time of exposure. The full symbols correspond to adsorption curves, the empty symbols to the correspondent desorption curves.

with the BET method and are shown in table 4.1.

The BET surface area of activated HKUST-1 is 1662 m^2/g, in line with those reported in literature and in section 2.3.[139–141] After 1 day of exposure the BET surface is halved, and after 4 and 60 days of exposure it is further reduced by more than 95% with respect to the activated sample. In contrast, the samples of STAM-1 and STAM-17-OEt show comparable BET surface areas during the whole period of the hydration, subjected only to small fluctuations without a regular trend at different times of exposure.

TABLE 4.1: BET surface areas of HKUST-1, STAM-1 and STAM-17-OEt at different exposure times.

Exposure	BET surface area (m^2/g)		
	HKUST-1	STAM-1	STAM-17-OEt
Activated	1662	81	77
1 days	860	74	46
4 days	26	93	56
60 days	62	90	36
60 days - Reactivated	62	94	32

4.2 Discussion

As well-known in literature and also reported in section 2.3.2, the reported data clearly show that HKUST-1 rapidly undergoes irreversible hydrolysis process upon exposure to moisture.[67,140,141,150,156,157,159] This was confirmed by the results obtained by PXRD,

EPR, Raman and NMR spectroscopy and nitrogen adsorption isotherms. In more detail, the PXRD patterns concerning the hydrated HKUST-1 progressively lose almost all of the peaks characteristic of the crystalline ordered MOF. The EPR measurements of Figure 4.6 reveal a sequence of spectra characterized by a signal centered at about 320 mT with an increase in the intensity with the time of the exposure, similar to those reported by Todaro and coworkers[140] during their experiment on the effects of air moisture on HKUST-1 (section 2.3.2). This signal arises from an increase in number of centers with spin S=1/2, whose origin arises from that fraction of paddlewheels in which water molecules have broken some of the planar Cu-O bonds after a prolonged exposure. That breakage lead to a transition from Cu^{2+} to Cu^{1+} of one copper ion in each paddlewheel, and consequently the pairs of copper ions involved lose their antiferromagnetic coupling. Since the Cu^{2+} ion left is the only paramagnetic center of the pair Cu^{2+}-Cu^{1+}, such paddlewheel contributes to the EPR signal as a center with S=1/2.[140] Consequently, the observation of S=1/2 centers suggests the beginning of the hydrolysis of HKUST-1, and we detect this signal just after 6 hours of exposure to humidity with the experimental conditions used here. It is necessary to clarify that the shorter time here reported compared to those of our previous works, in which the hydrolysis started after about 20 days,[140,144,155] is only due to the type of exposure to humidity used. For the present work, the samples have been kept at ∼100% RH (instead of ∼70% RH in Todaro and co-authors[140,144,155]) and in sample-holders which have favored the interaction with humidity. These are the only two causes for such shorter time of the hydrolysis process. In other words, the process here described is the same of that previously reported in section 2.3.2, but intentionally sped up.

The spectra acquired after 4 days of exposure are characterized by features with different line shape and intensity compared to those previously reported by Todaro and co-authors[140], indicating that now we have hydrated the material more extensively and that we have been able to observe a further step in the decomposition process. As previously proposed by Pöppl and co-authors[158], it is reasonable to assume that the final step of the process (probably reached around the 60th day in our experiments) is the complete transformation of the paddlewheels to monomeric Cu(II) centers which have S=1/2 spin, similarly to the small fraction of $[Cu(H_2O)_6]^{2+}$ defects typically present in the pristine HKUST-1.

The Raman data obtained for HKUST-1 are in line with this picture. In fact, all the peaks arising from the Cu-O bonds of the paddlewheels disappeared upon prolonged exposure (from the 4th day of exposure onwards), indicating that the environment of the metal centers of the material is significantly changed. The NMR spectra are also in line with this timescale, showing relevant changes of the local structure (related to connectivity of the linkers) after 1 day of exposure. The nitrogen isotherms confirm the substantial loss of porosity and surface area with exposure to moisture. In contrast to HKUST-1, STAM-17-OEt has already been proved to be more hydrolytically stable.[83] The PXRD patterns acquired for STAM-17-OEt clearly show that no detectable changes and/or damages to the crystal lattice are occurred after 60 days of exposure to 100% RH.

Indeed, the pattern of the reactivated material is virtually indistinguishable from that of the starting STAM-17-OEt, confirming the hydrothermal stability of its framework. This trend has been observed also in the NMR, Raman and EPR data sets.

Some of the techniques we employed were shown to be also sensitive to the effects of the prior mild hydration: the NMR and EPR spectra and the PXRD patterns of the activated STAM-17-OEt show several changes during the first day of exposure to humidity. Such alterations in both the PXRD patterns and NMR spectra of STAM-17-OEt have been shown previously and explained by a single-crystal-to-single-crystal transition characteristic of this material (section 2.5).[83] The EPR data provide further evidence of this transition and also provide a new insight into this fundamental process which is inherent to the hemilability mechanism. For STAM-17-OEt we noticed the narrowing of the resonance at 480 mT in the hydrated samples compared with the same peak in the spectrum of the activated one. This effect is a direct consequence of the switchover between the two above-mentioned different structural arrangements of the material when it is in the activated form or in a hydrated form. Indeed, the material in its hydrated configuration finds a more ordered arrangement and the increase in the structural order leads to a narrowing of the resonances of the triplet centers in the hydrated sample compared to the activated one.

Similar considerations apply to STAM-1: although the structure of activated STAM-1 has not yet been fully defined, it is known that the dehydration leads to a lowering of the symmetry and an increase in the disorder of the framework as well (see section 2.4).[82,147,148] For these reasons, we believe that the phenomenon behind that narrowing is the same both in STAM-1 and STAM-17-OEt. This together with all the other spectroscopic and crystallographic changes caused by hydration were shown to be reversible.

However, the EPR data acquired for STAM-1 show that, from the first day onwards, a signal centered at about 315 mT is observed. As said before, it is naturally attributed to S=1/2 centers arising from hydrolyzed paddlewheels. Nevertheless, analyzing the positions of the positive and negative peaks in the EPR spectra for this signal, we can notice that they are virtually indistinguishable from those of the peak appearing in the spectra of hydrolyzed HKUST-1 and the evolution of this signal with exposure time follows the same trend as observed for HKUST-1 (figures 4.6 and 4.8). It is known in the literature[82] that impurities of HKUST-1 are always present in STAM-1, and we have roughly estimated from our PXRD patterns that the sample studied may contain a volume fraction of about 10% of HKUST-1. Using the EPR data, we have also evaluated the percentage of paddlewheels involved in the hydrolysis process of the STAM-1 sample, and it may be around 15% of the total amount of paddlewheels of the sample. These estimates suggest that simple conclusion that the damaged paddlewheels belong not to STAM-1 but to the HKUST-1 impurities present in the material. Therefore, in addition to STAM-17-OEt, also STAM-1 is found to be stable to water after an extensive hydration.

Until now, we focused on the differences of the evolution followed by the three materials, particularly in the timeframe beyond the sixth hour of hydration and, therefore, on the presence or absence of hydrolysis, without referring to the possible causes of such differences between the MOFs examined. Looking at the EPR spectra acquired at 300 K for all of the three MOFs, it is noteworthy that they show the same behavior during the first 6 hours of hydration: the intensity decreases without significant changes of the line shape. This effect has been already reported for HKUST-1 previously, but its cause remains uncertain. It is also known that, in STAM-17-OEt, the transition from the activated material to the hydrated form is accompanied by several clear differences in the PXRD pattern[83], and it is also known that it occurs after the adsorption of the first molecule of water which breaks the weak Cu···O interactions between adjacent paddlewheels.[83] Figure 4.4 brings the PXRD pattern of the sample hydrated for 1.5 hours which clearly shows that the material is not fully hydrated: this means that not all the Cu^{2+} ions have established the fifth bond with a water molecule after 1.5 hours. In contrast, the pattern acquired after 6 hours of hydration shows only the typical peaks of the hydrated material, suggesting a more homogeneous hydration. The EPR data acquired for STAM-17-OEt at 300 K shows that the changes of the intensity and the line shape take place only within the first 6 hours of hydration whereas, after 1.5 hours of exposure, the spectral intensity is intermediate between that of the activated and that of subsequent more hydrated samples. The two phenomena are therefore correlated.

STAM-1 and HKUST-1 also show EPR changes of similar magnitude and with the same time scale of those observed for STAM-17-OEt. However, HKUST-1 does not exhibit any reversible flexibility of the framework or hemilability, therefore we cannot attribute such effect to significant structural changes of the lattice as we may be tempted to do looking for an explanation valid for the STAM materials, nor it is not possible to follow the first adsorption with PXRD diffractometry.

By combining this information, it is clear that the reduction of the EPR signal within the first 6 hours (under the humidity conditions used here) correspond to the adsorption of the first water molecule at the axial site of each Cu^{2+} and, furthermore, this process is common to all three MOFs.

At this point of the discussion, it may appear pointless to underline that this part of the hydration is reversible in the STAM materials, but it is important to notice that it is reversible even for HKUST-1. In fact, this phase of the hydration has been already shown to be totally reversible for HKUST-1 and such information make clear that the adsorption of the first molecule of water on the Cu^{2+} ions do not necessarily involve the starting of the hydrolysis process. On the contrary, it is more likely that the subsequent water molecules are the real responsible of the hydrolysis in HKUST-1, as suggested by many previous works.[51,67,130,142,146] It has been already widely discussed (section 2.3.2) that the hydrolytic stability of the MOFs may be linked to the impossibility of water to clustering around the metal center.[51,67,130,142,146] At variance, the model reported

by McHugh and co-authors[83] suggests that the first molecule of water binds to copper and simultaneously breaks one of the four equatorial Cu-O bonds (maintaining a four-coordinate copper ion). Subsequent water molecules replace further bonds to the carboxylate oxygens, leading to framework degradation.[83,140] Thanks to the presence of the "crumple zones" in hemilable materials like STAM-17-OEt, this hydrolysis cannot take place.[83] Our results suggest that the adsorption of the initial water molecule is fully reversible and occurs in the same manner, regardless of whether the MOF possesses "crumple zones" (as in STAM-17-OEt and STAM-1) or not (as in HKUST-1). Therefore, one could believe that such eventual breakage of a Cu-O bond in a HKUST-1 paddle-wheel could be recovered if the material is dehydrated before the adsorption of the subsequent water molecules. Under such assumption, the framework would be able to recover the broken Cu-O bonds, returning to the pristine configuration.[140] In contrast, if the hydration continues, the subsequent changes lead to the well-known irreversible hydrolysis. However, we think that such breakage of one planar bond in HKUST-1 due to the first molecule of H_2O, if actually present, should involve only a very small percentage of the paddlewheels. Indeed, the magnetic evolution of the spectra acquired at 300 K for the three MOFs is equivalent and therefore it seems unlikely that such a hard phenomenon as a breakage of one axial Cu-O bond occurring only in HKUST-1 does not imply any evidences in its EPR spectra compared to the other two during the first 6 hours of measurements. Similar information comes also from the Raman data.

This result implies that controlling the clustering of water inside the pores of the MOFs is of fundamental importance to the control of the stability of the MOFs. The physical causes of the reduction (by the same magnitude) in the intensity of the EPR signal obtained at 300 K remain uncertain.

In order to gain deeper understanding of the structural changes taking place in these MOFs during the hydration process, we have further investigated them by extracting quantitative structural parameters from the EPR spectra using computer simulations. We followed the Hamiltonian models used generally in literature for HKUST-1 and already reported in eq. 1.28 and 1.22.[133,140] The simulations have been run on the spectra acquired at 77 K for the three samples, activated and after 6 hours of exposure to humidity. In this way we can monitor the change occurred during the first step of hydration. All the results are shown in the following figures and tables (figures from 4.23 to 4.25 and tables from 4.2 to 4.7).

Introducing the g strain parameters, we assume that the g values follow Gaussian distributions whose such g strain are the widths. Such introduction is necessary to obtain a good optimized EPR curve. For the activated HKUST-1 we obtained $g_x=g_y=2.04$, $g_z=2.36$. These values are comparable to those obtained previously by Pöppl and co-authors[133] and Todaro and co-authors[140] . For activated STAM-1 the g-parameters obtained are comparable with those reported by Mkami and co-authors[179]. For the activated STAM-17-OEt there are not previous investigations in literature. For this material we found g values indicating orthorhombic symmetry, in contrast to the axial
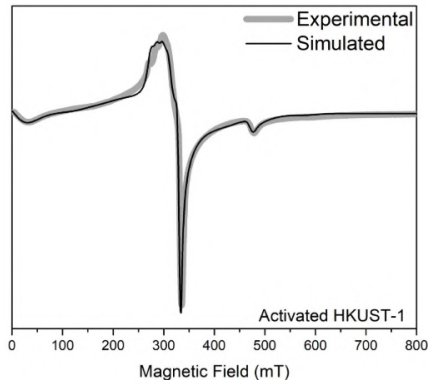
FIGURE 4.23: Comparison between experimental and simulated EPR spectra for activated HKUST-1.
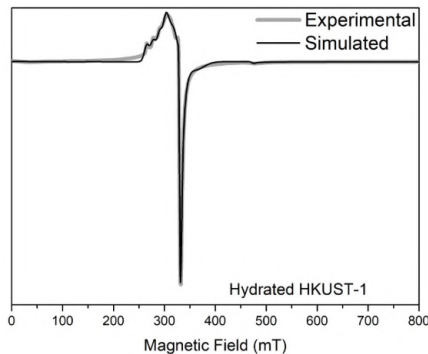
HKUST-1 activated	g	g_{strain}	D and E (cm^{-1})
Triplet	2.04	0.07	0.321
	2.04	0.59	<0.001
	2.36	0.45	

TABLE 4.2: Parameters of the simulated EPR spectrum for activated HKUST-1.

FIGURE 4.24: Comparison between experimental and simulated EPR spectra for hydrated HKUST-1.

HKUST-1 hydrated	g	g_{strain}	D and E (cm^{-1})
Triplet	2.04	0.07	0.321
	2.04	0.59	<0.001
	2.36	0.45	
Spin 1/2	2.07	0.01	
	2.11	0.20	
	2.40	0.09	

TABLE 4.3: Parameters of the simulated EPR spectrum for hydrated HKUST-1.

symmetry of HKUST-1 and STAM-1. Such difference of the symmetry of the paddle-wheel might arise from the small deformations resulting from the presence of the Cu···O interactions with the adjacent paddlewheels. Furthermore, the g-parameters are also accompanied by very large g-strains. Since there are two crystallographically different groups of paddlewheels in activated STAM-17-OEt, it is likely that the observed signal contains contributions from two different species of triplet centers, but these cannot be evidently distinguished owing to the large g strains as we observe only one very broad EPR line attributable to a triplet center. It is also noteworthy the STAM-1 and HKUST-1 show similar g-parameters in activated form. The effects of the hydration are also easily detectable from the strong changes of the g-parameters. Interestingly, those of STAM-1 change significantly after the start of the hydration. Evidently, the adsorption of the water molecule on the Cu^{2+} ion entails a significant change of the environment along the axis of symmetry, but without losing the axial symmetry. After hydration STAM-17-OEt acquires axial symmetry ($g_x=g_y \neq g_z$) with low g-strains, reflecting the higher crystallographic symmetry of the hydrated material (previously pointed out by XRD, see section 2.5). The sample of HKUST-1 hydrated for 6 hours shows the same
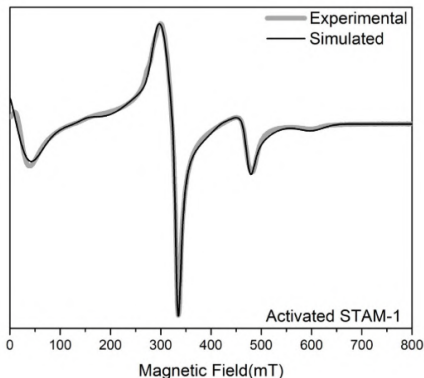
FIGURE 4.25: Comparison between experimental and simulated EPR spectra for activated STAM-1.

STAM-1 activated	g	g_{strain}	D and E (cm^{-1})
Triplet	2.06 2.06 2.32	0.09 0.71 0.45	0.328 0.002

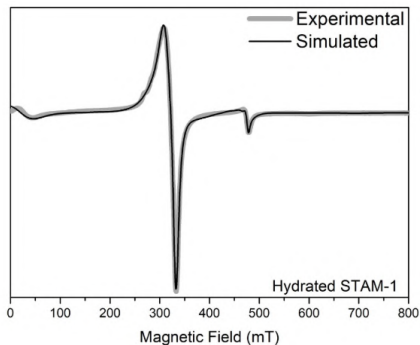TABLE 4.4: Parameters of the simulated EPR spectrum for activated STAM-1.

FIGURE 4.26: Comparison between experimental and simulated EPR spectra for hydrated STAM-1.

STAM-1 hydrated	g	g_{strain}	D and E (cm^{-1})
Triplet	2.06 2.06 2.02	0.03 0.29 0.30	0.334 0.002

TABLE 4.5: Parameters of the simulated EPR spectrum for hydrated STAM-1.

g-parameters of the activated one for the triplet centers. However, in this sample the S=1/2 component becomes relevant, because it involves not only the synthesis defects but also those centers formed due to hydrolysis. For these reasons, we characterized also such S=1/2 centers, obtaining similar results to those of Todaro and co-authors for their E'$_2$ centers.[140]

Speaking about the Raman data acquired, the spectra concerning HKUST-1 showed some changes caused by hydration on the vibrational modes, an effect previously observed in literature[84,144] and discussed in section 2.3. In contrast, the Raman spectra obtained for STAM-1 and STAM-17-OEt does not exhibit observable effects attributable to hydration effects. In fact, the spectra acquired for the STAM-1 and STAM-17-OEt are virtually identical, and very few differences can be observed between these and the activated MOFs. Despite this, the Raman study permitted us to characterize for the first time the vibrational modes of these materials. In particular, comparing the Raman spectrum of pristine HKUST-1 with those of STAM-1 and STAM-17-OEt, we observed a significant change of the position of some of the bands directly involving the coppers
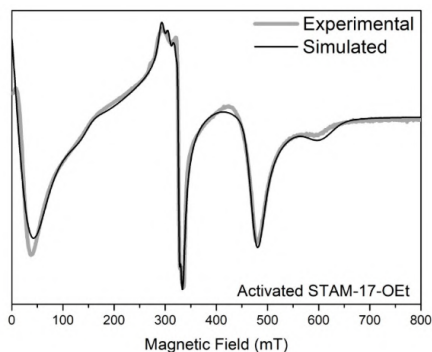
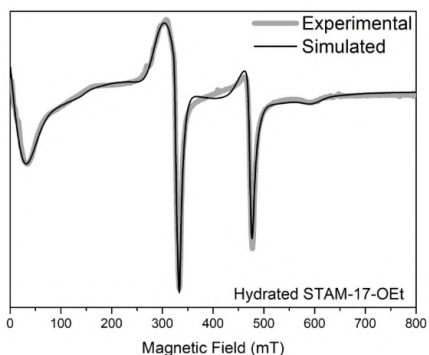FIGURE 4.27: Comparison between experimental and simulated EPR spectra for activated STAM-17-OEt.

STAM-17-OEt activated	g	g_{strain}	D and E (cm^{-1})
Triplet	2.05	0.15	0.314 0.002
	2.09	0.59	
	2.25	0.41	

TABLE 4.6: Parameters of the simulated EPR spectrum for activated STAM-17-OEt.

FIGURE 4.28: Comparison between experimental and simulated EPR spectra for hydrated STAM-17-OEt.

STAM-17-OEt hydrated	g	g_{strain}	D and E (cm^{-1})
Triplet	2.04	0.04	0.318 <0.001
	2.04	0.19	
	2.30	0.32	

TABLE 4.7: Parameters of the simulated EPR spectrum for hydrated STAM-17-OEt.

of the paddlewheels. This result indicates that the change of the organic linker significantly affects also the environment of the Cu^{2+} ions, particularly the strength of the axial Cu-O bonds. Further investigations may be carried out in order to determine the role of such changes on the stability of carboxylate MOFs.

Finally, it is important to point out that although the water stability of STAM-1 and STAM-17-OEt has previously been reported,[82,83] the present work provides the first demonstration of the total atomic-scale reversibility of extensive hydration. Indeed, with EPR measurements we could detect even very small differences occurred in the adjacent environment of the paddlewheels, but the data obtained have clearly shown that, for STAM-1 and STAM-17-OEt, no significant differences can be observed between the two dehydrated samples measured before ("Activated") and after the hydration treatment ("Reactivated").

Conclusions of the chapter

This work has presented some important information about the hydrolytic stability of the three copper MOFs, HKUST-1, STAM-1 and STAM-17-OEt, during the 60 days of exposure to 100% RH at T=300 K. Under the exposure conditions used, HKUST-1 begins the process of irreversible decomposition within 24 hours. In contrast, STAM-17-OEt shows no evidence of hydrolysis during the 60 days of monitoring. The STAM-1 sample shows traces of decomposition but these can be attributed entirely to the HKUST-1 impurities present in the material. Consequently, our data prove that STAM-1 is also resistant to water and it does not decompose under the conditions used here. All these results attest the longer resistance of STAM-1 and STAM-17-OEt materials towards water compared to HKUST-1. The reversible structural transitions occurring upon hydration of both STAM-1 and STAM-17-OEt were also clearly detected by EPR, permitting to find the structural parameters proper of the configuration on the lattice both in hydrated and dehydrated configuration. The lowering of the crystallographic order in the activated STAM-1 and STAM-17-OEt has a significant impact on the width of the lines of the EPR spectra arising from the paddlewheels. Furthermore, we revealed that, in spite of the strong differences between the three MOF studied, the first hours of exposure to water lead to a virtually indistinguishable evolution. This process is also known to be fully reversible and it reasonable represents the process of adsorption of the first molecule of water onto the axial sites of the Cu^{2+} ions. It proves that the differences in the hydrolytic stability of this type of MOFs take over at a later stage, during the adsorption of additional water molecules on the firsts. When on average more than one water molecule approaches each copper ion, HKUST-1 begins to undergo irreversible hydrolysis, whereas STAM-1 and STAM-17-OEt fully retain their framework structure. Such differences may be reasonably linked to the amount of free space available in the pores of the materials, which is significantly larger in HKUST-1 (up to $\sim$14 Å) than in STAM-1 ($\sim$6 Å) and STAM-17-OEt ($\sim$6 Å). Lastly, in this work, thanks to the use of EPR and NMR spectroscopy, we proved the total atomic-scale reversibility of extensive hydration.

Chapter 5

HKUST-1 tablets

We have already deeply discussed that, in order to maximize the packing density, mechanical strength, stability in reactive environments and many other properties of MOFs, the compaction of their powders is a fundamental step for the application field of the research. In this respect, HKUST-1 is among the most promising and studied MOFs.

Contrary to what reported so far in literature, in this chapter we show that the tableting of HKUST-1 powders without any damage of the lattice is possible and easy to get. For the first time, this kind of investigation has been performed exploiting its peculiar magnetic properties with the aid of the electron paramagnetic resonance spectroscopy. Indeed, they have allowed us to explore in detail all the smallest changes induced in the paramagnetic paddlewheel units by application of the mechanical pressure on the material. This original approach has permitted us to unveil the main source of structural instability of HKUST-1 during compaction, i.e. the water molecules adsorbed by the powdered sample before tableting, and finally to establish a proper compaction protocol. Our conclusions are also fully supported by the results obtained with powder X-ray diffraction (XRD), thermogravimetric analysis (TGA), water sorption isotherms and surface area estimation with BET method, which prove that the HKUST-1 tablets obtained by this new protocol actually preserve both the crystal structure and the porosity of the pristine powders. A morphological characterization has also been conducted with a combined use of optical and atomic force microscopies (AFM).

5.1 Results

The pictures of some of the tablets we have produced are been reported in figure 3.5. Only the tablets obtained with pressures of 30 MPa or higher were found to be self-standing. In figure 5.1, the effective density (mass/volume of the tablet) measured after tableting as a function of the values of the pressure applied to the powder is reported. As shown, the density increases on increasing the applied pressure by following a sublinear dependence and it reaches a value of about 0.95 ± 0.03 g/cm^3 for a pressure of 40 MPa. For sake of comparison, in figure 5.1 we also indicate by red lines the calculated skeletal density of activated HKUST-1[97], 0.88 g/cm^3, and that pertaining to the same system when it has adsorbed just one water molecule for Cu^{2+} site, 0.96 g/cm^3. This latter is a pertinent value of reference because the tableting process takes place in air and
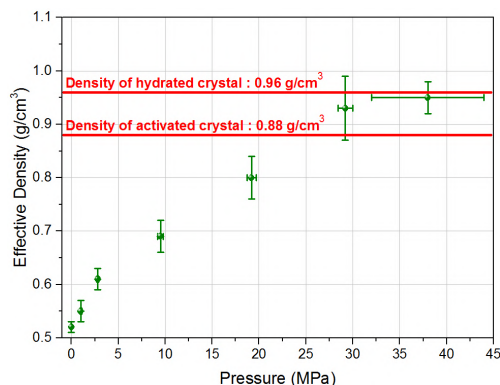
FIGURE 5.1: Effective density of tablets as a function of the applied pressure on HKUST-1 powder. The horizontal red lines indicate the calculated densities for activated HKUST-1 (0.88 g/cm^3) and for the same material after adsorption of just one water molecule for Cu^{2+} site (0.96 g/cm^3).

consequently we expect that a relevant fraction of the Cu site of the sample become actually saturated by a water molecule. The effective density estimated for the tablet obtained with a pressure of 40 MPa falls just between the two red lines, indicating an excellent volume packing of the powder. On the basis of this promising result, we have decided to investigate with a particular detail the properties of the tablet obtained by using a mechanical pressure of about 40 MPa.

EPR characterization of the tablets

We begin showing the results obtained for the tablets produced from hydrated powders (H1 and H2, see section 3.1.6).

EPR spectra for H-type tablets of HKUST-1.   EPR measurements of the tablet H1-40MPa obtained at 77 K and 300 K are reported in figure 5.2(a) and (b), respectively. In order to recognize the effects of the various treatments considered, in figure 5.2 we
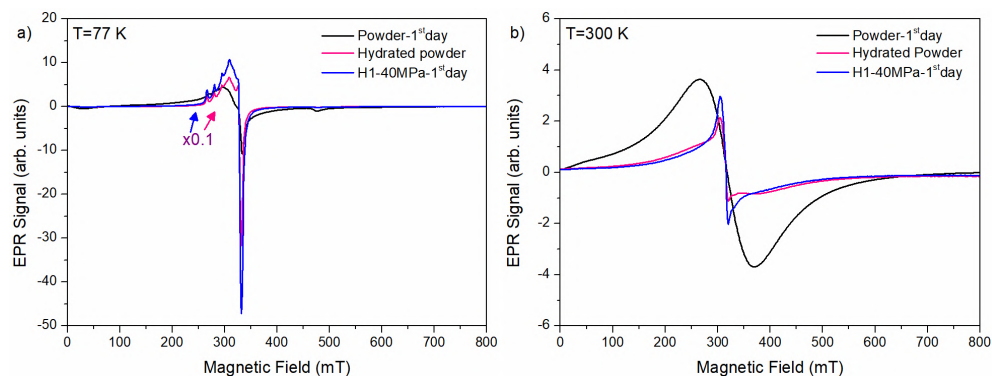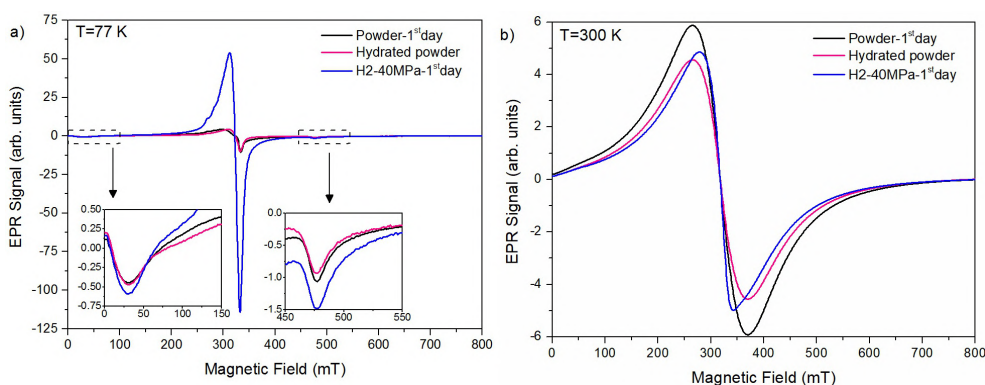

FIGURE 5.2: EPR spectra of the activated (black) and hydrated powders (pink) used to produce the 40MPa hydrated tablet (blue) acquired at 77 K (a) and 300 K (b).To make them easier to see, the spectra obtained at 77 K (except that of Powder) were multiplied by a factor of 0.1.

have also reported the spectra obtained for the same sample before exposure to air and tableting (Powder-1st day) and after hydration but before tableting (Hydrated Powder).

The two graphs show that very relevant changes take place already when HKUST-1 powders are exposed to air. Indeed, at both temperatures, the hydrated powder shows the characteristic EPR spectrum of HKUST-1 severely damaged by hydrolysis. Furthermore, figure 5.2(a) and (b) reveal that the effect of compaction on such hydrolyzed powders is negligible, as the EPR spectra before and after preparation of the tablet are comparable.

EPR measurements of the H2-40MPa obtained at 77 K and 300 K are reported in figure 5.3(a) and (b), respectively. In this case, the spectra of the hydrated powder are

FIGURE 5.3: EPR spectra of the activated (black) and hydrated powders (pink) used to produce the H2-40MPa sample (blue) acquired at 77 K (a) and 300 K (b). The two insets in (a) show the zooms of the spectrum regions enclosed by the dashed panels.

very similar to that of the activated powder, in line with the less effective exposure to moisture of this sample compared to the previous one H1-40MPa. We have noted just a reduction of the EPR signal acquired at T=300 K (figure 5.3(b)). However, it has been well established previously that this effect is reversible and inherently related to the hydration process of HKUST-1. At variance, after compaction of the powders we have observed the growth of a very large contribution attributable to hydrolyzed paddlewheels in the spectra acquired at T=77 K (main central resonance in figure 5.3(a)).[140] These changes are less evident at T=300 K, presumably because they are mitigated by the inter-paddlewheels exchange interaction which strongly affect the line shape of the resonance. In addition, we have observed a rapid evolution of the magnetic properties of the tablet as a function of time after preparation. This effect is shown in figure 5.4 were for the same sample we have reported the comparison between the spectra acquired the day of the tableting and one week later: after just one week of storing of the sample in sealed glass tube, the signal attributed to hydrolyzed paddlewheels increases by about a factor 5.

EPR spectra for A- and B-type tablets of HKUST-1 at different pressures.
EPR measurements of the most representative A-type tablets obtained at 77 K and 300 K are reported in figure 5.5(a) and (b), respectively. In particular, by comparing
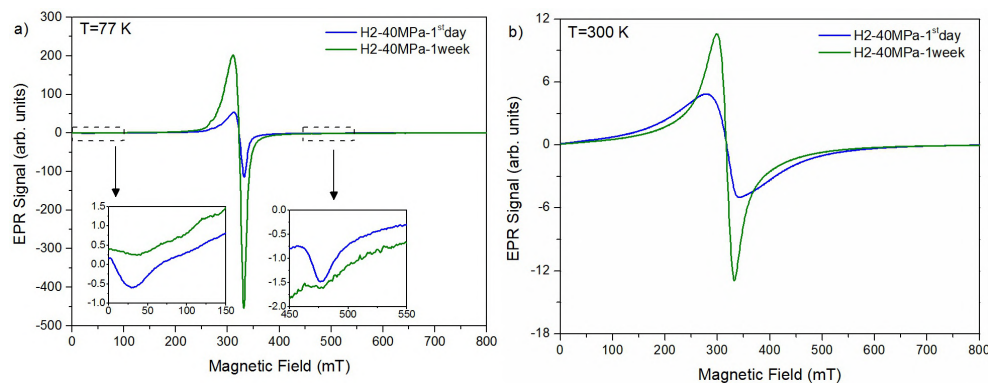
FIGURE 5.4: EPR spectra of the tablet H2-40MPa acquired at 77 K (a) and 300 K (b) the day of the tableting and one week after. The two insets in (a) show the zooms of the spectrum regions enclosed by the dashed panels.
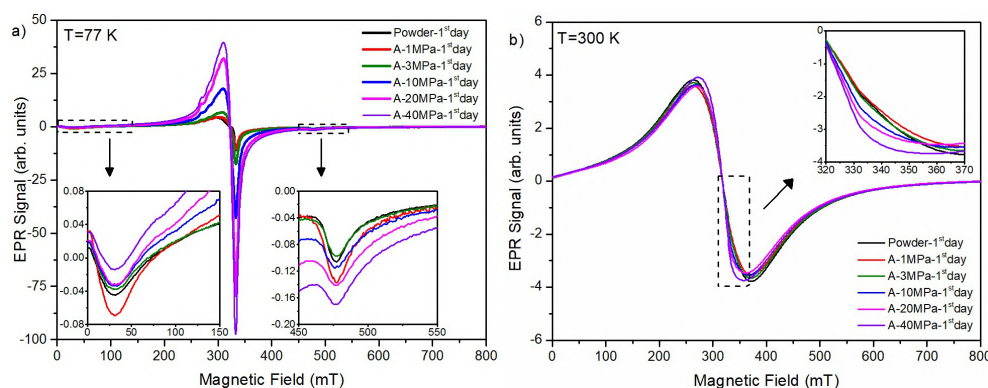

FIGURE 5.5: EPR spectra of some representative A-type tablets obtained just after tableting and of the Powder sample (in black), acquired at 77 K (a) and 300 K (b). The insets in both the graphs (a) and (b) show the zooms of the spectrum regions enclosed by the dashed panels.

the spectra acquired at 77 K, the principal difference concerns the intensity of the main resonance, which increases on increasing the pressure applied for the tableting of the sample. At variance, the spectra obtained at T=300 K present less significant differences: it is possible to notice only a small narrowing of the line shapes on increasing the pressure, without detectable changes in intensity. As anticipated, B-type samples have been activated just after preparation of the tablets. In order to evaluate the effect of the thermal treatment, we have compared the EPR spectra obtained for the sample B-40MPa before and after activation. These data are shown in figure 5.6(a) and (b) for 77 K and 300 K, respectively. For sake of comparison, the EPR spectra at both temperature of the Powder sample are also reported. Interestingly, the data reported in figure 5.6 shows that the post-tableting activation induces a significant recovery of both the intensity and the lineshape of the central resonance.
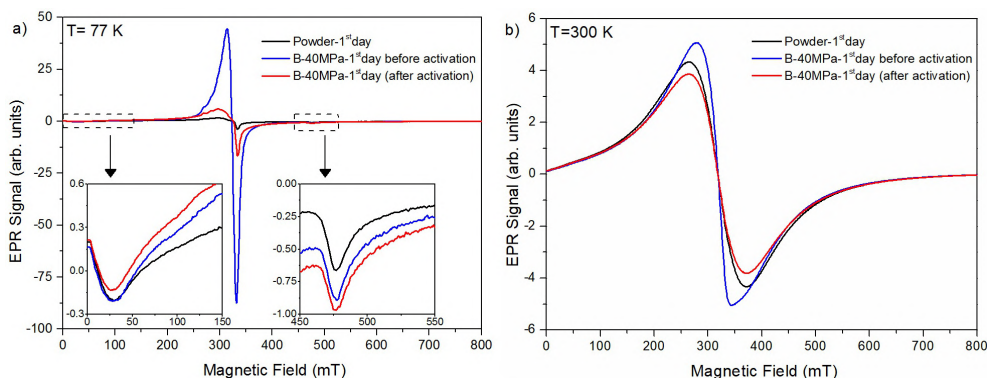
FIGURE 5.6: EPR spectra of the sample B-40MPa before activation and B-40MPa (after activation) obtained at 77 K (a) and 300 K (b). In black, the corresponding spectra of Powder-1stday are also shown for comparison. The two insets in (a) show the zooms of the spectrum regions enclosed by the dashed panels.

Evolution of the EPR spectra for powder sample and for A-, and B-type tablets of HKUST-1 during the 5 weeks after activation and/or tableting. EPR measurements of Powder sample acquired at different times after the first activation and obtained at 77 K and 300 K are reported in figure 5.7(a) and (b), respectively. Figure 5.7(a) shows an increase of the amplitude of the main peak from the activation
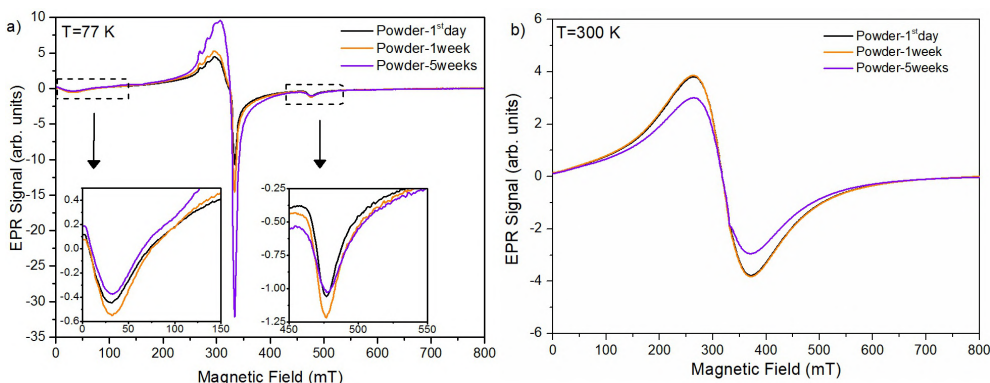

FIGURE 5.7: EPR spectra of the Powder sample acquired at different times after its first activation and obtained at 77 K (a) and 300 K (b). The two insets in (a) show the zooms of the spectrum regions enclosed by the dashed panels.

to 5 weeks later. In parallel, in figure 5.7(b) we note a decrease of the amplitude of the central peak 5 weeks after the activation. No relevant change of the EPR lineshape is detected both at 77 K and 300 K. As already anticipated, both these effects are due to hydration and they have been observed and studied in depth by Todaro and co-authors previously.[140] It is also known that this stage of the process of hydration of HKUST-1 is totally reversible through an activation process (figure 5.10).[140]

EPR spectra acquired for sample A-40MPa at 77 K and 300 K at different times after its tableting are shown in figure 5.8(a) and (b) respectively, compared with those obtained for Powder-1stday at both temperatures. These measurements indicate that in the days following tableting, the EPR spectra undergo some relevant changes. In the spectra obtained at 77 K we observe the growth of new unknown spectral components
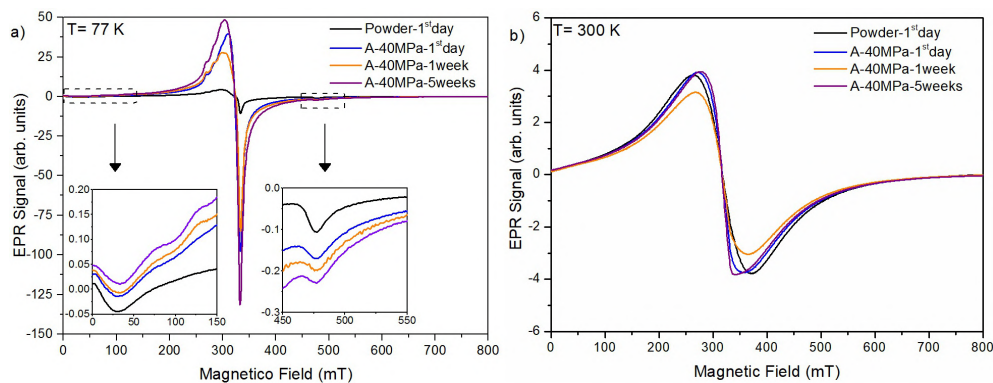
FIGURE 5.8: EPR spectra of the sample A-40MPa acquired at different time after its tableting and obtained at 77 K (a) and 300 K (b). In black, the corresponding spectra of Powder-1stday are also shown for comparison. The two insets in (a) show the zooms of the spectrum regions enclosed by the dashed panels.

peaked in the range of magnetic field from 60 mT to 150 mT (see the inset on the left in figure 5.8(a)), whereas at room temperature a significant change of the lineshape is easily recognizable. These changes indicate that a relevant fraction of the paddlewheels of the material become significantly distorted during the 5 weeks after preparation of the tablet.

Figure 5.9 shows EPR measurements obtained at 77 K (a) and 300 K (b) for the B-40MPa immediately after reactivation and 5 weeks after it, compared with those obtained for Powder-1stday. At both temperatures, we have observed very negligible
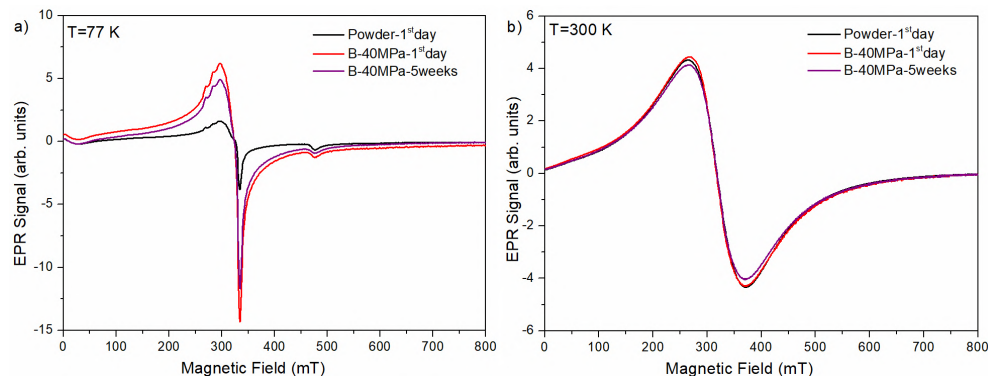

FIGURE 5.9: EPR spectra of the sample B-40MPa at the day of reactivation process and 5 weeks later, obtained at 77 (a) and 300 K (b). In black, the corresponding spectra of Powder-1stday are also shown for comparison.

variations of intensity and line shape. Therefore, from the point of view of its magnetic properties, the sample B-40MPa is a tablet which preserves almost unchanged the pristine properties of the material stably in time.

EPR spectra for powder sample and for A- and H-type tablets of HKUST-1 reactivated after 5 weeks of aging. After 5 weeks of aging the Powder sample has shown some spectroscopic changes (figure 5.7). Figure 5.10 shows EPR measurements obtained at 77 K (a) and 300 K (b) for activated Powder-1stday and for reactivated

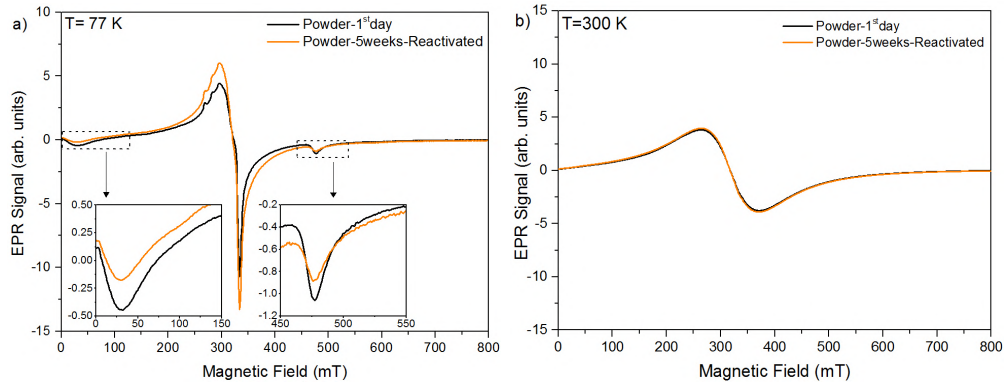Powder sample after 5 weeks of aging in the EPR tube. Figure 5.11 shows EPR mea-

FIGURE 5.10: EPR spectra acquired at 77 K (a) and 300 K (b) of the Powder sample reactivated after 5 weeks of aging (orange). In black, the corresponding spectra of Powder-1stday are also shown for comparison.

surements obtained at 77 K (a) and 300 K (b) for the A-40MPa tablet reactivated 5 weeks after the tableting, compared with those obtained for Powder-1stday. The corre-
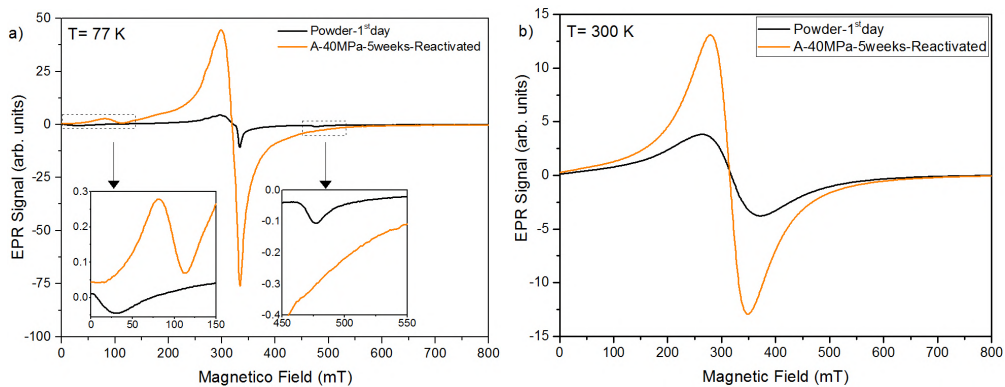

FIGURE 5.11: EPR spectra acquired at 77 K (a) and 300 K (b) of the sample A-40MPa reactivated after 5 weeks of aging from the tableting (orange). In black, the corresponding spectra of Powder-1stday are also shown for comparison

sponding comparison has also been made for H2-40MPa tablet and it is shown in Figure 5.12.

After reactivation of the sample Powder-5weeks-reactivated, the amplitude of the main peak of the spectrum acquired at 77 K has a partial recovery and returns close to that observed in the spectrum acquired for Powder-1stday. Likewise, in figure 5.3(b) (at 300 K) we note a total recovery of the signal after the reactivation, as it has almost the same intensity of that of Powder-1stday. In conclusion, as already reported previously, this heat treatment has a total recovery effect in the aged Powder sample.[140]

Contrary to what was seen for B-40MPa and Powder, in this case A-40MPa-5weeks-Reactivated and H2-40MPa-Reactivated have dissimilar spectra with very different line-shapes, both at 77 K and at 300 K compared to the Powder sample. In particular, at 300 K (figures 5.11(a) and 5.12(a)), we observe that the spectra are symmetric and now centered at 315 mT, but they are visibly narrower than the Powder sample, with a width of about 70 mT. Furthermore, the A-40MPa-5weeks-Reactivated spectrum has
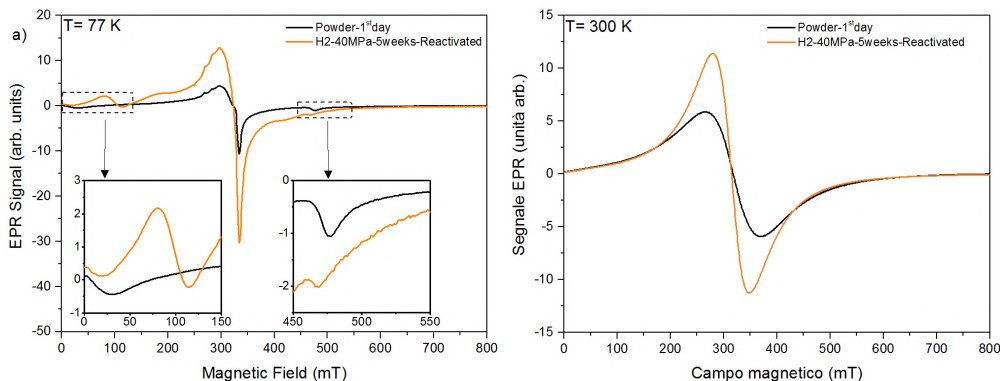
FIGURE 5.12: EPR spectra acquired at 77 K (a) and 300 K (b) of the sample H2-40MPa reactivated 5 weeks after the tableting (orange). In black, the corresponding spectra of Powder-1stday are also shown for comparison.

an amplitude at least three times larger than A-40MPa-1stday. Similar remarks apply also to the H2-40MPa sample. Both the spectra of the two tablets obtained at 77 K (figures 5.11(b) and 5.12(b)) show the disappearance of the contributions attributed to the triplet signal, located at 12 mT and 470 mT. At the same time, the central peak changes significantly shape and a new feature having a maximum at about 80 mT appears.

5.1.1 XRD patterns and nitrogen isotherms.

Figures 5.13 and 5.14 show the XRD patterns and the N_2 isotherms of the powdered sample (Powder-1[st]day) and of the samples A-40Mpa e B-40MPa, before and after aging (A-40MPa-1[st]day, B-40MPa-1[st]day, A-40MPa-5weeks, B-40MPa-5weeks). As indicated
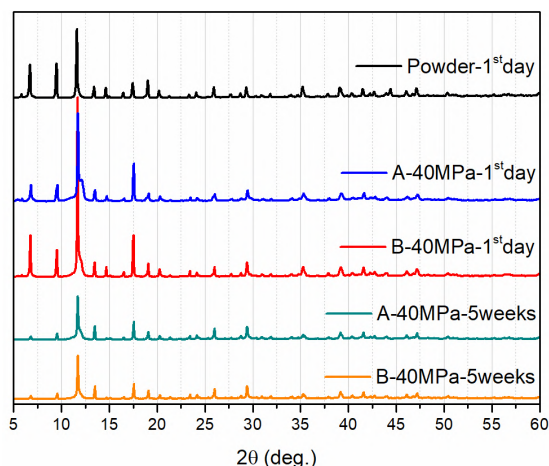

FIGURE 5.13: XRD patterns of Powder sample, A-40MPa-1[st]day, B-40MPa-1[st]day, A-40MPa-5weeks and B-40MPa-5weeks tablets.

in figure 5.13, the Powder sample can be identified as typical HKUST-1 material possessing Cu-units in paddlewheel conformation arranged through BTC ligands in cubic Fm-3m open framework lattice. Compression process does not have significant effect on the overall crystal structure, confirming the rigidity of the Cu-BTC network. Unit cell
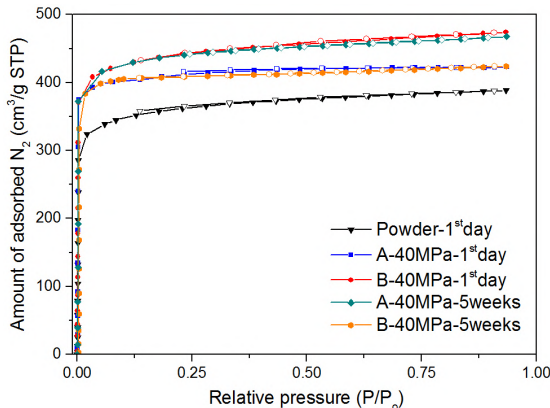
FIGURE 5.14: N$_2$ isotherms of Powder sample, A-40MPa-1stday, B-40MPa-1stday, A-40MPa-5weeks and B-40MPa-5weeks tablets.

TABLE 5.1: Unit cell parameters.

Sample	$a(\text{Å})$	$V(\text{Å}^3)$
Powder	26.348(2)	18291(4)
A-40MPa-1stday	26.343(6)	18282(12)
A-40MPa-5weeks	26.374(5)	18346(10)
B-40MPa-1stday	26.347(3)	18289(7)
B-40MPa-5weeks	26.371(3)	18338(7)

volume of the sample A-40MPa-1stday decreases by just 0.05% (table 5.1) but more significant are the changes in broadening and occurrence of the separate broad peaks near (111) and (222) reflections on the XRD pattern, or rather near the peaks at 5.8° and 11.5° respectively, due to the tetragonal strain of cubic lattice along [111] crystal plane.

Such a high-pressure lattice distortion was already predicted by DFT calculations and can be described as a consequence of the deformation of interfacial angles between paddlewheels and interatomic O-C$_{carboxylate}$-C$_{phenyl}$ angles.[195] However, lattice deformation seems to be partially reversibly recovered after subsequent reactivation of the tablets (sample B-40MPa-1stday) indicated by the less pronounced peak broadening in comparison with the sample A-40MPa-1stday. Moreover, unit cell parameters of the sample B-40MPa-1stday become almost identical to the ones of the powdered sample. In both the aged tablets, broadening of the peak at about 11.5°, that is (222) reflections seems to be less pronounced than in fresh tablets, but aging apparently causes a small reduction of the intensity of the peaks below 20° and a slight expansion of the unit cell for 0.3%. The peak at about 14.5° seen in the fresh tablets changes in two smaller peaks in the aged tablets (reflections (331) and (420)). This effect was already observed by Schlichte and co-authors[135] and it is caused by the presence of water in the lattice.

N$_2$ sorption isotherm of all the samples show typical Type I isotherm commonly observed for pure microporous materials with no desorption hysteresis and no increase

TABLE 5.2: BET surface area of the Powder sample and some A- and B-type tablets.
The analysis was performed in the relative pressure range of the increasing trend of
the Rouquerol plot.

Sample	BET Surface Area (m^2/g)
Powder	1620
A-40MPa-1st day	1685
A-40MPa-5weeks	1848
B-40MPa-1st day	1935
B-40MPa-5weeks	1622

in N_2 uptake at relative pressures p/p_0 close to 1 (see section 1.6). The BET surface
areas of the samples are shown in table 5.2. BET surface area of the powdered sample is
in the expected range for HKUST-1 powdered materials. Surprisingly, the compression
has positive effect on the microporosity which is indicated by the substantial increase of
the S_{BET} values to 1685 m^2/g for A-40MPa-1st day and becomes even more significant for
the tablet B-40MPa-1st day ($S_{BET} = 1935$ m^2/g). The aging of the tablet does not affect
the porosity significantly, and the BET surface areas change only for approximately 15%
for both the A and B samples. Furthermore, the load capacity of the tablet samples
(both as-prepared and aged) is slightly higher than that of the powder sample.

5.1.2   Morphological studies

Combined optical/AFM studies have been performed in order to gain more information
on the morphological properties of the investigated samples. In particular, we have
deeply investigated the properties of the B-40MPa tablet and compared it with those
of the pristine powder of HKUST-1. The results are reported in figures 5.15 (powder)
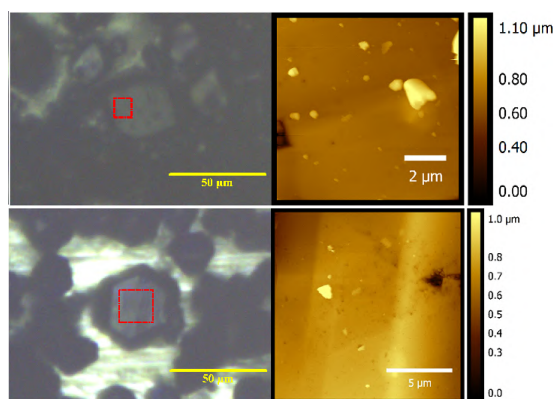and 5.16 (B-40MPa tablet).

FIGURE 5.15: Optical and AFM images of HKUST-1 powder.

They confirm that the B-40MPa tablet retains the granular morphology of HKUST-1
in powder form, as suggested by the optical images previously shown in 3.1.6.
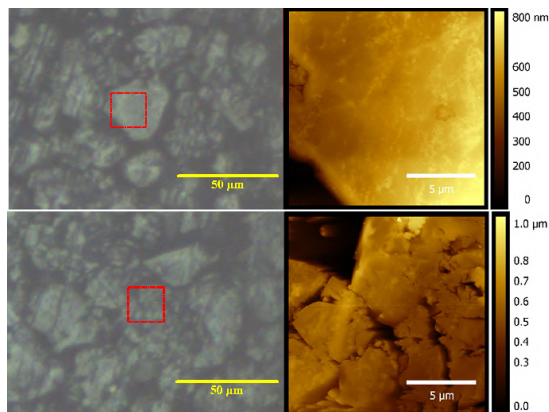
FIGURE 5.16: Optical and AFM images of HKUST-1 tablet B-40MPa.

5.1.3 Water sorption isotherms and thermogravimetric analysis

In order to further compare the properties of B-40MPa tablet with those of the Powder sample, water isotherm measurements have been run (figure 5.17). Pristine HKUST-1
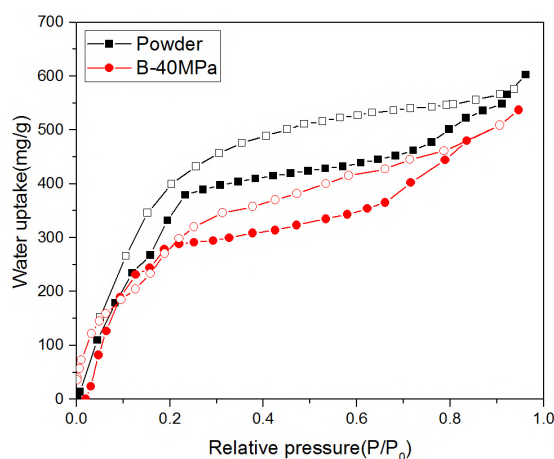

FIGURE 5.17: Water isotherms of the samples Powder (black squares) and B-40MPa (red circles) measured at 300 K. Adsorption – full points, desorption – empty points.

powder shows typical near type I water isotherm, characterized by two distinctive uptake contributions: the first step is up to relative pressure of 0.25 and it is assigned to the coordination of water on unsaturated Cu^{2+} sites whereas the second step is due to the consecutive filling of the remaining large pore space.[141] Above $p/p_0 = 0.25$ the water uptake curve shows a saturating tendency. Additional uptake at higher relative pressures ($p/p_0 > 0.75$) is due to the water condensation within the interparticle voids. The significant desorption hysteresis of HKUST-1 powder is a consequence of the strong hydrogen bonding between the cluster of water molecules located within the large hydrophilic pores. Desorption of water does not seem to be completely reversible since the coordinated water is bonded to coordinately unsaturated sites by chemisorption. The water isotherm of the sample B-40MPa shows a similar rapid increase in water uptake at relative pressures $p/p_0 > 0.15$ as in the case of the pristine powder, however the second step is much less pronounced and the water sorption capacity at saturation is

lower for approximately 25% if compared with powdered HKUST-1. The change of the isotherm shape of the tablet indicates that even if the free Cu^{2+} sites are fully available for the water coordination, the filling of the remaining large pore becomes somewhat obstructed. Anyway, desorption is almost completely reversible.

The TGA curves for the A-, B- and H- type samples are compared in figure 5.18. These measurements clearly show that the considered samples have a different degree of hydration, which increases in the following order: B-, A-, H2- and H1- sample. All the considered samples have a comparable thermal stability, as they exhibit just minor changes of the temperature of crystal decomposition. Interestingly, smaller temperatures of crystal breakdown are observed for the samples with higher degree of hydration. Furthermore, as it is evident in figure 5.18, above the temperature of decomposition the TGA curves obtained for tablets share common features between them, but they differ significantly from those observed for powder samples, suggesting that the decomposition pathway is somewhat different for HKUST-1 in powder and tablet forms.
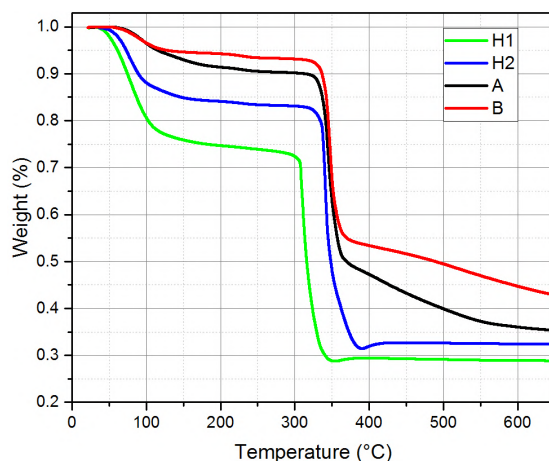

FIGURE 5.18: Normalized TGA traces of HKUST-1 tablets B-40MPa (red) and A-40MPa (black), and hydrated powder samples H_1(green) and H_2 (blue).

5.2   Discussion

The experimental data reported in figure 5.2 concerning H1-40MPa sample prove that 20 minutes of exposure to air on a petri suffice to severely damage the crystal structure of HKUST-1 material and to compromise any eventual further treatment as, in our case, tableting. At variance, the EPR spectra of the sample H2-40MPa (figure 5.3(a)) indicate that a soft hydration does not compromise the structure of the powders of HKUST-1. However, after tableting of the hydrated powders, both the EPR spectra obtained at 77 K and 300 K undergo relevant changes (figures 5.3), suggesting that the matrix of HKUST-1 is distorted and/or broken in many sites. Finally, let us consider the spectra reported in figure 5.5 for the sample A-type compacted with a pressure of 40 MPa, that is a tablet obtained from powders not intentionally exposed to air but just rapidly handled in air during the procedure of tableting. The changes induced in the

EPR spectra at 77 K and 300 K are significantly reduced compared to the previous one (H2-40MPa, figure 5.3). Since the sole difference between the latter two samples is the degree of hydration, higher for the former than for the latter, this comparison points out that the water adsorbed on HKUST-1 powders before compaction is one fundamental source of instability of the structure of the material during compaction. In particular, we believe that water molecules may facilitate the distortion and/or the breaking of the lattice during the application of the mechanical pressure to the sample. The distortions may be simply related to steric factors, whereas permanent bond breaking may be due to hydrolyses processes presumably promoted to allow the network to release part of the huge stress induced during compaction of the powders. We have estimated, on the basis of the TGA measurements, a number of water molecules adsorbed for Cu^{2+} site of about 3.8, 2.1, 1.0 and 0.67 for the samples H1 powder, H2 powder, A- and B-type tables, respectively. A compatible value of 0.6 has also been obtained for B-40MPa by referring to the water isotherm measurements (figure 5.17) and considering that the tableting process takes place at RH=70% and at room temperature.

On the basis of all of these preliminary experimental evidences, we have decided to focus our attention in particular on tablets obtained from dry HKUST-1 powders.

In figure 5.5, we have shown the EPR spectra of A-type tablets. In figure 5.5(a) in particular, we have noted that the amplitude of the central resonance increases on increasing the applied pressure. This new contribute has some spectral features very similar to that assigned to the paramagnetic centers $[Cu(H_2O)_6]^{2+}$.[133] Therefore, it is reasonable to assume that this additional signal is also due to the spin 1/2 of Cu^{2+} ions, as well as the centers induced by the hydration effects (see chapter 4 and section 2.3.2). Considering that the concentration of preexisting $[Cu(H_2O)_6]^{2+}$ complex is a fixed quantity, the increase in intensity of this peak reasonably involves the decoupling (partial or total) of some Cu^{2+} pairs in a certain number of paddlewheels of the material. In other words, there are two different S=1/2 spin centers which have comparable resonance magnetic fields, leading to a superimposition of the correspondent peaks.

The paddlewheel decoupling mentioned may have origin from a reversible distortion of the paddlewheels or from some irreversible processes, in which the breakdown of some Cu-O bonds is involved. On the basis of these assumptions and of data in figure 5.5(a), we argue that the higher is the pressure involved, the greater is the damage induced in the lattice. Calculating the double integral (DI) of the EPR signal due to S=1/2 species induced by pressure, we have obtained an evaluation of the damage induced to the lattice.

We can express these results in terms of spin concentration, for a quantitative estimate of the percentage of damaged paddlewheels (with the method explained in section 3.2.1). The outcomes are shown in figure 5.19, where we report the percentage of paddlewheels per unit volume damaged by compaction as a function of the applied pressure. The amount of broken paddlewheels increases on increasing the pressure and it reaches the maximum value of only about 4% for a pressure of 40 MPa. Since the powders pressed at 40 MPa show a good mechanical strength (figure 3.5) and a very small
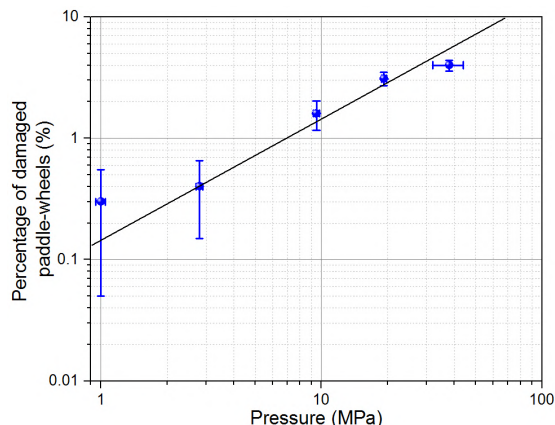
FIGURE 5.19: Percentage of damaged paddlewheels as a function of the applied pressure in logarithmic scale. The traced line has slope of 1.

amount of damaged paddlewheels, a pressure of 40 MPa represents the best choice for tableting HKUST-1 powder. It is important to underline that the growth of the signal due to the spin $S=1/2$ centers cannot be easily quantitatively correlated to the decrease of the signal due to the triplet centers present in the spectra obtained at 77 K. In fact, as discussed in section 1.1, the two species of paramagnetic centers involved, spin $1/2$ and interacting spin $1/2$ pairs, follow Curie and Bleaney-Bowers laws of magnetic susceptibilities, respectively. The latter, in particular, is characterized by an exponential functional dependence with respect to the coupling constant J_0 (eq. 1.8) and consequently even small change of the value of J_0 induced by compaction may significantly affect the amplitude of the EPR signal relative to the triplet centers.

The experimental data discussed above make clear that if the starting HKUST-1 in powders form is enough dry and preserved from air moisture, its lattice undergoes only negligible damages when it is subjected to a pressure of 40 MPa. In other words, by preserving the material from air moisture before tableting it is possible to obtain HKUST-1 tablets of great quality; but there is more: reactivating the tablets immediately after tableting, an almost complete recovery of the spectral characteristics of the pristine HKUST-1 powders is observed, as proved by the results obtained for the sample B-40MPa (figure 5.6). In particular, the resonance located at about 325 mT at 77 K, whose intensity quantify the damage induced in the crystalline matrix, drastically reduces its amplitude as a consequence of this reactivation. Furthermore, the peaks of the hyperfine structure become again clearly evident (as opposed to sample A-40MPa where they disappeared), indicating a sort of recovery of the pristine structure for most of the paddlewheels.

Our results also indicate that A-type tablets are affected by a gradual spontaneous structural degradation process (figure 5.4), whereas these effects are absent in B-type tablets (figure 5.9), indicating that the post tableting activation is also capable to prevent this undesired evolution of the sample and consequently to make the tablets stable in time. Again such outcomes suggest the involvement of water molecules as a source of

structural instability. In fact, the spontaneous degradation of the crystal of HKUST-1 network after tableting is reasonably related to the release of the residual mechanical stress induced by tableting on the network by hydrolysis of highly strained bonds. This process is probably due to the water molecules adsorbed by the sample during the procedure of tableting, which may be located into the cavities of HKUST-1 or into the interstices between the grains packaged to form the tablet. According to this hypothesis, the reactivation after tableting has the effect to allow the network to release most of the stress induced by compaction and contemporarily to further release water molecules from the sample. Anyway, it is clear from figures 5.11 and 5.12 that the reactivation has a recovery effect on the properties of the tablets only if it is performed within few hours from the tableting. This picture about B-type samples is in line with the results of XRD, which indicate a reduction of the lattice deformation as a consequence of post-tableting reactivation (figure 5.13).

The properties discussed above, obtained mainly on the basis of the study of the magnetic properties of the samples, are also fully supported by the results coming from BET analysis. Indeed, it proves that the sample B-40MPa has a value of specific surface that is even better than that of the pristine HKUST-1 powders, a result which mark a new relevant goal in the research field focused on MOF tableting. In addition, we have also experimental evidences of an excellent degree of packaging of the tablets, obtained from the optical/AFM images (figures 3.1-5.16). Such excellent degree of packaging, while preserving a granular structure similar to that of the pristine material, agree very well with the other results we have found indicating that B-40MPa tablet actually has an effective density comparable to that of the skeleton of HKUST-1, but without a significant damage of the crystalline network. Although the main initial granular structure of the pristine powders of HKUST-1 is preserved in type-B tablet, it is clearly evident from AFM images that the largest grains are broken in many fragments as a consequence of the tableting process (figures 5.15 and 5.16). These effects, together with the spatial reorganization of the grains, presumably helps the system to reach a better level of volume packaging during the application of the pressure.

For the sake of completeness, we could also analyze the compaction from a microscopic point of view: in these terms, the transformation from powder to tablet can be seen as an interparticulate bonding process.[196] The nature of these bonds traditionally spaces from intermolecular/electrostatic forces to mechanical interlocking, or to the establishment of solid bridges and so on. In our case, we deal with dry powder and then the dominating processes involved are typically considered to be both the bonding due to intermolecular forces and that due to the formation of solid bridges; in contrast, the mechanical interlocking between particles is considered much less significant.[196] Assuming we have brought into intimate contact two solid surfaces, intermolecular forces act at separation distances of approximately 10÷100 nm. Differently, the development of a solid bridge involves the formation of a continuous solid phase at the interface of the particles, which in turn requires a certain degree of mobility of the particles compressed, at least temporarily. In addiction, some bonds may also be formed between adjacents

granule involving a small degree of "*fusion*" of their surfaces during compaction, but this phenomenon is generally considered less significant than the establishment of intermolecular forces above mentioned.[196] Lastly, the mechanical interlocking involves an interparticulate hooking which generally requires particles with irregular shapes or rough surfaces.[196] In our case, since the AFM images clearly show that the grains have typically smooth surfaces, we can assume, in accordance with literature, that the mechanical interlocking cannot have a high impact on the effects of the compaction process. However, since the research on MOF packaging, as well as this thesis, is primarily focused on what happens to the crystal structure and to the adsorption properties of these materials upon compaction, in the MOF literature this approach is generally not even mentioned. For this reason, a deeper characterization of the microscopic forces involved is also out of the scope of this thesis and, apart from the previous brief comments, in the following we will not dwell on this particular aspect of the compaction processes.

Conclusions of the chapter

Here we have reported an original experimental investigation on the effects of mechanical compaction on the structure and on the properties of HKUST-1 powders by monitoring the changes induced by tableting on its magnetic properties by EPR spectroscopy. Thanks to the extraordinary potentialities of this technique in investigating the properties of magnetic materials, we were able to unveil many fundamental properties of the process of tableting of HKUST-1. In particular, we have recognized for the first time that tableting process always induces the growth of S= 1/2 paramagnetic centers in the materials, whose number increases on increasing the applied pressure. This component derives from the distortion and/or breaking of a fraction of the paddlewheels of the material, and thus it can be used to obtain a quantitative estimate of the damage induced by compaction in the lattice in correspondence of the metal group. Thanks to this approach, we have unveiled that the number of such defects, and consequently the degree of degradation induced in HKUST-1 upon mechanical compaction, is strictly related to the level of hydration of the starting powders.

In particular, we have estimated that the percentage of paddlewheels damaged by tableting with a pressure of about 40 MPa is as low as 4% for HKUST-1 tablets obtained from dry powders, i.e. containing less than one water molecule adsorbed for Cu^{2+} ion. In addition, we have proved that subjecting the tablets to a further thermal activation just after compaction, this defective EPR component is further drastically reduced and the proprieties of the system becomes virtually indistinguishable to those of activated powders of HKUST-1 with the pristine structure. Furthermore, the same reactivation treatment was found to make the tablet stable in time.

All these outcomes are fully supported even by all the other experimental techniques we used in the present work, which are: XRD, N_2 absorption and BET analysis, TGA, water sorption isotherms and atomic force (AFM) microscopies.

Summarizing, our results have proved that it is possible to obtain stable tablets of HKUST-1 with the pristine structure by simply taking care to activate the material just before and just after tableting.

Chapter 6

Monolithic HKUST-1: properties and comparisons.

In this chapter a detailed comparison between three different forms of HKUST-1 are shown: commercial powder, compacted tablets and sol-gel monolith. The objective is a systematic study of the two different densified HKUST-1 materials and of powders, comparing structural and adsorption properties as well as water stability.

In chapter 5, we paid special attention on the tablet produced by using a mechanical pressure of 40 MPa and then subjected to a reactivation process (or else, named B-40MPa). Also in this chapter we use the tablet B-40MPa as representative for the HKUST-1 powders densified by mechanical compaction. Hereafter it is named simply "*tablet*".

Using the commercial powder as reference point, we report on the water stability properties of these materials. By EPR spectroscopy, monitoring the changes induced on the magnetic properties of the materials by densification and/or by air moisture, we have been able to estimate how many damages are induced by the densification process and the degree of hydration after which each material undergo hydrolysis.

6.1 Structural Properties

Before investigating its water stability, we report on the main properties of the monolithic HKUST-1, in order to compare it with the commercial MOF powder.

PXRD pattern and nitrogen isotherm. Figure 6.1 shows the PXRD pattern acquired for a HKUST-1 monolith. For comparison, the correspondent pattern for the commercial powder is also shown in black. The comparison establishes that the monolith synthesized has the same crystal lattice of the commercial powder. The peaks in the monolith pattern are only less intense: this may be due to the co-presence of an amorphous phase in the monolith structure; this assumption has been already done by Tian and co-authors (see section 2.3.3).

Figure 6.2 shows the nitrogen isotherm acquired for the monolith. Its shape is that typical of materials with micropores with dimensions not exceeding 1 nm (see section 1.6). The only difference with the isotherms generally observed for HKUST-1 powder
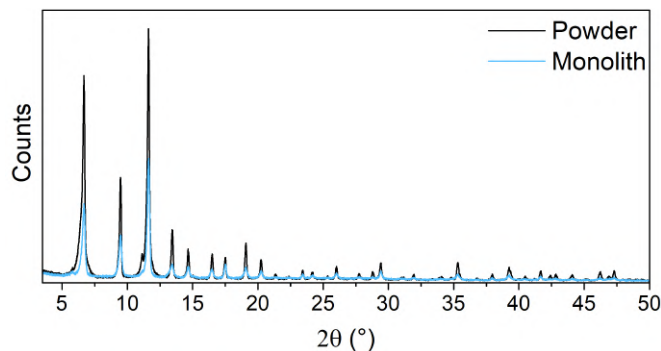
FIGURE 6.1: PXRD patterns of a HKUST-1 monolith compared with that of a standard powder sample.

samples is that these latter generally are perfect type I isotherms with a saturation value, whereas for the monolith we observe an increasing in uptake at high relative pressures, indicative of the presence of macropores or sites promoting the *pore condensation.*
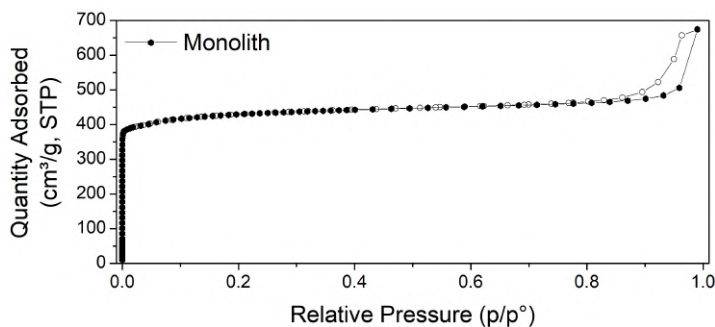

FIGURE 6.2: Nitrogen adsorption (—●—) and desorption (—○—) isotherm acquired for HKUST-1 monolith.

A surface areas of 1670 m^2/g was estimated by fitting the adsorption curves with the BET method. The value is strongly comparable with that of standard HKUST-1 powders (see also previous result chapters).

Raman spectrum. Figure 6.3 shows the Raman spectrum acquired for a HKUST-1 monolith. Because of the irregular shape and roughness of the monolithic sample, contrary to the measurements performed on the other samples, the objective "20×" working at a distance of 1.3 mm has been used, but obtaining a worse signal-to-noise ratio. Due to this, only few peaks can be well detected and characterized. Nevertheless, most of the characteristic peaks of the powder sample are clearly recognizable even in the spectrum of the monolith. For this reasons, no significant differences may be individuated between the spectrum of the monolith and that of the standard powder, indicating virtually indistinguishable vibrational properties.

EPR spectra. Figure 6.4 shows the EPR spectra acquired at 77 (a) and 300 K (b) for the HKUST-1 monolith. For comparison, those of the commercial powder and of the tablet are shown.
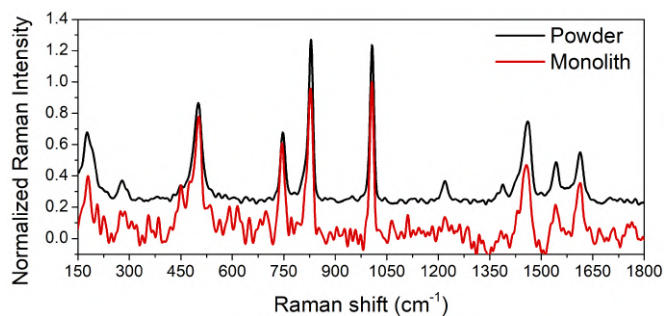
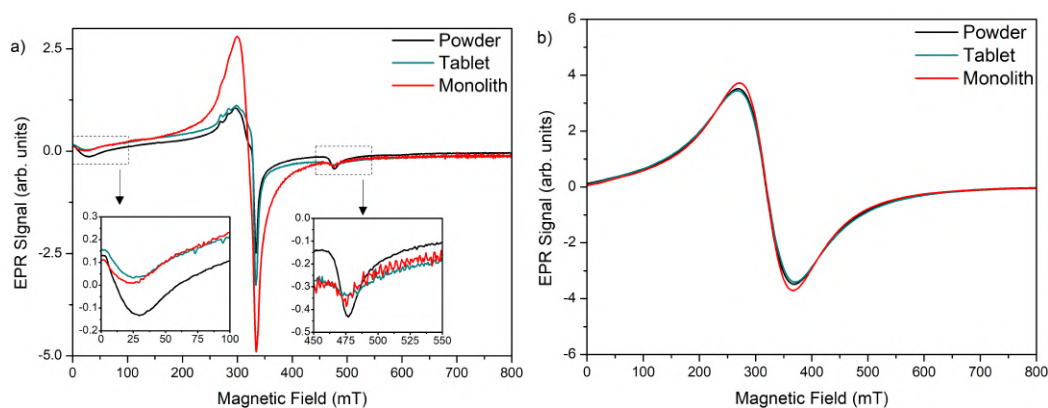FIGURE 6.3: Raman spectrum of an as made HKUST-1 monolith compared with that of a standard powder sample.

FIGURE 6.4: Comparison of the EPR spectra acquired at (a) 77 and (b) 300 K for powder (black), monolith (red) and 40 MPa tablet (dark cyan) HKUST-1.

If the EPR spectra of the three samples obtained at room temperature are virtually indistinguishable, those acquired at 77 K show some minor differences. The triplet resonance is clearly visible, even though the two peaks are slightly larger, probably due to a diffuse small disorder which leads to a slight structural inhomogeneity between the paddlewheels. The typical shape of the peak centered at $\sim$320 mT due to the monomeric complexes is generally characterized by a well-resolved hyperfine structure and a slight shoulder is quite different in the spectrum of the monolith, showing a barely detectable hyperfine and no shoulders. Probably, this synthesis method leads to heterogeneous synthesis defects.

6.2 Water stability: comparison with powder and tablet

In chapter 4 we have already seen the effects of the interaction with water on a sample of commercial powder on a time scale of 60 days. Since HKUST-1 powder shows remarkable signs of decomposition already during the first day of exposure in conditions of 100% RH, in order to compare the water stability of the three different forms of HKUST-1, we have considered sufficient a time scale of only 24 hours.

In figure 4.6 we report a more detailed EPR characterization of such effects on a HKUST-1 powder sample exposed to 100% RH for a total time of 24 hours, both at 77

and 300 K. For the sake of clarity, some of the spectra have been vertically scaled as indicated in the legends.
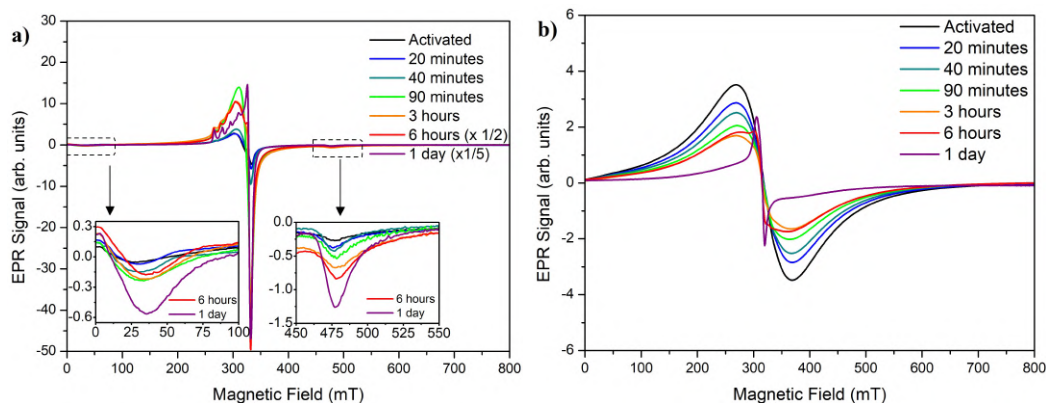

FIGURE 6.5: EPR spectra obtained for HKUST-1 powder acquired at 77 (a) and 300 K (b) after exposure to humidity for the indicated times. In the two insets, showing the zooms of the spectrum regions enclosed by the dashed panels, the spectra are not multiplied by any factor.

As already discussed previously, EPR spectra acquired for HKUST-1 in powder form show the most significant changes after 6 hours of exposure: in particular, a new signal is observed at about 320 mT at both temperatures, ascribed to paramagnetic centers originating from the hydrolysis of a fraction of Cu paddlewheels (see section 2.3.2 and chapter 4). Although this peak is only just outlined at 300 K after 6 hours, it becomes the dominant component in the spectrum acquired after 1 day of exposure. Differently, in the spectra obtained at 77 K, this signal is superimposed to that present also in the pristine sample (which is centered at about 320 mT too) and ascribed to the synthesis defects involving monomeric Cu complexes. However, its growth has the same time scale.

Figures 6.6 and 6.7 show the correspondent spectra acquired at both 77 and 300 K for the tablet and the monolith.
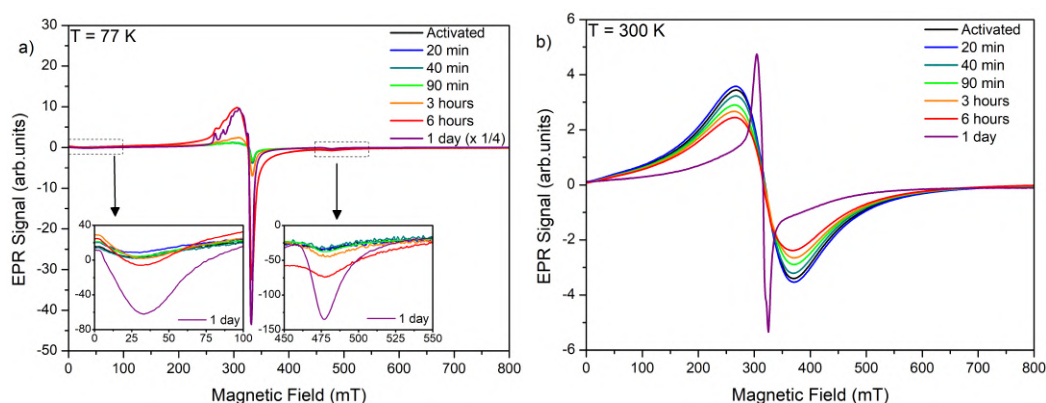

FIGURE 6.6: EPR spectra obtained for HKUST-1 B-40MPa tablet acquired at (a) 77 and (b) 300 K after exposure to humidity for the indicated times. In the two insets (panel a), showing the zooms of the spectrum regions enclosed by the dashed panels, the spectra are not multiplied by any factor.
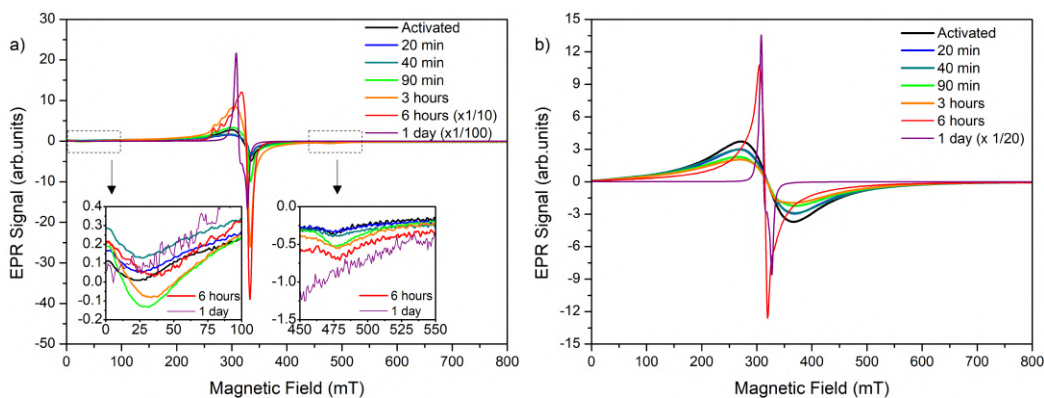
FIGURE 6.7: EPR spectra obtained for HKUST-1 monolith acquired at (a) 77 and (b) 300 K after exposure to humidity for the indicated times. In the two insets (panel a), showing the zooms of the spectrum regions enclosed by the dashed panels, the spectra are not multiplied by any factor.

The spectra of the tablet sample show changes very similar to those observed for the powder sample. More in detail in the spectra obtained at 77 K we observe an increase of the signal peaked in the field range of about 320 mT which becomes significant after 6 hours of exposure. The triplet resonance is clearly visible even after 1 day of exposure, whereas at 300 K the progressive decrease in intensity of the triplet curve is regular up to 6 hours of exposure and followed by the sudden appearance of the narrow peak centered at 320 mT.

Significantly different is the evolution of the spectra acquired for the monolith sample. In fact, in the spectra obtained at 77 K we observe a very abrupt increase in intensity of the peak centered at 320 mT, also accompanied by the disappearing of the resonance of the triplet centers, whereas in those obtained at 300 K the narrow resonance becomes much faster than the dominant component already in the spectrum acquired after 6 hours of exposure and even with a very large intensity.

6.2.1 Discussion

The characterization performed concerning the structural properties of the monolith pointed out that the monolith synthesized via the sol-gel method is strongly similar to the commercial HKUST-1 powder: it even shows a comparable BET surface area despite the presence of an amorphous component, mainly highlighted by the XRD pattern and the wide triplet resonance in the EPR spectrum. In particular the BET surface area calculated of 1670 m^2/g is even higher than those found in literature[97], even though the nitrogen isotherm points out a pore condensation phenomenon at high p/p$_0$.

However, the water stability of the monolithic HKUST-1 is sensibly different to that of the standard powder.

Similarly to what has been done for the analysis of the spectra acquired for the study on the mechanical compaction of HKUST-1 (see chapter 5), we can calculate the double integral of the EPR signal under the peak centered at 320 mT in the EPR spectra acquired at 77 K in order to obtain an estimate of the defects induced by the

hydrolysis. Figure 6.8 shows the estimated number of paramagnetic S=1/2 spin centers per unit volume present in each samples as a function of the exposure time (from 0 to 24 hours). It can be useful to recall that these values represent the sum of the starting
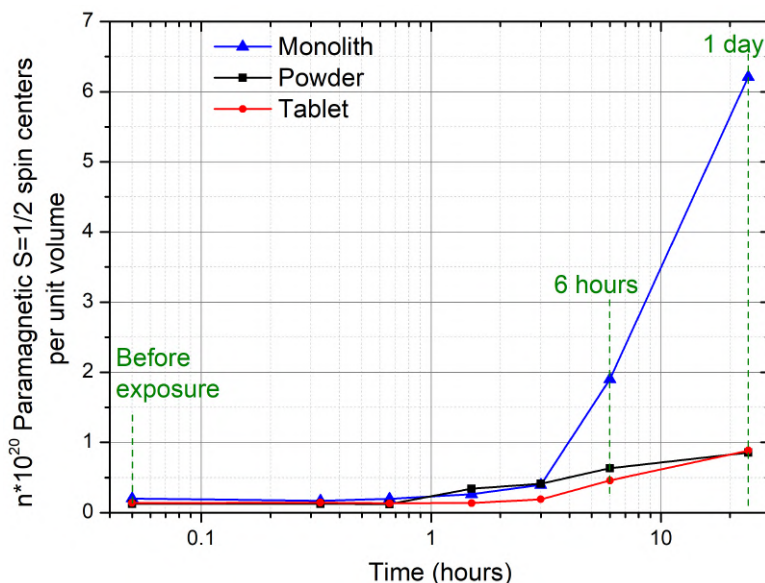

FIGURE 6.8: Estimated number of paramagnetic S=1/2 spin centers per unit volume present in each samples after a given exposure time to 100% RH.

defect synthesis (that is the monomeric complexes present in the pristine materials) and of the paramagnetic centers induced by the hydrolysis. The amounts of pre-existing S=1/2 spin centers in each sample are simply done by the "*Before exposure*" point values in the figure 6.8, and then they are not exceeding $\sim 0.02 \cdot 10^{21}$ centers per unit volume.

From figure 6.8 it becomes evident that the monoliths undergo a more severe decomposition process than both powder and tablet, which show a similar evolution. Considering that a content of about 1.3×10^{21} paddlewheels per unit volume can be theoretically estimated for an ideal crystal of HKUST-1, the formation of $\sim 0.62 \cdot 10^{21}$ S=1/2 spin centers after 1 day of exposure is indicative of the breakage of at least half of the total amount of paddlewheel.

For the reasons explained so far, the monolith appears as a material which limits the potential application in humid environment even more than the commercial powder, which is already considered prohibitive for the commercial industrialization (see section 2.2.2). In contrast, the tablet obtained with the optimized procedure discussed in the previous chapter not only did not show a worsening in the stability properties, but rather exhibits a slight delay of the trigger of the hydrolysis effects.

Conclusions of the chapter

The monolith synthesized showed interesting potentialities: it shows a high BET surface area which is comparable with that of the standard HKUST-1 powder, it can be considered overall highly crystalline, and it even exhibits spectroscopic properties very similar to those of the commercial material. As a novelty, it provides the vantages proper of a monolithic material and then it shows a better ease of handle and, as known from the literature data, a significantly improved bulk density.

Despite this, from our comparative study about the water stability properties, we determined that the most promising form of densified HKUST-1 material are the tablets, because they result to be the most water-resistant as well as the easiest to get densified system.

Certainly, a deeper characterization on the adsorption properties is necessary in order to do a complete panoramic on the performances of these two densified forms of HKUST-1. In particular our future perspective regarding this subject involves measurements of methane adsorption, as well as hydrogen or carbon dioxide. If also the tablets produced by our protocol are able to achieve the *US Department of Energy target* (see section 2.3.3) about the CH_4 uptake as previously reported for monoliths[97], we could decisively assert that the production of HKUST-1 tablet according to our protocol constitutes an easy and cheap method to introduce HKUST-1 to industrial and commercial chain.

Chapter 7

STAM-17-OEt tablets

In the previous chapters 5 and 6 we have discussed about the properties of densified HKUST-1 materials, in the form of monolith and of tablets obtained by application of mechanical pressure on HKUST-1 powder. Both the forms have been compared with the standard commercial HKUST-1 powder.

In this chapter, we discuss about the effects induced on STAM-17-OEt by the application of a mechanical pressure on the powders, in order to produce STAM-17-OEt tablets with high bulk density. We will prove that it is very resistant and suitable for the mechanical compaction with pressures up to at least 200 MPa, with a significant increase of its packing density. Furthermore, both its hemilability and the water stability characteristic of STAM-17-OEt are preserved.

These properties were proved by electron paramagnetic resonance spectroscopy, powder X-ray diffraction, Raman spectroscopy and atomic force microscopy.

7.1   Results and discussion

EPR measurements on the STAM-17-OEt tablets

For sake of clarity of the following EPR spectra, in figure 7.1 we show the direct comparison between the spectra of an activated powder (black line) sample with a hydrated powder sample (purple line), acquired at 77 (a) and 300 K (b).
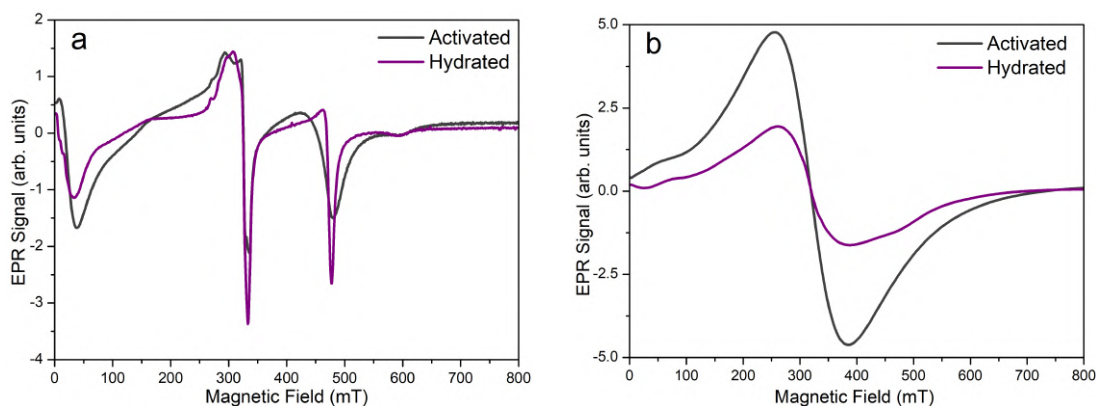

FIGURE 7.1: EPR spectra obtained at 77 (a) and 300 K (b) for a sample of STAM-17-OEt powder activated (black) and hydrated (purple).

As already discussed in chapter 4, the EPR signals obtained for activated and hydrated STAM 17-OEt differ significantly in many aspects at both temperatures. Some of such differences are directly related to the hemilability of the material. Between them, first of all, at 77 K, in the hydrated spectra the peak at 470 mT is significantly narrower and with a larger amplitude than the equivalent features in the spectrum of the activated powder. We have concluded in chapter 4 that this variation in lineshape is due to the change in the inter paddlewheels connections. In fact, as a consequence of the adsorption of water molecules, a crystal transition occurs, leading the framework to a structural arrangement with a higher order, which determines the reduction of the inhomogeneous component of the EPR line width. Furthermore the peak at about 15 mT shows a progressive shift to lower fields, accompanied by the appearance of a fine structure. The differences between the lineshapes of the two spectra acquired at 300 K are less marked, but small shoulders are visible in the hydrated samples both at low fields and at about $460 \div 490$ mT; the stronger difference between the two spectra is instead the intensity, which is significantly higher in the activated sample than in the hydrated one. We have seen in chapter 4 that this latter aspect seems to be characteristic of the copper paddlewheel unit based MOFs; in fact, it has been also observed in HKUST-1 after few hours of exposure to air moisture.

We have also already proved that for STAM-17-OEt material the transitions between the hydrated and activated configurations are totally reversible in the powder material but it is unknown if this property is preserved in the mechanically compacted samples.

In order to study the effects of mechanical compaction on powder of STAM-17-OE, we prepared tablets starting from activated powders using different pressures, following the optimized protocol defined in 3.1.7, very similar to that used for HKUST-1 (see 5).

The tablets have been measured by EPR, re-hydrated and measured again to evaluate the reversibility of the hydration process in the compacted samples. The EPR spectra obtained at 77 K for the tablets of the *set A* (or else, produced from activated powders, see section 3.1.7) are shown in figure 7.2: STAM-17-OEt in powder form before any mechanical treatment (a) and after the compaction (and the reactivation) at a pressure equal to 3 MPa (b), 20 MPa (c), 50 MPa (d), 100 MPa (e) and 200 MPa (f).

In figure 7.3 the correspondent EPR spectra acquired at 300 K are shown.

The spectra of figure 7.3 shows virtually indistinguishable features, whereas the spectra in figure 7.2 shows just small differences arising only from the peak at about 350 mT. However these discrepancies are not significant, because they do not show any systematic dependence on the pressure applied during the compaction of the powders and also because the amplitude of the peak in each spectrum is lower or at most comparable with that observed in the spectrum of the pristine powder. These differences are quantitatively comparable with the variability of the amount of pre-existing defects observed in the pristine powders and consequently they are naturally attributed to it.

Figure 7.4 shows the EPR spectra obtained at 77 K for some representative tablets of *set A* after the re-hydration treatment. The correspondent spectra acquired at 300 K are shown in figure 7.5.
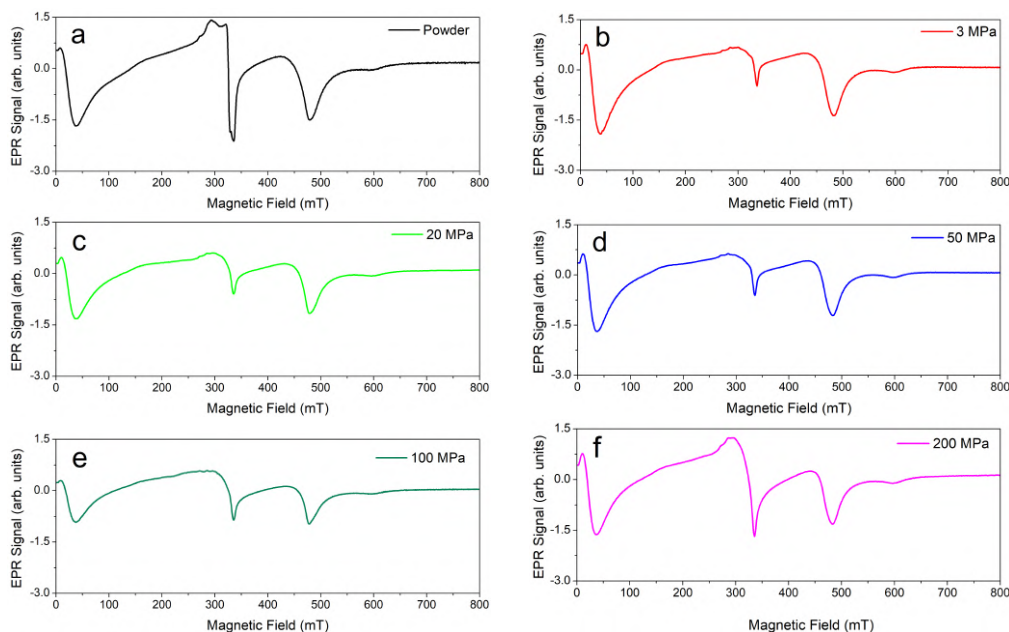
FIGURE 7.2: EPR spectra of the most significant tablets (*set A*) acquired at 77 K.

As shown, each spectrum exhibits the typical spectroscopic features of the EPR spectra obtained for hydrated STAM-17-OEt (compare with figure 7.1). The presence of these features proves that reversible flexibility of the material is preserved. Furthermore, the absence of any sign of decomposition in the EPR spectra in Figure 7.4 and 7.5, indicates that the tablets of STAM-17-OEt preserve also the strong stability towards exposure to water, a characteristic of the pristine powders. In other words, the outstanding stability of STAM-17-OEt is not affected by the mechanical compaction up to at least 200 MPa.
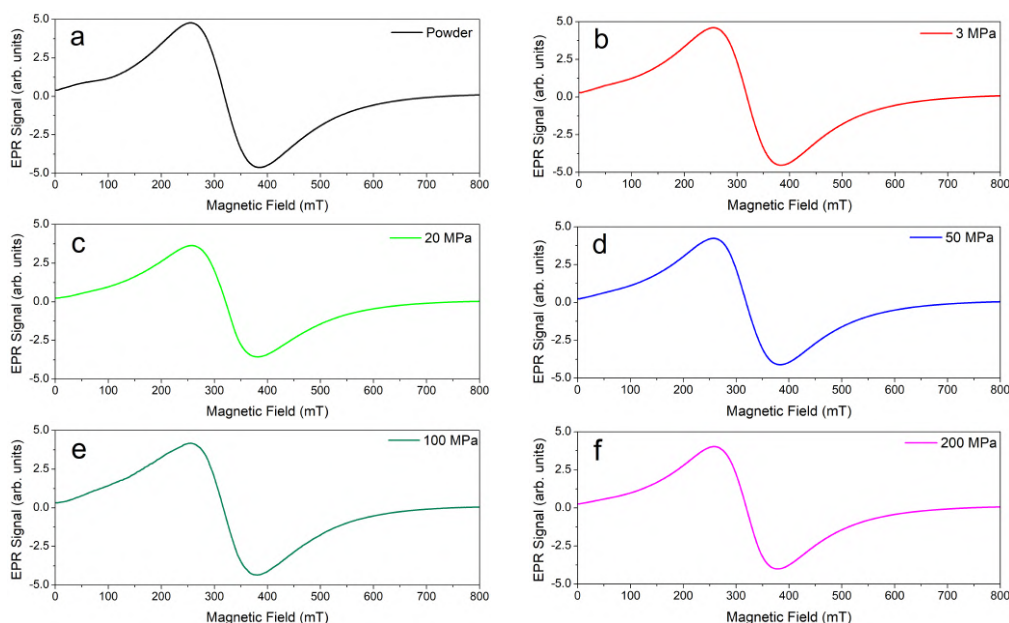
FIGURE 7.3: EPR spectra of the most significant tablets (*set A)* acquired at 300 K.
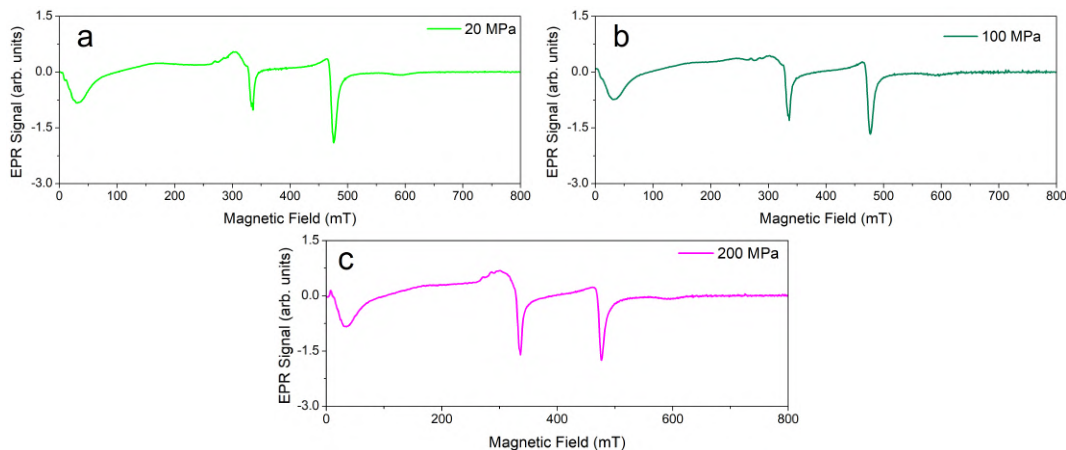
FIGURE 7.4: EPR spectra of the most significant tablets acquired at 77 K after the re-hydration.
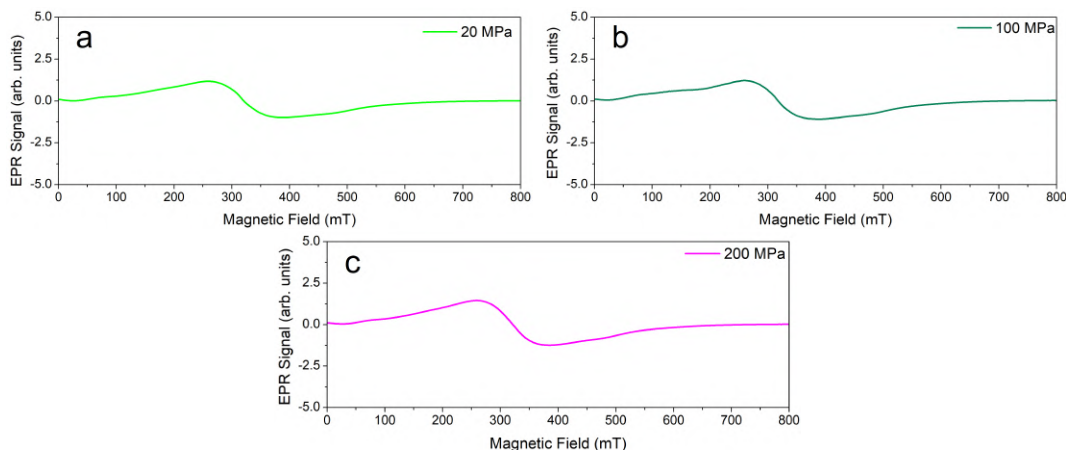

FIGURE 7.5: EPR spectra of the most significant tablets acquired at 300 K after the re-hydration.

In order to further support this conclusion, X-ray diffraction measurements have been performed. Figure 7.6 shows the PXRD patterns acquired for the most significant samples of the *set A*. The tablets used (and the powder sample measured for comparison) have been re-hydrated, because each PXRD measurement requires many hours during which the sample is left in air and consequently it is not possible to catch the pattern of the activated samples. The diffraction pattern of the powder sample (figure 7.6, black line) shows the well-known characteristic peaks of this material in hydrated form (see figures 4.2 and 2.36). The PXRD patterns of the tablets are virtually indistinguishable among them and with that of the powder sample, with peaks of comparable intensity and position. We just note that all the patterns pertaining to the tablets samples show two new small peaks at 11.5° and 12°, indicating that minor but detectable distortions of the long range structure of the material are actually induced.

Figure 7.7 shows the EPR spectra at 77 and 300 K acquired for a tablet of STAM-17-OEt of the set B (or else produced starting from hydrated powders, see section 3.1.7) produced with a pressure of 100 MPa, measured in each step in chronolgical order: activated powder form (a-b), hydrated powder (c-d), pressed at 100 MPa (e-f), after
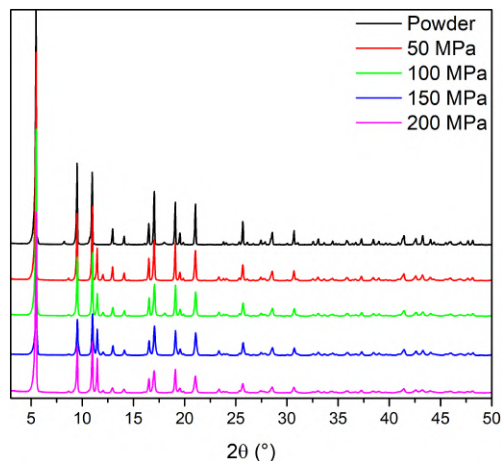
FIGURE 7.6: PXRD patterns acquired for powder and for the tablets pressed at 50, 100, 150, 200 MPa.

reactivation (g-h) and after the re-hydration (i-j).

FIGURE 7.7: EPR spectra obtained at 77 (a-c-e-g-i) and 300 K (b-d-f-h-j) during the different steps of production of the 100 MPa tablet produced from hydrated powders.

In each of these measurements we easily recognize the characteristic features of the activated material (7.7 (a),(b),(g),(h)) or of the hydrated material (7.7 (c),(d),(e),(f),(i),(j)). The correspondent spectra of the tablet 50 MPa and 200 MPa of the set B are shown in figure 7.8 and 7.9, respectively.

FIGURE 7.8: EPR spectra obtained at 77 (a-c-e-g-i) and 300 K (b-d-f-h-j) during the different steps of production of the 50 MPa tablet produced from hydrated powders.
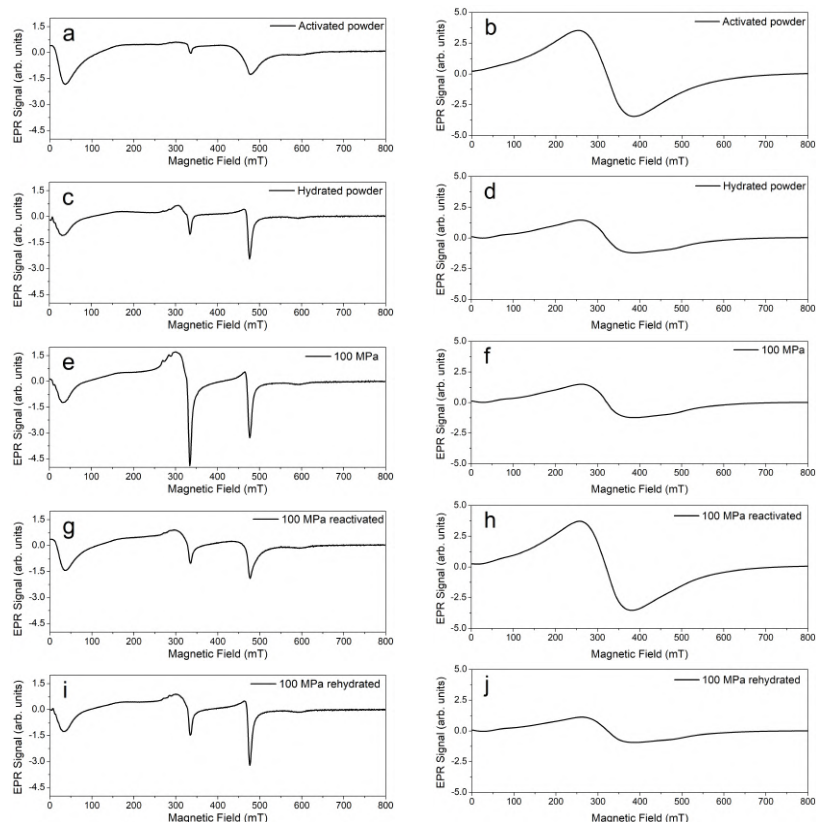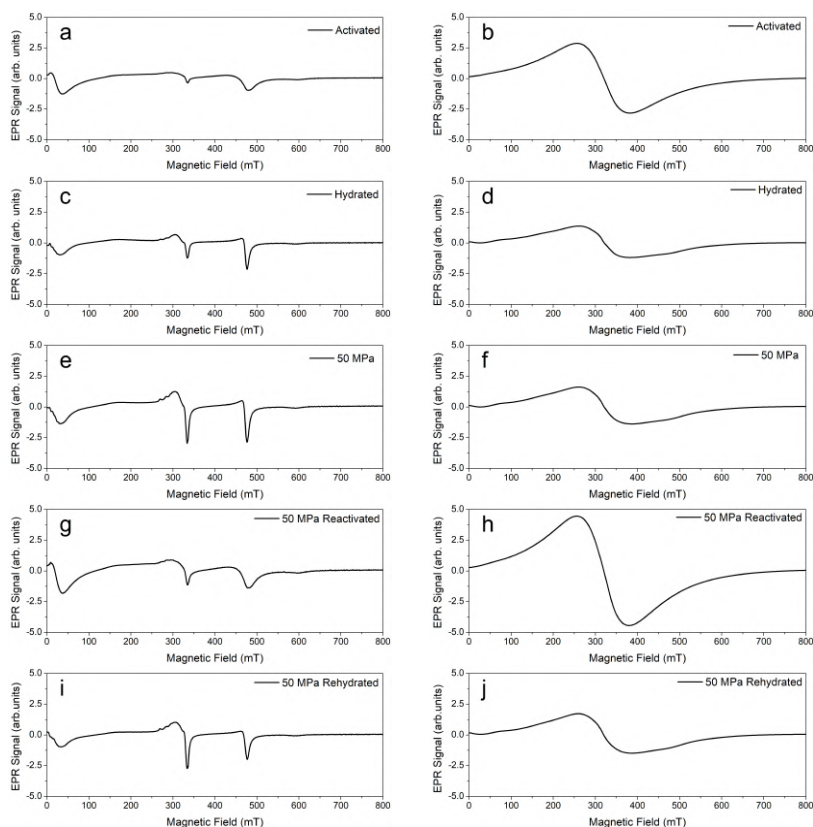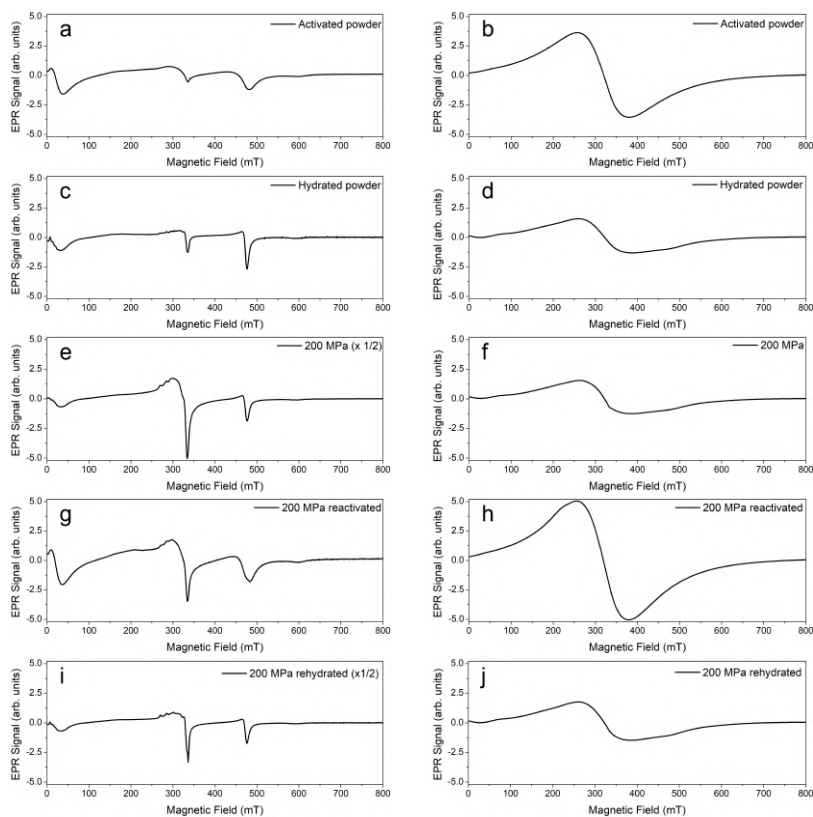

FIGURE 7.9: EPR spectra obtained at 77 (a-c-e-g-i) and 300 K (b-d-f-h-j) during the different steps of production of the 50 MPa tablet produced from hydrated powders.

All these results confirm that the flexibility is preserved in STAM-17-OEt material even when it is pressed starting from hydrated powders. This result is very important because it has been seen for HKUST-1 that a very small degree of hydration is sufficient to irreversibly damage the material upon compaction. At variance, the EPR data reported here (figure 7.7, 7.8 and 7.9) clearly show that there are neither signs of degradation of the material nor impacts on its flexibility. Both these results reasonably arise from the strong resistance to water of STAM-17-OEt compared to HKUST-1.

A further deep characterization of the compacted powders of STAM 17-OEt has been performed by vibrational spectroscopy. Figure 7.10 shows the Raman spectra acquired for a set of representative tablets of the set A.
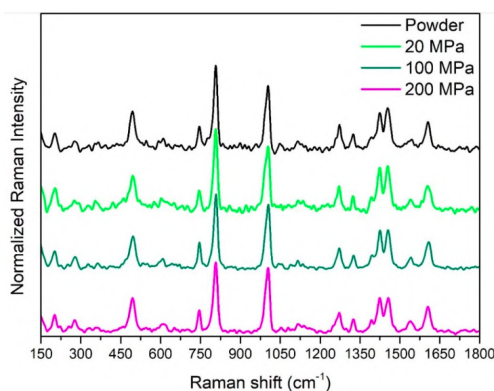
FIGURE 7.10: Raman spectra of some representative tablet of set A.

The Raman spectrum of STAM-17-OEt in powder form shows its characteristic peaks (see section 4.1.3). No significant changes are recognizable between the spectra of the powder and those of the tablets, neither in the peaks directly involving the paddlewheels, nor in those pertaining the organic part. This result gives a further strong support to the conclusion that the compaction process does not affect significantly the short/intermediate range structure of STAM-17-OEt.

The values of measured and calculated densities of the samples considered in the present work are shown in table 7.1.

The density estimated for the sample compacted with a pressure of 200 MPa (in its activated form) is $\sim$1.6 g/cm^3, a value very close to that calculated for the ideal crystalline bulk structure.

Figures 7.11 and 7.12 report AFM images acquired for the powder sample and the 100 MPa (*set B*) respectively. They do not show any significant difference in the morphology of the two samples: in both the couples of images we can recognize wide smooth surfaces in correspondence of the larger grains and rough areas associated to the presence of large aggregate of smaller grains.

TABLE 7.1: Calculated or estimated density values for different samples.

Calculated crystalline density[83]	
Sample	Density (g/cm^3)
Activated	1.652
Hydrated	1.479
Estimated effective density - Set A	
Pressure (MPa)	Density (g/cm^3)
Powder (activated)	0.6
3	0.9
20	1
50	1
100	1.2
200	1.6
Estimated effective density - Set B	
Pressure (MPa)	Density (g/cm^3)
Powder (hydrated)	0.5
50	1.0
100	1.1
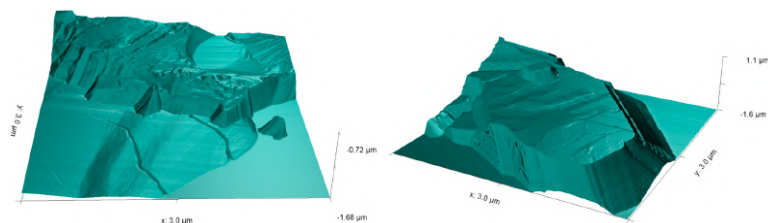
FIGURE 7.11: AFM images acquired for a sample of hydrated powder of STAM-17-OEt.
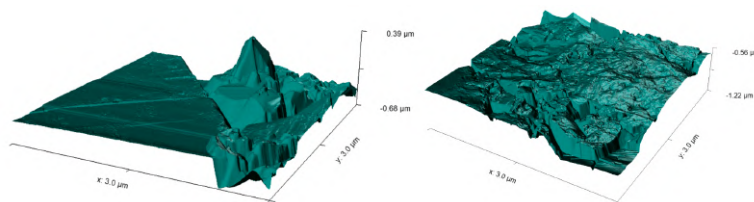
FIGURE 7.12: AFM images acquired for a sample of tablet of STAM-17-OEt produced with a pressure of 100 MPa (*set B*).

Conclusions of the chapter

The present study proves that STAM-17-OEt is a MOF able to withstand high pressures without significant damages and without loosing its granular form, maintaining its crystallinity, its peculiar flexibility and hemilability and the strong chemical stability to water. The strong resistance of the material towards mechanical pressure allows the preparation of tablets of STAM-17-OEt which preserve the properties of the pristine materials and, at the same time, gives the advantages of a sample very well packaged in space, with a value of the effective density comparable with that of the bulk crystal. Our conclusions are fully supported by the results we have obtained with EPR and Raman spectroscopies, X-ray diffraction and atomic force microscopy.

Chapter 8

STAM-17-OEt-Activated Carbon Composite

In this chapter we have studied the potentiality of STAM-17-OEt about the removal of toxic industrial chemicals (TICs) from contaminated airstreams. We have prepared a series of three MOF-activated carbon composite materials with different MOF to carbon ratios, by growing STAM-17-OEt crystals inside the commercially available BPL activated carbon. The composite materials display an increased uptake of ammonia gas when compared to pristine BPL.

The composites here shown overcome the key problem of the physical form of standard MOFs which typically consist of fine powders. In fact, they exhibit the easy-handling form of the activated carbon without the necessity of a subsequent pelletization. For this reason and also for the performances shown concerning the gas removal, they result very promising in the fields of air purification and personal protective equipment.

8.1 Properties and performances of the composite system

Figure 8.1 shows the PXRD patterns of the original STAM-17-OEt, pristine BPL activated carbon and of the three composite samples. The comparison of the patterns confirms the presence of the parent STAM-17-OEt in the composite materials, since some of the crystallinity associated with STAM-17-OEt may be observed along with amorphous character arising from the carbon. The peaks pertaining to the MOF may be observed at all three MOF loadings, but the sample containing the highest weight percentage of MOF, i.e. STAM-17-OEt@BPL_1, displays the greatest intensity. Accordingly, STAM-17-OEt@BPL_3 shows considerably less intensity due to the lower quantity of MOF incorporation. The patterns acquired for the composite systems also show a slight broadening of the peaks. This effect may arise from the different size of the STAM-17-OEt grains synthesized within the carbon matrix compared to those obtained by the ordinary solvothermal procedure. In fact, it is reasonable to expect that the confinement of the grains inside the carbon pores affects their size: the mesopores of
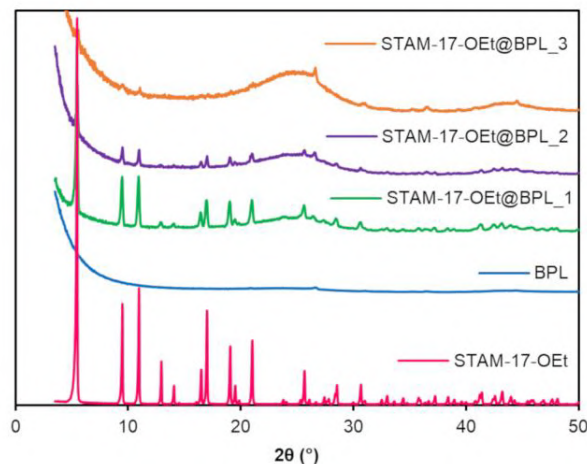
FIGURE 8.1: Powder X-ray diffraction patterns of the original MOF, unimpregnated BPL activated carbon and the three composites with varying weight percentages of MOF incorporation.

the carbon matrix do not exceed 40÷50 nm of dimension, whereas the ordinary synthesis protocol can produce grains with sizes in the range of the micrometers (see section 3.1.3).

Figure 8.2 shows the results of the nitrogen BET adsorption measurements, performed to investigate the effect of MOF incorporation on carbon porosity. BPL acti-
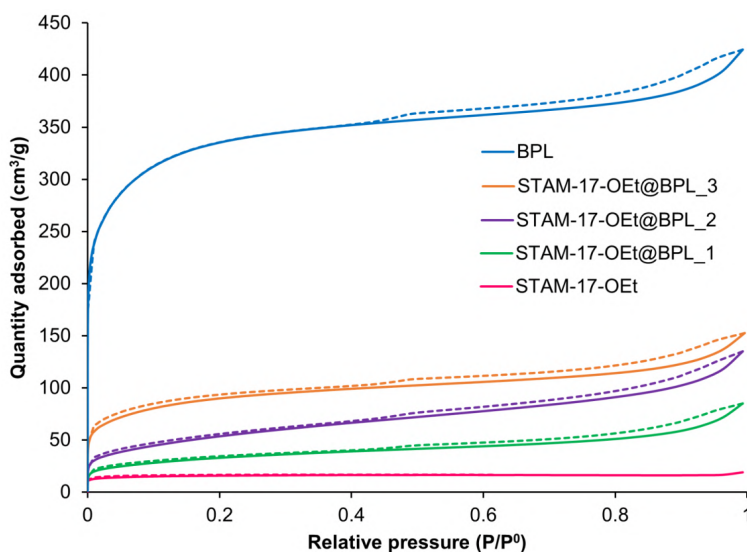
FIGURE 8.2: Nitrogen isotherms recorded at 77 K of STAM-17-OEt, STAM-17-OEt@BPL_1, STAM-17-OEt@BPL_2, STAM-17-OEt@BPL_3 and BPL activated carbon. Solid lines represent adsorption and dashed lines represent desorption.

vated carbon has a wide pore size distribution, with both micro and mesopores and a measured surface area of 1209 m^2/g, which is comparable to the literature value of 1200 m^2/g.[197] STAM-17-OEt, like other MOFs, is microporous, though has a surprisingly low surface area of 58 m^2/g.[83] The low porosity in STAM-17-OEt may be ascribed to its switchable structure, where upon activation, the pores in STAM-17-OEt become

TABLE 8.1: BET surface areas of STAM-17-OEt, BPL activated carbon and the three STAM-17-OEt@BPL composites.

Sample	BET Surface Area(m^2/g)
STAM-17-OEt	58
STAM-17-OEt@BPL_1	116
STAM-17-OEt@BPL_2	188
STAM-17-OEt@BPL_3	323
BPL Activated Carbon	1209

constricted by the change in the coordination environment of the copper paddlewheels. This constriction consequently impacts the porosity, and therefore the low surface area observed for STAM-17-OEt is probably not fully representative of the overall gas adsorption capability of the material.

The significant drop in the porosity of the carbon upon incorporation of the MOF provides further evidence that STAM-17-OEt is inside the carbon, due to partial poreblocking by STAM-17-OEt crystals. The BET surface area value calculated are shown in table 8.1.

As expected, the surface areas of the composites fall in-between those of the MOF and carbon alone, where the higher the MOF content, the lower the surface area. In fact, the greatest loss of porosity is observed in the highest loading sample: STAM-17-OEt@BPL_1, with a percentage decrease of 90% compared to unimpregnated BPL activated carbon.

In order to investigate the TIC gas adsorption capacity of the materials, micro breakthrough experiments were undertaken, using ammonia as the challenge gas. The resulting micro breakthrough curves are shown in figure 8.3(a): it results that BPL carbon alone is fairly ineffective in the removal of ammonia, with an ammonia uptake percentage of 0.43% based on sample weight. In contrast, STAM-17-OEt performs significantly better, adsorbing 4.33% based on the weight of sample. The highest loading MOF-carbon sample STAM-17-OEt@BPL_1 adsorbs 1.78% based on the weight of sample, which is almost halfway between the values for unimpregnated BPL carbon and STAM-17-OEt. The trend across the series may result clearer observing the graph shown in figure 8.3(b): increasing MOF loading in the composites leads to an overall increase in the uptake of ammonia.

Comparison of the ammonia uptakes with the loadings of MOF on the composites suggests that about 55-60% of the MOF is available for ammonia removal. This indicates that some of the MOF is either not accessible to the ammonia, or becomes inaccessible as a result of the ongoing reaction between ammonia and MOF.

EPR characterization. Electron paramagnetic resonance (EPR) spectra of activated STAM-17-OEt and the STAM-17-OEt@BPL materials, acquired at T= 77 K
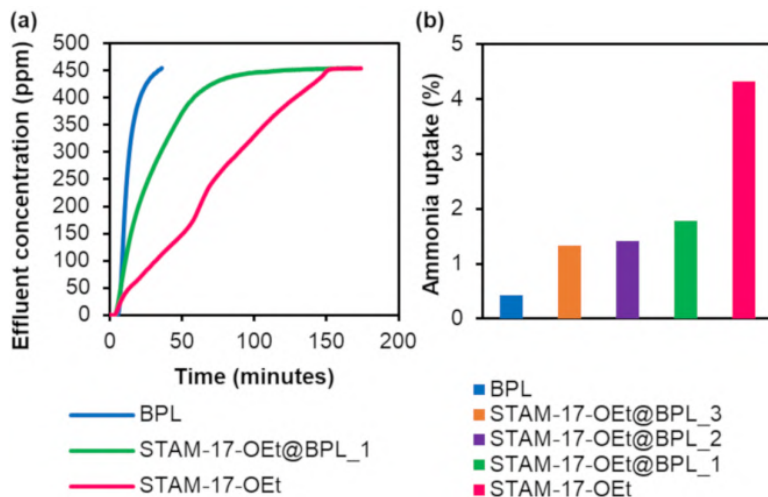
FIGURE 8.3: a) Ammonia micro breakthrough curves of BPL activated carbon, STAM-17-OEt and STAM-17-OEt@BPL_1; b) ammonia uptake across the STAM-17-OEt@BPL series.

and 300 K, are shown in 8.4. The spectra were normalized by all instrumental parameters and the estimated mass of STAM-17-OEt present in each sample (figure 8.4(a,b)) and normalized by the amplitude of the main peak (figure 8.4(c,d)). The EPR spectra of STAM-17-OEt@BPL samples are very different from that of the standard STAM-17-OEt powder, at both temperatures (pink lines). The peaks corresponding to the triplet centers in STAM-17-OEt are no longer present and only a single resonance at both temperatures with similar features is observed. This narrower resonance, centered at ∼340 mT, shows a fine structure comprising a multiplet of four lines, which can be ascribed as usual to the hyperfine interaction between the electron spin S $=1/2$ of the Cu^{2+} ion and its nuclear spin $I_{Cu} = 3/2$. In pristine STAM-17-OEt this multiplet is much less evident. Significant changes were also observed in the EPR spectra of a similar MOF in another hybrid system, where HKUST-1 was confined within mesostructured silica.[138] The changes in the spectra were attributed to the significantly reduced number of neighboring paramagnetic centers due to the typically widely spaced pores. The almost total disappearance of the resonances concerning the triplet centers at 77 K suggests a stronger change in the electronic environment of the paddlewheels with respect to the cited case and it appears that the signals observed at both 77 and 300 K in the STAM-17-OEt@BPL spectra arise from decoupled copper ions. A similar change in the magnetic properties of MOFs upon incorporation into an activated carbon matrix was observed for HKUST-1.[185] The reasons of this apparent decoupling are still unclear, but appear to be closely linked to the nature of MOF growth inside a porous carbon matrix.

8.2 STAM-17-OEt powder interacting with ammonia

In order to better understand the processes involving STAM-17-OEt when it interacts with ammonia vapors, we carried out a preliminary study focused on the effects which the MOF undergoes when it interacts with this toxic substance. More in details, due
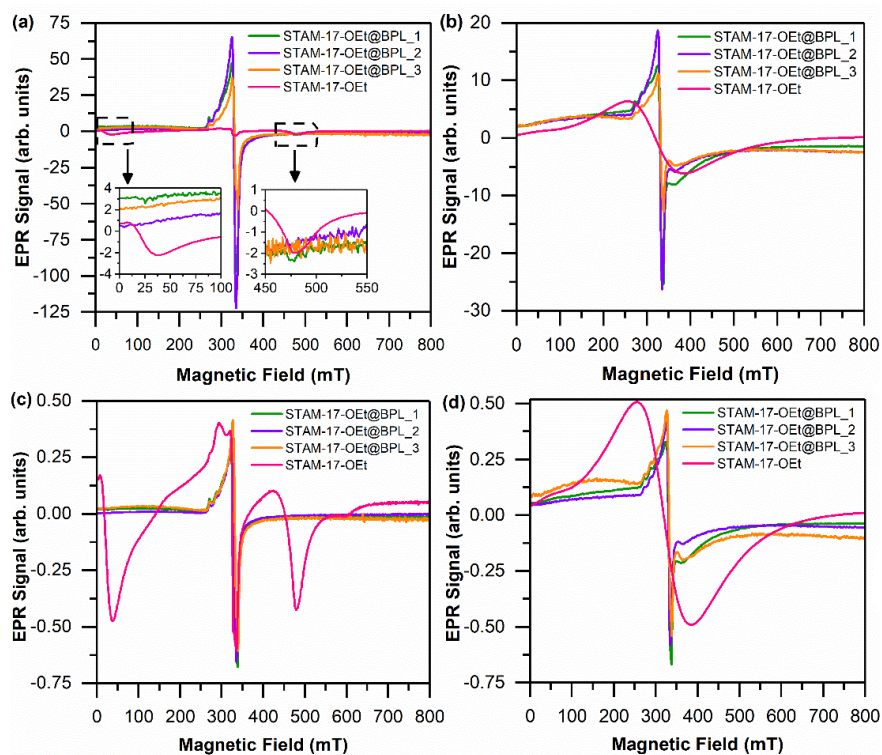
FIGURE 8.4: a,b) EPR spectra normalized by the estimated mass of STAM-17-OEt in each sample at 77 K and 300 K respectively; c,d) EPR spectra normalized by the peak-to-peak amplitude of the central resonance line at 77K and 300 K respectively.

to experimental setup limits, we studied this interaction by using aqueous ammonia solutions, containing different solute percentages (see section 3.1.9).

Figure 8.5 shows the EPR spectra collected at 77 (a) and 300 K (b) for STAM-17-OEt samples after the treatments with ammonia.
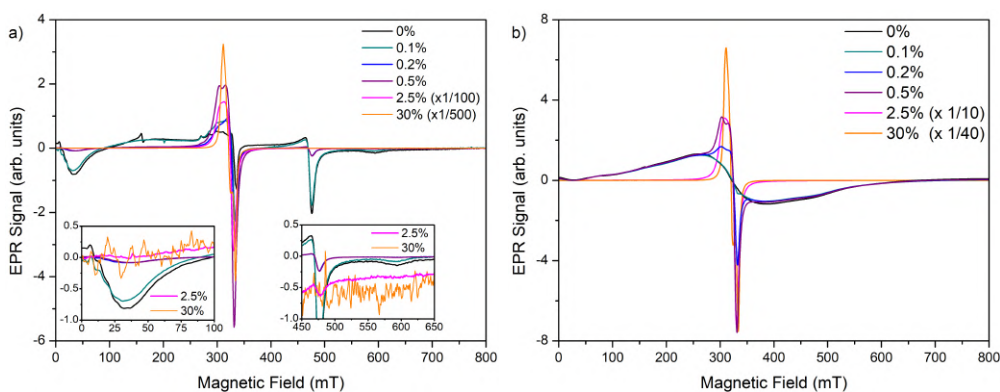
FIGURE 8.5: EPR spectra obtained at 77 (a) and 300 K (b) for the powder samples of STAM-17-OEt after the treatment with ammonia solution.

The spectra shown in black ("0%") in both the graphs represent the powder treated with distilled water without any content of ammonia. It is considered as a reference sample. Comparing it with the typical spectra acquired for the hydrated MOF at both

temperature (for example figure 4.7), no significant differences are observed. This indicates that the MOF is stable even when treated with liquid water.

In total contrast to the effects induced by exposure to the sole water, the EPR spectra acquired upon interaction with ammonia solutions show clear signs of decomposition. In fact, a new signal is observed at about 320 mT at both temperatures, ascribed to S=1/2 paramagnetic centers. These centers are reasonably originated from the breakage of a certain fraction of the copper paddlewheels, analogously to what occurs in HKUST-1 by hydrolysis (see chapters 4, 5 or 6). More in detail, the peak arising from these new centers appears even at the lowest concentrations of ammonia (0.2%) and it increases on increasing the NH_3 concentration. Furthermore, the triplet resonance decreases until it disappears completely (orange spectra, acquired upon the treatment with the stock solution).

Further study may reveal if the decomposition products observed by EPR in our study are analogous to those previously observed for HKUST-1 upon interaction with water (see section 2.3.2). At this stage we can only affirm that the interaction between STAM-17-OEt and ammonia is significantly degrading.

Conclusions of the chapter

This work proves that it is possible to synthesize STAM-17-OEt-carbon composite materials, where the MOF has been incorporated into the commercially available BPL activated carbon at a series of loadings. PXRD patterns, nitrogen isotherms and EPR measurements suggest the presence of the MOF formed within the pores of BPL carbon. The microbreakthrough experiments show that the MOF-carbon composite materials increase the quantities of ammonia removed from contaminated airstreams compared with the carbon. In fact while activated carbon has low effectiveness in removing smaller molecules such as ammonia from airstreams, as it lacks the strong and selective interactions formed between the metals in MOFs and the gases themselves, STAM-17-OEt forms, in contrast, strong and favorable interactions with this kind of adsorptives and this makes it much better for the adsorption of gases such as ammonia.

The granular form of the STAM-17-OEt@BPL composites also overcomes a major hurdle in the engineering of materials used in personal protective equipment, whereby a powdered MOF has been manufactured into a form that can potentially be used inside a filter. These findings suggest that MOF-carbon composites are exciting materials for use in air purification and, by altering the loading of MOF within the composites, the materials may be tailored to remove a broader range of contaminants than the individual components alone.

However, the low chemical stability shown by the STAM-17-OEt powder samples remains a significant issue to overcome, because even with low ammonia concentrations the material undergo to severe damaging.

Conclusions

In the present thesis we reported an experimental investigation focused on the stability of copper carboxylate MOFs, in particular HKUST-1, STAM-1 and STAM-17-OEt. Their chemical and mechanical stability have been deeply treated, in order to establish the causes of damages on the crystal structures upon interaction with substances like water or ammonia or upon application of mechanical pressures.

Our survey allowed us to deep understand which are the main mechanism involving the crystalline matrix of a MOF when it undergoes to mechanical compaction, both with or without a significant presence of air moisture adsorbed in the MOF pores. A comparison between two different densified forms of the same MOF has been developed, namely between HKUST-1 tablet and HKUST-1 monolith. In addition, an interesting composite MOF system involving an active carbon matrix containing STAM-17-OEt has been studied, which exhibits some of the properties of a densified MOF without the employ of external pressures or chemical binders.

These investigations needed to be preceded by a systematic study on the evolution of different carboxylate MOFs when they interact with water. We found, after few hours of water exposure, some strong similarities in their crystalline evolution even between MOFs with very different chemical stability in the long time range.

In the following, we summarize the main experimental results obtained and reported in the previous chapters, as well as some suggestions for further investigations.

Hydration on copper carboxylate MOFs

The systematic study on the effects of hydration on the copper carboxylate MOFs HKUST-1, STAM-1 and STAM-17-OEt pointed out some significant information. The samples were monitored for 60 days of exposure to air moisture in conditions of 100% RH at 300 K. As expected, HKUST-1 began to undergo hydrolysis first. In particular, within 24 hours strong evidences of some damages caused by the chemisorption of water molecules on the copper sites of the material. In complete contrast, both STAM-1 and STAM-17-OEt showed no significant evidence of hydrolysis or other kind of irreversible damages, allowing us to conclude that both the MOFs are water resistant and, furthermore, because of the use of EPR and NMR spectroscopies, we proved the complete atomic-scale reversibility of the effects of extensive hydration.

The heart of our comparative study was that, in spite of the strong differences between the water stability of the three MOF investigated, the first hours of exposure to water lead to a similar evolution: in particular, a fully reversible process was observed in

the three MOFs. Reasonably, it represents the process of adsorption of the first molecule of water onto the axial sites of the Cu^{2+} ions. This result then proves that only at a later stage, during the adsorption of additional water molecules linked to the first ones directly bonded to the copper, the hydrolysis process takes place. Under this point of view, HKUST-1 begins to undergo irreversible hydrolysis when on average more than one water molecule approaches each copper ion. In contrast, STAM-1 and STAM-17-OEt fully retain their framework structure, because of the limited amount of available space for the adsorbates.

Despite the strong water stability shown, an interesting effect was observed as a consequence of the hydration in STAM-1 and STAM-17-OEt: the structural transitions which occurs at each hydration or dehydration treatment. This single-crystal-to-single-crystal, previously studied by XRD or NMR, was clearly detected by EPR spectroscopy and its recognition in the subsequent spectra constituted an essential method for the understanding of the occurrence of the transition or of the permanence of the hemilabile properties in the materials. The structural parameters calculated by running simulations on the EPR spectra confirmed the lowering of the crystallographic order in the two hemilabile MOFs upon dehydration.

Densified HKUST-1: tablets and monoliths

We produced two different densified HKUST-1 products: the first one was a tablet obtained by mechanical compaction of commercial powder, the second one was a monolith produced by bench-scale synthesis.

The production of tablets has been possible because of the development of a method involving EPR spectroscopy for the estimation of the amount of damages induced in the MOF structure upon the application of the mechanical pressure. In fact, we have recognized for the first time that, as occurs upon hydrolysis, the tableting process always induces the growth of S= 1/2 paramagnetic centers in the materials, arising from the distortion and/or breaking of a fraction of the paddlewheels of the material. In particular, their number increases on increasing the applied pressure and thus it can be used in order to obtain quantitative estimates of the damage induced in the lattice in correspondence of the metal group upon compaction.

By applying this method to our tablets, we have unveiled that the number defects individuated as S=1/2 spin centers is strictly related to the level of hydration of the starting powders. A very small degree of degradation was observed in the tablets produced starting from activated powders. Under this condition, we have estimated that the percentage of paddlewheels damaged by tableting with a pressure of about 40 MPa is as low as 4% for HKUST-1 tablets. An additional thermal activation just after the compaction further reduces this defective EPR component, to the point that the properties of this tablet become virtually indistinguishable from those of activated powders of HKUST-1 with the pristine structure. Prolonging this study up to 5 weeks from

the tableting of the powders, we have ensured that the system does not show signs of delayed structural instability.

Summarizing, we proved that we are able to obtain a stable HKUST-1 tablet having a pristine structure but a high bulk density, simply taking care to activate the material just before and just after tableting.

The monolith synthesized showed interesting potentialities too, like its high BET surface area and also the spectroscopic and crystallographic properties comparable with those of the standard HKUST-1 powder.

In order to investigate the water stability of this new product, we performed a systematic EPR study conducted on powder, tablet and monolith maintaining the three materials in condition of 100% RH at 300 K for 24 hours. We determined that the monolith undergo severe hydrolysis much more rapidly than powder and tablet, leading to the conclusion that the tablet constitutes the best densified HKUST-1 product under this point of view. Furthermore, our tablets are very easy to get because of the large-scale synthesis already available for the HKUST-1 powder.

A future study a systematic study about the adsorption properties of the three HKUST-1 materials is essential, for establishing the limits but also the new milestones that the performances of our monoliths and tablets may reach. The investigation on the methane adsorption uptakes is highly meaningful, as well as those regarding other interesting gases like hydrogen o carbon dioxide.

STAM-17-OEt studies: powder, tablets, composites

A similar investigation carried out on STAM-17-OEt powders proved that this MOF is very resistant up to relatively high pressure values as 200 MPa: we observed that the MOF in tablet form preserves its hemilability, its crystallinity as well as its granular form. Not even the water resistance is compromised. On this basis, we proved that even for STAM-17-OEt it is possible to prepare tablets exhibiting the properties of the pristine material but with a bulk density comparable with that calculated for an ideal STAM-17-OEt crystal. The possibility of producing packaged STAM-17-OEt tablets contributes to its introduction in the industrial application, because it improves the easy handling and the performances.

Another STAM-17-OEt-based product which enhances both these properties is the carbon composite system we have shown in chapter 8. In these products, the MOF is incorporated into commercially available BPL activated carbon, with the possibility of having different loadings. In this form, the material is able to remove higher ammonia quantities from the contaminated airstreams compared to the lone BPL. In other words, the composite MOF here studied shows an optimized compromise between the large granular nature of the BPL and the open-metal sites present in STAM-17-OEt, which allows a strong and favorable interaction with adsorptives like ammonia. Their

combination, in summary, provides a material which can be tailored altering the MOF loading within the cavities of the BPL, allowing to remove a wide range of contaminants, certainly broader than the individual STAM-17-OEt and activated carbon alone.

Although STAM-17-OEt is a MOF with an unexpectedly high chemical stability, it is not very resistant to ammonia. By treating the MOF with aqueous ammonia solutions with different concentrations, we have seen that STAM-17-OEt undergoes a severe decomposition, showing paramagnetic signals very similar to those previously observed when HKUST-1 is subject to hydrolysis.

This is a further prove that the MOF chemical stability, after more than 20 years from their first appearing on the research field, is still probably the most important challenge to overcome.

Bibliography

[1]   Robert Eisberg and Robert Resnick. "Quantum physics of atoms, molecules, solids, nuclei, and particles". In: *Quantum Physics of Atoms, Molecules, Solids, Nuclei, and Particles, 2nd Edition, by Robert Eisberg, Robert Resnick, pp. 864. ISBN 0-471-87373-X. Wiley-VCH.* (1985), p. 864.

[2]   AJ Dekker. "Solid State Physics, Vol. 6". In: *Seitz and D. Turnbull, eds., Academic Press, New York* (1958), p. 251.

[3]   Olivier Kahn. "Molecular magnetism". In: *VCH Publishers, Inc.(USA)* (1993), p. 393.

[4]   Paolo Mazzoldi, Massimo Nigro, and Cesare Voci. *Fisica. Volume 2: Elettromagnetismo-Onde.* EdiSES, 1998.

[5]   Alessandro Bencini and Dante Gatteschi. *EPR of exchange coupled systems.* Springer-Verlag Heidelberg, 1951.

[6]   Davide Tiana, Christopher H Hendon, and Aron Walsh. "Ligand design for long-range magnetic order in metal–organic frameworks". In: *Chemical Communications* 50.90 (2014), pp. 13990–13993.

[7]   John A. Weil and James R. Bolton. *Electron paramagnetic resonance: elementary theory and practical applications.* John Wiley & Sons, 2007.

[8]   Anatole Abragam and Brebis Bleaney. *Electron Paramagnetic Resonance of Transition Ions.* OUP Oxford, 1970.

[9]   Bojan Kozlevčar. "Structural analysis of a series of copper (II) coordination compounds and correlation with their magnetic properties". In: *Croatica Chemica Acta* 81.2 (2008), pp. 369–379.

[10] B Bleaney and KD Bowers. "Proc. R. Soc. London". In: *Ser. A*. Vol. 214. 1952, p. 451.

[11] Stephen Blundell. *Magnetism in condensed matter.* American Association of Physics Teachers, 2003.

[12] Malcolm A. Halcrow. "Jahn–Teller distortions in transition metal compounds, and their importance in functional molecular and inorganic materials". In: *Chemical Society Reviews* 42.4 (2013), pp. 1784–1795.

[13] Hermann Arthur Jahn and Edward Teller. "Stability of polyatomic molecules in degenerate electronic states-I—Orbital degeneracy". In: *Proceedings of the Royal Society of London. Series A-Mathematical and Physical Sciences* 161.905 (1937), pp. 220–235.

[14]   Horst Köppel, David R Yarkony, and Heinz Barentzen. *The Jahn-Teller Effect: Fundamentals and Implications for Physics and Chemistry*. Vol. 97. Springer Science & Business Media, 2009.

[15]   Ingmar Persson et al. "Structure of Jahn–Teller distorted solvated copper (II) ions in solution, and in solids with apparently regular octahedral coordination geometry". In: *Journal of the Chemical Society, Dalton Transactions* 7 (2002), pp. 1256–1265.

[16]   Ingmar Persson. "Hydrated metal ions in aqueous solution: How regular are their structures?" In: *Pure and Applied Chemistry* 82.10 (2010), pp. 1901–1917.

[17]   Jesús Chaboy et al. "The hydration of Cu 2+: Can the Jahn-Teller effect be detected in liquid solution?" In: *The Journal of chemical physics* 124.6 (2006), p. 064509.

[18]   Vyacheslav S Bryantsev et al. "Hydration of copper (II): new insights from density functional theory and the COSMO solvation model". In: *The Journal of Physical Chemistry A* 112.38 (2008), pp. 9104–9112.

[19]   Robert W Henning et al. "Structural and EPR Study of the Dependence on Deuteration of the Jahn- Teller Distortion in Ammonium Hexaaquacopper (II) Sulfate,$(NH_4)2[Cu(H_2O)_6](SO_4)2$". In: *Inorganic chemistry* 39.4 (2000), pp. 765–769.

[20]   Ivan Shtepliuk, Mikhail Vagin, and Rositsa Yakimova. "Electrochemical Deposition of Copper on Epitaxial Graphene". In: *Applied Sciences* 10.4 (2020), p. 1405.

[21]   Bhagawati Charan Guha. "Magnetic properties of some paramagnetic crystals at low temperatures". In: *Proceedings of the Royal Society of London. Series A. Mathematical and Physical Sciences* 206.1086 (1951), pp. 353–373.

[22]   Antonio Rodríguez-Fortea et al. "Exchange Coupling in Carboxylato-Bridged Dinuclear Copper (II) Compounds: A Density Functional Study". In: *Chemistry– A European Journal* 7.3 (2001), pp. 627–637.

[23]   Ayhan Elmali. "The magnetic super-exchange coupling in copper (II) acetate monohydrate and a redetermination of the crystal structure". In: *Turkish Journal of Physics* 24.5 (2000), pp. 667–672.

[24]   Stephen S.-Y. Chui et al. "A chemically functionalizable nanoporous material [Cu3 (TMA) 2 (H2O) 3] n". In: *Science* 283.5405 (1999), pp. 1148–1150.

[25]   Christopher H Hendon and Aron Walsh. "Chemical principles underpinning the performance of the metal–organic framework HKUST-1". In: *Chemical science* 6.7 (2015), pp. 3674–3683.

[26]   Omar K Farha et al. "De novo synthesis of a metal–organic framework material featuring ultrahigh surface area and gas storage capacities". In: *Nature chemistry* 2.11 (2010), pp. 944–948.

[27] Gilvaldo G da Silva et al. "Metal-organic framework: Structure and magnetic properties of $[Cu_3(BTC)_2(L)x \cdot (CuO)y]n(L= H_2O, DMF)$". In: *Journal of Solid State Chemistry* 253 (2017), pp. 1–5.

[28] Partha Mahata, Debajit Sarma, and Srinivasan Natarajan. "Magnetic behaviour in metal-organic frameworks—Some recent examples". In: *Journal of Chemical Sciences* 122.1 (2010), pp. 19–35.

[29] JB Goodenough. "Magnetism and the chemical bond, RE Krieger Pub". In: *Co, Huntington NY* (1976).

[30] Daniel Maspoch, Daniel Ruiz-Molina, and Jaume Veciana. "Old materials with new tricks: multifunctional open-framework materials". In: *Chemical Society Reviews* 36.5 (2007), pp. 770–818.

[31] John E Wertz and James R Bolton. *Electron Spin Resonance. Elementary Theory and Practical Applications'*. New York: McGraw-Hill, 1972.

[32] Douglas A Skoog, F James Holler, and Stanley R Crouch. *Principles of instrumental analysis.* Cengage learning, 2017.

[33] Daniel C Harris and Michael D Bertolucci. *Symmetry and spectroscopy: an introduction to vibrational and electronic spectroscopy.* Courier Corporation, 1989.

[34] Frank Edward Mabbs and David Collison. *Electron paramagnetic resonance of d transition metal compounds.* Elsevier, 1992.

[35] GE Pake and TL Estle. "The Physical Principles of Electron Paramagnetic Resonance". In: (1973).

[36] Charles P Poole. *Electron spin resonance: a comprehensive treatise on experimental techniques.* Wiley, 1967.

[37] Bettina Jee. "Cw and pulsed EPR spectroscopy of Cu (II) and V (IV) in metal-organic framework compounds: metal ion coordination and adsorbate interactions". PhD thesis. Leipzig, Germany: Universität Leipzig, 2013.

[38] Edel Wasserman, Lawrence C. Snyder, and William A. Yager. "ESR of the triplet states of randomly oriented molecules". In: *The Journal of Chemical Physics* 41.6 (1964), pp. 1763–1772.

[39] Joseph B. Lambert and Eugene P. Mazzola. *Nuclear Magnetic Resonance Spectroscopy, an Introduction to Principles, Applications, and Experimental Methods.* Pearson Education Inc., New Jersey, 2004.

[40] Paul T. Callaghan. *Principles of nuclear magnetic resonance microscopy.* Oxford University Press on Demand, 1993.

[41] Roger S Macomber. *Complete Introduction to Nuclear Magnetic Resonance NMR Spectroscopy.* 1998.

[42] Derek Albert Long. *The Raman effect: a unified treatment of the theory of Raman scattering by molecules.* Wiley, 2002.

[43]   John R Ferraro, Kazuo Nakamoto, and Chris W Brown. *Introductory raman spectroscopy.* Elsevier, 2003.

[44]   Yoshio Waseda, Eiichiro Matsubara, and Kozo Shinoda. *X-ray diffraction crystallography: introduction, examples and solved problems.* Springer Science & Business Media, 2011.

[45]   Werner Massa. *Crystal structure determination.* Springer Science & Business Media, 2013.

[46]   William Lawrence Bragg. "The Specular Reflection of X-rays." In: *Nature* 90.2250 (1912), pp. 410–410.

[47]   Vitalij Pecharsky and Peter Zavalij. *Fundamentals of powder diffraction and structural characterization of materials.* Springer Science & Business Media, 2008.

[48]   René Guinebretière. *X-ray diffraction by polycrystalline materials.* John Wiley & Sons, 2013.

[49]   Matthias Thommes et al. "Physisorption of gases, with special reference to the evaluation of surface area and pore size distribution (IUPAC Technical Report)". In: *Pure and Applied Chemistry* 87.9-10 (2015), pp. 1051–1069.

[50]   Hiroyasu Furukawa et al. "The chemistry and applications of metal-organic frameworks". In: *Science* 341.6149 (2013), p. 1230444.

[51]   Nicholas C. Burtch, Himanshu Jasuja, and Krista S. Walton. "Water stability and adsorption in metal–organic frameworks". In: *Chemical reviews* 114.20 (2014), pp. 10575–10612.

[52]   Jesse L.C. Rowsell and Omar M. Yaghi. "Metal–organic frameworks: a new class of porous materials". In: *Microporous and mesoporous materials* 73.1-2 (2004), pp. 3–14.

[53]   Harry Marsh and Francisco Rodríguez Reinoso. *Activated carbon.* Elsevier, 2006.

[54]   Werner Kast. "Adsorption aus der Gasphase". In: *Ingenieurwissenschaftliche Grundlagen und technische Verfahren, VCH-Verlag* (1988).

[55]   Ralph T Yang. *Gas separation by adsorption processes.* Butterworth-Heinemann, 2013.

[56]   Krista S Walton and Randall Q Snurr. "Applicability of the BET method for determining surface areas of microporous metal- organic frameworks". In: *Journal of the American Chemical Society* 129.27 (2007), pp. 8552–8556.

[57]   S Lowell et al. "Surface area analysis from the langmuir and bet theories". In: *Characterization of Porous Solids and Powders: Surface Area, Pore Size and Density.* Springer, 2004, pp. 58–81.

[58]   Stephen Brunauer, Paul Hugh Emmett, and Edward Teller. "Adsorption of gases in multimolecular layers". In: *Journal of the American chemical society* 60.2 (1938), pp. 309–319.

[59] Andreas Schneemann et al. "Flexible metal-organic frameworks". In: *Chemical Society Reviews* 43.16 (2014), pp. 6062–6096.

[60] Ze Chang et al. "Flexible metal–organic frameworks: recent advances and potential applications". In: *Advanced Materials* 27.36 (2015), pp. 5432–5441.

[61] Ricardo García. *Amplitude modulation atomic force microscopy.* John Wiley & Sons, 2011.

[62] Greg Haugstad. *Atomic force microscopy: understanding basic modes and advanced applications.* John Wiley & Sons, 2012.

[63] Peter Eaton and Paul West. *Atomic force microscopy.* Oxford university press, 2010.

[64] Bert Voigtländer. *Atomic Force Microscopy.* Springer, 2019.

[65] Clement Duval. *Inorganic thermogravimetric analysis.* North-Holland, 1963.

[66] Omar M. Yaghi, Markus J. Kalmutzki, and Christian S. Diercks. *Introduction to Reticular Chemistry: Metal-Organic Frameworks and Covalent Organic Frameworks.* John Wiley & Sons, 2019.

[67] Kui Tan et al. "Water interactions in metal organic frameworks". In: *CrystEngComm* 17.2 (2015), pp. 247–260.

[68] Peyman Z Moghadam et al. "Development of a Cambridge Structural Database subset: a collection of metal–organic frameworks for past, present, and future". In: *Chemistry of Materials* 29.7 (2017), pp. 2618–2625.

[69] Yukio Kinoshita, Ikuo Matsubara, and Yoshihiko Saito. "The crystal structure of bis(succinonitrilo)copper(I) nitrate". In: *Bulletin of the Chemical Society of Japan* 32.7 (1959), pp. 741–747.

[70] Yukio Kinoshita, Ikuo Matsubara, and Yoshihiko Saito. "The crystal structure of bis(glutaronitrilo)copper(I) nitrate". In: *Bulletin of the Chemical Society of Japan* 32.11 (1959), pp. 1216–1221.

[71] Yukio Kinoshita et al. "The crystal structure of bis (adiponitrilo) copper (I) nitrate". In: *Bulletin of the Chemical Society of Japan* 32.11 (1959), pp. 1221–1226.

[72] Omar M. Yaghi and Hailian Li. "Hydrothermal synthesis of a metal-organic framework containing large rectangular channels". In: *Journal of the American Chemical Society* 117.41 (1995), pp. 10401–10402.

[73] S. Subramanian and Michael J. Zaworotko. "Porous solids by design: $[Zn(4,4'-bpy)_2(SiF_6)]_n \cdot xDMF$, a single framework octahedral coordination polymer with large square channels". In: *Angewandte Chemie International Edition in English* 34.19 (1995), pp. 2127–2129.

[74] Omar M. Yaghi, Guangming Li, and Hailian Li. "Selective binding and removal of guests in a microporous metal–organic framework". In: *Nature* 378.6558 (1995), p. 703.

[75]   Hailian Li et al. "Establishing microporosity in open metal- organic frameworks: Gas sorption isotherms for Zn(BDC)(BDC= 1, 4-benzenedicarboxylate)". In: *Journal of the American Chemical Society* 120.33 (1998), pp. 8571–8572.

[76]   Hailian Li et al. "Design and synthesis of an exceptionally stable and highly porous metal-organic framework". In: *nature* 402.6759 (1999), p. 276.

[77]   Nathaniel L. Rosi et al. "Hydrogen storage in microporous metal-organic frameworks". In: *Science* 300.5622 (2003), pp. 1127–1129.

[78]   Mitch Jacoby. "Heading to market with MOFs". In: *Chem. Eng. News* 86.34 (2008), pp. 13–16.

[79]   San-Yuan Ding and Wei Wang. "Covalent organic frameworks (COFs): from design to applications". In: *Chemical Society Reviews* 42.2 (2013), pp. 548–568.

[80]   Mohamed Eddaoudi et al. "Systematic design of pore size and functionality in isoreticular MOFs and their application in methane storage". In: *Science* 295.5554 (2002), pp. 469–472.

[81]   Hexiang Deng et al. "Large-pore apertures in a series of metal-organic frameworks". In: *science* 336.6084 (2012), pp. 1018–1023.

[82]   M. Infas H. Mohideen et al. "Protecting group and switchable pore-discriminating adsorption properties of a hydrophilic–hydrophobic metal–organic framework". In: *Nature chemistry* 3.4 (2011), p. 304.

[83]   Lauren N. McHugh et al. "Hydrolytic stability in hemilabile metal–organic frameworks". In: *Nature chemistry* 10.11 (2018), p. 1096.

[84]   Carmelo Prestipino et al. "Local structure of framework Cu (II) in HKUST-1 metallorganic framework: spectroscopic characterization upon activation and interaction with adsorbates". In: *Chemistry of materials* 18.5 (2006), pp. 1337–1346.

[85]   Omar M Yaghi et al. "Reticular synthesis and the design of new materials". In: *Nature* 423.6941 (2003), pp. 705–714.

[86]   Yang Peng et al. "Simultaneously high gravimetric and volumetric methane uptake characteristics of the metal–organic framework NU-111". In: *Chemical Communications* 49.29 (2013), pp. 2992–2994.

[87]   Shengqian Ma et al. "Metal-organic framework from an anthracene derivative containing nanoscopic cages exhibiting high methane uptake". In: *Journal of the American Chemical Society* 130.3 (2008), pp. 1012–1016.

[88]   Yong Yan et al. "Modifying cage structures in metal–organic polyhedral frameworks for H2 storage". In: *Chemistry–A European Journal* 17.40 (2011), pp. 11162–11170.

[89]   Eugenio Garribba and Giovanni Micera. "The determination of the geometry of Cu (II) complexes: an EPR spectroscopy experiment". In: *Journal of chemical education* 83.8 (2006), p. 1229.

[90] Ryan J Kuppler et al. "Potential applications of metal-organic frameworks". In: *Coordination Chemistry Reviews* 253.23-24 (2009), pp. 3042–3066.

[91] Nazmul Abedin Khan, Zubair Hasan, and Sung Hwa Jhung. "Adsorptive removal of hazardous materials using metal-organic frameworks (MOFs): a review". In: *Journal of hazardous materials* 244 (2013), pp. 444–456.

[92] Alistair C McKinlay et al. "BioMOFs: metal–organic frameworks for biological and medical applications". In: *Angewandte Chemie International Edition* 49.36 (2010), pp. 6260–6266.

[93] Shun-Li Li and Qiang Xu. "Metal–organic frameworks as platforms for clean energy". In: *Energy & Environmental Science* 6.6 (2013), pp. 1656–1683.

[94] Jian Liu et al. "Progress in adsorption-based CO 2 capture by metal–organic frameworks". In: *Chemical Society Reviews* 41.6 (2012), pp. 2308–2322.

[95] Trevor A Makal et al. "Methane storage in advanced porous materials". In: *Chemical Society Reviews* 41.23 (2012), pp. 7761–7779.

[96] Shengqian Ma and Hong-Cai Zhou. "Gas storage in porous metal–organic frameworks for clean energy applications". In: *Chemical Communications* 46.1 (2010), pp. 44–53.

[97] Tian Tian et al. "A sol–gel monolithic metal–organic framework with enhanced methane uptake". In: *Nature materials* 17.2 (2018), pp. 174–179.

[98] Ka-Kit Yee et al. "Effective mercury sorption by thiol-laced metal–organic frameworks: in strong acid and the vapor phase". In: *Journal of the American Chemical Society* 135.21 (2013), pp. 7795–7798.

[99] Fang Zou et al. "Microwave-assisted synthesis of HKUST-1 and functionalized HKUST-1-@ H3PW12O40: selective adsorption of heavy metal ions in water analyzed with synchrotron radiation". In: *ChemPhysChem* 14.12 (2013), pp. 2825–2832.

[100] Xing Meng et al. "A stable, pillar-layer metal–organic framework containing uncoordinated carboxyl groups for separation of transition metal ions". In: *Chemical Communications* 50.48 (2014), pp. 6406–6408.

[101] Manjula I. Nandasiri et al. "Adsorption, separation, and catalytic properties of densified metal-organic frameworks". In: *Coordination Chemistry Reviews* 311 (2016), pp. 38–52.

[102] Norbert Stock and Shyam Biswas. "Synthesis of metal-organic frameworks (MOFs): routes to various MOF topologies, morphologies, and composites". In: *Chemical reviews* 112.2 (2012), pp. 933–969.

[103] Editorial Staff. "Frameworks for Commercial Success". In: *Nat. Chem.* 8 (2016), p. 987.

[104] Hyunho Kim et al. *Sorption-based Atmospheric Water Harvesting Device*. US Patent App. 16/377,146. 2019.

[105]   Jiewei Liu et al. "Applications of metal–organic frameworks in heterogeneous supramolecular catalysis". In: *Chemical Society Reviews* 43.16 (2014), pp. 6011–6061.

[106]   Satoshi Horike, Satoru Shimomura, and Susumu Kitagawa. "Soft porous crystals". In: *Nature chemistry* 1.9 (2009), p. 695.

[107]   Shaozhou Li and Fengwei Huo. "Metal–organic framework composites: from fundamentals to applications". In: *Nanoscale* 7.17 (2015), pp. 7482–7501.

[108]   Xiao-Wei Liu et al. "Composites of metal–organic frameworks and carbon-based materials: preparations, functionalities and applications". In: *Journal of Materials Chemistry A* 4.10 (2016), pp. 3584–3616.

[109]   Imteaz Ahmed and Sung Hwa Jhung. "Composites of metal–organic frameworks: preparation and application in adsorption". In: *Materials today* 17.3 (2014), pp. 136–146.

[110]   Qi-Long Zhu and Qiang Xu. "Metal–organic framework composites". In: *Chemical Society Reviews* 43.16 (2014), pp. 5468–5512.

[111]   Pia Küsgens et al. "Metal-organic frameworks in monolithic structures". In: *Journal of the American Ceramic Society* 93.9 (2010), pp. 2476–2479.

[112]   Rainer Ostermann et al. "Metal–organic framework nanofibers via electrospinning". In: *Chemical Communications* 47.1 (2011), pp. 442–444.

[113]   Megan C Kreider et al. "Toward 3D printed hydrogen storage materials made with ABS-MOF composites". In: *Polymers for advanced technologies* 29.2 (2018), pp. 867–873.

[114]   Laura D O'Neill, Haifei Zhang, and Darren Bradshaw. "Macro-/microporous MOF composite beads". In: *Journal of Materials Chemistry* 20.27 (2010), pp. 5720–5726.

[115]   Jana Juan-Alcañiz, Jorge Gascon, and Freek Kapteijn. "Metal–organic frameworks as scaffolds for the encapsulation of active species: state of the art and future perspectives". In: *Journal of materials chemistry* 22.20 (2012), pp. 10102–10118.

[116]   Omar K Farha and Joseph T Hupp. "Rational design, synthesis, purification, and activation of metal- organic framework materials". In: *Accounts of chemical research* 43.8 (2010), pp. 1166–1175.

[117]   Joseph E Mondloch et al. "Activation of metal–organic framework materials". In: *CrystEngComm* 15.45 (2013), pp. 9258–9264.

[118]   Mohamed Infas Haja Mohideen. "Novel metal organic frameworks: synthesis, characterisation and functions". PhD thesis. University of St Andrews, 2011.

[119]   Pradip Chowdhury et al. "Comparison of adsorption isotherms on Cu-BTC metal organic frameworks synthesized from different routes". In: *Microporous and Mesoporous Materials* 117.1-2 (2009), pp. 406–413.

[120] Jianwei Ren et al. "Review on processing of metal–organic framework (MOF) materials towards system integration for hydrogen storage". In: *International Journal of Energy Research* 39.5 (2015), pp. 607–620.

[121] Delphine Bazer-Bachi et al. "Towards industrial use of metal-organic framework: impact of shaping on the MOF properties". In: *Powder technology* 255 (2014), pp. 52–59.

[122] Ovidiu Ardelean et al. "Volumetric hydrogen adsorption capacity of densified MIL-101 monoliths". In: *International Journal of Hydrogen Energy* 38.17 (2013), pp. 7046–7055.

[123] Jianwei Ren and Brian C North. "Shaping porous materials for hydrogen storage applications: a review". In: *Journal of Technology Innovations in Renewable Energy* 3.1 (2014), pp. 12–20.

[124] Vincent Finsy et al. "Separation of CO2/CH4 mixtures with the MIL-53 (Al) metal–organic framework". In: *Microporous and Mesoporous Materials* 120.3 (2009), pp. 221–227.

[125] Jérôme Canivet et al. "Water adsorption in MOFs: fundamentals and applications". In: *Chemical Society Reviews* 43.16 (2014), pp. 5594–5617.

[126] Kui Tan et al. "Water interactions in metal organic frameworks". In: *CrystEngComm* 17.2 (2015), pp. 247–260.

[127] John J Low et al. "Virtual high throughput screening confirmed experimentally: porous coordination polymer hydration". In: *Journal of the American Chemical Society* 131.43 (2009), pp. 15834–15842.

[128] Sihai Yang et al. "Selectivity and direct visualization of carbon dioxide and sulfur dioxide in a decorated porous host". In: *Nature chemistry* 4.11 (2012), pp. 887–894.

[129] Jared M Taylor, Karl W Dawson, and George KH Shimizu. "A water-stable metal–organic framework with highly acidic pores for proton-conducting applications". In: *Journal of the American Chemical Society* 135.4 (2013), pp. 1193–1196.

[130] Luca Bellarosa et al. "On the mechanism behind the instability of isoreticular metal–organic frameworks (irmofs) in humid environments". In: *Chemistry–A European Journal* 18.39 (2012), pp. 12260–12266.

[131] Marta De Toni et al. "How Can a Hydrophobic MOF be Water-Unstable? Insight into the Hydration Mechanism of IRMOFs". In: *ChemPhysChem* 13.15 (2012), pp. 3497–3503.

[132] Stephen D Worrall et al. "Metal-organic framework templated electrodeposition of functional gold nanostructures". In: *Electrochimica Acta* 222 (2016), pp. 361–369.

[133]   Andreas Pöppl et al. "CW and Pulsed ESR Spectroscopy of Cupric Ions in the Metal- Organic Framework Compound Cu3 (BTC) 2". In: *The Journal of Physical Chemistry C* 112.7 (2008), pp. 2678–2684.

[134]   Yang Peng et al. "Methane storage in metal–organic frameworks: current records, surprise findings, and challenges". In: *Journal of the American Chemical Society* 135.32 (2013), pp. 11887–11894.

[135]   Klaus Schlichte, Tobias Kratzke, and Stefan Kaskel. "Improved synthesis, thermal stability and catalytic properties of the metal-organic framework compound Cu3 (BTC) 2". In: *Microporous and Mesoporous Materials* 73.1-2 (2004), pp. 81–88.

[136]   Jun Kim et al. "Bench-scale preparation of Cu $_3$(BTC)$_2$ by ethanol reflux: Synthesis optimization and adsorption/catalytic applications". In: *Microporous and Mesoporous Materials* 161 (2012), pp. 48–55.

[137]   Osama Shekhah et al. "Growth mechanism of metal–organic frameworks: insights into the nucleation by employing a step-by-step route". In: *Angewandte Chemie International Edition* 48.27 (2009), pp. 5038–5041.

[138]   Matjaž Mazaj et al. "Confined crystallization of a HKUST-1 metal–organic framework within mesostructured silica with enhanced structural resistance towards water". In: *Journal of Materials Chemistry A* 5.42 (2017), pp. 22305–22315.

[139]   Gregory W. Peterson et al. "Effects of pelletization pressure on the physical and chemical properties of the metal–organic frameworks Cu3 (BTC) 2 and UiO-66". In: *Microporous and Mesoporous Materials* 179 (2013), pp. 48–53.

[140]   Michela Todaro et al. "Decomposition process of carboxylate MOF HKUST-1 unveiled at the atomic scale level". In: *The Journal of Physical Chemistry C* 120.23 (2016), pp. 12879–12889.

[141]   Pia Küsgens et al. "Characterization of metal-organic frameworks by water adsorption". In: *Microporous and Mesoporous Materials* 120.3 (2009), pp. 325–330.

[142]   Jared B. Decoste et al. "Enhanced stability of Cu-BTC MOF via perfluorohexane plasma-enhanced chemical vapor deposition". In: *Journal of the American Chemical Society* 134.3 (2012), pp. 1486–1489.

[143]   Qing Min Wang et al. "Metallo-organic molecular sieve for gas separation and purification". In: *Microporous and mesoporous materials* 55.2 (2002), pp. 217–230.

[144]   Michela Todaro et al. "Investigation by Raman spectroscopy of the decomposition process of HKUST-1 upon exposure to air". In: *Journal of Spectroscopy* 2016 (2016).

[145] Nilesh R. Dhumal et al. "Molecular interactions of a Cu-based metal–organic framework with a confined imidazolium-based ionic liquid: a combined density functional theory and experimental vibrational spectroscopy study". In: *The Journal of Physical Chemistry C* 120.6 (2016), pp. 3295–3304.

[146] Kui Tan et al. "Stability and hydrolyzation of metal organic frameworks with paddle-wheel SBUs upon hydration". In: *Chemistry of Materials* 24.16 (2012), pp. 3153–3167.

[147] Daniel M. Dawson et al. "High-resolution solid-state 13C NMR spectroscopy of the paramagnetic metal–organic frameworks, STAM-1 and HKUST-1". In: *Physical Chemistry Chemical Physics* 15.3 (2013), pp. 919–929.

[148] Daniel M. Dawson et al. "13C pNMR of "crumple zone" Cu (II) isophthalate metal-organic frameworks". In: *Solid state nuclear magnetic resonance* 101 (2019), pp. 44–50.

[149] Daniel M. Dawson. "Combined theoretical and experimental investigations of porous crystalline materials". PhD thesis. St Andrews, United Kingdom: University of St Andrews, 2014.

[150] Farhana Gul-E-Noor et al. "Time dependent water uptake in Cu3 (btc) 2 MOF: Identification of different water adsorption states by 1H MAS NMR". In: *Microporous and Mesoporous Materials* 180 (2013), pp. 8–13.

[151] Farhana Gul-E-Noor et al. "Effects of varying water adsorption on a $Cu_3(BTC)_2$ metal–organic framework (MOF) as studied by $_1H$ and $_{13}C$ solid-state NMR spectroscopy". In: *Physical Chemistry Chemical Physics* 13.17 (2011), pp. 7783–7788.

[152] Gregory W Peterson et al. "Ammonia vapor removal by $Cu_3(BTC)_2$ and its characterization by MAS NMR". In: *The Journal of Physical Chemistry C* 113.31 (2009), pp. 13906–13917.

[153] Xi Xiang Zhang, Stephen S.-Y. Chui, and Ian D. Williams. "Cooperative magnetic behavior in the coordination polymers $[Cu_3(TMA)_2L_3]$ (L= H_2O, pyridine)". In: *Journal of Applied Physics* 87.9 (2000), pp. 6007–6009.

[154] Winfried Böhlmann et al. "Characterization of the Metal- Organic Framework Compound $Cu_3(benzene_{1,3,5}-tricarboxylate)_2$ by Means of $_{129}Xe$ Nuclear Magnetic and Electron Paramagnetic Resonance Spectroscopy". In: *The Journal of Physical Chemistry B* 110.41 (2006), pp. 20177–20181.

[155] Michela Todaro et al. "Determination of Geometry Arrangement of Copper Ions in HKUST-1 by XAFS During a Prolonged Exposure to Air". In: *The Journal of Physical Chemistry C* 121.44 (2017), pp. 24853–24860.

[156] Paul M. Schoenecker et al. "Effect of water adsorption on retention of structure and surface area of metal–organic frameworks". In: *Industrial & Engineering Chemistry Research* 51.18 (2012), pp. 6513–6519.

[157]   Jared B. DeCoste et al. "The effect of water adsorption on the structure of the carboxylate containing metal–organic frameworks Cu-BTC, Mg-MOF-74, and UiO-66". In: *Journal of Materials Chemistry A* 1.38 (2013), pp. 11922–11932.

[158]   Andreas Pöppl et al. "Untersuchungen zur chemischen Stabilität von Cu3 (btc) 2 (HKUST-1) durch N2-Adsorption, Röntgenpulverdiffraktometrie und EPR-Spektroskopie". In: *Chemie Ingenieur Technik* 82.7 (2010), pp. 1025–1029.

[159]   Juan Manuel Castillo, Thijs J.H. Vlugt, and Sofía Calero. "Understanding water adsorption in Cu- BTC metal- organic frameworks". In: *The Journal of Physical Chemistry C* 112.41 (2008), pp. 15934–15939.

[160]   Barbara Panella et al. "Hydrogen adsorption in metal–organic frameworks: Cu-MOFs and Zn-MOFs compared". In: *Advanced Functional Materials* 16.4 (2006), pp. 520–524.

[161]   Nadeen Al-Janabi et al. "Mapping the Cu-BTC metal–organic framework (HKUST-1) stability envelope in the presence of water vapour for CO2 adsorption from flue gases". In: *Chemical Engineering Journal* 281 (2015), pp. 669–677.

[162]   Hong Ki Kim et al. "A Chemical route to activation of open metal sites in the copper-based metal–organic framework materials HKUST-1 and Cu-MOF-2". In: *Journal of the American Chemical Society* 137.31 (2015), pp. 10009–10015.

[163]   Lukas Grajciar, Ota Bludsky, and Petr Nachtigall. "Water adsorption on co-ordinatively unsaturated sites in CuBTC MOF". In: *The Journal of Physical Chemistry Letters* 1.23 (2010), pp. 3354–3359.

[164]   Jordi Toda et al. "Water adsorption on a copper formate paddlewheel model of CuBTC: A comparative MP2 and DFT study". In: *Chemical Physics Letters* 587 (2013), pp. 7–13.

[165]   Wenjuan Xue et al. "Theoretical Insight into the Initial Hydrolytic Breakdown of HKUST-1". In: *The Journal of Physical Chemistry C* (2019).

[166]   Tianyi Wang et al. "Strategies for Overcoming Defects of HKUST-1 and Its Relevant Applications". In: *Advanced Materials Interfaces* 6.13 (2019), p. 1900423.

[167]   Mohamed EA Safy et al. "Probing the Water Stability Limits and Degradation Pathways of Metal-Organic Frameworks (MOFs)". In: *Chemistry–A European Journal* (2020).

[168]   Raynald Giovine et al. "The Surprising Stability of Cu3 (btc) 2 Metal–Organic Framework under Steam Flow at High Temperature". In: *Crystal Growth & Design* 18.11 (2018), pp. 6681–6693.

[169]   Petko St. Petkov et al. "Defects in MOFs: a thorough characterization". In: *ChemPhysChem* 13.8 (2012), pp. 2025–2029.

[170]   Arnau Carné-Sánchez et al. "Protecting Metal–Organic Framework Crystals from Hydrolytic Degradation by Spray-Dry Encapsulating Them into Polystyrene Microspheres". In: *Advanced Materials* 27.5 (2015), pp. 869–873.

[171] Zhedong Lin et al. "Postsynthetic strategy to prepare ACN @ Cu-BTCs with en-hanced water vapor stability and CO2/CH4 separation selectivity". In: *Industrial & Engineering Chemistry Research* 57.10 (2018), pp. 3765–3772.

[172] Kai Müller et al. "Dissolving uptake-hindering surface defects in metal–organic frameworks". In: *Chemical science* 10.1 (2019), pp. 153–160.

[173] Gerardo Majano et al. "Solvent-Mediated Reconstruction of the Metal–Organic Framework HKUST-1 (Cu$_3$(BTC)2)". In: *Advanced Functional Materials* 24.25 (2014), pp. 3855–3865.

[174] Xuejiao Sun et al. "A novel mechanochemical method for reconstructing the moisture-degraded HKUST-1". In: *Chemical Communications* 51.54 (2015), pp. 10835–10838.

[175] J. Dhainaut et al. "Systematic study of the impact of MOF densification into tablets on textural and mechanical properties". In: *CrystEngComm* 19.29 (2017), pp. 4211–4218.

[176] Arnau Carné-Sánchez et al. "A spray-drying strategy for synthesis of nanoscale metal–organic frameworks and their assembly into hollow superstructures". In: *Nature Chemistry* 5.3 (2013), p. 203.

[177] Adham Ahmed et al. "Hierarchical porous metal–organic framework monoliths". In: *Chemical Communications* 50.92 (2014), pp. 14314–14316.

[178] Yabing He et al. "Methane storage in metal–organic frameworks". In: *Chemical Society Reviews* 43.16 (2014), pp. 5657–5678.

[179] Hassane E.L. Mkami et al. "EPR and magnetic studies of a novel copper metal organic framework (STAM-I)". In: *Chemical physics letters* 544 (2012), pp. 17–21.

[180] Nour Nijem et al. "Ammonia adsorption and co-adsorption with water in HKUST-1: spectroscopic evidence for cooperative interactions". In: *The Journal of Physical Chemistry C* 119.44 (2015), pp. 24781–24788.

[181] Alexander Chucholowski et al. *Sulfuric acid esters of sugar alcohols*. US Patent 5,521,160. 1996.

[182] Heba Abourahma et al. "Coordination polymers from calixarene-like [Cu$_2$(dicarboxylate)$_2$]4 building blocks: structural diversity via atropisomerism". In: *Crystal growth & design* 3.4 (2003), pp. 513–519.

[183] Harry W Gibson et al. "Rotaxanes from tetralactams". In: *Macromolecules* 45.3 (2012), pp. 1270–1280.

[184] Mirian Elizabeth Casco et al. "Improved mechanical stability of HKUST-1 in confined nanospace". In: *Chemical Communications* 51.75 (2015), pp. 14191–14194.

[185] Ohad Fleker et al. "Preparation and properties of metal organic framework/activated carbon composite materials". In: *Langmuir* 32.19 (2016), pp. 4935–4944.

[186] *EMX User's Manual.* 1998.

[187] Stefan Stoll and Arthur Schweiger. "EasySpin, a comprehensive software package for spectral simulation and analysis in EPR". In: *Journal of magnetic resonance* 178.1 (2006), pp. 42–55.

[188] S Agnello et al. "Instantaneous diffusion effect on spin-echo decay: experimental investigation by spectral selective excitation". In: *Physical Review B* 64.17 (2001), p. 174423.

[189] *Avance Beginners Guide. User Guide NMR.*

[190] *Manual Bruker SENTERRA.*

[191] *STADI P. The Rapid, comprehensive modular system with unsurpassed reliability.*

[192] *ASAP 2020. Accelerated Surface Area and Porosimetry System.*

[193] *TA Instruments. Thermal Analysis.*

[194] George Socrates. *Infrared and Raman characteristic group frequencies: tables and charts.* John Wiley & Sons, 2004.

[195] Hui Wu, Taner Yildirim, and Wei Zhou. "Exceptional mechanical stability of highly porous zirconium metal–organic framework UiO-66 and its important implications". In: *The journal of physical chemistry letters* 4.6 (2013), pp. 925–930.

[196] Michael E Aulton and Kevin M G Taylor. *Aulton's Pharmaceutics E-Book: The Design and Manufacture of Medicines.* Elsevier Health Sciences, 2017.

[197] Bradley P Russell and M Douglas Levan. "Pore size distribution of BPL activated carbon determined by different methods". In: *Carbon* 32.5 (1994), pp. 845–855.

List of related publications

- **Terracina, A., Todaro, M., Mazaj, M., Agnello, S., Gelardi, F. M., Buscarino, G.** (2018). *Unveiled the source of the structural instability of HKUST-1 powders upon mechanical compaction: Definition of a fully preserving tableting method.* The Journal of Physical Chemistry C, 123(3), 1730-1741.

  COVER OF THE JOURNAL *of Physical Chemistry C* of the Volume 123, Issue 3 (2019), Pages 1527-2010 (https://pubs.acs.org/toc/jpccck/123/3)

- **Terracina, A., McHugh, L. N., Todaro, M., Agnello, S., Wheatley, P. S., Gelardi, F. M., Morris, R. E., Buscarino, G.** (2019). *Multitechnique Analysis of the Hydration in Three Different Copper Paddle-Wheel Metal–Organic Frameworks.* The Journal of Physical Chemistry C, 123(46), 28219-28232.

  COVER OF THE JOURNAL *of Physical Chemistry C* of the Volume 123, Issue 46 (2019), Pages 28219–28232 (https://pubs.acs.org/toc/jpccck/123/46)

- **McHugh, L. N., Terracina, A., Wheatley, P. S., Buscarino, G., Smith, M. W., Morris, R. E.** (2019). *Metal–Organic Framework-Activated Carbon Composite Materials for the Removal of Ammonia from Contaminated Airstreams.* Angewandte Chemie International Edition, 58(34), 11747-11751.

- **Vrtovec, N., Mazaj, M., Buscarino, G., Terracina, A., Agnello, S., Arčon, I., Janez Kovač, Zabukovec Logar, N.** (2020). *Structural and CO_2 Capture Properties of Ethylenediamine-modified HKUST-1 Metal-organic Framework.* Crystal Growth & Design.

- **Terracina, A., McHugh, L. N., Mazaj, M., Agnello, S., Cannas, M., Gelardi, F. M., Morris, R. E., Buscarino, G.** *Effects of mechanical compaction on the structure and on the hemilability of STAM-17-OEt powders.* Under submission.

Curriculum Vitae

Personal Information

Surname	Terracina
First Name	Angela
Nationality	Italian
Date of birth	September 18, 1992

Education

2017: Master Degree in Physics (110/110 cum laudem) at the University of Palermo, Italy.
Thesis: "*Modifiche delle proprietà magnetiche di polveri di HKUST-1 indotte da compattamento meccanico.*"; Tutor: Prof. G. Buscarino.

2015: Bachelor Degree in Physical Sciences (110/110 cum laudem) at the University of Palermo, Italy.
Thesis: "*Sensori distribuiti basati sulle fibre ottiche*"; Tutor: Prof. M. Cannas.

2011: Scientific High School (100/100) "Luigi Failla Tedaldi" of Castelbuono (PA), Italy.

Conferences

EuroMOF 2019, 3rd International Conference on Metal Organic Frameworks and Porous Polymers, Maison de la Chimie, Paris, France. October 27-30 2019:

- Talk contribution (Young Investigators Symposium): *Multi-technique analysis of the hydration in copper carboxylate Metal Organic Frameworks: a comparison between STAM-1, STAM-17-OEt and HKUST-1.*

- Poster contribution: *Hydration process of HKUST-1 and of its water-resistant counterparts STAM-17-OEt and STAM-1 investigated by Electron Paramagnetic Resonance*

FisMat 2019, Italian National Conference on Condensed Matter Physics, Catania, Sep 30 - Oct 4, 2019. Talk contribution: *Mechanical Compaction of MOF Powders: Definition of a Fully Preserving Tableting Method for Cu-BTC.*

MOF2020[WEB], Virtual Conference on Metal-Organic Frameworks and Open Framework Compounds, Sep 21 - 24, 2020.

Schools

First International School on Advanced Porous Materials (MOFSchool), Villa del Grumello, Como, June 17-21, 2019. **Poster presentation**: *Hydration process of HKUST-1 and of its water-resistant counterpart STAM-17-OEt investigated by electron paramagnetic resonance.*

Experiences

Participation to Erasmus Plus project: Oct 1, 2018 - Mar 31, 2019. Host Institution: St Andrews University, School of Chemistry. Referent person: Russell E. Morris.

Awards and prizes

MOF School 2019 Best Poster Award: for the poster presentation "Hydration process of HKUST-1 and of its water-resistant counterpart STAM-17-OEt investigated by electron paramagnetic resonance" at Summer MOF School, June 21, 2019.

Cover of The Journal *Physical Chemistry C* of the Volume 123, Issue 3 (2019), Pages 1527-2010 (https://pubs.acs.org/toc/jpccck/123/3)

Cover of The Journal *Physical Chemistry C* of the Volume 123, Issue 46 (2019), Pages 28219–28232 (https://pubs.acs.org/toc/jpccck/123/46)

Teaching Activities

- Lecture for the class *Fisica degli stati condensati*, for the Master degree in "Fisica", for the academic year 2017/2018.

  Title: *Effetti del compattamento meccanico e dell'interazione con l'acqua sulla struttura dei Metal-Organic Frameworks.*

Curatorship: Prof. Simonpietro Agnello

- Lecture for the class *Fisica degli stati condensati*, for the Master degree in "Fisica", for the academic year 2018/2019.

  Title: *Metal-Organic Frameworks: sintesi e caratterizzazione.*

  Curatorship: Prof. Simonpietro Agnello

- Lecture for the class *Fisica degli stati condensati*, for the Master degree in "Fisica", for the academic year 2019/2020.

  Title: *Metal-Organic Frameworks: sintesi e caratterizzazione.*

  Curatorship: Prof. Simonpietro Agnello

Acknowledgements